

Honda R&D

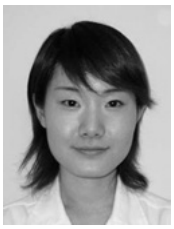
Technical Review

April 2005



Comment on the Cover

I created this because I wanted to depict the vivid, lively expressions of the engineers who work at Honda with a simple and warm touch. My intent was to represent the "joy of making things with individual quality and technical craftsmanship at Honda."



Akiko Taguchi
Wako R&D Center

Presentation of “RTL250F” Four-stroke Engine Trials Motorcycle

Toshinao TAKIGAWA* Eiichi ISHIKAWA*
Hiroyuki KAKINUMA* Fuyuki KOBAYASHI*

ABSTRACT

The RTL250F has a compact and lightweight 249 cm^3, water-cooled, 4-stroke engine. As the world’s first off-road vehicle with a batteryless electronically controlled fuel injection system (hereinafter referred to as batteryless PGM-FI system), the RTL250F has obtained the same or better racing performance than the RTL250R with a 2-stroke engine. Furthermore, the RTL250F motorcycle employs a kick-starter for engine ignition. The batteryless PGM-FI system utilizes a lower cost ECU (Engine Control Unit) integrated throttle body developed for small motorcycles. A control system was developed to obtain the drivability and usability required by a trials motorcycle. As a result, a commercially available trials motorcycle with a 4-stroke engine has been realized. This trials vehicle has shown competitive performance for the World Championship Trials.

1. Introduction

All manufacturers including Honda currently use two-stroke engines in trial competition motorcycles. The main reasons for this are that two-stroke engines feature superior throttle response from low engine speeds, and are lightweight and compact. However, due to a change in Federation Internationale de Motorcyclisme (FIM) regulations, the use of four-stroke engines from 2006 onward for all participating motorcycles has been mandated. Honda has taken the initiative and developed a four-stroke engine that provides superior competition ability, consisted with a high level of environmental suitability. The “RTL250F” trial motorcycle equipped with this engine was released in January 2005.

* Asaka R&D Center

2. Development Concept

The performances demanded to trial motorcycles include (1) a lightweight, slim body with lower center of gravity, (2) an engine with sufficient low-speed torque and the ability to deliver bursts of power up to high engine speeds, and (3) a linear throttle response during rapid opening. Therefore, the following four important development goals were set as the development concepts for a four-stroke engine trial machine with superior environmental suitability and racing potential.

(1) Equivalent or better handling, stability, and drivability than the two-stroke engine RTL250R.
(2) A compact and lightweight four-stroke engine.

(3) No noticeable differences in engine characteristics when switching from the current two-stroke engine model.
(4) Provide both environmental compliance and superior drivability.

3. Model Overview

Figure 1 shows an external view of the RTL250F, and Table 1 lists the major specifications along with those of the current two-stroke RTL250R. To provide the approximate equivalent racing potential as the two-stroke RTL250R, it was necessary to keep the same vehicle mass of 72 kg (dry vehicle mass). The RTL250F compensated for the increased engine mass, due to the change to a four-stroke engine, by reducing the vehicle body mass. These mass reductions were concentrated in the main frame, front and rear wheels, and brakes, etc (Fig. 2). In addition, the electrical parts were collected behind the engine in order to lower the center of gravity and concentrate the mass.

As shown in Fig. 3, in the batteryless PGM-FI system, the fuel injector is mounted directly onto the cylinder head to enhance throttle response, and the fuel pump is located inside the fuel tank to provide a stable supply of fuel even while undergoing intense vehicle body behavior, such as during trial competition (Fig. 4). The throttle body is based on an ECU integrated throttle body for small displacement motorcycles, but has been changed to an air screw type that enables the user to adjust the engine idle speed (Fig. 5). A batteryless system is used to reduce vehicle mass. Power is supplied only to the fuel pump and ECU during kick starting. In addition, a decompression cam is used and the kick ratio has been revised to enable smooth kick startability.



Fig. 1 External view of RTL250F

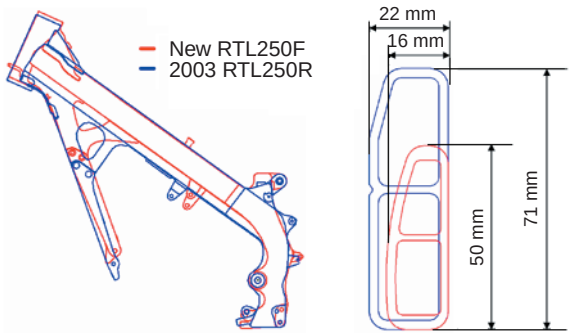


Fig. 2 Comparison of frame body

Table 1 Major specifications of RTL250R and RTL250F

RTL250R		
Items		Specifications
Overall length (mm)		2 020
Overall width (mm)		830
Overall height (mm)		1 130
Wheelbase (mm)		1 330
Ground clearance (mm)		340
Seat height (mm)		650
Caster angle (deg)		23° 20'
Trail length (mm)		65
Vehicle dry mass (kg)		72
Engine type		Liquid cooled 2-stroke single cylinder
Valve train		Crank case reed valve
Engine displacement (cm^3)		249
Bore × Stroke (mm)		72.2 × 61
Max. power (kW/r/min)		12.9/5 000
Max. torque (Nm/r/min)		26.5/4 000
Fuel supply system		Delorto PHBL26BS
Ignition system		Digital CDI
Transmission		5 speed constant mesh
Clutch type		Wet multi-plate type (hydraulic)
Fuel capacity (Liter)		2
Frame type		Aluminum twin-tube
Brake system	Front	Single 180 mm disc with twin-piston caliper
	Rear	Single 100 mm disc
Tire size	Front	2.75 × 21
	Rear	4.00 × 18
Suspension	Front	Telescopic
	Rear	Pro-link

RTL250F		
Items		Specifications
Overall length (mm)		2 010
Overall width (mm)		830
Overall height (mm)		1 130
Wheelbase (mm)		1 320
Ground clearance (mm)		335
Seat height (mm)		650
Caster angle (deg)		23°
Trail length (mm)		63
Vehicle dry mass (kg)		72
Engine type		Liquid cooled 4-stroke OHC single cylinder
Valve train		SOHC 4 valves
Engine displacement (cm^3)		249.1
Bore × Stroke (mm)		76.5 × 54.2
Max. power (kW/r/min)		14/7 000
Max. torque (Nm/r/min)		21.8/5 500
Fuel supply system		PGM-FI
Ignition system		Full transister
Transmission		5 speed constant mesh
Clutch type		Wet multi-plate type (hydraulic)
Fuel capacity (Liter)		1.9
Frame type		Aluminum twin-tube
Brake system	Front	Single 180 mm disc with twin-piston caliper
	Rear	Single 100 mm disc
Tire size	Front	2.75 × 21
	Rear	4.00 × 18
Suspension	Front	Telescopic
	Rear	Pro-link

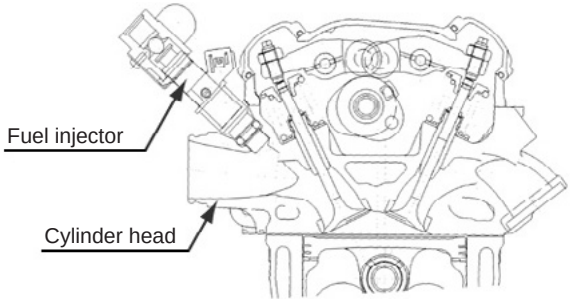


Fig. 3 Layout of fuel injector

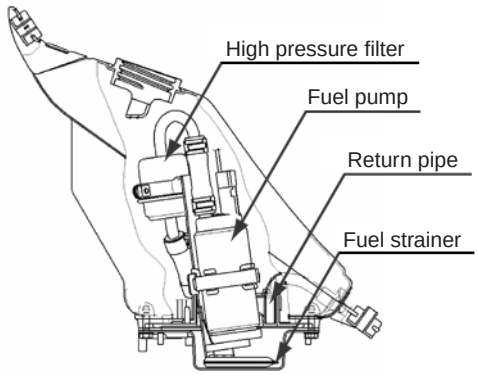
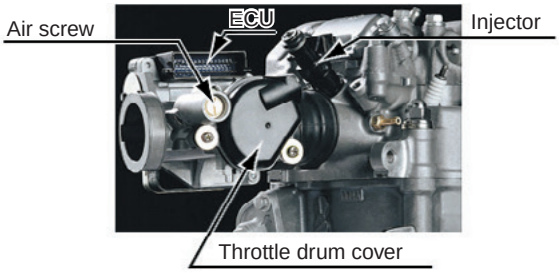


Fig. 4 Fuel tank assembly



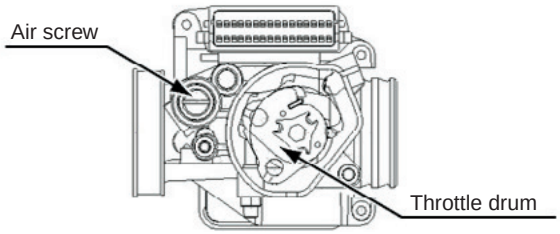


Fig. 5 Throttle body assembly

4. Engine

The engine layout is based on the commercial motocrosser, CRF250R, but significant modifications have been made to the crank case and other locations in order to satisfy the performance requirements of trial motorcycles such as a lower center of gravity and more compact size. Figure 6 shows a comparison of the overall engine size.

Figure 7 shows the output characteristics of the RTL250R (two-stroke) and RTL250F (four-stroke). The maximum output was controlled to 14 kW. The torque characteristics were flattened and priority was given to enhancing torque at low engine speeds. In addition, by increasing output in the range of partial throttle opening at low engine speeds, the equivalent or better torque feeling in the range of wide throttle openings was achieved. Although, the torque in this range is actually inferior to that of two-stroke engines.

4.1. Fuel Supply System

When a carburetor is used for the fuel supply, the intake duct area of the air cleaner must be reduced to enhance response during rapid throttle opening, but this factor lowers the output at high engine speeds. The employment of the batteryless PGM-FI system in the developed engine enabled simultaneous achievement of good throttle response and output at high engine speeds without reducing the intake duct area.

4.2. Exhaust System

The three-chamber silencer used in a conventional four-stroke engine trial motorcycle was changed to a straight type silencer. This reduced the reflected exhaust gas inside the silencer and made it possible to obtain flat output characteristics at entire engine speed range. In addition, the silencer material was also changed to aluminum to reduce mass.

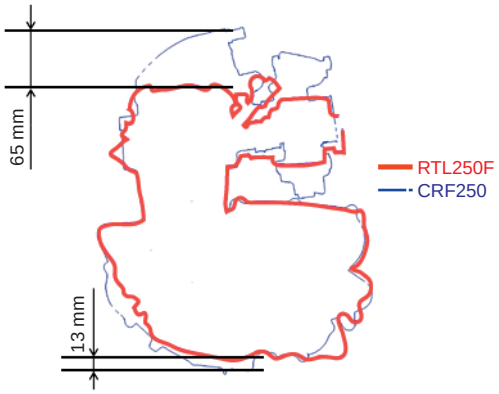


Fig. 6 Comparison of engine size

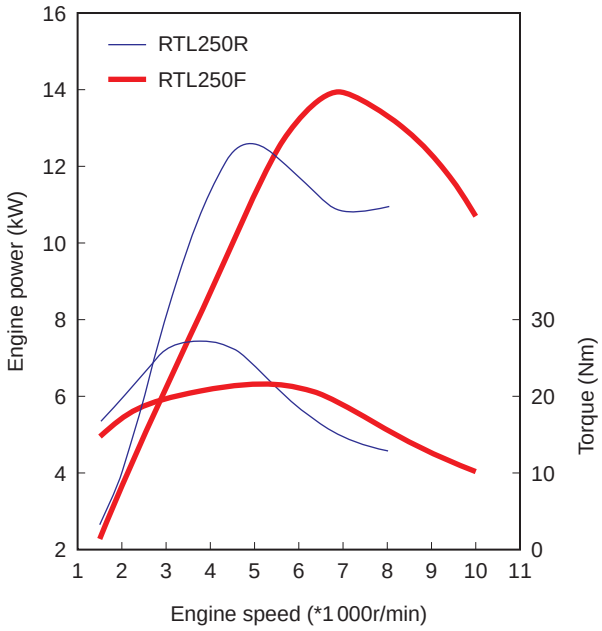


Fig. 7 Engine performance curve

4.3. Flywheel

A large diameter flywheel was used to enhance running using inertia mass (a running method in which high engine speed is maintained in the no-load state with the throttle wide open and rapid clutch connection performed in order to accelerate quickly from a standstill). The large diameter flywheel also increased anti engine stall performance and torque feeling at low engine speeds (Fig. 8).

4.4. Clutch

A large capacity (diameter 140 mm) hydraulically actuated, release bearing, right-side directly actuated type clutch was used. This allows the rider to realize a lever load that can be operated by a single finger, and maintain connecting performance that responds linearly to rider operation and is stable even with the clutch half-engaged at high engine speeds. In addition, the slave piston was incorporated into the clutch cover to achieve a more compact size (Fig. 9).

4.5. Lubrication System

Regarding engine lubrication, the CRF250R's closed type crankcase was modified, mainly by changing the area around the intake port (Fig. 10). Like the CRF250R, the AC generator chamber is used as the oil tank, but the RTL250F has a structure with additional separators and ribs and a modified oil port that supplies the oil around the strainer during driving, using the oil adhered to the external side of the rotating large diameter flywheel. This made it possible to reduce the amount of oil from 830 cm^3 to 600 cm^3 and increased ground clearance by 13 mm. With this reduction in oil the piston rings were changed from two rings to three, with the aim of reducing oil consumption. In addition, the modification to three rings also contributed to an enhanced torque feeling at low engine speeds.

Regarding lubrication of the transmission, the oil recovery ability using the clutch outer was increased by changing the shapes of the oil return guide ribs and transmission cover. This made it possible to reduce the amount of transmission oil from 770 cm^3 (CRF250R 2004 model year) to 570 cm^3 while maintaining seizure resistance of the transmission (Fig. 11).

4.6. Three-point Support Crankshaft Structure

A needle roller bearing was used on the left side of the three-point support crankshaft. The rotational deflection inhibiting effects of this roller bearing reduced vibration and increased durability (Fig. 12).

4.7. Valve Train

In order to reduce the engine height, the unicam system (a single cam shaft system that drives the intake valve with a valve lifter, and the exhaust valve with a rocker arm) used by the CRF250R was changed to a SOHC system in which both the intake and exhaust valves are actuated by a rocker arm (Fig. 13). This made it possible to reduce the cylinder head height by 65 mm. In addition, the spark plug inclination was kept below 28° by greatly offsetting the camshaft, thus allowing a central arrangement (Fig. 14).

The conventional two-valve system is adequate for engines that emphasize torque at low engine speeds, but the engine must also be rotated smoothly at high engine speeds, so a four valve system

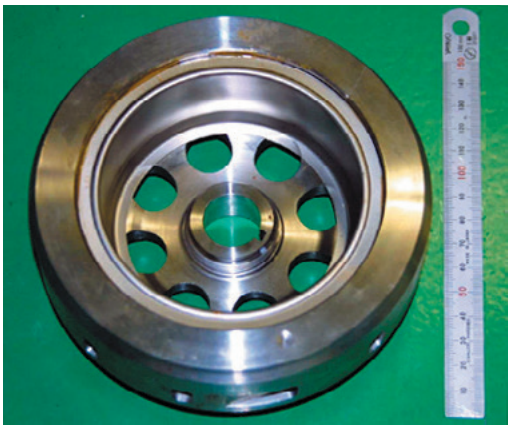


Fig. 8 AC generator flywheel

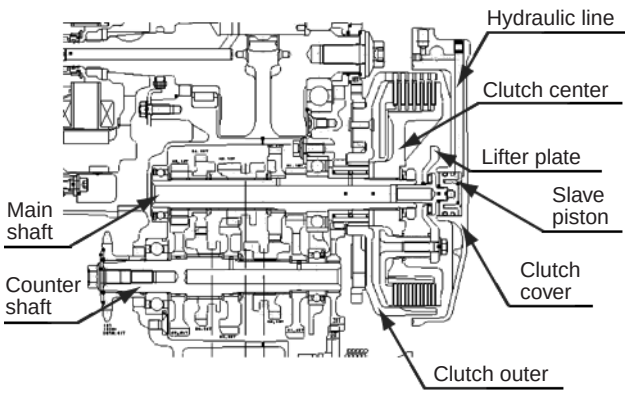


Fig. 9 Clutch system

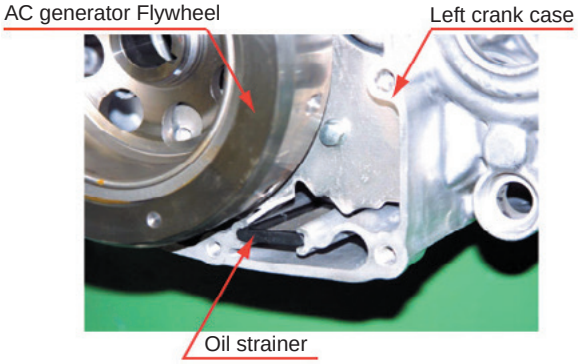


Fig. 10 Engine oil lubrication system

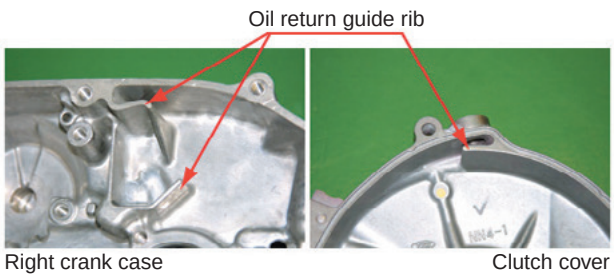


Fig. 11 Transmission oil return system

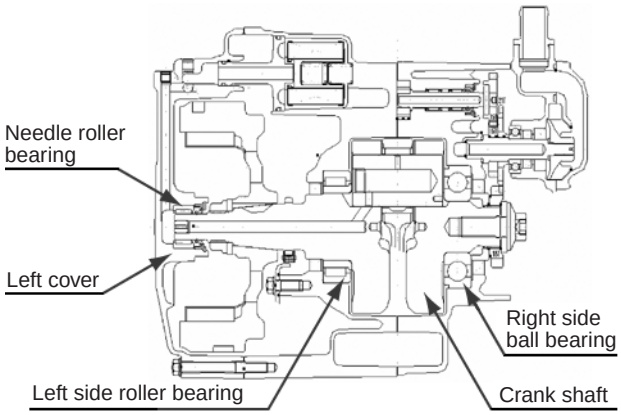


Fig. 12 Crankshaft

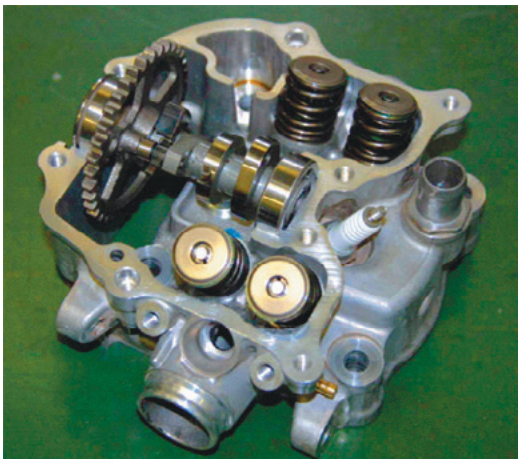


Fig. 13 Cylinder head with valve system

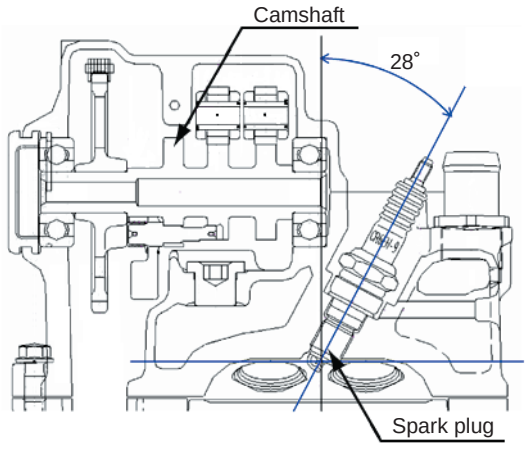


Fig. 14 Arrangement of camshaft and spark plug

was used. SCM carburizing and quenching was performed on the camshaft to reduce the mass without loss of fatigue strength.

5. Batteryless PGM-FI System

Figure 15 shows an overview of the batteryless PGM-FI system. Gasoline fed by pressure from the fuel pump passes through a high pressure filter inside the tank and is then sent via a high pressure fuel pipe to the injector. The high pressure gasoline is adjusted to 294 kPa by a pressure regulator, and then returned to the tank by a fuel return pipe.

The ECU of the batteryless PGM-FI system calculates the fuel injection quantity and timing based on the engine speed, throttle opening, negative pressure in the intake pipe, intake air temperature, atmospheric pressure calculated from the negative pressure in the intake pipe, water temperature, and crank angle information. The ECU then determines the targeted air fuel ratio in accordance with the load.

The ignition timing is controlled to the optimum timing based on a three-dimensional map determined by the throttle opening and engine speed.

Drivability requirements for trials competitions include the response during rapid throttle opening from low engine speeds and the torque feeling at low engine speeds. When expert riders drive through rock sections such as shown in Fig. 16, they control the machine by opening and closing the throttle and subtle clutch operations. At such times it is extremely important that the throttle response be exactly as the rider wishes. Figure 17 shows the throttle speed ($\Delta\theta$th: delta throttle) data per unit time during trial competition, together with $\Delta\theta$th data for the first lap from the start of Moto GP Japan GP (Motegi) 2004 for reference. This shows that trial competition differs from road races in that high throttle speeds are often used from low engine speeds. In order to meet these requirements, the RTL250F is the first mass production motorcycle to use fuel injection control after double calculating at engine speeds of 5 000 rpm or less. An overview of this control is described below.

As mentioned above, the greatest drivability requirement issue is the ability to follow rapid throttle opening operations from extremely low engine speeds near idling. Conventionally, the fuel injection quantity was calculated one time for a crank rotation angle of 720° through the intake, compression, expansion, and exhaust process. However, this produced a long fuel injection quantity calculation interval. The issue of insufficient response, due to delayed calculations with respect to rapid throttle operations, such as during trial competition, was present. Therefore, calculation of the fuel injection quantity was increased to two times, with recalculation (the second calculation) performed just before the intake timing. The fuel injection timing was then modified based on these recalculation results. This allowed optimal adjustment of the fuel injection quantity in response to rapid throttle operations, which in turn made it possible to supply the targeted air fuel ratio. In addition, double calculation was performed only at engine speeds of 5 000 rpm or less. The calculation of the fuel injection quantity was performed only once at high engine speeds, which have shorter calculation intervals. This system can be controlled by even a low cost ECU with slow processing speed (Fig. 18).

Figure 19 shows the in-cylinder pressure during rapid throttle opening. The pressure for the two-stroke engine (RTL250R) rises significantly from the start of throttle opening, so riders experience good throttle response. As mentioned above, in order to allow a smooth switchover from two-stroke engine motorcycles, the development concept for the RTL250F focused on achieving a response during rapid throttle opening equivalent to that of a two-stroke engine. As a result, adoption of the new control system described above obtained the same pressure rise as a two-stroke engine, thus realizing a good throttle response.

Stabilization of the air fuel ratio can be given as a major reason for using the batteryless PGM-FI system. In preliminary tests performed with carburetor specifications, the air fuel ratio fluctuated

widely in accordance with the large changes in vehicle body behavior of typical trial driving. This caused the engine to stall during rapid throttle opening from idling, or when braking (when running downhill, etc.). In addition, throttle response delay occurred due to the delay of the negative pressure in the intake pipe during rapid throttle opening. However, adopting the PGM-FI system and modifying the fuel pump arrangement completely eliminated these phenomena.

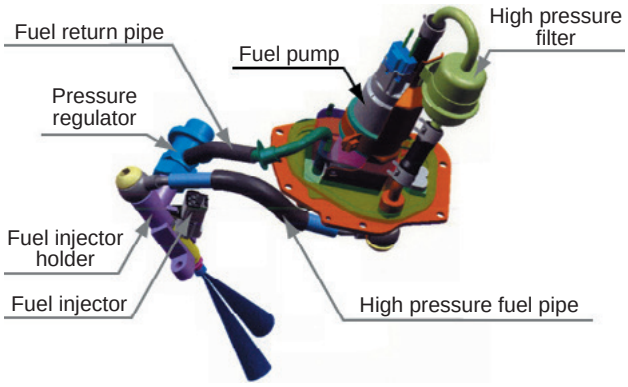


Fig. 15 Fuel line system



Fig. 16 Rock section

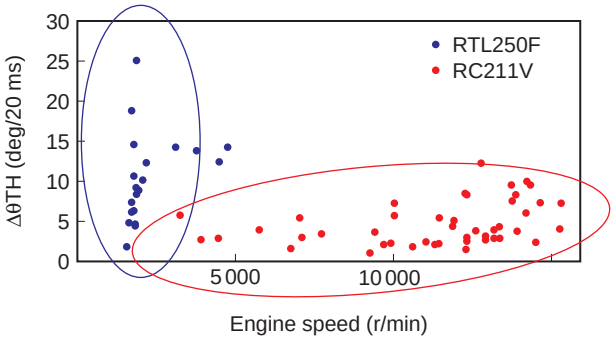


Fig. 17 Comparison data of throttle speed

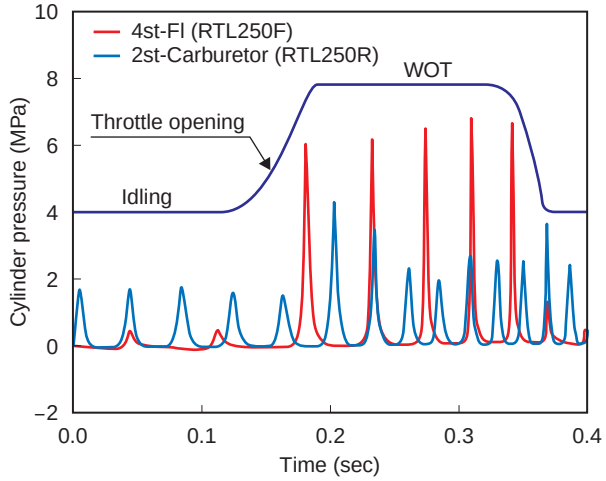


Fig. 19 Comparison of cylinder pressure at rapid throttle opening

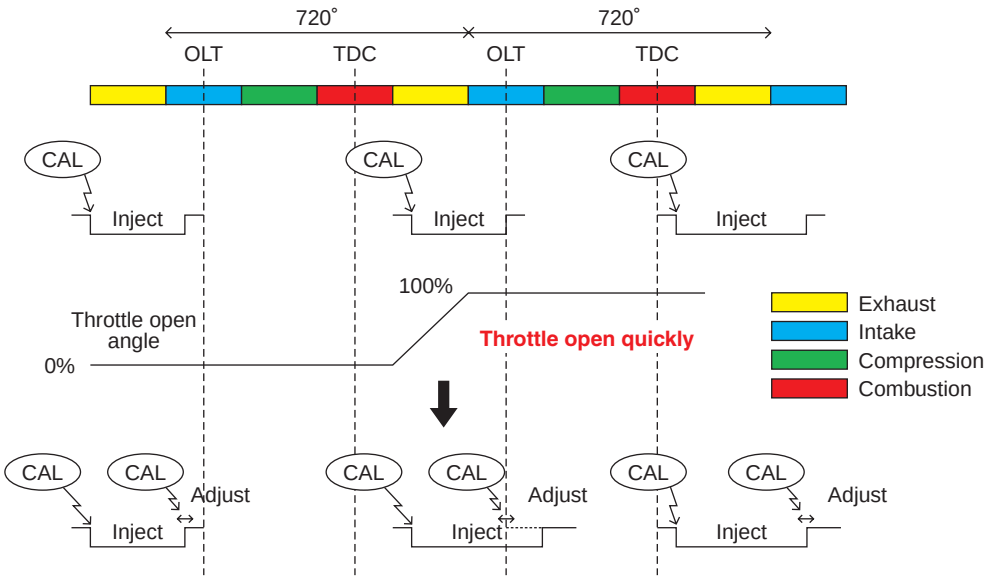


Fig. 18 Injection timing chart

6. Electrical System

The electrical system uses a batteryless system to reduce vehicle mass. In order for this batteryless system to allow kick starting, the AC generator is a three-phase star connection type that generates an output current of 7.5 A at a rotational speed of 1 000 rpm, and has characteristics that provide the necessary amount of electric power at low rotations during kick starting. Figure 20 shows the output characteristics of the AC generator. The current and voltage of the electrical power generated by the AC generator are regulated to 14.4 VDC by a three-phase full-wave commutator type regulator rectifier, smoothed by a 10 000 μF capacitor, and then supplied to each electrical load. The regulator and capacitor are located together with the bank angle sensor and fan motor relay on the electrical equipment stay in order to reduce the voltage drop and simplify wiring. These parts are fixed on the crankcase which also helps to concentrate the mass. Figure 21 shows an external view of the electrical equipment stay and the electrical equipment located on it. When kick starting electric power is supplied only to the fuel pump, fuel injector, ignition coil and control ECU, but not to the cooling fan motor. This makes it possible to supply sufficient fuel from the first rotation of the crankshaft. The voltage drop and vehicle mass were reduced by eliminating the drive relay and connecting the fuel pump directly to the power supply.

When the motorcycle falls down the engine is stopped by stopping the ignition coil and the injector, approximately seven seconds after the stacking signal is input to ECU from the bank angle sensor. The system is batteryless so when the engine stops the AC generator does not generate power and the fuel pump stops automatically. Figure 22 shows an overview of the electrical system.

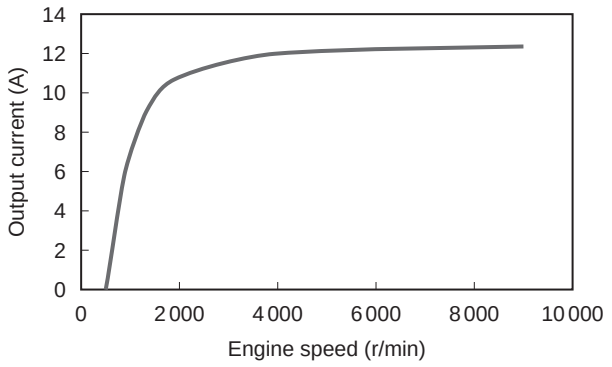


Fig. 20 Output characteristic of AC generator

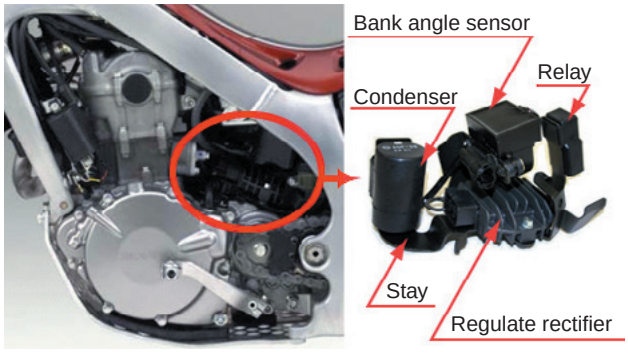


Fig. 21 External view of electrical equipments

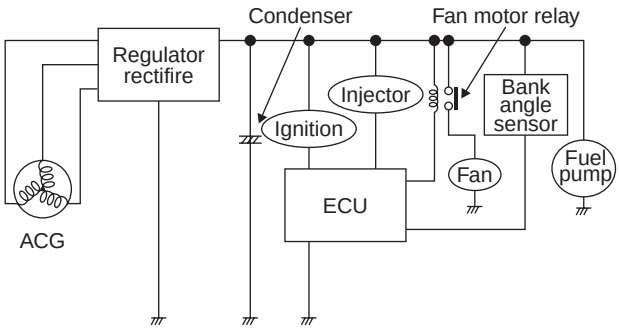


Fig. 22 Electrical system

7. Conclusion

The RTL250F was developed with a wide target market from beginning riders to World Championship Trial (WCT) users. A commercial prototype motorcycle participated in the WTC Motegi Round held in Japan in 2004, and achieved the favorable results of 9th place on both days of the two-day competition. This 250 cm^3 four-stroke commercial prototype motorcycle was able to achieve sufficient results amidst upper ranks dominated by the two-stroke works motorcycles of various manufacturers, thus the high potential of the new engine was verified.

Reference

(1) Shimada, N., Akamatsu, S., Ueda, M., Hayashi, A., Hirakata, Y.: Development of an ECU Integrated Throttle Body System Module for Compact Fuel Injection System Used in Small Motorcycles and Scooters, Honda R&D Technical Review, Vol. 15, No. 1, p. 83-88

■ Authors ■



Toshinao TAKIGAWA



Eiichi ISHIKAWA



Hiroyuki KAKINUMA



Fuyuki KOBAYASHI

Development of 2005 Model Year US Odyssey Incorporating “King of Minivans” Concept

Satoshi SAGARA* Makoto FUKUDA* Toshiya KANDA*
Yoshikazu TAKAHIRA* Masatoshi TANIOKA* Yuichi TSUKADA**

ABSTRACT

The 2005 model year US Odyssey was developed as the “King of Minivans,” providing superior styling and excellent utility combined with drivability and quality that rival any luxury sedan. It is built on the foundation of Honda safety and environmental leadership, and will become the benchmark for the next generation of minivans.

The Odyssey powertrain employs North America’s first Variable Cylinder Management (VCM) engine, achieving best-in-class fuel economy. The chassis ensures a quiet cabin through a subframe supported with rubber mountings, and at the same time, achieves handling stability.

The interior incorporates many new ideas for the small item storage spaces required of a minivan, adopting features such as the world’s first rotary in-floor storage unit. The seats work to provide maximum utility, with the adoption of one- motion stowing for the 3rd row seats, and in the eight-passenger specification, a stowable 2nd Row PlusOne Seat that can be easily fitted in the center of the second row.

The vehicle structure is designed to perform well in frontal impacts, offset impacts, and car-to-car collisions with the adoption of Honda’s Advanced Compatibility Engineering Body structure. In addition, the Odyssey combines existing safety features with side curtain airbags and Vehicle Stability Assist (VSA) as standard for all grades. The Odyssey is a vehicle that demonstrates Honda’s commitment to “Safety for Everyone.”

1. Introduction

In 1994, Honda entered the US minivan market with the US Odyssey. Accompanying the full model change in 1998, the Odyssey became the true North American benchmark minivan, continuing to receive high praise through today.

Japanese manufacturers have actively entered the North American minivan market, facing the competition of minivans produced by US manufacturers. The market competition is now getting more intense. In the development of this third generation Odyssey, Honda has carried out thorough market research and product comparisons with competitor vehicles, and restudied the features and uses required of a minivan to develop the new Odyssey with the aim of creating a next generation minivan that will set the benchmark.

At the development stage, never forgetting the essence of Honda, the new Odyssey was developed so that the customer is impressed with its appearance, with its drivability, and with its utility. To

* Tochigi R&D Center
** Wako R&D Center

achieve this, technology was developed that actualizes the drivability expected of a Honda, and new features have been developed that incorporate new ideas in all aspects of the exterior and interior. As a result, this next generation minivan provides safety, drivability and a feeling of quality equal to that of a luxury sedan.

2. Concept and Development Goals

The concept of “King of Minivans” was selected for the 3rd generation Odyssey. To actualize this, the new Odyssey was developed as a fun and adventurous product for young families in their 30’s, the main users of minivans, as one target group. It also provides quality on a par with a luxury sedan, appealing to empty nesters as a second target group, based on the results of market research.

Development proceeded towards the following targets, in order to actualize the concept.

(1) Safety and Environmental Performance
- Development of best-in-class collision safety performance and safety features
- Best-in-class fuel economy and emissions performance

(2) Styling
- An innovative luxury and high-quality feel that exceeds expectations of the minivan class
- An exterior that feels powerful and solid
- An interior that makes one think of high quality and makes a first class impression

(3) Drive Performance and Handling Stability
- Best-in-class engine power and drivability
- Handling, ride comfort, and quietness performances on a par with European luxury sedans, breaking out of the minivan segment

(4) Utility
- A seat arrangement that can accommodate eight passengers, and that anyone can easily operate
- Ensuring convenient, easy-to-use storage space, never before seen in a minivan
- Creation of an environment that is comfortable for children and adults, with enhanced comfort features

3. Product Performance and Main Technologies

3.1. Design

3.1.1. Packaging

The goal of the package was to provide best-in-class practicality in the minivan category, by increasing interior space and improving the convenience of storage and seats.

While adding many new features such as a sunroof, curtain airbags, and a power tailgate, etc., the interior space was increased. Knee clearance in the 3rd row was increased over that of the previous model, by reducing front overhang by 50 mm, ensuring the largest 3rd row space in the class and achieving increased collision safety performance, so that even adults can easily sit in the 3rd row. This was accomplished without increasing total length. Moreover, the layout is such that the 3rd row seats can be stowed without removing their headrests. By moving the spare tire from under the floor to the side of the 3rd row seats, in-floor storage has been given a new design (Fig. 1).

3.1.2. Exterior design

While the exterior design maintains the minivan package, it has broken free of the strong, existing minivan image of the family, and moved towards the key words of “Powerful and Solid.” This expresses the character of emphatic and majestic solidity.

The styling is based on the watchword “Cyber Lion,” with a handsome sense of presence and strong legs.

In addition, plated mold, lights, and the grill, etc., have all been created using luxury sedan methods, exhibiting a premium feel that has not been seen in a minivan previously (Fig. 2).

3.1.3. Interior styling

The concept for the interior styling is “Premium Class Interior.” By combining a comfortable first class lounge space with an innovative cockpit, the functionality of a family car is emphasized, while the family image is wiped away. These contradictory elements are both achieved.

The instrument panel extends laterally, with the driver as the reference point making it driver-oriented. The lateral expansion is strengthened by gauges that are shaped as if they have wings extended. The styling is horizontal in tone, like that of a luxury sedan, and unlike the vertical orientation of other companies’ minivans (Fig. 3).

The gauges are large in diameter, making them easy to read, with a freshness added through the use of a light gradation that gives the image of a lunar eclipse. The shift knob is given an optimum location, optimum shape, and optimum operation feel vis-à-vis the driving position. At the same time, due consideration has been given to the shift knob as well as instrument panel for achieving easy walk-through, which is an essential part of a

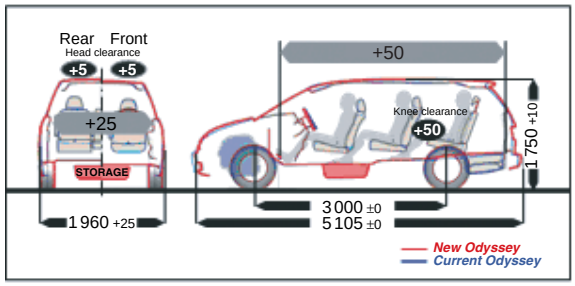


Fig. 1 Comparison of packaging design of new and previous models

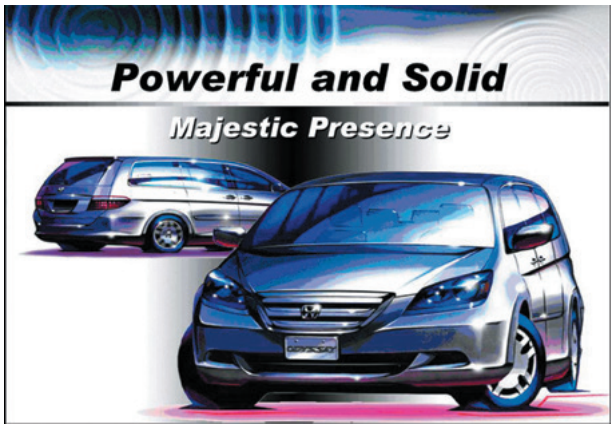


Fig. 2 Exterior design concept for new Odyssey

minivan. The linings such as on the sliding doors are of deeply sculpted shapes, with a finish like that of a luxury sedan. They increase the quality feel for the interior as a whole.

The luxury specification has a sporty, formal interior trim of black leather not available in minivans to date. In addition, the seats achieve both an excellent feeling of hold and a relaxed quality ride comfort. The fabric is modern with a quality taste.

Moreover, many clever utilities, seat arrangements, and features have been incorporated so that families can use it while having fun.

3.2. Interior

The interior, particularly in the front seats, was aimed to express a strong feeling of quality with metallic tone panels and illuminated gauges. At the same time, based on the results of many surveys of use by the targets users and thorough investigations and research, it was aimed to incorporate the convenience and practicality required of a minivan in the actual vehicle.

3.2.1. Seats

In terms of product appeal for a US minivan, the market requires not only a seat giving ride comfort but also the easy-to-use seat arrangement. Therefore, the goal was to satisfy both of these requirements.

The second row side seats are captain's chairs of a generous size. It is possible to accommodate eight passengers with the adoption of 2nd Row PlusOne Seat, which is a compact and lightweight seat in the center of the vehicle (Fig. 4). This PlusOne Seat can be used as a table if the cushion is removed and the seat back is folded down. It can be removed with a simple operation, creating a seven-passenger vehicle with a center walk-through. The use of high tensile steel reduces its weight, so it can easily be carried or moved. In addition, removing the Lazy Susan (described later), stowed under the floor in front of the 2nd row, creates a space where the PlusOne Seat can be stored, if its legs are folded in.

The 3rd row seats have evolved beyond the old rotary stowing type. They have been given a 60/40 split, and are even easier to operate thanks to one motion stowing which makes it possible to stow them simply by folding the seat back over, once the lock has been released (Fig.5). When returning the seats to their upright position, the operation load is less than half of what it was, thanks to the use of a spring at the pivot points on each side. One person can carry out these operations.

3.2.2. Interior trim

Part of the interior concept is revolutionary storage. This focuses on in-floor storage, together with additional trays and large pockets creating advanced storage capabilities. In-floor storage, in particular, has been enhanced with a new rotary stowing box (Lazy Susan) in the floor at the foot of the 2nd row. This contributes to greater product appeal, with its convenience and new design (Fig. 6). The structure of the storage box is such that the lock mechanism releases when the lid is opened, and it can easily be rotated manually. There is a small window in the lid, meaning it can also be reached from the front seats.

The sliding doors have integrated sunshades, increasing the functionality of the vehicle as a minivan, in which children often ride in the 2nd row.



Fig. 4 Second row seats arrangement (2nd row +1 seat)



Fig. 3 Interior design concept for new Odyssey



Fig. 5 Third row seats (6:4 split)

A curved mirror has been added to the roof console. Use of the back of the sunglasses holder as a conversation mirror makes it possible for a driver to glance at the faces of the children in the back seat. This plays an important role in improving communication within the cabin (Fig. 7).

3.2.3. Air-conditioning

Adoption of Tri-Zone Automatic Climate Control system that includes dual zone automatic climate control for the front and a separate control for the 2nd row and rearward enables the product appeal for all seats to be increased. In addition, with the adoption of floor ducts and outlets, 2nd row and 3rd row heater performance is improved.

In the heater control panel, locations of the switches and function displays were designed based on the feedback and requests of actual customers and local staff in the US, improving ease of use (Fig. 8).

3.3. Electrical Equipment

The electrical features have been enhanced with the aims of improving the convenience of a minivan for the family, and the Touring grade is provided with features similar to those of a luxury sedan.

3.3.1. Rear Entertainment System (RES)

The RES is made up of a display screen for the rear seats that is mounted in the ceiling and a DVD player, and functions to prevent boredom for the passengers in the 2nd and 3rd rows even on long drives. The visual image is even better than before, with North America’s first 9-inch wide display. Moreover, the system has been made thinner by having the tall parts inside the display offset from the screen itself, and when the display is stowed, there is minimal protrusion from the ceiling. While it is a large screen, the walk-through performance maintained by open space is beyond comparison with other vehicles. An infrared wireless remote control that can be stored on the ceiling is used for operation for the first time in RES, reducing the possibility of forgetting where the remote control is. Consideration has been given to improving operation at night, and illumination has been added to the operation buttons. In addition, there are fewer buttons, making it easier for children to operate (Fig.9). The remote control for the RES is a two-handed type familiar to children through video and computer games. The special headphones have an ASIMO motif, creating friendliness.

Personal surround technology has been developed that provides sensation of a 5.1 channel surround audio output through the headphones. With conventional headphones, the stereo image is in the middle of the person’s head, creating a feeling of pressure. In comparison, with this personal surround system, transmission within the cabin, characteristics of sound dispersion into the external ear canal, and characteristics of head-related transmission are corrected by a special IC before sound is output to the headphone. This means that the stereo image moves outside the head, and sound with releasing and surrounding feelings is given as if listening to a 5.1 channel speaker. This contributes to a reduction in fatigue, when listening to the headphones for a long period.

3.3.2. Audio, NAVI

The Touring model provides the high quality, high power sound appropriate for a luxury minivan with its premium audio system having a 360-watt amplifier as standard equipment. For superb sound quality, the system has 17 cm aramid reinforced polypropylene cone speakers, aluminum dome tweeters, and a specially designed subwoofer box. The subwoofer box is positioned under the front passenger seat. The shape of the box utilizes resonance, and low sounds with punch are actualized in compact and lightweight speakers.

The NAVI (navigation system) features an 8-inch display for better visibility, which opens and closes electronically. It holds a 6-disc CD changer, and achieves a compact instrument panel layout. Operating switches on the steering wheel makes it possible to search



Fig. 6 Lazy Susan



Fig. 7 Conversation mirror



Fig. 8 Heating control switches



Fig. 9 Rear entertainment system display

for street names and location names through voice recognition. To give one example of enhanced content, it includes data from the 2004 Zagat restaurant guide data, the highest volume restaurant guide in the USA. Provision of information to the customers is better than ever (Fig. 10).

Furthermore, the NAVI specification includes an XM radio, with more than 100 channels of programming provided by satellite, so that it is not necessary to change stations even when traveling across the entire continent. The liquid crystal display, which can display up to 16 characters of written information, is placed within the head unit.

3.3.3. Gauges

The gauges of the Odyssey Touring model employ a multi-information display that can display tire pressure (using TPMS), a compass (8 directions), trip functions (immediate and average fuel economy, distance traveled, driving period, average speed), a welcome display, external temperature, oil deterioration index, corner sensor nearing indication, and various warnings (Fig. 11).

Using this display, it is also possible to create a customized menu that matches customer preferences, such as door lock settings, lighting, etc. These customized items can be activated on either of the two key fobs, and the memory seat operation can be carried out. In addition, the adoption of steering switches makes operation easier.



Fig. 10 Navigation system display



Fig. 11 Multi-information meter display

3.4. Engine Performance

In order to realize the new Odyssey's power plant concept of "Best Minivan Drivability and Fuel Economy," the power plant employs a V6 i-VTEC VCM engine, based on the North American MDX V6 SOHC-VTEC engine fitted with a Variable Cylinder Management (VCM) system that was installed in the Japanese INSPIRE[(1)]. The following fundamental targets were set to make this minivan the best in class.

(1) Best-in-class acceleration performance
(2) Best-in-class fuel economy
(3) Low emissions performance

3.4.1. Engine overview and main specifications

Figure 12 shows the external appearance of an engine for the new Odyssey, output characteristics are given in Fig. 13, and Table 1 gives the main specifications.

3.4.2. Drivability and fuel economy

In order to achieve both drivability and fuel economy, VCM technology was added to the 3.5L V6 engine, achieving acceleration performance and reduced fuel consumption as shown in Fig. 14.

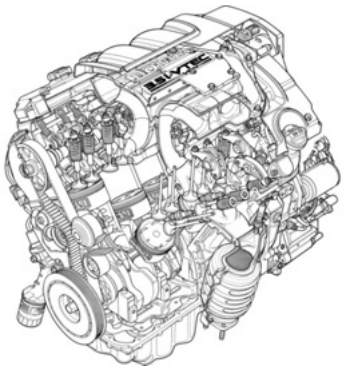


Fig. 12 View of V6 i-VTEC VCM Engine

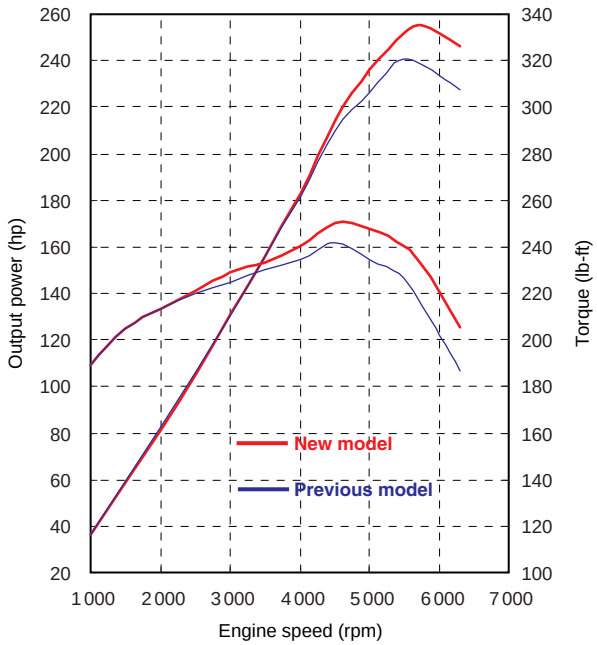


Fig. 13 Output performance

Table 1 Main specifications of engine

	New model		Previous Odyssey
Engine type	60°V-6 SOHC VTEC	60°V-6 i-VTEC VCM	60°V-6 SOHC VTEC
Displacement (cm³)	3471	3471	3471
Compression ratio	10.0	10.0	10.0
Fuel	Regular unleaded	Regular unleaded	Regular unleaded
Max·power (hp/rpm)	255/5 750	255/5 750	240/5 500
Max·torque (lb-ft/rpm)	250/5 000	250/4 500	242/4 500
Transmission	5AT	5AT	5AT
Fuel economy	19/25	20/28	18/25
Emissions	LEV II-ULEV	LEV II-ULEV	NLEV (LDT2)

3.4.3. Environmental performance

Figure 15 outlines the systems used to achieve low emissions in this engine. The V6 SOHC-VTEC/i-VTEC VCM engines use high-atomization, multi-hole fuel injectors, and each bank has its own independent emission control systems.

In addition to the above emission control systems, adoption of a high-precision A/F ratio control system has helped achieve excellent environmental performance of a 75% reduction in NOx, in comparison with the current model’s NLEV (LDT2). This performance meets the “LEV II – ULEV” standards (Fig. 16).

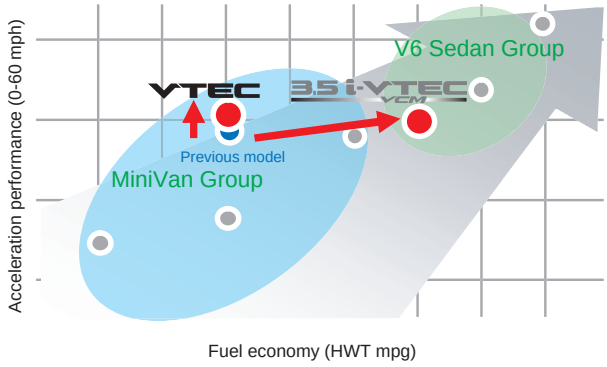


Fig. 14 Driving performance and fuel consumption

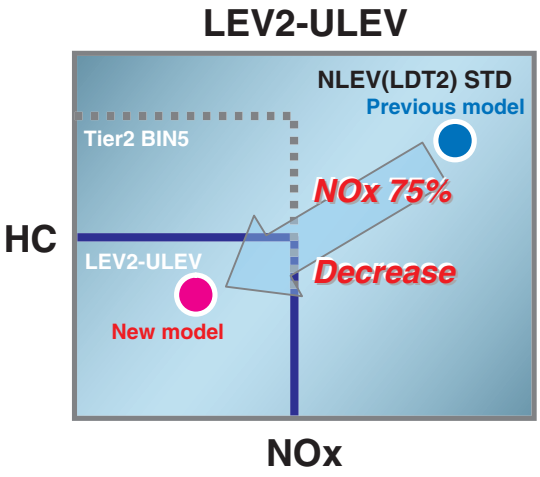


Fig. 16 Emissions performance

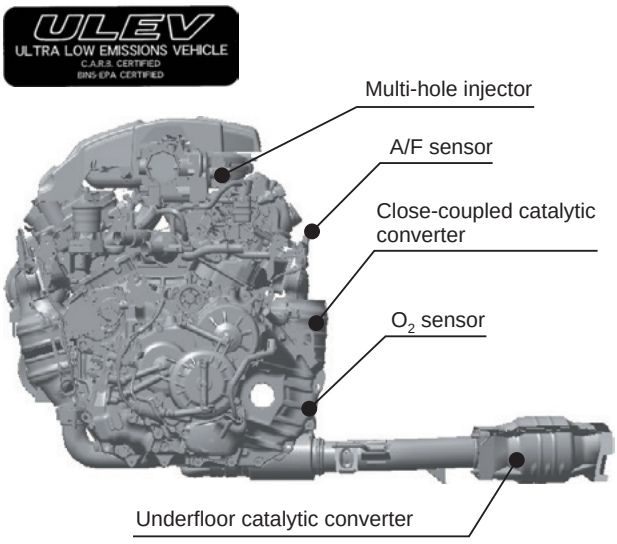


Fig. 15 Emission control system

3.5. Chassis Performance and Technology

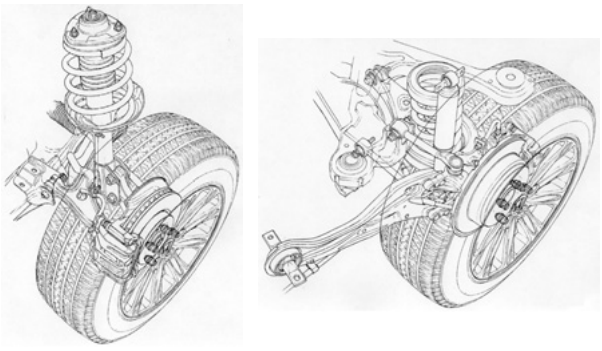
A carpool lane is a special lane on US highways, where it is permitted to drive only if there are two or more people in the vehicle. Taking as its key word “Carpool Express,” this vehicle can drive with superior steering stability and excellent riding quality in the carpool lane. The chassis has been developed in order to actualize this concept.”

3.5.1. Suspension

In order to achieve both steering stability and ride comfort, based on the previous model acclaimed in the market, the front suspension utilizes struts, while the steering stability has been enhanced though optimization of geometry. In addition, adoption of force axis control springs wound symmetrically left and right, optimization of steering friction, and high-precision alignment are combined to give enhanced straight-line performance (Fig. 17).

The rear suspension is based on an existing in-wheel, double-wishbone suspension. Responsiveness has been enhanced through a damper layout close to the axle fluctuation locus, and a 30% increase in side force rigidity was promoted through the adoption of a 3rd generation bearing.

In addition, the diameter of the tires was increased (225/60R16 → 235/65R16), and other measures taken in order to improve ride comfort.



Front suspension Rear suspension

Fig. 17 View of suspension for new Odyssey

3.5.2. Subframe structure

In order to reduce road noise, the subframes were given a vibration-resistant structure, which is effective in attenuating road surface input, but conventionally this has been an issue when seeking to balance it with steering stability performance (side force rigidity, etc.).

This subframe was developed with the goals of continuing to increase steering stability, which has been evaluated highly thus far, while making improvements in ride comfort and road noise performances. Based on the following points of view, the ideal body support points were set at the design stage considering the suspension mounting points, and a vibration resistant structure with the enlarged rear subframe was adopted. At the same time, the previously mentioned suspension characteristics were tuned uniquely for minivans.

(1) Enlarging the front and rear, left and right spans of the vibration resistant support rubber mountings, optimizing those spring constants

(2) The front and rear supporting points to the body are set so that subframe steering, in which the suspension geometry moves in the toe-in direction, is achieved when turning (that is, side force is input) (Fig. 18, A < B)

As a result, there is no disruption of alignment when there is side force input, and it is possible to ensure a greater vibration insulating performance than what has been offered conventionally.

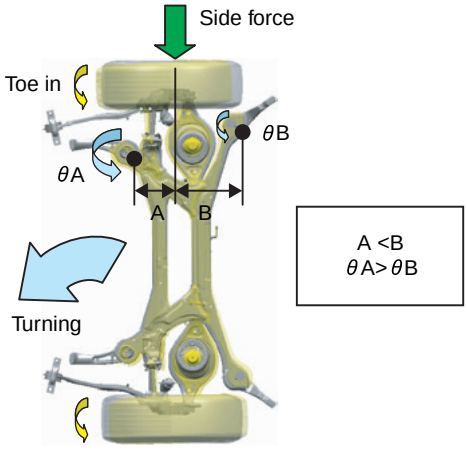


Fig. 18 Configuration of rear suspension subframe

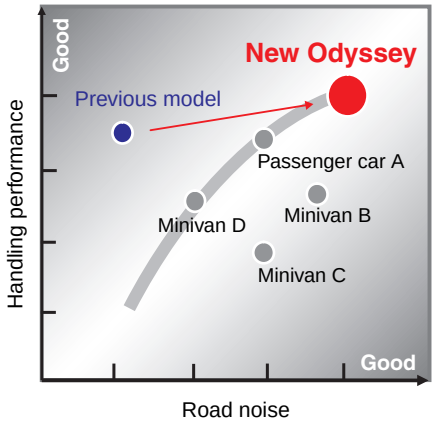


Fig. 19 Handling and road noise performance

This enables increased steering stability that is best in the minivan class, and at the same time road noise and ride comfort were achieved (Fig. 19).

3.5.3. New pedal system

Honda has adopted its first adjustable pedal system, designed to enhance the comfort of drivers of various sizes. Forward and back adjustment of the pedal position makes it possible for the driver to have a comfortable driving position. The switch has been placed on the instrument panel for ease of operation.

A special feature of this system is that a link mechanism is used, making it possible to move the acceleration and brake pedals 76 mm to the back, with the forward-most position being taken as the standard position, using a single motor. The structure is such that there are no changes to the tread level difference between the acceleration and brake pedals, nor to pedal ratio, within the adjustment range (Fig. 20).

As for the acceleration pedal, at the same time as integrating the mechanism generating tread force and the position sensor, a compact, lightweight acceleration pedal module was adopted.

3.5.4. Run-flat tire system

A US market survey shows that there is a demand has grown for run-flat tires, for safety, convenience, and security reasons.

The new model Odyssey has adopted the PAX system, an inner support ring type of flat-running tire that is beneficial in helping reduce rollovers, and which gives better steering stability and ride comfort than side support flat-run tires (Fig. 21, 22). The structure of the system includes the tire, the wheel, a support ring that carries the load of the vehicle if pressure is lost, and a Tire Pressure Monitoring System (TPMS) that monitors tire pressure.

A completely new bead structure has been created, that helps prevent the tire coming off the bead, particularly when driving with low tire pressure, and at the same time helps to reduce hysteresis loss when the tires are rolling.

In this application development, body reinforcement to offset an increase in road surface input was optimized. At the same time, steering stability when driving with low tire pressure was increased and unique suspension settings were established so that even when the vehicle has a flat tire, the vehicle can be driven at 50 mph for 125 miles without needing to fit the spare tire.

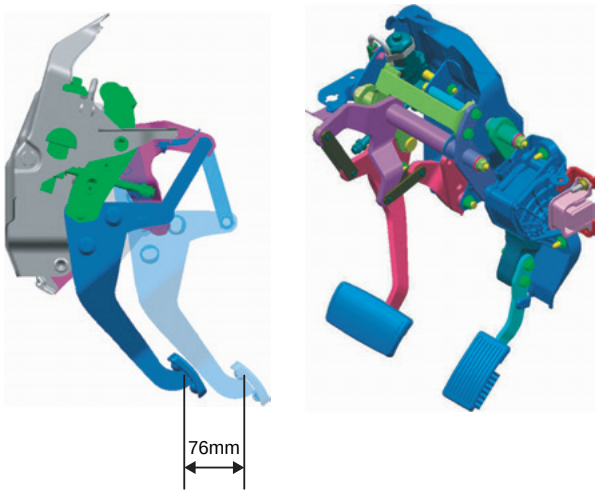


Fig. 20 Adjustable pedal system

3.6. Body Performance

3.6.1. Collision safety performance

Based on the “Safety for Everyone” concept, North America’s first body with compatibility measures (Advance Compatibility Engineering: ACE)[2] was applied to the minivan segment. In addition, Honda has addressed the new regulations in FMVSS208 and FMVSS301, as well as the Insurance Institute for Highway Safety’s new Side Impact Crashworthiness Evaluation (IIHS SICE) standard.

From the point of view of minimizing collision stroke in front impact collisions due to the expansion of the cabin area, an ACE body structure was adopted in which the front bulkhead section was given a closed structure, and formed to a board (Fig. 23). The force load is distributed to the frame and the pillar, to help achieve high collision safety performance. In addition, light truck vehicles like minivans can cause more damage to small cars in car-to-car collisions. However, the ACE body structure disperses and absorbs collision energy, to help reduce such damage. For side impact collisions, the center pillar has been given a divided structure, actualizing a lightweight, high-rigidity pillar. In addition, concerning passenger protection performance, all grades have an interior with head impact protection on cabin pillars and roof sides, as well as side curtain airbags with rollover sensors for side impacts. As pedestrian protection measures, the front of the body uses an impact absorbing structure that helps reduce injury to a pedestrian.

3.6.2. Body rigidity

Computer simulations were used in designing the body, making it possible to achieve sedan-level body rigidity by optimizing members for a frame having the same body length but an increased cabin length of 50 mm, an increased overall length of 25 mm, and large cabin openings.

The basic framework combines the aforementioned North American first ACE body structure for the engine bay, with a member around the front damper base and a cross member underneath the upper dashboard to ensure rigidity for steering stability. In the rear, the structure includes highly efficient connecting cross members between the floor and frame (Fig. 24). In addition, weight-reducing techniques were adopted for fuel economy improvements, including the adoption of 440/590 grade high tensile steel sheets with a steel sheet weight ratio of 45.3%. The body-in-white weight is the same as the previous model, and the body torsion rigidity is improved by 20% while the cabin is larger.

3.7. Noise and Vibration

In order to provide passengers in every seat with a quiet and comfortable space, full consideration was given to improving noise and vibration (NV) product appeal performance. At the same time, one goal was NV product appeal that does not cause the passengers to be aware of the switch to the VCM system adopted in the high output 3.5L engine.

3.7.1. Active Noise Control technology[3],[4]

With the engine adopted, one issue was an increase of noise and vibration level due to an increase in torque changes when the VCM

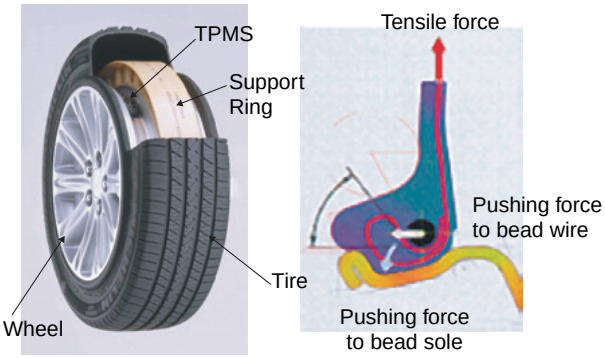


Fig. 21 Run flat tire system (Pax Tire system)

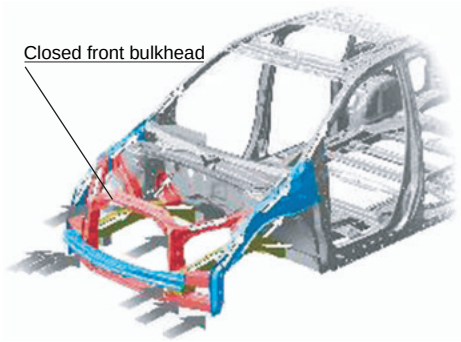


Fig. 23 Advanced compatibility engineering construction

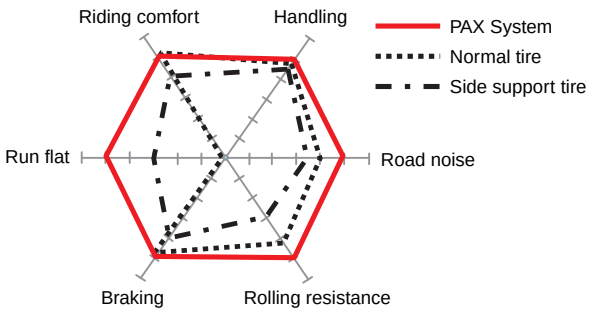


Fig. 22 Comparison of tire system performance

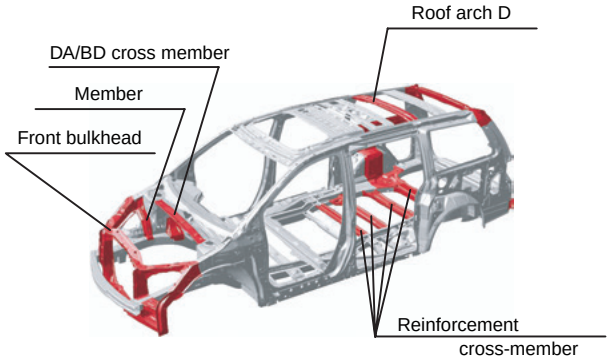


Fig. 24 Configuration of whole body construction

Table 2 Technologies for noise and vibration control

	Boom	Vibration	Shock
Active control engine mount	○	○	
Active noise control system	○		
Electric throttle control			○
Lock up control Lock up long torsion spring		○	○

system operated. However, the Active Control Engine Mount (ACM) system and Active Noise Control (ANC) technologies, used in the INSPIRE and the ELYSION, have been adopted in the new Odyssey, with special settings. In addition, switch shock was reduced through cooperative controls between the electronic throttle control and lock up control (Table 2).

As a result, booming noise, vibration, and shock were reduced, achieving a high NV performance with which the passengers are not aware of switching in the VCM system.

3.7.2. Engine noise reduction

The 3.5L V6 engine installed in the new model Odyssey uses a thin, lightweight intake manifold that achieves both weight reduction and quietness.

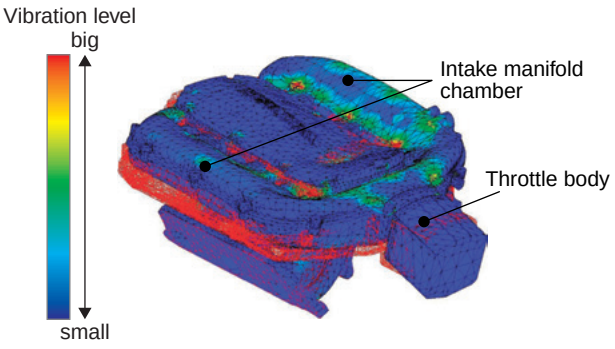


Fig. 25 Radiation noise from inletmanifold

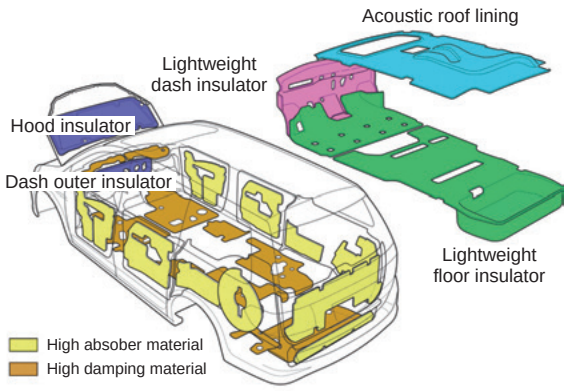


Fig. 26 Lightweight soundproofing materials

Starting with the intake manifold chamber, which contributes greatly to radiation noise, the rigidity tuning of each part was efficiently carried out, minimizing the worsening of noise due to weight reduction (Fig. 25). As a result, best-in-class noise reduction for a minivan (engine quietness) was maintained, and at the same time, weight reduction was achieved (-26%).

3.7.3. Lightweight soundproofing package

Traditionally, soundproofing materials to reduce transmission noise with sound insulation materials are applied to reduce cabin noise. However, the new model Odyssey applies a damping material to reduce noise radiated from the floor surface, and adopts a lightweight, sound-absorbing type of soundproofing system. Parts using sound absorbing material include the dashboard insulator, floor mat, and roof lining, as well as a wide variety of other components. This means that the surface area for sound absorption is extended, noise in the high frequency range is greatly reduced, and a level of quietness that is best in the minivan class is ensured.

As a result, at the same time as quietness in the cabin is improved, a weight reduction of –15 kg has been achieved, in comparison with the previous model.

4. Conclusion

The new model Odyssey has inherited the acclaim of the old model, and development started with the expectation of creating new value.

In addition to the technology that aimed at actualizing high safety and environmental performances, which should ensure the new Odyssey's position as the next generation minivan benchmark, it was aimed to actualize high levels of sophisticated styling, performance, and utility. For that purpose, the Odyssey should provide joy to its users and should be the best in class vehicle.

Efforts were made to improve performance of the interior and exterior design, powertrain, body, and chassis, etc. and to enhance comfort features that included safety features. As a result, the 2005 model year US Odyssey was developed as the "King of Minivans" providing drivability and a quality feel that match those of a luxury sedan.

The development engineers have always put themselves in the customer's position, have persistently pursued new and creative ideas for product development, and have strived to actualize their dreams. They believe that they have created a minivan that is full of appealing features.

This development project was completed thanks to the generous cooperation of many people, both in the company and outside it. The authors would like to take this opportunity to express their sincere gratitude and appreciation.

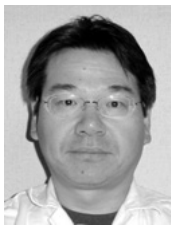
References

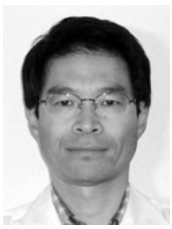
(1) Yasuki, S., Asaki, Y., Tashiro, H., Matsuoka, H., Kono, T.: Development of New Intelligent Tourer 2004 Model INSPIRE, Honda R&D Technical Review, Vol. 16, No. 1, p. 1-10

(2) Yoshimoto, T., Taguchi, Y.: Innovative Body Structure for Compatibility, 2004 JSAE Annual Congress Proceedings, No. 45-04, p. 11-14 (2004)

(3) Matsuoka, H., Mikasa, T., Nemoto, H.: Development of Active Control Engine Mount, Honda R&D Technical Review, Vol. 15, No. 2, p. 209-214
(4) Inoue, T., Takahashi, A., Minowa, S., Sano, H.: Development of Active Noise Control System for Engine Booming Noise, Honda R&D Technical Review, Vol. 15, No. 2, p. 201-208

■ Authors ■


Satoshi SAGARA


Makoto FUKUDA


Toshiya KANDA


Yoshikazu TAKAHIRA


Masatoshi TANIOKA


Yuichi TSUKADA

Development of 2005 Model Year ACCORD Hybrid System

Masaaki KAIZUKA* Toshitaka IMAI* Susumu ISHIKAWA*
Manabu NIKI* Hiromitsu ADACHI*

ABSTRACT

The 2005 model year ACCORD Hybrid was developed to enhance the driving performance of a V6 luxury sedan while retaining the fuel economy of a compact-class, 4-cylinder CIVIC sedan. The base 3.0L V6 engine has been equipped with Variable Cylinder Management (VCM) to decrease parasitic pumping losses in the engine, while motor assist has been employed to extend the operating range of the 3-cylinder operation mode. Both these factors have contributed to improved fuel economy. The Integrated Motor Assist (IMA) system applies new technologies to the high-voltage electrical equipment, including fine patterning of the inverter chips as well as the use of an Interior Permanent Magnet (IPM) rotor. The result has been a 20% increase in maximum power and a 26% increase in maximum torque. A hybrid compressor fitted with a high-voltage drive has been employed to increase the commercial appeal of idle stop. In order to offset the increase in weight from the IMA system, aluminum has been employed in the bumper beams and certain other parts to reduce weight. All of these fuel saving technologies have resulted in a level of fuel economy, equal to that of the compact-class, 4-cylinder CIVIC sedan, achieving 29 mpg in US City mode and 37 mpg in US Highway mode.

1. Introduction

The demand for vehicles with high fuel economy and low emissions continues to increase, given the need to protect the quality of our air and slow the depletion of fossil fuel resources. A great deal of attention has therefore been focused on high fuel economy vehicles employing hybrid systems. In order to respond to the demands for improved fuel economy and reduced emissions, Honda released the ultra-high fuel economy hybrid vehicle Insight[1),2)] in 1999, and the compact class CIVIC Hybrid[3)] in 2001. For the 2005 model year ACCORD Hybrid, Honda has equipped its 3.0L V6 engine with Variable Cylinder Management (VCM)[4)], a cylinder idling system with the capacity to disable multiple cylinders in cruising mode. This, coupled with an efficient five-speed automatic transmission results in high cruising efficiency, increasing the vehicle's appeal in the US market. The IMA system employed in the ACCORD Hybrid was designed on the basis of the system fitted in the CIVIC Hybrid.

2. Issues in Achieving High Fuel Economy and Development Goals

To achieve high fuel economy in the CIVIC Hybrid, a motor assist system was employed while reducing the displacement of the engine from the base 1.5L to 1.3L. The increased power

* Tochigi R&D Center

provided by the motor assist was not used to contribute to enhanced dynamic performance but to compensate for the reduction in power caused by the reduced displacement of the engine. The 3.0L V6 engine employed in the ACCORD Hybrid is provided with VCM, which means that the engine effectively runs at a displacement of 1.5L when the rear bank of three cylinders is closed. In this way, the VCM generates the same effect in terms of improved fuel economy as previously achieved by the reduction in displacement of the CIVIC Hybrid engine, which enables the increased power provided by the motor assist system to be used to enhance dynamic performance.

The development goal for the new system in the ACCORD Hybrid was therefore to employ VCM to effectively reduce the displacement of the engine, enabling the development of a mid-size hybrid vehicle combining superior dynamic performance to existing 3.0L models with fuel economy equivalent to that of the compact-class, 4-cylinder Civic sedan (Fig. 1). This paper will discuss the technologies employed to improve fuel economy, the IMA system and the vehicle technologies that were instrumental in enabling the achievement of the target fuel economy and driving performance.

3. Hybrid System and Technologies for Improved Fuel Economy

As Fig. 2 shows, the new IMA system employs the identical layout and configuration used in the CIVIC Hybrid system. The power train, located at the front of the vehicle, positions a motor between the engine and transmission, while an Integrated Power Unit (IPU), equipped with a high-voltage 144 V battery and a Power Control Unit (PCU), is located at the rear. The system is electrically connected by 3-phase high-voltage cables running between the front and rear of the vehicle. Figure 3 shows an exterior view of the power train.

Drive-By-Wire (DBW) and torque management control, which operates in cooperation with the cylinder idling system, were added to the existing idle stop, power assist and regeneration systems to improve fuel economy. In addition, the power of the electric motor and high-voltage electrical equipment was increased to enhance dynamic performance over the base vehicle. The ratio of contribution of each of the various systems to the improvement of fuel economy over the base vehicle is shown in Fig. 4. In the previous system, power assist was provided to aid mainly in increasing engine torque. In the new system power assist is also employed to increase the operating range of the cylinder idling mode, further improving fuel economy.

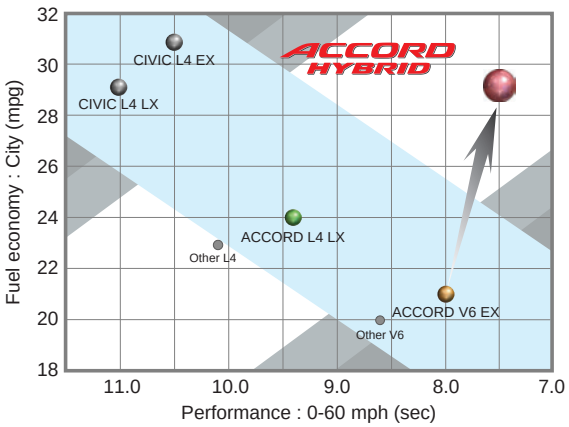


Fig. 1 Fuel economy vs. performance

To ensure the efficient use of energy and power, the driving pattern in which fuel consumption was lowest, as shown in Fig. 5, was employed as the basic control pattern for the system. Power from the electric motor is used to increase the frequency of cylinder idling. This enables 3-cylinder operation to be maintained even under gentle acceleration, whereas under the previous cylinder idling control the system would revert from 3-cylinder to 6-cylinder operation under these same conditions. In addition, monitoring of brake pressure has enabled power regeneration in the motor to be increased and cylinder idling to be activated under braking, thus increasing the amount of energy regeneration.

Figure 6 shows a conceptual diagram of the engine torque and electric motor torque in relation to the total torque output by the power plant during acceleration. Torque output and distribution of

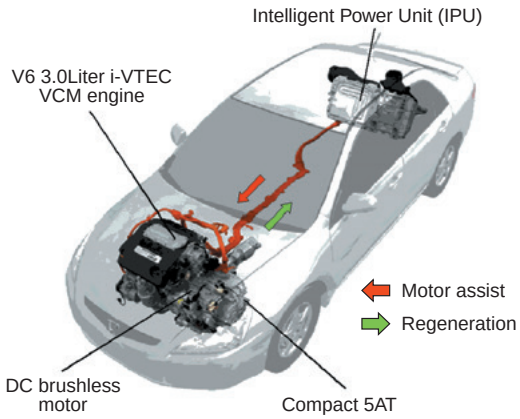


Fig. 2 IMA system configuration

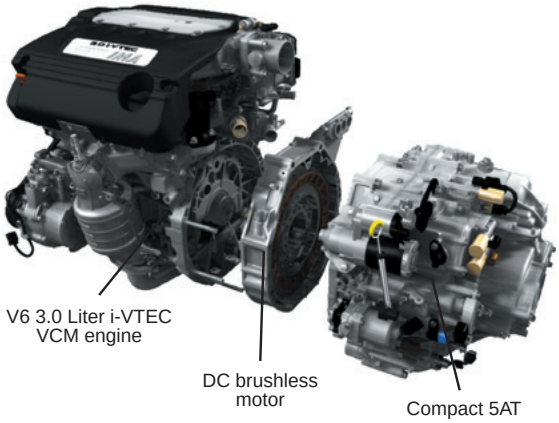


Fig. 3 Layout of IMA power plant

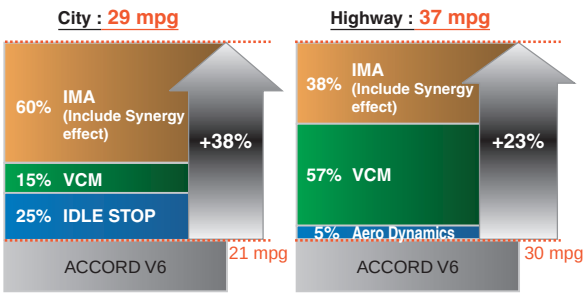


Fig. 4 Ratio of contribution of various systems of US LA4 mode fuel economy

the engine and electric motor are decided by target torque requirements at the crankshaft according to the energy management software. In addition to extending the range of cylinder idling discussed above, the system cuts fuel and draws torque from the electric motor to drive the vehicle when throttle opening is low, further improving fuel economy. Figure 7 shows the range of 3- and 6-cylinder operation in this system. The use of motor assist has enabled 3-cylinder operation in ranges that previously required 6-cylinders.

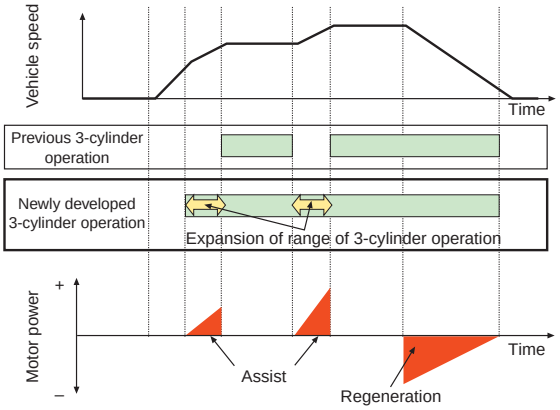


Fig. 5 Characteristics of 3-cylinder operation

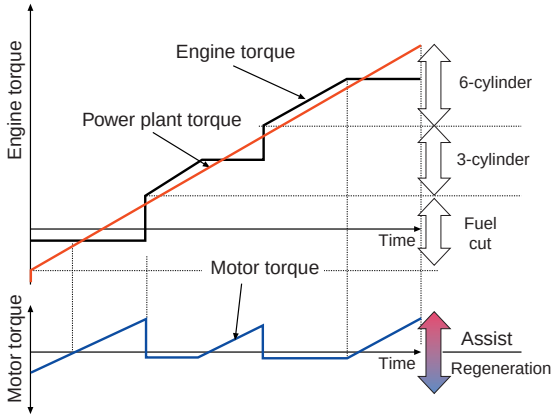


Fig. 6 Characteristics of torque output

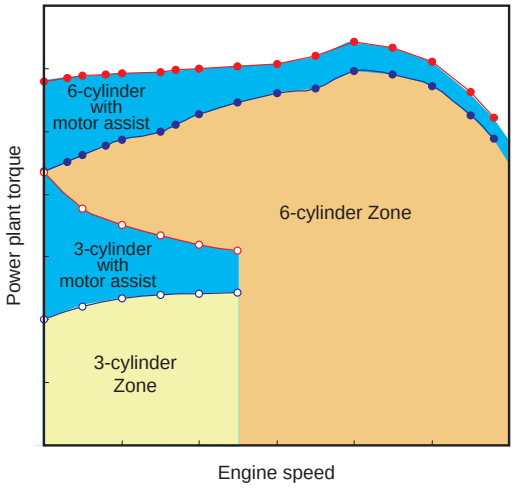


Fig. 7 Ranges of 3- and 6-cylinder operation

4. Power Plant Configuration and IMA System

4.1. Engine / Transmission

The 3.0L V6 engine used as the main power source in the ACCORD Hybrid has been equipped with the VCM system employed in the Japanese INSPIRE and the US Odyssey, enabling pumping losses to be reduced by means of instantaneous closure of the valves in one bank of cylinders and engaging 3-cylinder operation in response to changes in driving load.

To give the vehicle greater appeal in the US market, a 5-speed automatic transmission offering superior efficiency in cruising mode has been employed together with the newly developed trochoid-type electrical oil pump shown in Fig. 8. The electrical oil pump maintains oil pressure in the hydraulic circuits which are closed when the idle stop system is in operation, ensuring a solid coupling with the starting gear clutch to enable smooth takeoff (Fig. 9).

The highly responsive lock-up clutch shown in Fig. 10 has been employed to further improve fuel economy. The response time of the new clutch is one-third that of the former model, improving fuel economy by approximately 1.9% (Fig. 11).

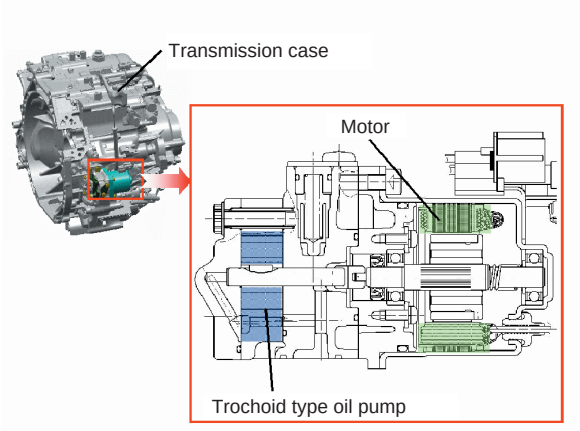


Fig. 8 Electric oil pump

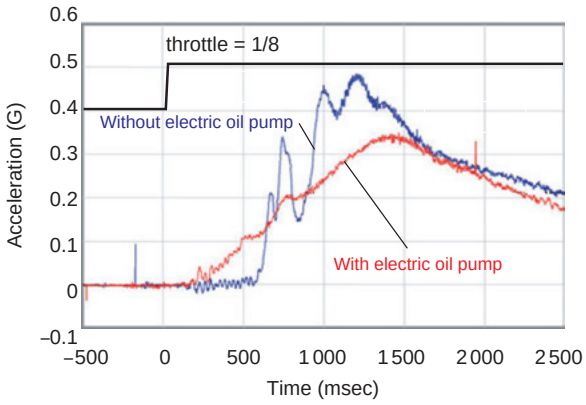


Fig. 9 Difference in acceleration with and without electric oil pump

4.2. IMA System

In addition to making the IMA system more advanced than the unit employed in the CIVIC Hybrid, power of the motor was increased while its size was reduced. Additionally, weight and size of the high-voltage electrical equipment and battery were reduced to better match them to the V6 engine and ACCORD body.

4.2.1. Electric motor

In the electric motor, the rotor type Surface Permanent Magnet (SPM) employed in the former model has been replaced by a rotor type Interior Permanent Magnet (IPM) to enable efficient use of reluctance torque (Fig. 12). In addition, the thermal resistance of the rare earth magnet built into the rotor has been enhanced, and its maximum energy production capacity increased by approximately 15%.

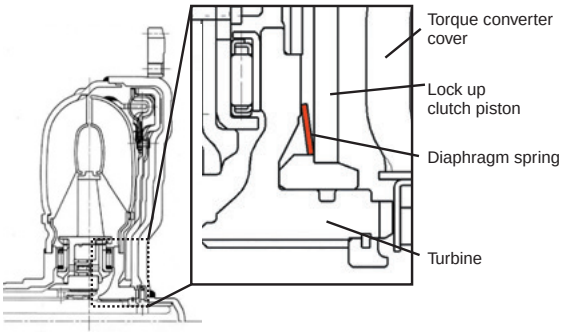


Fig. 10 High-speed lock-up clutch

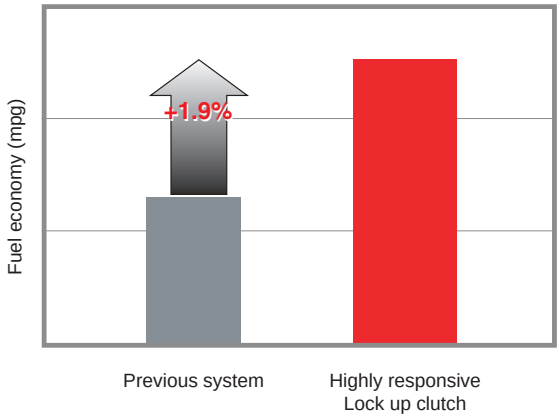


Fig. 11 Optimization of torsion damper for lock-up clutch

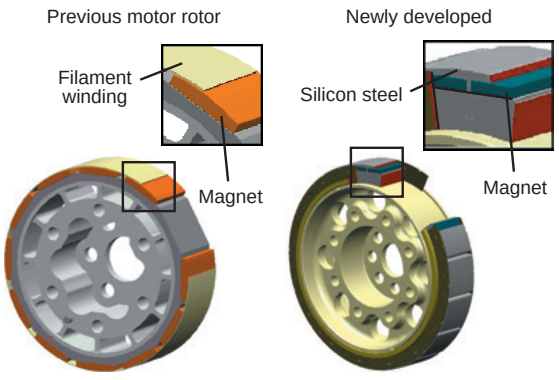


Fig. 12 Electric motor rotor

The magnetic pick-up sensor used formerly has been replaced by a resolver type sensor. Increased accuracy in the detection of rotor position as well as the application of vector control have also enabled efficiency to be increased. These enhancements have increased maximum torque by approximately 26%, maximum power by approximately 20%, and efficiency in all ranges by 1-3% over the electric motor employed in the CIVIC Hybrid (Fig. 13).

4.2.2. High-voltage unit

The size of the IPU was reduced to respond to increased power and to enable a hybrid compressor inverter (discussed below) to be fitted in a single high-voltage package. Figure 14 shows the configuration of the IPU.

Loss reduction achieved by fine patterning of the Insulated Gate Bipolar Transistor (IGBT) chips in the inverter fitted in the IPU, the employment of an inbuilt film condenser, and reduction of the number of components has resulted in a 50% reduction in the size of the inverter (Fig. 15).

Further, a Digital Signal Processor (DSP) has been employed in the DC-DC converter. The use of digital rather than analog control has enabled output current to be increased by 60% while the unit has undergone a 17% reduction in size (Fig. 16).

Despite the increase in the power of the IMA system, the development of these new technologies has enabled the volume of the IPU to be reduced by 5%, even with the installation of the hybrid compressor inverter.

4.2.3. High-voltage battery and battery box

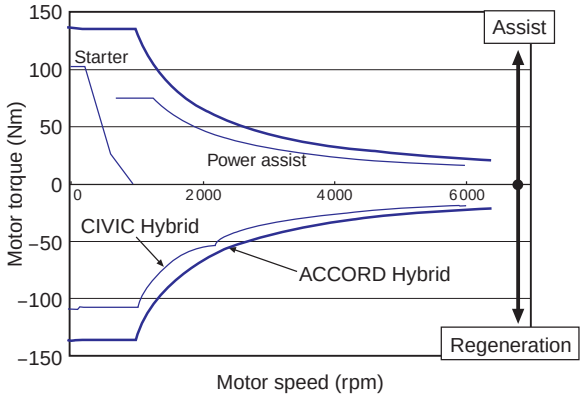


Fig. 13 Electric motor performance curve

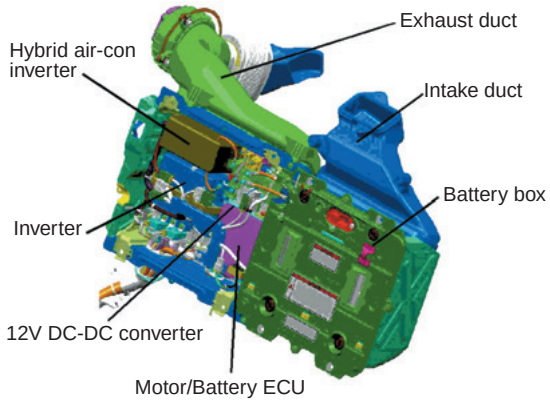


Fig. 14 IPU system

As in the CIVIC Hybrid, a Nickel Metal Hydride (Ni-MH) battery module was employed. Compared with lead-acid batteries, Ni-MH batteries have higher power density per unit weight, higher energy density, and longer life[5] making them the better choice for the electrical power system. In the ACCORD Hybrid, modifications have been made to achieve the required increases in regenerated power and power assist. To increase power, the shape and form of the current collectors was modified to reduce internal resistance (Fig. 17). This enabled the number of welding points to be increased and equalized the current density in the collectors, resulting in a reduction of approximately 39% in internal resistance.

To enable the size of the battery box to be reduced, the previous integrated plastic-molded box[6] was replaced by an assembled model. Reduction of size and integration of the component parts has both increased ease of assembly and reduction in size of the box by 10% (Fig. 18).

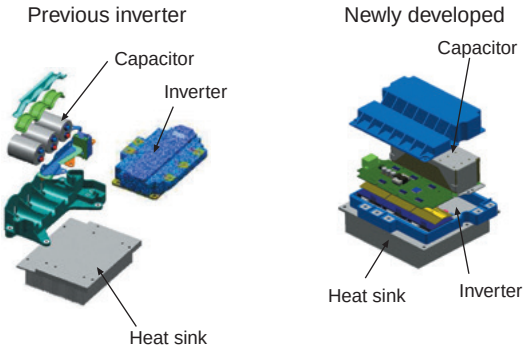


Fig. 15 View of inverter system

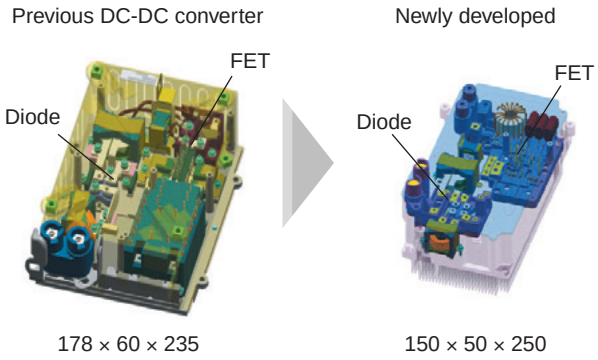


Fig. 16 Reduction in size of DC-DC Converter

	Previous battery	Newly developed
Current collector		
Number of welding points	56	104
Internal resistance	19.6 mΩ	12 mΩ

Fig. 17 Current collecting plate

4.2.4. Cooling system

As in the CIVIC Hybrid, the cooling system in the ACCORD Hybrid is mounted in the trunk. The system takes in air through the intake duct in the rear tray and uses it to cool the high-voltage battery and equipment in IPU. The cooling channels employed in the ACCORD Hybrid enable some of the cooling air to be exhausted out the vehicle via the rear outlet as shown in Fig. 19. As Fig. 20 shows, this has resulted in a reduction of approximately 10°C in the temperature of the cooling air when the vehicle is driven after having sat for a period of time in warm quiescent air. This helps prevent any losses in power of the IMA system caused by increases

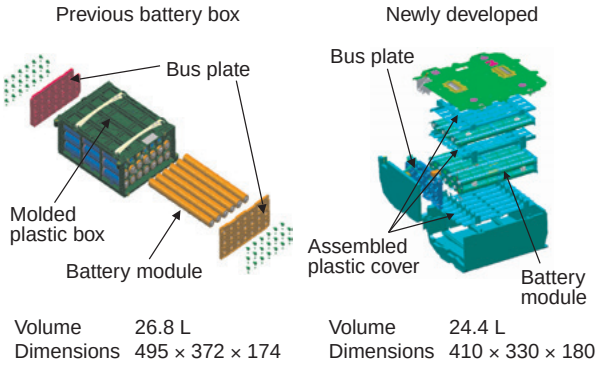


Fig. 18 Comparison of battery boxes

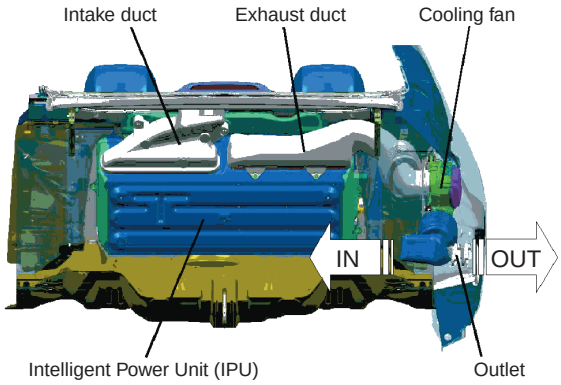


Fig. 19 Cooling system for IPU

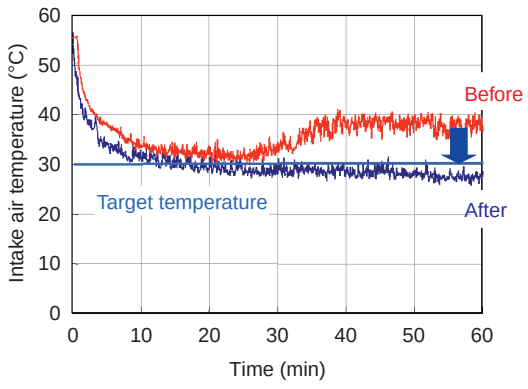


Fig. 20 Intake temperature

in the temperature of the high-voltage system.

The increased power of the motor and the high-voltage equipment discussed above has resulted in the achievement of a maximum power of 190 kW (255 hp) in the power plant (engine + motor). In contrast with the base ACCORD, the new ACCORD Hybrid produces more torque at lower engine speeds with much of the torque generated by the electric motor (Fig. 21).

5. Body Technologies

5.1. Hybrid Air Conditioner

To further increase the commercial appeal of the vehicle, a hybrid compressor with partial motor drive has been developed which enables the air conditioner to continue functioning when the engine is stopped (in idle stop mode). A motor-driven scroll compressor was added to a separate shaft at the end of the existing belt-driven scroll compressor, forming an integrated unit (Fig. 22).

The motor-driven scroll compressor goes into operation when the vehicle is in idle stop mode and the belt-driven compressor cannot operate, ensuring that a cool cabin temperature is maintained (Fig. 23).

A comparison of the estimated power consumed in operating the belt-driven compressor and the motor-driven compressor when the engine was running enabled a more efficient compressor drive mode to be selected, contributing to further reductions in actual fuel consumption.

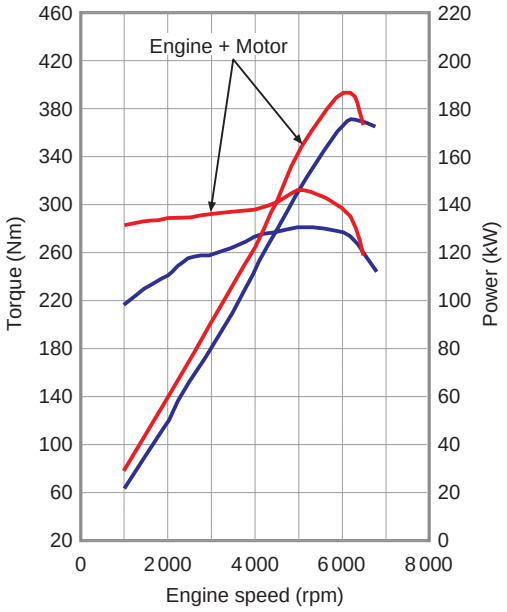


Fig. 21 Output performance of ACCORD Hybrid power plant

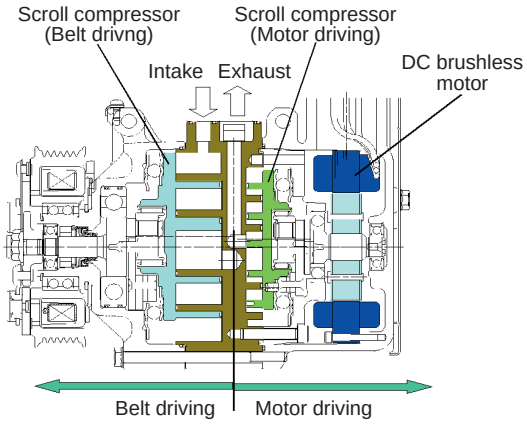


Fig. 22 Structure of hybrid compressor

5.2. ACM

The Active Control engine Mounts (ACM) system has been employed to counteract the increase in engine vibration when operating in 3-cylinder mode (Fig. 24). To respond to the increased operating range of the cylinder idling system the electromagnetic parts of the ACM have been enlarged in comparison to the previous

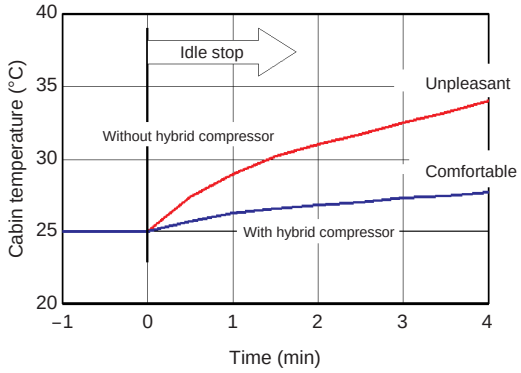


Fig. 23 Effect of hybrid compressor

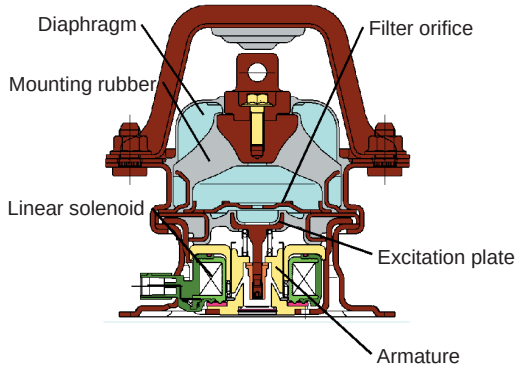


Fig. 24 Structure of ACM

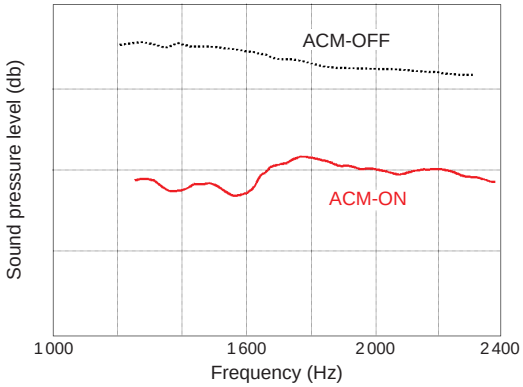


Fig. 25 Comparison of vibration level with ACM operation

model to increase its power. This has increased the level of vibration reduction by approximately 10 dB, reducing both booming noise and body vibration during cylinder idling (Fig. 25).

6. Weight Savings

In order to maintain a high level of performance despite the added weight of the IMA system, weight needed to be reduced in other areas. A reduction of approximately 80kg was achieved in the engine and various parts of the body to reach this goal.

In the body of the vehicle, aluminum has been employed in the rear knuckles, hood, and front and rear bumper beams, reducing weight by approximately 40 kg. In the engine, the use of magnesium in the intake manifold and head cover has resulted in a weight reduction of approximately 20 kg.

In addition, the spare tire has been replaced with a flat tire repair kit called the Instant Mobility System (IMS), further reducing weight (Fig.26).

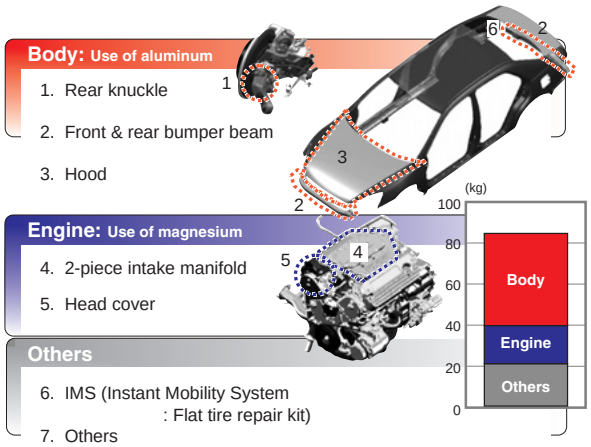


Fig. 26 Weight reduction

7. Conclusion

The major strategy for the improvement of fuel economy in the ACCORD Hybrid has been the employment of electric motor assist to increase the range of operation of the cylinder idling system. Together with the achievement of increased power in the IMA system and weight savings in the body, this has resulted in a vehicle that displays a level of dynamic performance exceeding that of the former V6 ACCORD as well as a level of fuel economy equivalent to that of the compact-class, four-cylinder CIVIC Sedan, with figures of 29 mpg in US City mode and 37 mpg in US Highway mode.

References

(1) Aoki, et al.: Development of Motor Type Hybrid Power Train, Automotive Technology Conference Proceedings, No. 98-99
(2) Ochiai, S., Uchibori, K., Hara, K., Tsurumi, T., Suzuki, M.: Development of the Motor Assist System for a Hybrid Car-INSIGHT, HONDA R&D Technical Review, Vol. 12, No. 1, p. 7-14
(3) Matsuki, M., Wakashiro, T., Kamiyama, T., Sato, T., Kaku, T., Kanda, M.: Development of a New Power Train for the Civic Hybrid, Honda R&D Technical Review, Vol. 14, No. 1, p. 39-48
(4) Noguchi, K., Fujiwara, M., Segawa, M., Sawamura, K., Suzuki, S.: Development of V6 i-VTEC Engine with Variable Cylinder Management, Honda R&D Technical Review, Vol. 16, No. 1, p. 85-92
(5) Trends in Battery Application Product Development: Battery and Configured Material Market 1999 - Market Trends in First Generation Batteries, Second Generation Batteries, Fuel Cells, Solar Batteries, Capacitor and Battery Configured Materials, CMC Publishing Co., Ltd., p. 180 (1999)
(6) Aitaka, K., Hosoda, M., Nomura, T.: Development of Intelligent Power Unit for Civic Hybrid, Honda R&D Technical Review, Vol. 14, No. 2, p. 83-90

■ Authors ■


Masaaki KAIZUKA


Toshitaka IMAI


Susumu ISHIKAWA


Manabu NIKI


Hiromitsu ADACHI

Development of High Power Density DC-DC Converter for IMA

Iwao SHIMANE* Kosuke OGURI*

ABSTRACT

A smaller and more powerful 12V DC-DC converter has been developed for Honda's Integrated Motor Assist (IMA) system. Low breakdown voltage FETs and a beam lead diode module in combination with high-efficiency soft switching circuits have reduced energy loss to increase the efficiency of the unit. Heat dissipation simulations were employed to optimize the component layout for efficient cooling. The new unit employs a digital signal processor, and the reduction in component numbers enabled by digital control has resulted in a 40% reduction in the size of the circuit board of the control section. The application of these technologies has enabled the unit volume to be decreased by 17% while output current has been increased by 60% against the former model.

1. Introduction

The demand for higher fuel economy and lower emissions for automobiles has been increased in order to ameliorate the global environment and conserve fossil fuels. Honda has responded to this demand by offering the high fuel economy and clean hybrid vehicles employing a lightweight, compact Integrated Motor Assist (IMA) system. In 1999, Honda introduced the Insight[(1)], and in 2001, the CIVIC Hybrid[(2)]. In December 2004, the ACCORD fitted with an enhanced IMA system giving even higher performance was launched in the North American market. This paper introduces technologies used in the development of a compact DC-DC converter with high output for the IMA system installed in the ACCORD Hybrid.

The DC-DC converter is one part of the Power Control Unit (PCU), converting high voltage electricity to 12 V. As shown in Fig. 1, it is placed in the Integrated Power Unit (IPU) in the rear of the vehicle, together with the high voltage battery.

In an ordinary gasoline vehicle, electricity generated by the alternator, which is powered by the engine, is supplied to the 12 V electrical devices such as lights, audio system, and ECU. In contrast, an IMA system uses a DC-DC converter to reduce high voltage electricity to 12 V before supplying to the devices as shown in Fig. 2. When the vehicle decelerates, the Power Drive Unit (PDU) converts the regenerated energy from the IMA motor to direct current (DC) at high voltage to recharge the batteries. In addition, it is possible to have electrical supply from the high voltage battery, even when the engine is off during idling stop.

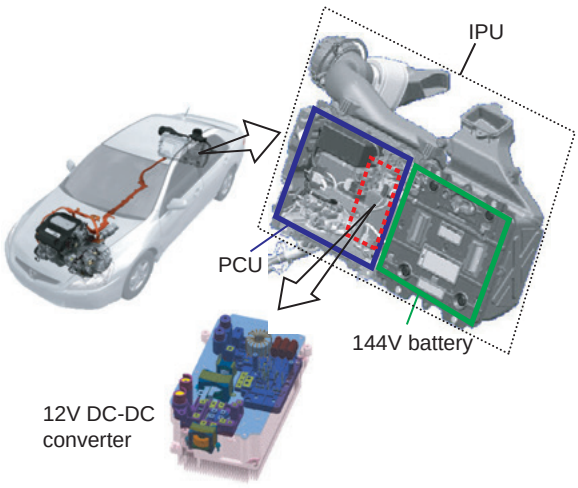


Fig. 1 Layout of DC-DC converter

* Tochigi R&D Center

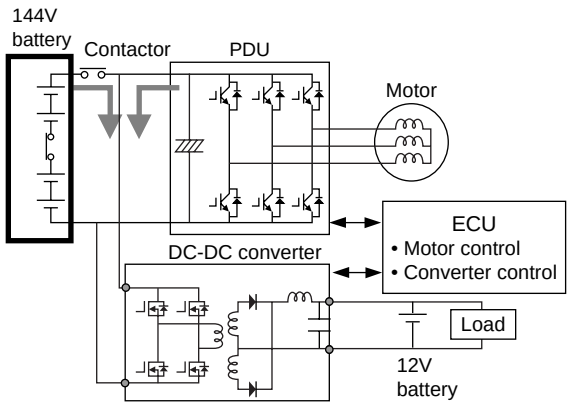


Fig. 2 IMA system

2. Development Goals and Means of Achievement

2.1. Development Goals

The DC-DC converter in the IMA system for the ACCORD Hybrid is required to provide greater output to enhance comfort features appropriate to the vehicle class, and electrical devices that contribute to fuel economy. It was also necessary to make the system more compact in order to fit it to the same body as the gasoline vehicle. Specifically, development goals were set as below based on the current DC-DC converter for the CIVIC Hybrid.

(1) Output Current +60%
(2) Volume –15%

2.2. Means of Achievement

In order to achieve a compact, high-output DC-DC converter, the following methods were studied.

(1) Higher output through reduction of element loss
Reduction of element loss decreases junction operating temperature for the same current. This decrease in temperature increases maximum forward current, enabling higher power to be output.

(2) Reducing size by enhancing cooling performance
Enhancement of the cooling performance of the heat sink that disperses the heat from the element allows the converter to have a layout that concentrates the heat generating parts, enabling the converter to be made smaller.

(3) Reducing size by reducing the number of parts and by having a higher density package
Change of the control circuit method and radio noise restraint method reduces the number of parts, and at the same time, raises actual element installation density, enabling the converter to be made smaller.

3. Technologies for Making a Compact Converter with Higher Output

3.1. Higher Output through Reduction of Element Loss

3.1.1. FET for switching

A Field Effect Transistor (FET) was adopted in the switching circuit. The switching circuit consists of an H bridge that is connected in parallel to the high voltage battery and PDU. With this FET, the lower the breakdown voltage, the smaller the on resistance, so it is possible to reduce loss. However, if the FET breakdown voltage is reduced, there is the possibility that when the electromotive force generated by the motor is raised, the voltage applied to the FET would exceed the element breakdown voltage. To address this, the over-voltage protection circuit was accelerated.

Figure 3 gives the DC-DC converter input voltage waveform, and the FET switching waveform. When the input voltage rises to the operating voltage of the over-voltage protection circuit and after a finite circuit response time passes, FET switching stops.

With the over-voltage protection circuit, the circuit board was designed to enhance toughness against switching noise, and revisions were made to the filter constant, shortening response time. As a result, switching voltage rise was controlled, making it possible to use low breakdown voltage elements having low loss features. FET on resistance, as shown in Fig. 4, is 47% less than the previous unit, and the reduction in loss is proportional to this.

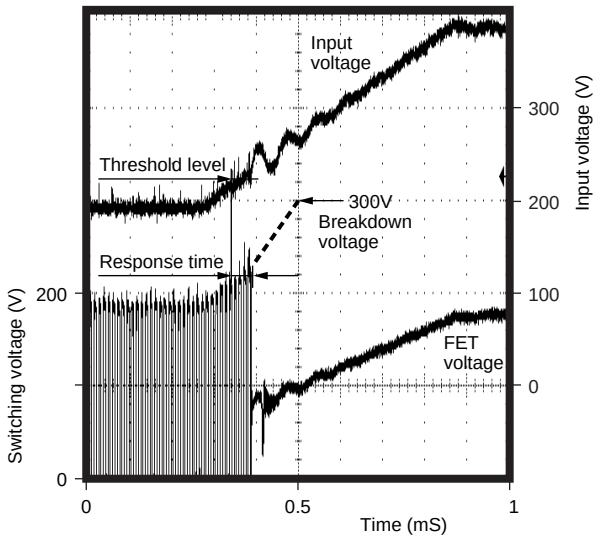


Fig. 3 Waveform of FET showing operation of voltage protection

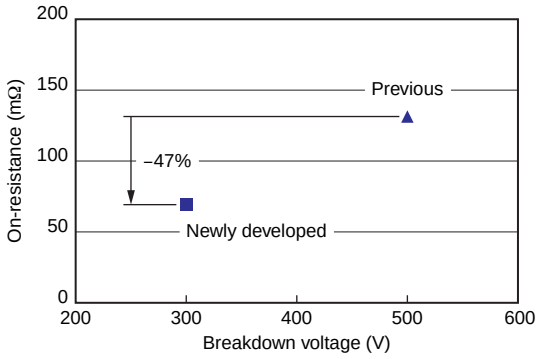


Fig. 4 Reduction of on-resistance

3.1.2. Output rectifying diode

By enlarging the output diode chip size to the limits where it can fit in the module, it is possible to reduce current density. Through these technologies, forward threshold voltage can be reduced from the 0.95 V of conventional products at the same current, to 0.85 V. As shown in Fig. 5, diode module loss is reduced by 11%. Because diode loss is expressed as the product of forward threshold voltage and output current, reducing the forward threshold voltage makes it possible to reduce element heat generation, making a smaller module possible.

Furthermore, the diode module package was given a beam-lead structure, as shown in Fig. 6. The connection between the diode chip anode and the anode terminal was changed from wire bonding to a beam-lead method. This allows large current to flow evenly through a thin copper sheet, enabling the height of the chip in the vertical direction to be minimized in comparison with the wire type.

As noted above, loss is reduced with the adoption of a low breakdown voltage FET and enlarged diode chip size, thereby minimizing heat generation while increasing output current. Combined with the benefits of a beam-lead structure, it is possible to increase output current from 75 A to 120 A while keeping the size of the module the same as the conventional module.

3.2. Enhanced Cooling Performance

Studies were carried out of the layout of heating elements and of the heat sink shape in order to enhance cooling performance.

3.2.1. Layout of heating elements

The devices that require cooling are the FET (switching element), resonance choke necessary for partial resonance control, main transformer that forms the current path, output diode, and output choke. A simulation was carried out to determine the effect of the layout of these parts, the thickness of the heat sink, the length of the fins, and the pitch of the fins on heat radiation and the reduction of heat resistance.

Figure 7 shows temperature distribution when looking at the DC-DC converter from above. The FET has its four elements laid out so that there is no heat interference between them, minimizing temperature rise. The output diode is placed on the windward side to effectively utilize the fins. For the output diode, in order to disperse the heat, the heat spread plate is placed on the bottom of the module, raising heat radiating capability.

3.2.2. Heat sink shape

The heat sink is formed through die-casting. To realize increased heat radiating performance, the surface area of the heat radiating fins was enlarged 30% over the previous unit. In addition, the case and the fins were integrated to counter the radio noise and to reduce

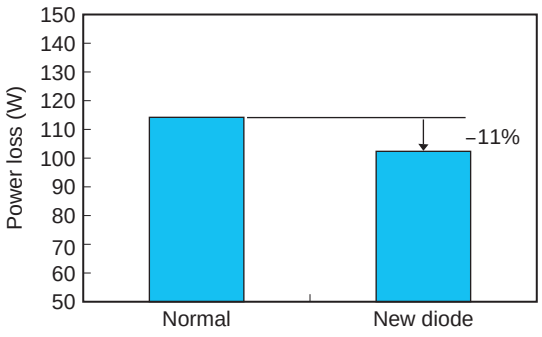


Fig. 5 Power loss characteristics of diode

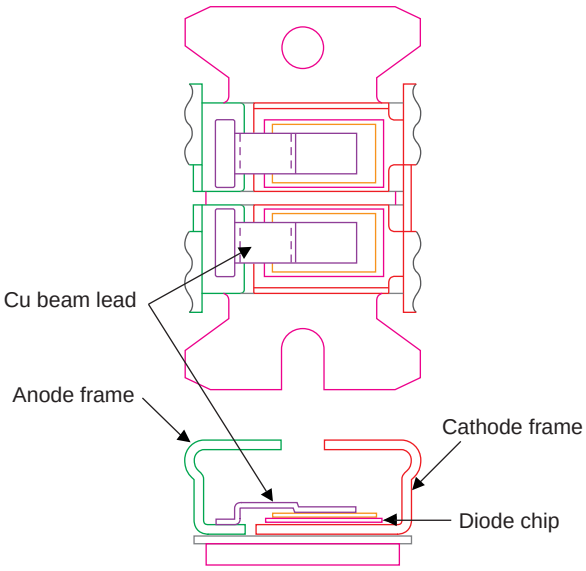


Fig. 6 Structure of diode module

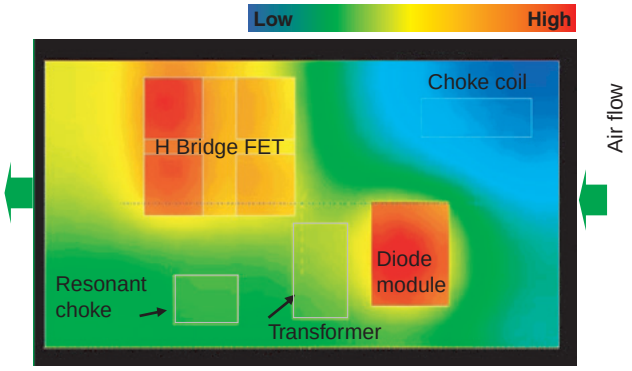


Fig. 7 Simulation of temperature distribution

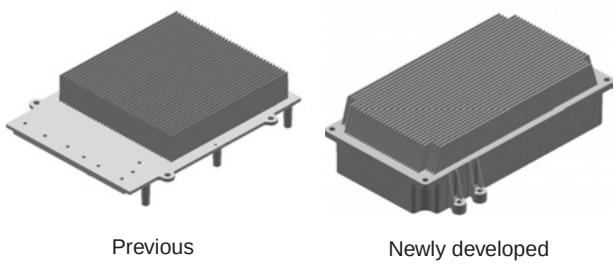


Fig. 8 Case design

the number of assembly processes. As a result, as shown in Fig. 8, the heat sink mold depth is at least twice what it was, and occurrence of air bubbles during forming was expected.

Figure 9 shows the results of the molten flow simulation. Before countermeasures, the metal flow concentrates along the walls, so the flow path becomes long and the molten material does not reach all areas of the fin, creating air pockets. In comparison, with the change to the gate shape and establishing a slope on both ends of the fin, the molten material flow is enhanced.

3.3. Reducing the Size by Digital Control

The highly efficient soft switching method[3] that has traditionally been adopted was digitalized[4] using a Digital Signal Processor (DSP) to make a smaller control board.

3.3.1. Phase shift control

As shown in Fig. 10, the DC-DC converter has constant voltage control from light load to rated output of 120 A. In the over electric current zone of 120 A and higher, voltage drooping characteristic control is carried out in order to reduce output voltage. Based on commands from the ECU, each voltage control determines the target output voltage, and the FET's are switched (from Q1 to Q4) by the PID control so that the target voltage is reached. The control circuit is composed, as shown in Fig. 11, of four FET in an H bridge circuit. By shifting Q4 phase with Q1 phase as the reference[5],[6], the current flows from Q1 to Q4 through the transformer. Q2 and Q3 also operate according to the timings shown in Fig. 12, generating voltage in the transformer. Through full-wave rectification of this voltage by the output diode, direct current output is obtained. Understanding of the output voltage and current state in this way enables voltage control and current control to be carried out.

3.3.2. Digitalization

If these controls are composed of general-purpose analog phase shift control IC's, there are issues in their use for the vehicle, such as not recovering from a stationary state due to latch operation when self-protection happens to operate. In this case, a latch release circuit has to be added as another external part. Therefore, it was necessary to produce a special customized IC. When carrying out phase shift control using a DSP, output voltage and current are input from the AD converter, and FET phase is digitally controlled so that it is at the target output voltage.

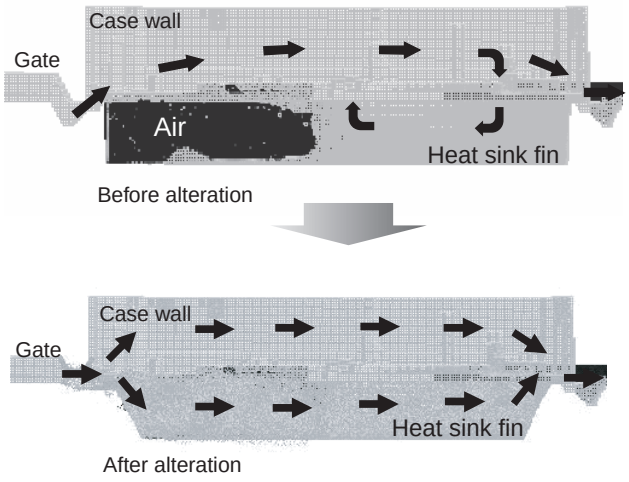


Fig. 9 Flow simulation of molten model

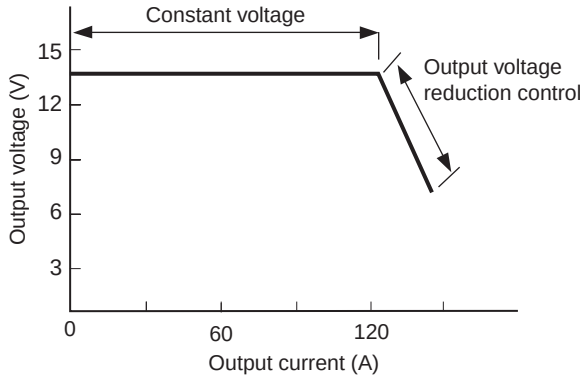


Fig. 10 Output characteristics

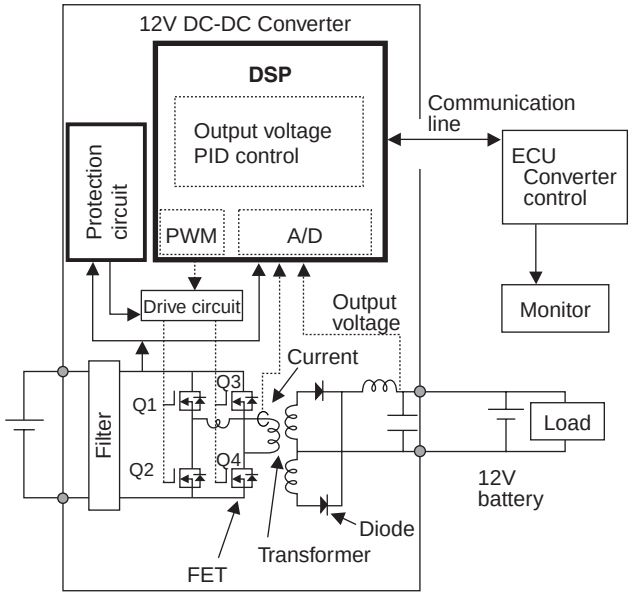


Fig. 11 Control block

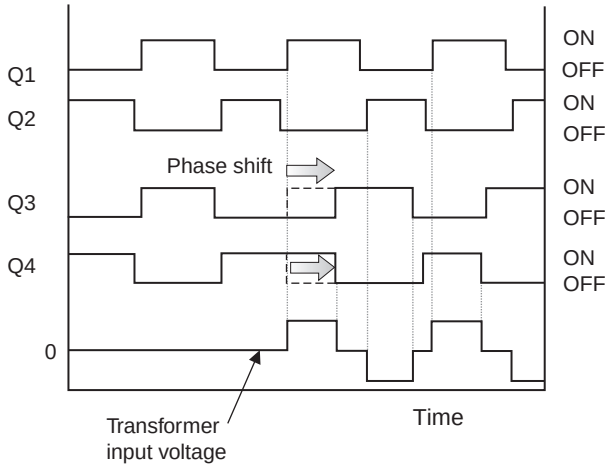


Fig. 12 FET switching pattern of phase shift control

Additionally, using DSP programs, it is possible to carry out operations such as information transmission as well as protection operations. These operations include sequencing operations based on commands from the vehicle ECU, cooling requirements to the ECU, requirements for warning lights, etc., for which it was necessary to have external parts when using analog circuits.

Furthermore, it is now possible to freely set the current change rate and the voltage change rate when the DC-DC converter is activated or stopped. Adjustable settings are also possible that match the vehicle high voltage battery management. Figure 13 shows the soft start and soft stop current waveform.

When the analog circuit has the configuration of operations necessary as a vehicle power supply system, the scale of the circuits becomes larger due to consideration of circuit part constant variations and temperature characteristics. In comparison with the use of analog circuits, digital controls can actualize diverse operations with high accuracy, using simple circuits. When comparing the same control specification, a digital circuit requires approximately 300 parts, while an analog circuit requires approximately 500 parts. Due to this reduction in the number of parts, it is possible to reduce the size of the circuit board as shown in Fig. 14.

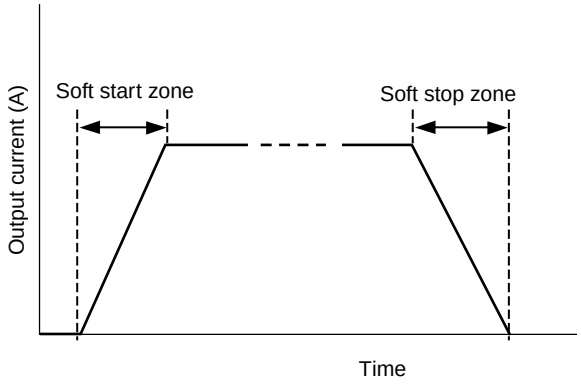


Fig. 13 Start-stop characteristics

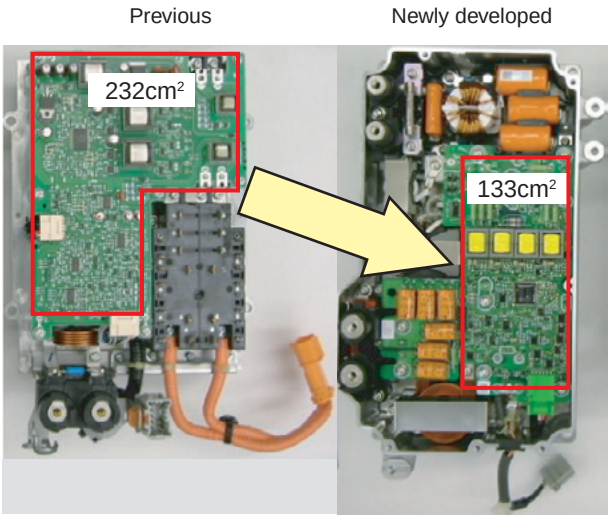


Fig. 14 Reduction of circuit board size

3.4. Reducing the Size of the Filter Preventing Radio Noise

The switching noise harmonics were matched with the AM radio broadcast carrier wave so that the effect of DC-DC converter switching noise on the in-vehicle radio is minimized and the noise filters can be reduced. The switching frequency was matched with overseas and domestic broadcast carrier waves. Figure 15 shows a schematic diagram of the alignment between broadcast carrier waves and interference waves. If the noise frequency is the same as that of the broadcast wave's carrier, the radio does not detect noise, and there is no mixing of noise in the voice signal. In addition, the switching frequency is derived by dividing down the DSP clock frequency of 36 MHz, so it is highly accurate. Therefore, the effect on radio audio due to departing from the broadcast carrier waves is eliminated. Through the means outlined above, it is possible to reduce the reliance on filters, and to reduce the large noise filter parts.

4. The Effects of Being Compact and Having High Output

The results of making the DC-DC converter with smaller size and higher output are shown in Table 1. In addition to the output current being increased 60%, there was a reduction in volume of 17%. As shown in Fig. 16, efficiency was raised by 1.5% in the normal operation range in comparison with the previous model.

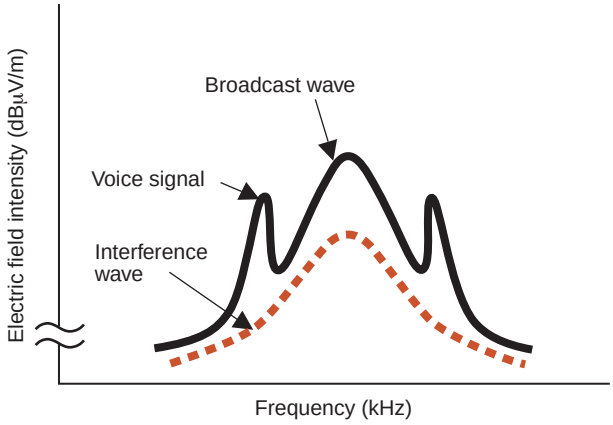


Fig. 15 Interference wave characteristics

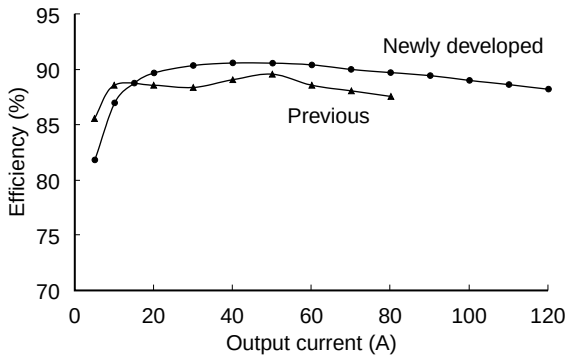


Fig. 16 12V DC-DC converter efficiency

Table 1 Specifications of DC-DC converter

	Previous	Newly developed
Output current (A)	75	120
Dimensions (mm)	178 × 60 × 235	150 × 50 × 250
Volume (cm^3)	2510	2100
Current density (mA/cm^3)	30	57

5. Conclusion

The following measures have been taken to develop the smaller DC-DC converter with higher output for the ACCORD Hybrid's IMA system.

(1) A low breakdown voltage FET and a diode module having a beam-lead structure were employed to increase converter efficiency.
(2) A heat dissipation simulation was carried out to develop a part layout that provides efficient cooling.
(3) Digital controls using DSP were employed to reduce the number of parts, enabling the control circuit board to be made 40% smaller.
(4) Switching noise harmonics were matched with AM radio carrier waves, minimizing the effect on audio signals. This reduced the number of filter parts.

As a result, in comparison with the previous DC-DC converter, output current is increased by 60% while volume is reduced 17%.

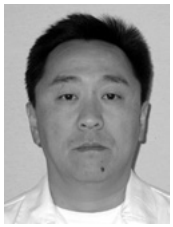
Acknowledgements

The authors would like to take this opportunity to express their gratitude for the generous cooperation of Shindengen Electric Manufacturing Co., Ltd. in this development project.

References

(1) Fukuo, K., Fujimura, A., Saito, M., Tsunoda, K., Takiguchi, S.: Development of the Ultra-Low-Fuel-Consumption Hybrid Car- INSIGHT, HONDA R&D Technical Review, Vol. 11, No. 2, p. 1-8
(2) Matsuki, M., Wakashiro, T., Kamiyama, T., Sato, T., Kaku, T., Kanda, M.: Development of a New Power Train for the Civic Hybrid, Honda R&D Technical Review, Vol. 14, No. 1, p. 39-48
(3) Aitaka, K., Hosoda, M., Nomura, T.: Development of Intelligent Power Unit for Civic Hybrid, Honda R&D Technical Review, Vol. 14, No. 2, p. 83-90
(4) Oshikata, T.: DSP niyoru digital dengen no jitsugen, SHINDENGEN TECHNICAL INFORMATION FILE "PASSWORD", Vol. 04-13 (2004) (in Japanese)
(5) Matsuda, Y.: Koukouritu full bridge gata DC/DC converter, SHINDENGEN TECHNICAL INFORMATION FILE "PASSWORD", Vol. 02-15 (2002) (in Japanese)
(6) Harada, K., Ninomiya, T., Kobunn, K.: Isouseigyo converter, Switching converter no kiso, CORONA PUBLISHING, p. 38 (1999) (in Japanese)

■ Authors ■



Iwao SHIMANE



Kosuke OGURI

Development of Compact Lightweight Muffler Valve for 2005 Model Year LEGEND

Hidenori HAMASHIMA* Masayuki UEGANE*
Satoshi WATANABE* Hidekazu AKIYAMA*

ABSTRACT

For the 2005 model year LEGEND, a compact lightweight muffler valve with new construction was developed for the variable flow rate muffler.

A conventional muffler valve rotates about a shaft. A load is applied to the rotating shaft by a coil spring. For this reason many parts are required for the valve to open and close. The body of the muffler valve traditionally covers the entire valve operating range, resulting in the valve being large and heavy.

As a method of reducing the number of parts and the weight of the valve, this development employed the mechanism of the reed valve. A reed valve is used in 2-cycle motorcycle engines to control the intake air volume at the intake port. The addition of a support plate to the reed valve structure was investigated to suppress valve vibration and to apply a pre-load.

The number of parts in the newly developed muffler valve was reduced from 13 parts in the conventional valve to four parts. Both the weight and volume were reduced to about 1/10. This enabled the cost to be reduced to about 1/7 of a traditional exhaust valve.

1. Introduction

To achieve sound levels and engine power appropriate for the Honda LEGEND (Honda's flagship vehicle), a new variable flow rate muffler was adopted in the exhaust system.

In the variable flow rate muffler, a muffler valve was established to switch exhaust gas passage between the low engine speed and high engine speed ranges. In the low engine speed range, priority was given to silencing noise by increasing exhaust resistance. In the high engine speed range, it was possible to raise power by reducing exhaust resistance.

The flow of exhaust gas at low engine speeds with the variable flow rate muffler is shown in Fig. 1.

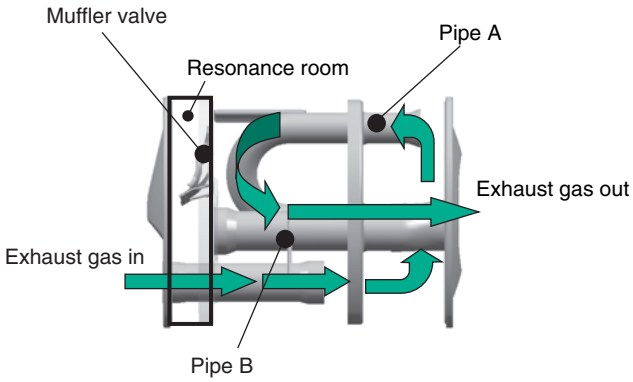


Fig. 1 Exhaust gas flow when muffler valve is closed

* Tochigi R&D Center

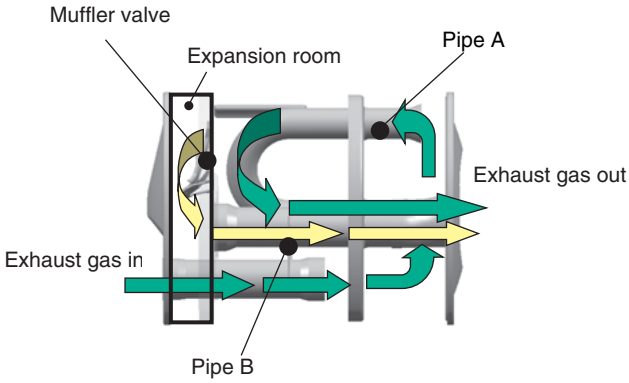


Fig. 2 Exhaust gas flow when muffler valve is opened

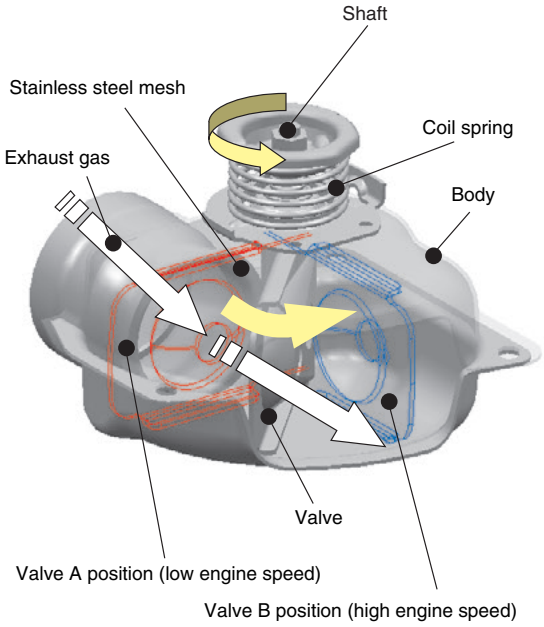


Fig. 3 Operation principle of conventional muffler valve

At low engine speeds the pressure inside the muffler is low, so the muffler valve is closed. When the valve is closed, exhaust gases are emitted without passing through pipe B. With the valve closed, the muffler valve room acts as a resonance room to silence noise.

The flow of exhaust gas at high engine speeds with the variable flow rate muffler is shown in Fig. 2.

At high engine speeds, the pressure inside the muffler rises. This causes the muffler valve to open. When the valve opens, exhaust gas passes through pipe B. The chamber that acted as the resonance room at low engine speeds now becomes part of the exhaust gas passage. This reduces exhaust resistance (backpressure).

The variable flow rate muffler uses a valve that switches the path of exhaust gas. The conventional muffler valve has traditionally been heavy and costly.

This paper reports on achievements in reducing weight and cost of mufflers by reducing the total part count of the exhaust valve assembly.

2. Development Goals

Figure 3 shows the operational states of a conventional muffler valve at high and low engine speeds.

In order to switch the exhaust gas passage with a conventional muffler valve, a shaft is established at the edge of a plate (referred to as the valve, hereafter). The valve rotates around this shaft.

When the engine is at low speeds, a load in the opposite direction to the exhaust gas flow (referred to as the pre-load hereafter) is applied on the shaft via a coil spring. The exhaust gas passage is closed in valve A position. At high engine speeds, a pressure exceeding the pre-load is applied. This pressure causes the valve to rotate about its shaft, and opens to valve B position. Exhaust gas flows inside the muffler valve body, reducing exhaust gas resistance.

A stopper function is added to the muffler valve so that valve opening is restricted during high engine speeds. This means that when it comes into contact with pipe A, the valve will not open any further (Fig. 4).

Conventional muffler valve component parts are shown in Fig. 5.

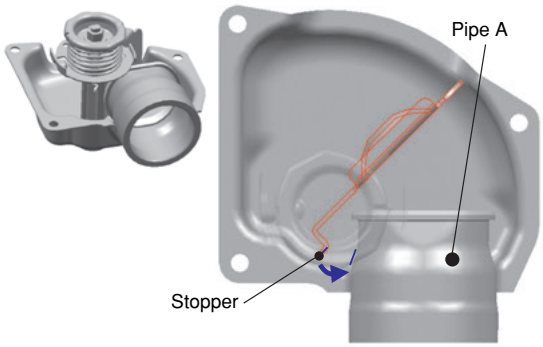


Fig. 4 Structure of stopper

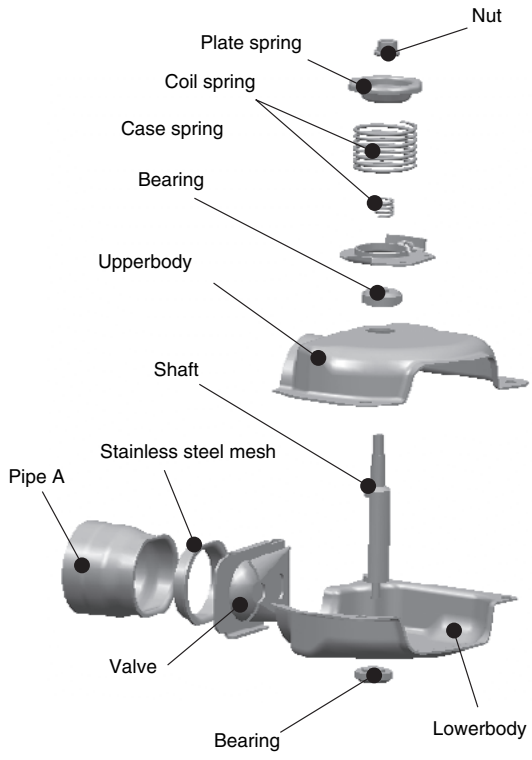


Fig. 5 Structure of conventional muffler valve

A rotational shaft is at the edge of the valve, and bearings are fitted on both ends of the rotational shaft. For installation purposes, plates are placed at both ends of the coil spring.

The shaft, bearings and the coil spring holding plates are fitted to the upper body and lower body. The upper and lower bodies cover the valve operating range. When the valve is open the upper and lower bodies form the exhaust gas passage way.

A conventional muffler valve has a more complex structure. The following three structural issues can be assumed with the use of a conventional muffler valve.

- Because the structure rotates around a shaft, the necessity for valves, shafts, and bearings is inevitable. This increases the number of parts.
- Because a coil spring is used, spring bearings are necessary. This also increases the number of parts.
- Because the entire valve operation range is covered by the muffler valve body, the unit becomes large and heavy.

The goal of this development project was to reduce the number of component parts. This is accomplished by creating a structure in which the valve itself opens and closes without any rotational shaft or coil spring. Additionally, the body does not cover the valve operation range. This makes the unit smaller.

3. Technologies Adopted

In order to address the issues raised in the previous section, a reed valve was chosen. Reed valves are used in 2-cycle motorcycle engines to control intake air volume at the intake port. This makes it possible to reduce the number of component parts.

Figure 6 shows the operation principles for this newly developed muffler valve.

In this structure a thin plate flexes open and closed. This controls the exhaust gas passage.

A conventional valve structure has a plate of 1.5 mm thickness that opens and closes on a rotational shaft. This has been replaced by a thin 0.2 mm thick plate. The function of the rotational shaft and the valve is integrated into the thin plate.

Two issues arise when the valve is to be replaced by a thin plate. The first issue is valve resonance. The other issue is that the pre-load typically applied by the conventional coil spring, cannot be applied.

To address these two issues, another thin plate acting as a spring (referred to as the support plate hereafter) has been placed in contact with the valve.

At low engine speeds the support plate is in support plate C position. A pre-load is applied to the valve at valve D position. This load closes the valve, and consequently the exhaust gas passage.

When the engine speed is high, pressure exceeding the pre-load is applied to the valve. This causes the valve unit to flex open to valve F position. The support plate slides on top of the valve to position E while flexing. With the valve in this position, the exhaust gas flows outside the muffler valve body.

Figure 7 shows the muffler valve structure.

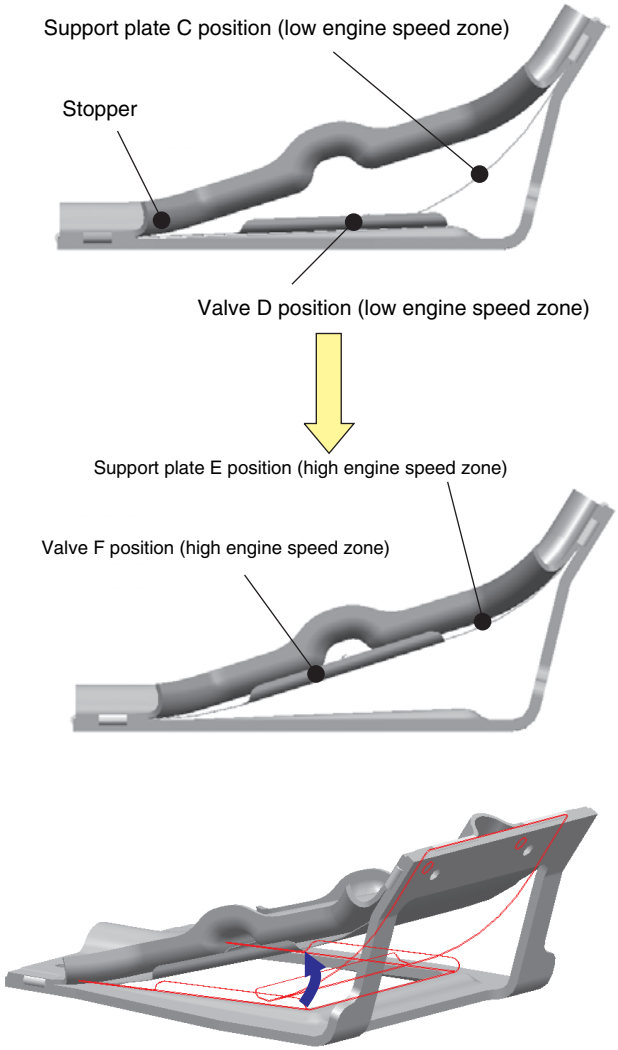


Fig. 6 Operation principle of developed muffler valve

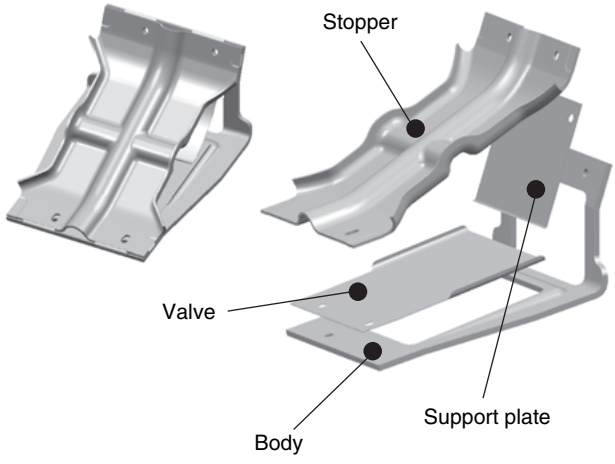


Fig. 7 Structure of developed muffler valve

A stopper has been added so that stress on the fixed ends does not exceed the material fatigue limit when the valve and support plate are fully open. The stopper limits the valve and support plate operation. At the same time, the stopper holds one side of the valve and the support plate.

Inconel material was used for the valve plate and the support plate. This was done so that both parts would have the same level of heat and corrosion resistance as that of the conventional coil spring.

Figure 8 shows a functional part comparison of the conventional muffler valve and the newly developed one.

Compared to the conventional muffler valve, the pre-load function was reduced from three parts to one. The rotational shaft function was reduced from six parts to one. The stopper function was reduced from two parts to one, and the exhaust gas passage was modified from two parts to one. The number of parts was reduced for each function.

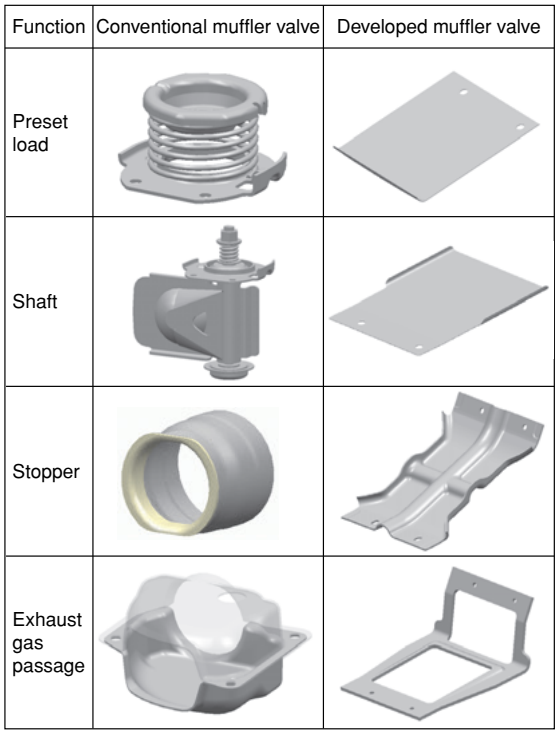


Fig. 8 Parts list for each function



Fig. 9 Size comparison of conventional and developed muffler valve

Table 1 Specification comparison of conventional and developed muffler valves

	Conventional muffler valve	Developed muffler valve
Wt (kg)	1.34	0.12
Number of parts	13	4
Volume (mm^3)	1.12×10^6	0.08×10^6

A size comparison between the conventional and newly developed muffler valves is shown in Fig. 9.

Table 1 shows a comparison of the main specifications for the conventional and developed muffler valves.

The new structure has the following advantages over the conventional structure.

- The number of parts has been reduced from thirteen to four.
- Weight and volume has been reduced to approximately one tenth that of conventional unit.
- Due to the reduction in part number and size, cost has also been reduced to approximately one-seventh of the conventional unit.

4. Effects on the Vehicle

The benefits of the variable flow rate muffler were verified on an actual vehicle with the valve forced open and forced closed. The exhaust noise results are shown in Fig. 10, and backpressure results are shown in Fig. 11.

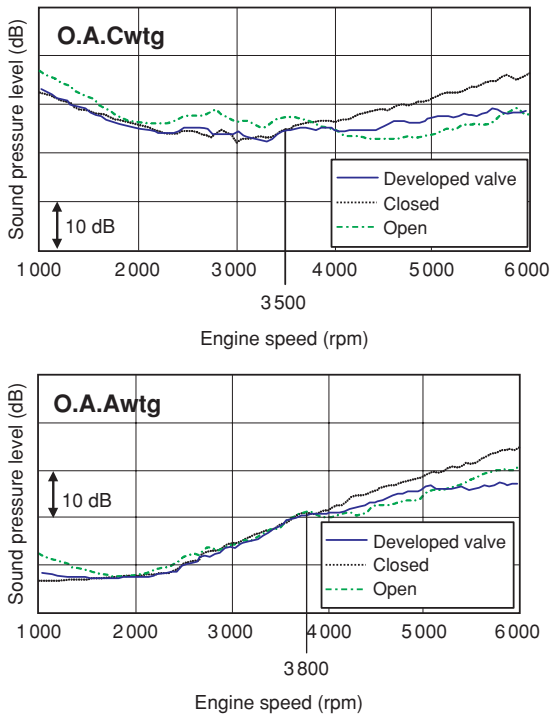


Fig. 10 Exhaust noise comparison by difference valve condition

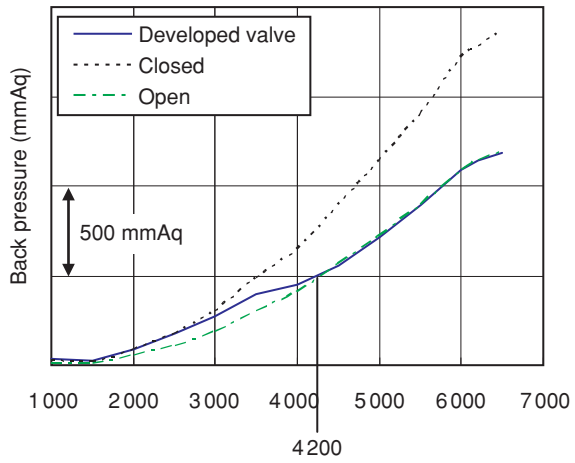


Fig. 11 Back pressure comparison by difference valve condition

Backpressure expresses exhaust gas resistance in terms of pressure inside the pipe.

Figure 10 shows the exhaust noise C weighted value dB-C measurement results from 1000 to 3500 rpm. Compared to the valve in a forcibly closed state, this newly developed variable flow rate muffler has the same noise silencing performance. It is clear that exhaust pulse noise level is equivalent. The exhaust noise A weighted value dB-A is also shown. In the 3800 rpm range and higher, the flow noise is clearly reduced by opening the muffler valve when compared to the state when the valve is forcibly closed.

In general, exhaust noise at 4000 rpm and higher is dominated by flow noise emitted from the tailpipe. If flow speed is increased then flow noise also increases. At engine speeds of 4000 rpm and higher if the exhaust gas flow path increases then flow noise is reduced.

Backpressure measurement results are show in Fig. 11. The valve begins to open at engine speeds of 3000 rpm and higher. This causes a reduction in backpressure of the newly developed variable flow rate muffler. The same muffler with the valve forced closed is shown for comparison. At engine speeds of 4200 rpm and higher, the backpressure performance is equivalent to when the valve is forcibly open.

It becomes clear that by adopting the variable flow rate muffler, it is possible to maintain a low exhaust pulse noise level. At the same time flow noise and backpressure at high engine speeds are reduced.

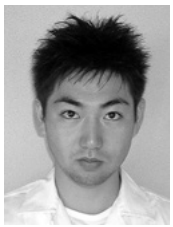
5. Conclusion

1. Adopting the newly developed muffler valve in the variable flow rate muffler for the 2005 model year LEGEND has many benefits. Both exhaust sound level and engine power appropriate for Honda's flagship vehicle has been achieved. This has been accomplished with low weight and low cost.
2. The variable flow rate muffler developed in this project has the same level of noise silencing performance between 1000 and 3000 rpm with the muffler valve closed, compared to when the valve is forcibly closed. At speeds of 3800 rpm and higher, by opening the muffler valve, it is possible to reduce flow noise. At 4200 rpm and higher, the newly developed muffler has the same backpressure performance, compared to when the valve is forcibly open.
3. In comparison with the conventional unit, the newly developed muffler valve has nine fewer parts, reduced from thirteen to four total. Weight and volume are approximately one-tenth of the conventional. Cost has also been reduced to approximately one-seventh, thanks to the reduction in the number of parts and the reduction in size.

6. References

(1) Murakami, M., et al.: Hydraulic Losses in Pipes And Ducts, The Japan Society of Mechanical Engineers, p. 3-126 (1998)
(2) Fukuda, M., Okuda, J.: The Solution To Noise And Silencing Design, KYOURITSU SHUPPAN CO., LTD., p. 160-225 (1982)
(3) Spring Technology Research Association. : Spring, Maruzen Co., Ltd., p. 13-387 (1982)
(4) Koibuchi, K., Kokubo, K.: Strength of materials and Strength design know-how for Products development, THE NIKKAN KOGYO SHINBUN, LTD., p. 160-225 (2002)
(5) Koizumi, T., Hara, T., Kasano, H., Minakuchi, Y.: Foundation Strength Of Materials, Yokendo Co., LTD., p. 55-98 (1996)
(6) JSAE. : Handbook Of Society Of Automotive Engineers Of Japan (Book Of design), p. 33-183 (1991)
(7) Miyagawa, O., Sakaki, T.: Metal Technology Generality, Asakurashoten Co., Ltd., p. 132-193 (1996)
(8) Mochizuki, O., Maruta, Y.: Introduction to Fluid Noise Engineering, Asakurashoten Co., Ltd., p. 60-138 (1991)

■ Authors ■


Hidenori HAMASHIMA


Masayuki UEGANE


Satoshi WATANABE


Hidekazu AKIYAMA

Development of Smart Card Key System for Motorcycles

Takeshi KONNO* Tadashi ONOZUKA* Seiichi YAMASHITA*

ABSTRACT

A motorcycles' smart card key system (duplex electric wave communication key system) with both, user-friendliness and antitheft certainty has been developed for the first time in the world. The system can unlock a main-switch, seat and console-box by one-push operation. The main-switch is changed to a knob type from the conventional key type. To protect the key cylinder from excess input torque, a torque-limiter was installed in the mechanism. An on/off switch that can stop the communication function at anytime was added on the smart card key because a motorcycle can be parked just outside a shop or other location when the main switch is still on and vehicle can be started. The lock and unlock available area was determined from the viewpoint of user's convenience. The function and layout of the communication system was determined by the performance of using one low frequency transmitting antenna. A factor and an analysis technique for influences of radio noises from other electrical components on the vehicles and surrounding environments was clarified.

1. Introduction

Keyhole shutters and immobilizers have been used in motorcycle steering lock systems with the aim of enhancing antitheft toughness. Also, steps for increased ease of operation have included modifying the keyhole shutter and making it possible to unlock the seat with the main key, but further modifications are needed for the sake of convenience and antitheft toughness. These backgrounds led the authors to focus on the smart card key systems (duplex electric wave communication key systems) that have been implemented into automobiles for both convenience and antitheft toughness. After determining the issues involved in putting such a system on a motorcycle and listing ways of dealing with them, the industry's first smart card key system on a motorcycle was developed and applied to the large-size scooter FORZA (Fig. 1).



Fig. 1 Photo of new FORZA

* Asaka R&D Center

2. Development Goals

The following were selected as their development goals for the smart card key system.

(1) Enhancing convenience
- To reduce the total number of operations involved in all unlocking and locking by at least half as compared to conventional large-size scooters

(2) Assuring theft tightness
- To design a measure to hinder the breaking and the tampering on the main switch knob (because main switches are exposed, as a peculiar issue to motorcycles)
- To protect from theft when motorcycles are parked in front of the home or a shop and the smart card key is within communication range, a peculiar issue to motorcycles
- To design it for preventing theft by direct wire connection to the ignition circuit

(3) Securing communication
- Two types of communication are used with smart card key systems: low frequency (LF) communication and ultra high frequency (UHF) communication. Whereas UHF communication has plenty of capacity, establishing communication is an issue with LF communication, so this was also set as a development goal.

3. System Construction

Figure 2 shows the layout of the developed smart card key system in an actual motorcycle, and Fig. 3 illustrates the system overview. To put a smart card key system on a motorcycle, the authors succeeded in creating a simple system configuration by providing satisfactory communication performance with a single LF antenna and integrating the smart ECU with the mechanical portion to make the steering lock module. The core components of this smart card key system are the steering lock module, LF antenna, UHF receiver and the smart card key, which the user carries. The functions of the core components are explained below.

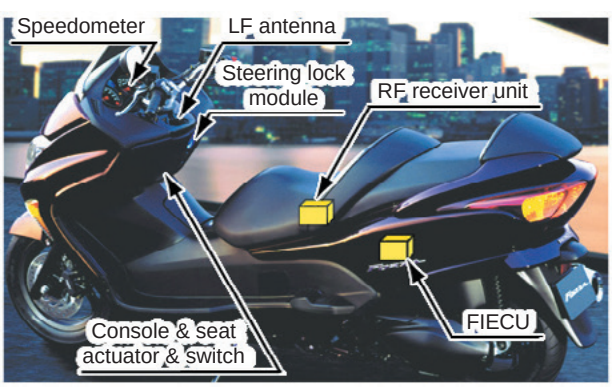


Fig. 2 Layout of smart card key system

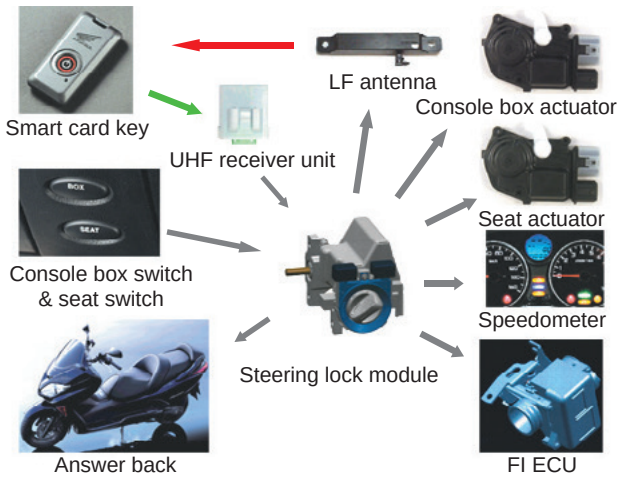


Fig. 3 Overview of smart card key system

3.1. Steering Lock Module

The steering lock module contains the main switch knob, knob torque limiter mechanism, cylinder, knob block solenoid, knob push switch, steering lock mechanism, main switch (contact point), the body (the case) and smart ECU. Figure 4 shows the structure. Figure 5 shows the diagram of the electrical system, of which the smart ECU is the central component.

When the user pushes the main switch knob (knob push switch), seat switch or box switch, the smart ECU starts up and performs two-way authentication with the smart card key. When the main switch knob is pushed and verification is performed, the knob can then be turned and at the same time the steering lock is released. When the motorcycle is in this state and the switch is turned to the ON position, the main power is turned on and an operating permission ID is sent to the FI-ECU. When the seat switch is pushed and verification is performed, the seat actuator is operated, and when the box switch is pushed and verification is performed, the console box actuator is operated.

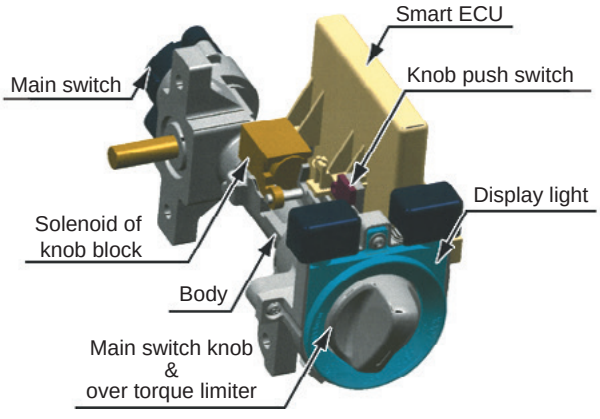


Fig. 4 Structure of steering lock module

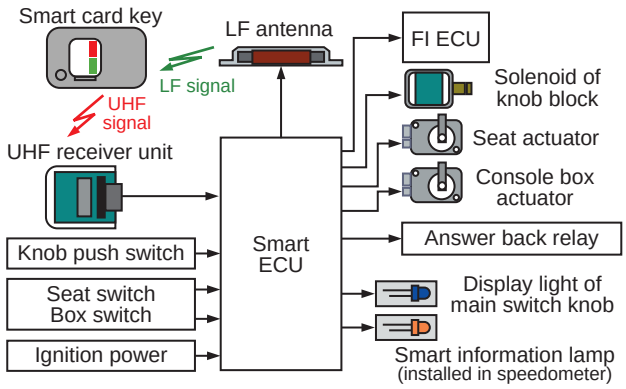


Fig. 5 Electric system diagram

3.2. LF Antenna

An LF signal (133 kHz) is sent from the LF antenna to the smart card key.

3.3. UHF Receiver

A UHF signal (320.65 MHz) from the smart card key is received by the UHF receiver and data is sent to the smart ECU inside the steering lock module.

3.4. Smart Card Key

If the LF signal transmitted from the vehicle is received and verified, a UHF signal is returned to the motorcycle. To protect motorcycles from theft when they are parked in front of a house or a shop (see Section 5.2 for details), the smart card key has a switch to turn communication on and off and an LED indicator showing whether communication is on or off.

Figure 6 shows a circuit block diagram, and Fig. 7 shows the operation timing chart. The three-axis antenna converts the LF signal sent as electric waves to an electric signal. The IC receiving LF receives this electrical signal, starts up, amplifies the signal and converts it to digital data. After the IC receiving LF starts up, the CPU starts up, uses the digital data to check the ID, and only if the ID is verified, sends an ID signal to the UHF transmission circuit. The UHF transmission circuit returns a UHF signal based on the ID signal.

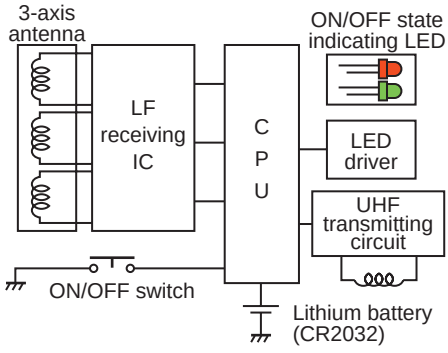


Fig. 6 Circuit diagram of smart card key

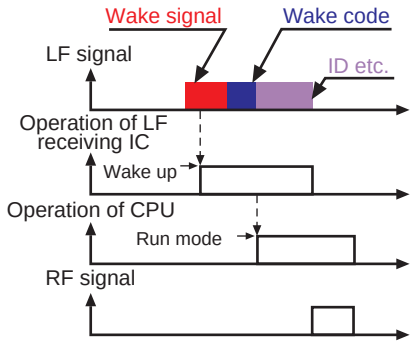


Fig. 7 Operation timing chart of smart card key system

4. Operability and User Usability

Specifications were chosen to enhance convenience. Table 1 compares the numbers of operations that need to be performed with motorcycles using the new system and with motorcycles using conventional key insertion systems. Additionally, in order to assure reliable operation, the system was designed so that the motorcycle will only operate when the user so intends and allows the user to check visually whether the system is locked or unlocked.

Table 1 Number of operations

System / Operation modes	Current system	Smart card key system
Engine running to steering lock	6	3
Steering lock to engine start	7	3
Seat open	3	1
Console box open	5	1

4.1. Operation When Riding (Main Switch Knob Unlock)

When the user approaches the motorcycle and pushes the main switch knob, the smart ECU inside the steering lock module starts up and communicates with the smart card key. When two-way authentication is approved, the main switch knob unlocks (i.e., can be turned). When it is in the unlocked state, the SMART display light situated in the meter turns on, notifying the user that the main switch knob is unlocked. At the same time, blue lighting on the periphery of the knob turns on. Further, when the main switch knob is turned to ON, the main power comes on and an operating permission ID is sent to the FI-ECU. When the FI-ECU verifies the operating permission ID, the motorcycle is ready to run.

4.2. Operation When Dismounting (Main Switch Knob Lock)

When the main switch is turned to OFF, the smart ECU communicates with the smart card key in one-second intervals and the system keeps the main switch knob unlocked as long as there is two-way authentication. If the user moves more than 2.5 meters away from the motorcycle, a locking process takes place, wherein the main switch knob locks (i.e. cannot be turned) and the turn signal blinks to notify the user. Moreover, even if the user is close to the motorcycle, a locking process will take place if either of the following actions is performed.

(1) The system is left alone for more than 20 seconds
(2) The switch on the smart card key is turned to OFF

4.3. Operation of Seat and Console Box

When the rider approaches the motorcycle and pushes the seat switch, the smart ECU starts up and communicates with the smart card key. If two-way authentication is approved, the seat pops up. Also, when the rider approaches and pushes the box switch, the smart ECU starts up and communicates with the smart card key. If two-way authentication is approved, the console box opens. For locking the console box, the construction allows manually locking just as with conventional seats.

5. Assuring Antitheft Toughness

5.1. Protecting Main Switch Knob from Tampering

Because the motorcycle's main switch knob is exposed and accessible to anyone, a torque limiter mechanism was used that lets the knob rotate freely and protects the internal mechanics if excessive torque is applied to the knob. The structure is shown in Fig. 8. Usually the knob and inner joint are connected by a click ball, but this click ball releases when subjected to excessive torque so that the knob alone rotates freely. Figure 9 shows how this works. The operating torque of the torque limiter was set to be approximately three times that of normal operation so that it would not move during normal operation. Figure 10 shows the torque of different operations.

5.2. Antitheft Measures When Parked in front of House or Shop

One of the characteristics peculiar to a motorcycle that makes it so user-friendly is that it can be parked in front of a home or shop. When the smart card key to a motorcycle parked this way is within communication range, it is possible for the main switch knob to unlock and the engine to start. Therefore a communication ON/OFF switch was added to the smart card key so that the user can turn off the communication function freely.

A long press on the switch (at least for one second) causes the communication status of the smart card key to change from ON to OFF (or from OFF to ON). The user can also check the communication status with a short press of the switch and a look at the LED indicator.

5.3. Prevention of Theft by Direct Wire Connection to Ignition Circuit

After SMART verification, an ID signal is sent from the smart ECU to the FI-ECU. Only when the FI-ECU is approved by ID verification, the system allows operating of the ignition and the FI.

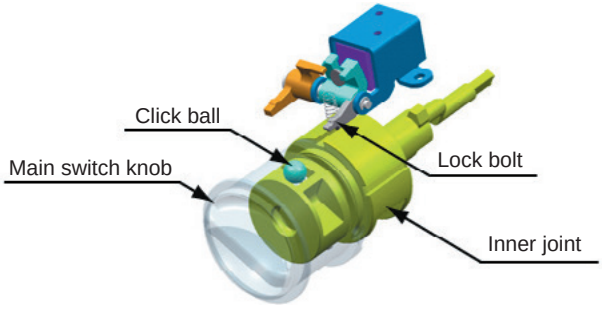


Fig. 8 Structure of over torque limiter

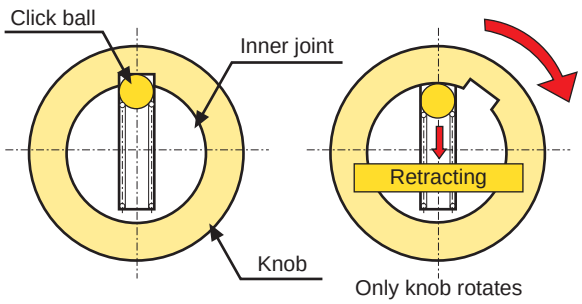


Fig. 9 Operation of over torque limiter

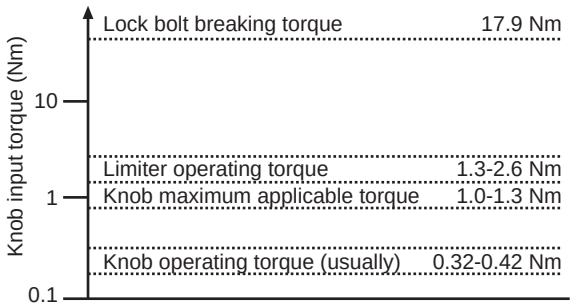


Fig. 10 Knob input torques of each operating

6. LF Communication Specifications

6.1. Unlocking Range and Locking Range

User-friendliness for the following two scenarios was considered, and the unlocking range was set at a radius of 0.8 m (with the main switch knob at the center) in the 180 degrees at the back (height 0.7 - 1.3 m). The unlocking range is shown in Fig. 11.

(1) The rider may push the main switch knob (i.e. knob unlock) before sitting or during sitting on the rider's seat
(2) The user may carry on the smart card key in the pocket of his trousers or jacket

The locking range was set at a radius greater than 2.5 m from the vehicle center (middle of the wheel base), a distance at which it could be sure that the user had definitely left the vehicle. Figure 12 shows the locking range.

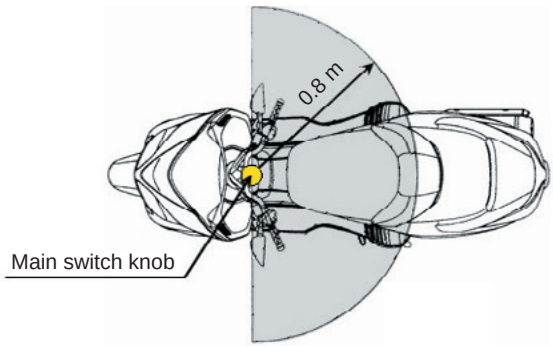


Fig. 11 Unlocking available range

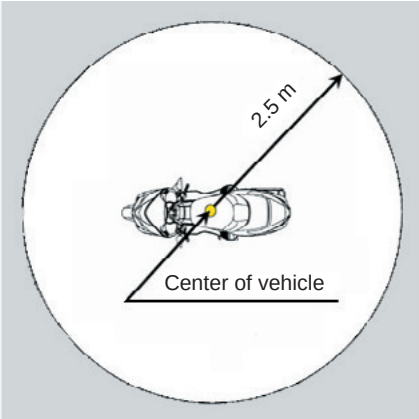


Fig. 12 Locking available range

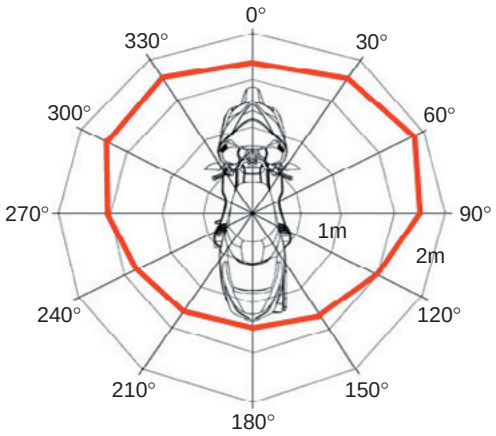


Fig. 14 Communication range

6.2. LF Receiving Sensitivity Margin and Communication Performance in Actual Motorcycle

This smart card key system's communication performance is affected by LF communications. To allow a single LF antenna to perform both locking and unlocking functions, the LF antenna was installed just above the main switch knob. Covering the entire unlocking range requires to enable communication within 1.0 m from the LF antenna installation point, while locking the knob at more than 2.5 m from the motorcycle center requires assuring that communication is not approved at more than 2.14 m from the LF antenna installation point. Figure 13 shows the voltage induced in the smart card key receiving antenna during communication[1]. With a 12 dB margin for the unlocking side, a 3 dB margin for the locking side and by using a layout that optimizes the placement of the LF antenna, it was possible to build a system with just one LF antenna.

Figure 14 shows the test results of the communication range with an actual motorcycle. The results indicated that the unlocking range shown in Fig. 11 was covered, and was smaller than the locking range shown in Fig. 12.

6.3. Impact of Motorcycle Own Noise on LF Communications

A radiation electromagnetic noise from the motorcycle's electric components and harness was detected, therefore the impact of this noise on LF communication was examined[2]. The greater the fluctuation in electric current per unit of time, and the closer the distance from the part emitting the noise, the greater the impact on LF communication tended to be.

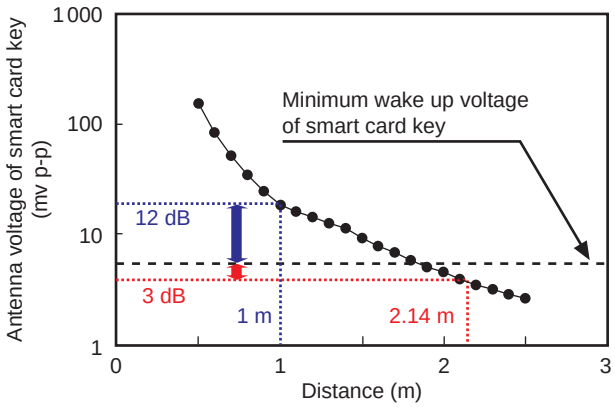


Fig. 13 Relation between distance and voltage of antenna

As an example, Fig. 15 shows a noise waveform occurring between both antenna terminals when the smart card key was close to the main harness and the electric current was varied. In response to a one-time change in electric current, a resonance begins in the antenna's tuning frequency and afterwards is attenuated. This is the result of LCR parallel resonance formed by the antenna circuit and it is commonly known that the attenuation quickens when the value of Q (resonance sharpness) is smaller.

The following types of electromagnetic noise caused by current change from proximity of the noise source are radiated at intervals shorter than the LF communication time (48-63 msec). Therefore it is impossible to avoid these even if communication is retried at the time of LF communication.

(1) Radiation from motor harness of electronically controlled transmission
(2) Radiation from ignition coil
(3) Radiation from charge regulator harness
(4) Radiation from LF antenna harness
(5) Radiation from main harness ground and +12 V line

In the development process, by conducting a wire layout change in the harness and measures to prevent leakage of radiation electromagnetic noise, it was enabled to obtain LF communication performance necessary for unlocking. Induced voltage in the LF receiving antenna was measured, and the value of the noise to signals (LO determination threshold of the regular signal) was designated as the S/N ratio. The results are shown in Fig. 16.

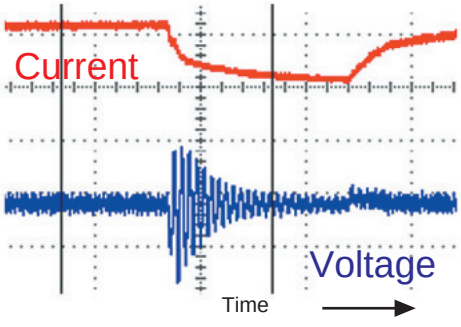


Fig. 15 Voltage waveform at spike noise reception

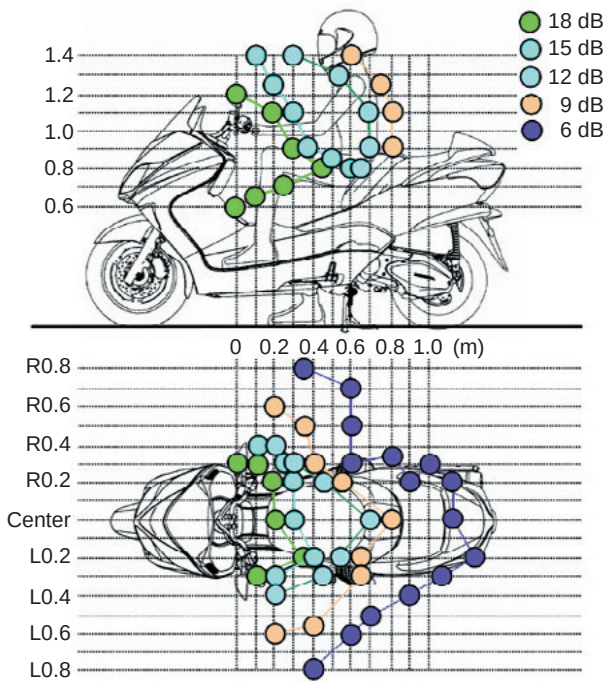


Fig. 16 S/N ratio under engine running

6.4. Impact of Environmental Noise on LF Communication

Continuous electromagnetic noise that exists in the environment to use motorcycles is thought to have an impact on LF communication, so this was checked as well. To prevent a draining of battery when the smart card key is started up continuously by picking up continuous noises, the smart card key performs noise judging after starting up. If it determines that the input is noise, it stops operations and prohibits restarting until the noise is cut off.

In this case LF communication becomes impossible, and to prevent this situation, the electric field intensity at which the smart card key starts up was set to be greater than the results of measurements taken in the field. Figure 17 shows the characteristic electric field intensity at which smart card keys start up.

The electric field characteristics were measured in various environments, including the area around broadcast equipment. As an example, a measurement result around a train guidance radio is presented here. Figure 18 shows the measurement result (measurements by a spectrum analyzer).

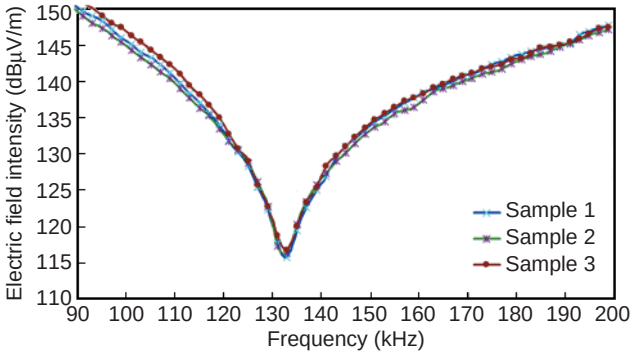


Fig. 17 Electric field intensity characteristics of smart card key starting

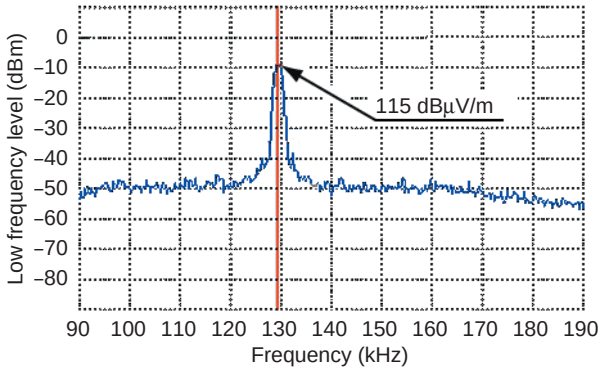


Fig. 18 Electric field intensity by train guidance radio system

7. Conclusion

The industry's firs't smart card key system for motorcycles was built.

(1) This system established a unique operation pattern for motorcycles and reduced the number of operations compared to the conventional key insertion systems.
- Number of operations to start engine: 1/2 (reduction of 50%)
- Number of operations to unlock seat: 1/3 (reduction of 67%)
- Number of operations to unlock console box: 1/5 (reduction of 80%)

(2) The system provided antitheft measures for cases where the vehicle is parked in front of a house or a shop, which is an issue with motorcycles.

(3) The system provided protection against tampering of the main switch knob, as another motorcycle issue.

(4) The communication range as a motorcycle smart card key system was defined, and a system that enabled communications with a single LF antenna was built.

Acknowledgements

The authors would like to thank Honda Lock Mfg. Co., Ltd. for their great assistance and cooperation during the development of this system.

References

(1) Matsuo, U.: Electric-wave Technology Handbook, p. 508 (1988)

(2) Nitta, S., et al.: Environment Electromagnetic Noise Handbook, p. 605 (1999)

■ Authors ■


Takeshi KONNO


Tadashi ONOZUKA


Seiichi YAMASHITA

Development of Prediction Method for Evaluation of Transmission Case Noise Radiation Characteristics

Kazutaka SAKAGUCHI* Kazuhiro SAITOU*

ABSTRACT

A method has been developed for predicting the sound radiation characteristics of transmission cases in order to reduce gear whine noise radiating from transmissions. Normal components of frequency response vectors on the transmission case surface calculated using an FE model of the case are used to predict sound radiation characteristics. To study the validity of the method, the correlation between sound pressure level, the level of vibration of the case surface during operation, and the predicted sound radiation characteristics was investigated. Results showed a good correlation between the figures and enabled equations of correlation between them that were unaffected by shape or type of transmission to be obtained, indicating that this method is sufficiently accurate for studying case specifications at the design stage.

This method enables the design of transmission cases fulfilling performance requirements for gear whine noise using only an FE -model of the case. The employment of the method in the development process commenced with the development of 2004 model year LIFE AT.

1. Introduction

Radiation noise from the transmission is dominant in the high frequency range of 1 kHz or more for gear whine noise inside the cabin. In this high frequency radiated noise range, there are occasions where the case surface vibration mode becomes an issue, and countermeasures such as adding ribs or increasing wall thickness have been implemented. On the other hand, studies have been made into the effect that weight reduction through the elimination of ribs or of reducing wall thickness has on radiated noise. In these cases, the method conventionally used to make predictive studies of case noise radiation characteristics was to build full models from inputs such as excitation force, internal structure, case, and acoustic fields, to outputs[(1),(2)].

However, with radiation noise in the high frequency range, there are many peaks generated from case surface localized resonance modes. In these cases, it is believed that the effect of frequency response characteristics is the dominant factor in radiated noise level. In addition, if it were possible to make independent predictive evaluations of the case noise radiation characteristics, it would be possible to set the specification for the case by itself, effectively reducing the design study period.

Therefore, this development project aimed to establish a prediction method for evaluation of case noise radiation characteristics which allows designers to create the rib and shape layout necessary to achieve the performance requirements for gear whine noise using the case FE model at the design stage.

* Tochigi R&D Center

Table 1 Size of FE -model

Number of nodes	Number of elements
544,571	301,433

※Element type : Isotropic tetrahedral element with midside nodes. (consisting of 10 nodes for a element)

2. FE Model and Noise Radiation Characteristics Prediction

The transmission case FE model was created from the CATIA-3D model using the automatic meshing function. The mesh size index was set for mesh count per unit volume and for mesh quality according to the accuracy verification from the experimental modal analysis results. Figure 1 shows an example of the components of a transmission case assembly model, and Table 1 shows that model's size.

Concerning each component's connection surface boundary conditions, non-adaptive meshes were connected by interpolated elements. The optimal connecting conditions were established from verifications with experimental modal analysis results.

From the concept of meshing transmission error, the excitation force was set to be a frequency spectrum of fixed displacement against frequency, and was input to each case bearing support part according to the ratio of divided load against meshing reaction force. In addition, eigen mode analysis was carried out in advance. Then, to represent the eigen mode shape, the case surface was divided into very small radiation surfaces, and those representative points were established as the evaluation points. From the results of combining frequency responses by each excitation force, the vibration level along the normal vector direction of each evaluation point was determined, and these were taken as the values of noise radiation characteristics predictions.

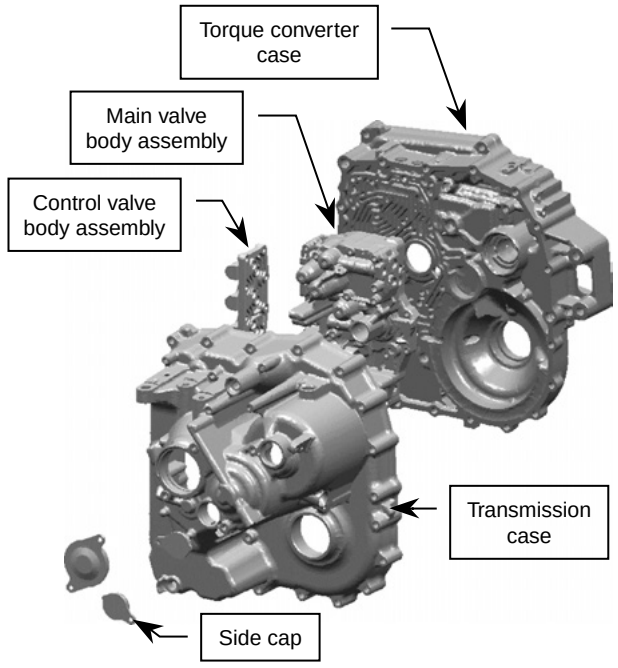


Fig. 1 Components of case model for analysis

3. Verifying the Correlation between Radiated Noise and Case Surface Vibration during Operation, and Noise Radiation Characteristics Predictions

In order to determine specifications at the design stage using noise radiation characteristics predictions, it is necessary to have a correlation between the noise radiation characteristics predictions and the radiated noise level during operation. In order to confirm that correlation, first, an analysis was made of the correlation between radiation noise and case surface vibration during operation. Figure 2 shows the results of correlation analysis of radiation noise peak values as measured on four types of transmissions and the maximum values of case surface normal vector direction vibration. Regardless of the type of transmission, it was confirmed that the correlation between radiation noise and case surface vibration could be expressed with a single equation of correlation for the peak values.

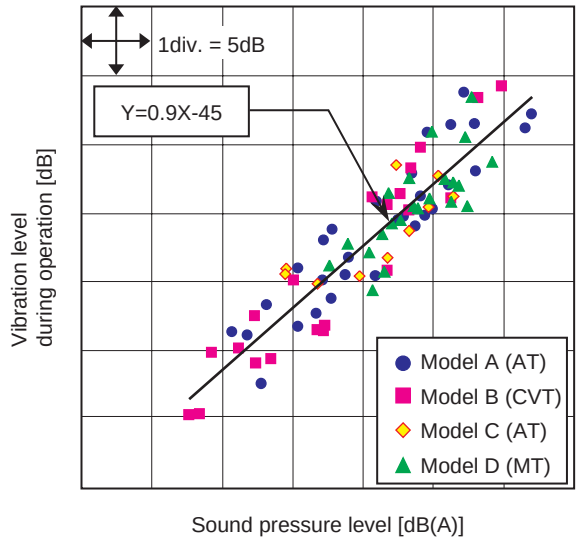


Fig. 2 Correlation between sound pressure level and vibration level

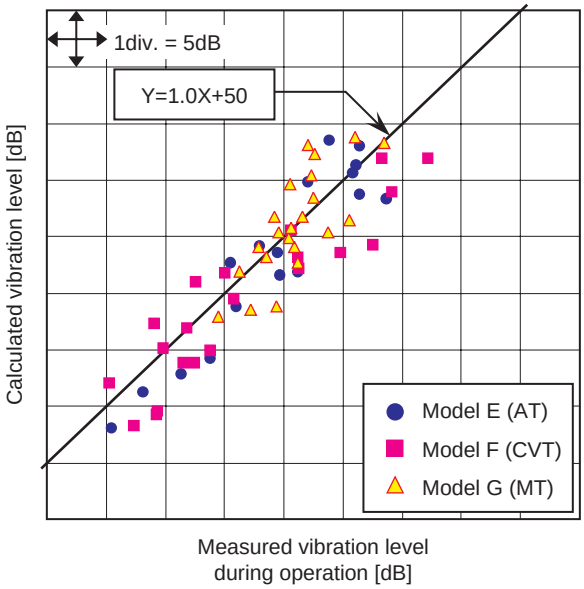


Fig. 3 Correlation of vibration level (measured vs. calculated)

Next, analysis was carried out to correlate case surface vibration during operation with noise radiation predictions for the case eigen mode that matched that vibration mode during operation. The values used in the correlation analysis were the maximum values in each mode, with the same evaluation points on the case surface. The results are given in Fig. 3. For three different types of transmissions, the correlation could be expressed with the same linear equation of correlation.

From the results above, the noise radiation characteristics predictions had sufficient linear correlation with the noise radiated during operation, with no effect from the transmission type. It can be used as an index to set specifications at the design stage.

4. Establishing Target Values for Noise Radiation Characteristics Predictions

By applying the two equations of correlation shown in Figs. 2 and 3 to the previously set targets for measured radiation noise during operation, the target values for noise radiation characteristics predictions are established (Fig. 4). The target for measured noise radiated during operation can help establish the values incorporating the specification, such as completed vehicle quietness targets and gear whine noise frequency characteristics, etc. Therefore, the prediction targets of noise radiation characteristics, too, can incorporate required performance according to specification.

5. Examples of Actual Applications

Figure 5 shows the results of applying this method to the 2004 model year LIFE AT case. The abscissa is indicating frequency, while the ordinate is indicating case vibration evaluation points, comparing each area. The color represents the level of difference

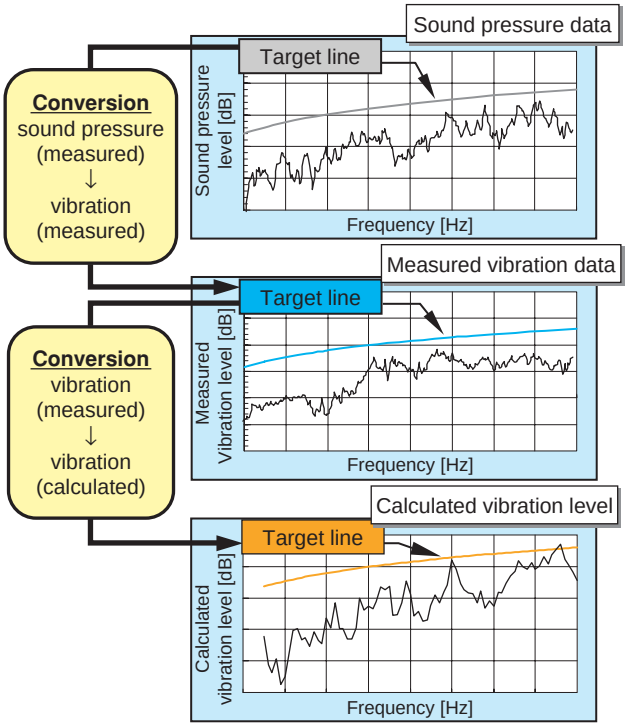


Fig. 4 Conversion of target line

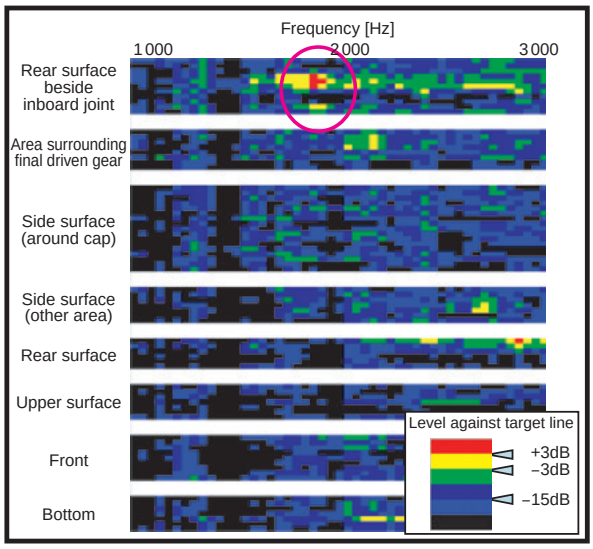


Fig. 5 Evaluation map for vibration level of original structure (calculated)

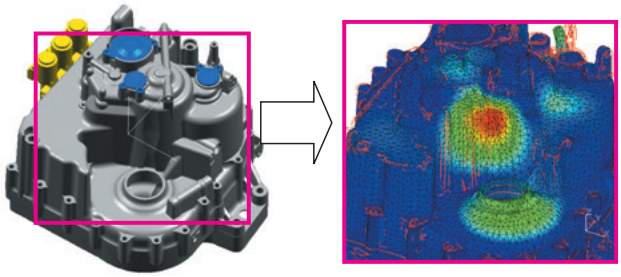


Fig. 6 Target mode shape

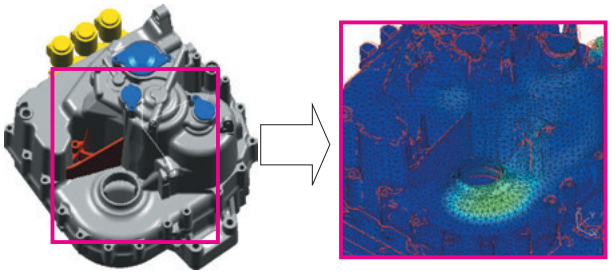


Fig. 7 Modified mode shape

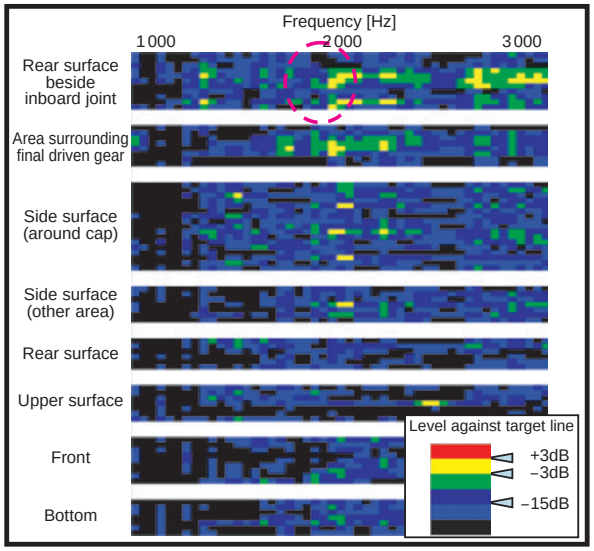


Fig. 8 Evaluation map for vibration level of modified structure (calculated)

from the judgment criteria of the noise radiation characteristics prediction. For this case, it was detected that there is an area of the case rear surface across the drive shaft inboard joint that exceeds the reference value in the range from 1 900 to 2 000 Hz, so countermeasures were studied for that area. Figure 6 shows the vibration mode subject to countermeasures.

Using this method, one or two models of countermeasures using additional parts, such as ribs, can be analyzed in a single day. Additional weight and reductions in radiation noise for a variety of countermeasure configurations were compared and studied. Figure 7 shows the configuration adopted and its vibration mode. The mode subject to countermeasures is clearly shown to be suppressed extremely well. In addition, Fig. 8 shows the results of that noise radiation characteristics predictive evaluation. The countermeasure specification has a 6 dB reduction effect in the subject mode, with a weight increase of 150 g. No increasing in other modes is expected. Figure 9 shows the results as confirmed through incorporation of this specification in an actual transmission. In the actual transmission, there was a radiation noise reduction of 6 to 8 dB, confirming its correspondence to predicted noise radiation characteristics.

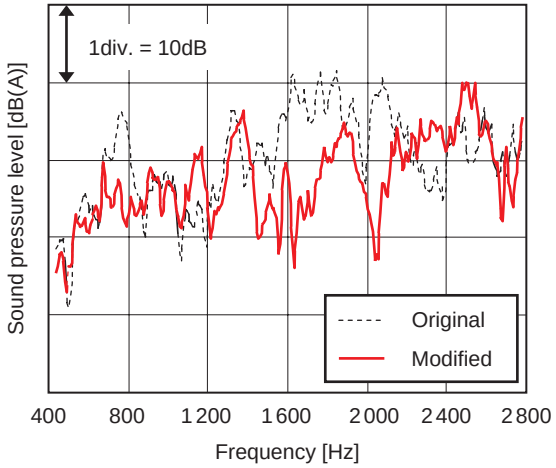


Fig. 9 Comparison of sound pressure level (original vs. modified structure)

6. Conclusion

In order to reduce gear whine noise in the high frequency range, studies were made of a method to predict and evaluate transmission noise radiation characteristics. The following results were achieved.

(1) This method uses normal vector direction components of case surface vibration as determined from case FE model frequency response characteristics. It was confirmed that regardless of the type of transmission, the values of noise radiation characteristics predictions have good linear correlation with radiated noise levels during operation.

(2) By using the equation of correlation obtained from the results above, it is possible to convert the radiation noise targets during operation into the prediction targets of case noise radiation characteristics. This makes it possible to have case specification design incorporating quality required concerning gear whine noise, for the case by itself.

(3) This method was applied in the development of the 2004 model year LIFE AT, and its effectiveness proved.

References

(1) Sumi, K., Yamamoto, K., Gielen, L.: Development of Hybrid Model for Powerplant Vibration, SAE 1999-01-1656 (1999)

(2) Kano, M., Hajika, T.: Useful Method to Calculate the Radiation Noise of Transmission, 2004 JSAE Annual Congress Proceedings No. 66-03, 20035523

■ Authors ■




Kazutaka SAKAGUCHI Kazuhiro SAITOU

Development of CFRP Propeller Shaft

Tomohiro SAKURABA* Shinji WADA*
Shunnosuke KAI* Yasushi SUGIURA*

ABSTRACT

A propeller shaft made of carbon fiber reinforced plastic (hereafter referred to as “CFRP”), a lightweight material, was developed and used on the 2005 model year LEGEND.

To utilize the characteristics of carbon fiber (CF) which is an anisotropic material, the CFRP tube was produced using filament winding molding method. The winding angle of CF was set at 30 degrees to help ensure tube torsional strength. The press-fitting allowance of the metallic stub shaft in the CFRP tube at the joint was optimized, and adequate margin in strength and durability was assigned with respect to other metallic members to help ensure reliability.

The press-fitted portion of the stub shaft was designed such that the tube broke when subjected to the specific axial load, and the ability of the vehicle to absorb shocks during a collision was ensured.

A 30% savings in weight was achieved in the developed CFRP propeller shaft compared to the conventional steel tube propeller shaft.

1. Introduction

The customers’ demand for safe and lightweight automobiles has been growing steadily in recent years. The appearance in the automotive field of lightweight materials that were very expensive in the past is noticeable. The application of carbon fiber reinforced plastics (CFRP) mainly in the aerospace industry is now pervading the automotive industry. The strength and stiffness of this material are being utilized effectively for parts development[(1)].

Conventionally, CFRP was mainly used in the development of the external parts for the hood, fender, and spoiler in racing cars and prototype vehicles, but it is now also being used in the propeller shaft, which is one of the mainstays of the drive system of the vehicle[(2)].

The 2005 model year LEGEND is a 4WD vehicle fitted with the newly developed Super Handling-All Wheel Drive (SH-AWD) system. This paper describes the technical overview of the CFRP propeller shaft fitted on the 2005 model year LEGEND. The shaft is shown in Fig. 1.

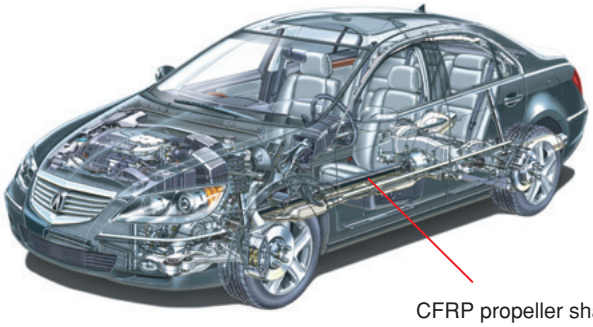


Fig. 1 Perspective drawing of new LEGEND

* Tochigi R&D Center

2. Materials and Method of Manufacture

2.1. Characteristics of CFRP

Because the reinforcing material carbon fiber (CF) has a low specific gravity, CFRP possesses high specific strength and stiffness, enabling the weight of parts to be reduced. However, the material also displays strength anisotropy dependent on the reinforcing fibers. Figure 2 shows the relationship between the direction of the fibers and the tensile strength of the material. Tensile strength is high in the fiber direction (0°), but drops to approximately one-tenth the original figure when the fibers are aligned at right angles (90°).

This characteristic can be exploited to achieve further weight reduction by aligning the fibers in the direction of the stress on the part.

2.2. Filament Winding Molding Method

Figure 3 shows the manufacturing process for the propeller shaft. CFRP tubes molded by filament winding (FW) method are cut to predetermined dimensions and metal stub shafts are press-fitted into the ends to complete the shaft. The remainder of this section will discuss FW molding, which is employed to exploit the characteristics of the CF.

24K PAN-based CF is applied, and a bisphenol A-based epoxy resin is applied as hardening resin. The CF is served from a creel stand. It is passed through a resin bath to impregnate it with epoxy resin, after which it is wound around a mandrel. The carbon fiber winding is produced from a hoop layer wound at an approximate right angle to the direction of the tube diameter and a helical layer wound at an angle. The helical layer is essential to ensuring the torsional strength of the propeller shaft. In the new shaft the helical layer is wound at an angle of 30°. When a preset amount of CF has been wound around the mandrel, it is placed in a heating oven and cured at 130 °C for 120 minutes. The heating oven is equipped with a rotating mechanism to help prevent deformation of the tube during curing. The FW molding process is completed when the CFRP tube is removed from the mandrel after curing. The tube then proceeds to the next process, in which it is cut into lengths. Figure 4 shows a schematic of the FW molding process.

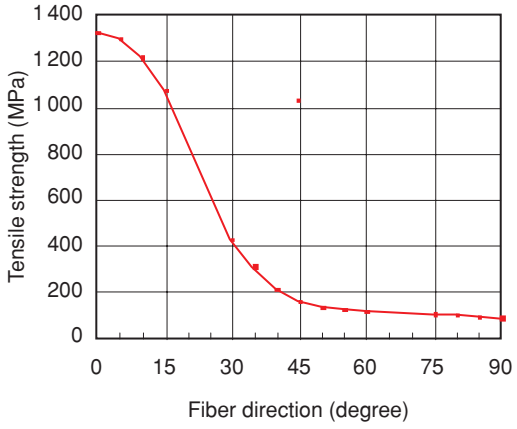


Fig. 2 Effect of fiber angle on tensile strength

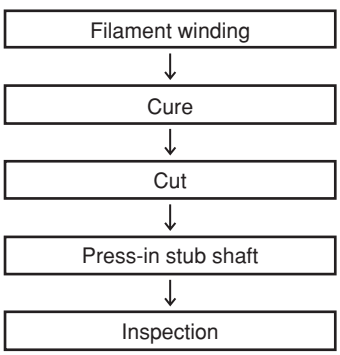


Fig. 3 Manufacturing flow for shaft

3. Basic Construction and Target Performance

In vehicles that use a propeller shaft such as four-wheel drive vehicles, the propeller shaft may obstruct the backward movement of the engine when the vehicle is involved in a collision.

To help prevent this, the structure of the propeller shaft must be designed to break stably in the axial direction when subjected to a specific load.

The basic construction of the CFRP propeller shaft is shown in Fig. 5. The CFRP propeller shaft is made of the No. 1 shaft, No. 2 shaft, three isokinetic joints, and the center bearing support.

A CFRP tube molded by FW molding was used, and the serrated portion of the metallic stub shafts was press-fitted at the two ends of the tube to complete the shaft.

In a conventional propeller shaft, the steel tube and stub shaft are joined by welding so an extremely high strength is retained to transfer the driving torque.

In the CFRP propeller shaft, the CFRP tube and stub shaft are joined by press-fitting the serrated portion. By adjusting the form of the serrated teeth, the number of teeth, the press-fitting length, and the press-fitting compaction allowance, the original function namely the transmission of the driving torque has been balanced to

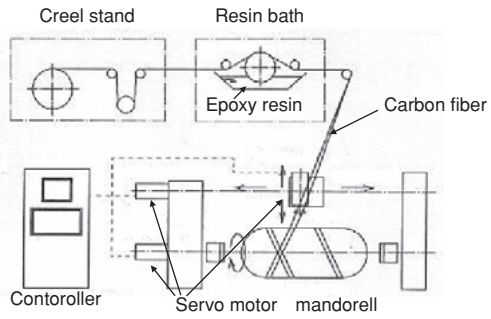


Fig. 4 Filament winding molding

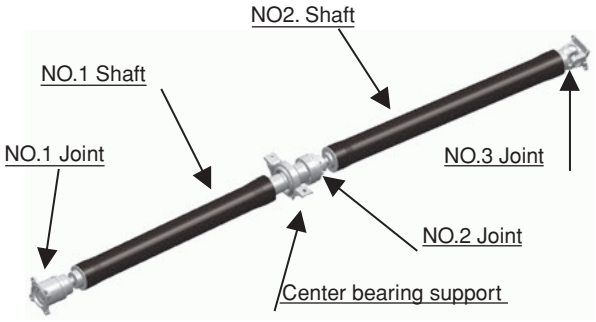


Fig. 5 Construction of CFRP propeller shaft

a higher level with the breakage in the axial direction at low load during a collision[3]. A diagram of the serrated portion is shown as Section AA in Fig. 6. The diagram demonstrates how press-fitting causes the stub shaft to bite into the inner walls of the CFRP tube.

The torsional strength of the metal stub shaft was established with reference to torque demands in an actual vehicle. The torsional strength of the press-fit portion of the stub shaft and the CFRP tube are designed to be higher than that of the stub shaft, to help ensure that it is the stub shaft that will break if the allowable torque is exceeded.

From considerations of the practicality of the vehicle, a sliding arrangement was used in the No. 1 joint so that the CFRP propeller shaft is protected from damage when engine displacement occurs during normal running or a light collision. The construction for absorbing the displacement is shown in Fig. 6.

When a larger load than that produced in a minor collision is imparted to the vehicle chassis, the load generated by rearward motion of the engine causes the stub shaft, the serrated portions of which were press-fitted into the ends of the tube, to slide inside the tube and break it from within.

It is essential that the breakage from within the tube occur at an appropriate load to help ensure that the shaft does not obstruct the rearward motion of the engine.

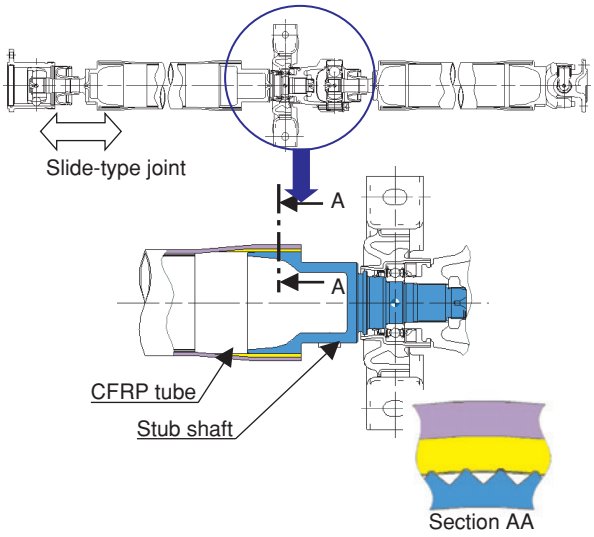


Fig. 6 Structure prior to breaking

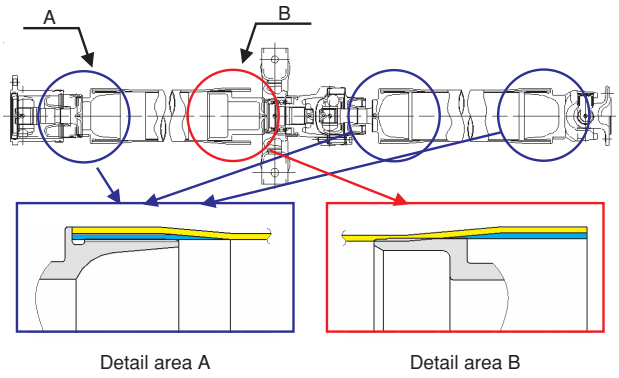


Fig. 7 Detail of press-in structure and shaft break mechanism

The construction before the breakage is shown in Fig. 6, while the construction after the breakage is shown in Detail B in Fig. 7.

To help ensure that the tube would only break at loads above a specific level, it was essential to control which press-fitted stub shaft section would slide inside it and cause the breakage. As shown in Fig. 7, the stub shaft is pressed into the propeller shaft at four locations. A structure was therefore devised to enable the press-fitted section which would break the tube when a load was applied in the axial direction to be specified, thereby ensuring predictable breakage of the tube.

A flange was fitted at the location (Detail A) in the stub shaft and touching the end face of the CFRP tube such that it does not cause breakage of the CFRP tube as shown in Fig. 7. Even if a load were applied, the stub shaft would not be pushed into the CFRP tube.

This arrangement enabled the position of breakage of the CFRP tube to be controlled.

4. Characteristics of Individual Parts

4.1. Load Performance

Figure 8 shows the target load and the relationship between load and stroke with the CFRP propeller shaft of the 2005 model year LEGEND.

Testing confirmed that the tube broke when the press-fit section of the stub shaft was pressed inside it, and that this breakage occurred predictably at a low load.

4.2. Torsional Strength

The propeller shaft was subjected to torsion tests under the type of conditions found in an actual vehicle. No cracks occurred in the joint sections under normal torque conditions. When excess torque was applied, a torsion breakage occurred at the press-fit section of the stub shaft, as predicted by the initial design specifications.

Fatigue tests were also conducted, and no cracks or other defects which would affect performance occurred at the joint sections of the shaft, confirming the achievement of an equivalent level of performance to that of a steel propeller shaft.

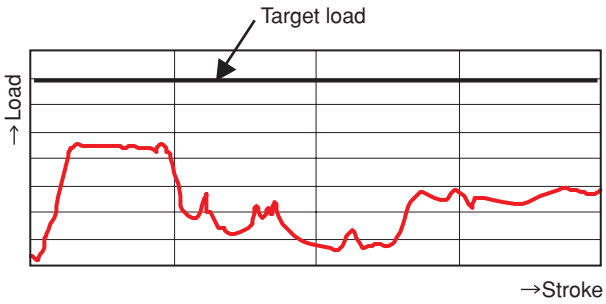


Fig. 8 Load characteristic

4.3. Environmental Resistance

The environmental resistance of the CFRP tube was confirmed.

To confirm resistance to engine oil, AT fluid, acid, alkali, and grease, the CFRP tube was subjected to immersion treatment, then subjected to a compression test with a load applied on the circumference of the tube to measure the strength retained by the tube as shown in Fig. 9. No difference in strength was observed before and after the treatment, thus confirming that no material deterioration occurred with respect to the items mentioned above.

In addition, no decline in performance was observed in durability tests conducted under actual use conditions, designed to test factors such as heat resistance and water resistance.

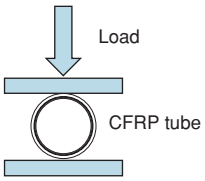


Fig. 9 CFRP compression test

5. Conclusion

A propeller shaft made of CFRP was developed and applied on the 2005 model year LEGEND.

1. The shaft was broken at the desired crushing load considering the construction of the press-fitted part of the stub shaft, and the performance of the actual vehicle in absorbing the load during collision was confirmed.
2. The stub shaft press-fitting compaction allowance was optimized to help ensure the strength of the joint sections.
3. Evaluation of the CFRP tube during FW molding confirmed that the material would possess adequate durability in actual use.
4. By using a two-part CFRP propeller shaft system instead of a steel three-part propeller shaft system approximately 30% of weight savings and approximately 25% of reduction in the number of parts were realized in the 2005 model year LEGEND.

References

(1) Yamane, Y., et al.: Development of a Lightweight CFRP Hood and Rear Spoiler, Honda R&D Technical Review, Vol. 15, No. 1, p. 209-214
(2) Kawarada, K., et al.: Development of New Composite Propeller shaft, TOYOTA Technical Review, Vol. 43, No. 2
(3) JP, 09-175202, A (1997)

■ Authors ■


Tomohiro SAKURABA


Shinji WADA


Shunnosuke KAI


Yasushi SUGIURA

Analysis of Vibration Behavior of Full Vehicle during Brake Judder

Tetsuya YAMAGUCHI*

ABSTRACT

A variety of components and systems in a vehicle are involved in brake judder. Up to the present, many papers have explored the roles of the brake and suspension in judder, but quite few have taken up the analysis of the vibration behavior of transfer systems, such as the steering system, subframe and body, from a viewpoint of their impact to brake judder.

This study employed bench tests to reproduce driving conditions. In order to analyze the transfer system, vibration of the entire vehicle was measured and behavior analysis was performed by visualization of vibration phenomena. Much was learned about the vibration behavior of the steering system, subframe and body, and the basic mechanism of brake judder involving the entire vehicle was proposed.

In addition, the influential factors in the transfer system were identified, and the contribution of each was analyzed.

1. Introduction

As examples of research into brake judder carried out to date, many reports of research on the brakes, which constitute the source of vibration, and on the suspension, which constitutes a resonance system[(1) - (6)] exist. However, there are few papers covering the analysis of the effect of the steering system, sub frame and body, which constitute the vibration transfer system.

In order to analyze the mechanism of vibration of the entire vehicle including the transfer system, using an experimental analysis method, it is necessary to measure the vibration behavior of each part of the vehicle. In some cases the total number of measurement points reaches 100. For this reason, data measurement at all necessary points in a track test in a single operation requires large-scale measuring equipment, so the test itself is difficult to carry out. On the other hand, when using a method that involves dividing measurements into several sets, it is challenging to stably generate the same vibration phenomenon during repeated tests, and thus the accuracy of the analysis becomes an issue.

There are cases in which a chassis dynamometer is used in bench tests, however, in these cases the excitation source remains torque variation, which depends upon the characteristics of the friction material of the brake. Consequently, it is not possible to obtain a significant modification from the viewpoint of stably generating a vibration phenomenon.

To address these issues, a bench test method with high reproducibility permitting the same vibration phenomenon to be generated during repeated tests, as well in contrast to a track test, and enabling high quality vibration data to be acquired, was studied in this research.

Next, to obtain a grasp of the basic mechanism of brake judder, this test method was used and all of the measured data for each test analyzed together, enabling the vibration mode of the entire vehicle to be visualized and behavior analysis performed.

This report details the identification of the influential factors affecting vibration and a contribution analysis of each of these factors from the results of vehicle behavior analysis and track testing.

* Tochigi R&D Center

2. Bench Test

2.1. Selection of the Test System

In the study of the bench test method, a comparison of the following two types of test system was carried out.

(1) Chassis dynamometer (Fig. 1)

(2) Tire patch exciters (hereafter called TPE. See Fig. 2)

The former is used in general brake tests and is well known. The latter (TPE) is test system made by MTS, which uses two shakers and air bearings to shake the left and right front wheels of the vehicle.



Fig. 1 Chassis dynamometer



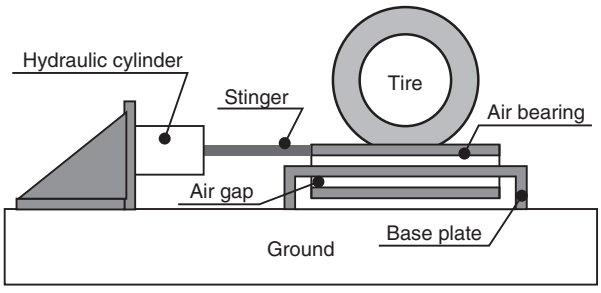


Fig. 2 Tire Patch Exciters

In a test using a chassis dynamometer, it is possible to use a test method that directly substitutes a bench test for a track test, so the reproducibility of the vibration phenomenon with respect to the track test is very high. However, as in the case of the track test, the excitation source is the brake torque variation, which depends on the friction material characteristics, so the same issues remain with regards to stably generating the same vibration phenomenon in repeated tests.

Also, because it is necessary to use the brakes for vibration excitation, waiting time is needed to allow the brake components to cool down between one measurement and the next. This results in long test times for multiple point measurements or under conditions where repeated testing is required to compensate for poor stability of the generated phenomenon. Consequently, in product development where reduction of development time and elimination of prototype vehicles are demanded, the use of a dynamometer is considered unsuitable as a study method due to the poor time efficiency of the work involved.

To solve these tasks, a study of the TPE was carried out next. By using an excitation method employing a shaker to stabilize the input of the excitation source, it is possible to generate the vibration phenomenon repeatedly and stably. In addition, there is no need to carry out braking using brakes, so there is no need to wait for the brake components to cool down between one measurement and the next.

For the above reasons, a TPE was selected as the test system in this research.

2.2. TPE Bench Test Method

As the input condition for securing reproducibility of the vibration phenomenon with respect to a track test, it is necessary to control the shaker so that typical brake torque variation is reproduced when a disk rotor of non-uniform thickness is installed. Figure 3 shows the torque variation of an average brake obtained from a single dynamometer test. The torque variation characteristics are converted into a longitudinal force at the point where the tire

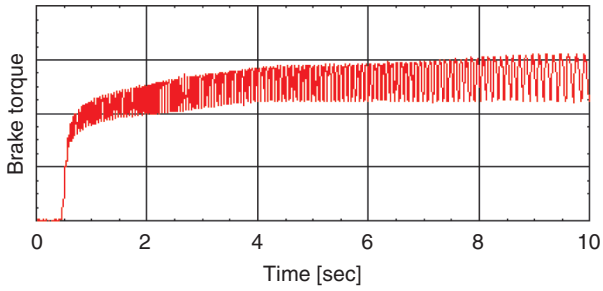


Fig. 3 Measurement data: brake torque variation (single dynamometer)

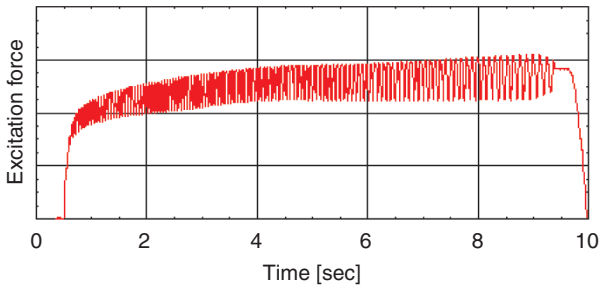


Fig. 4 Excitation force: Tire Patch Exciters

touches the ground, to become the input data. The results of reproducing this force with a TPE are shown in Fig. 4. There is good agreement between both sets of results, indicating that the reproducibility is adequate.

Figure 5 shows the measured results of the acceleration of the steering rotational vibration (tangential direction component at the outer radius of the steering wheel) obtained from 10 repetitions of a track test, compared with the measured results obtained from a bench test using a TPE. Here, the change of amplitude over time is represented in graphical form by plotting only the peak value for each wavelength (Fig. 6). By comparing these two results, it can be seen that steering rotational vibration during the bench test matches the average value for the track tests, and the change of vibration over time is reproduced well.

It was therefore judged that, as a result of the above, the test method established had high reproducibility with respect to the track test, and was able to stably generate the same vibration phenomenon on a bench test. This method is used to perform multiple point measurements for the purpose of performing vehicle behavior analysis.

3. Basic Mechanism

An adequate number of measurement points were used for each component and each system, in order to create an operational deflection shape during the occurrence of the vibration phenomenon. Figures 7 and 8 show the respective operational deflection shapes in time history, created from the data at these measurement points. As a result of analyzing these operational deflection shapes, the basic mechanism of brake judder occurrence, shown in Fig. 9, was understood.

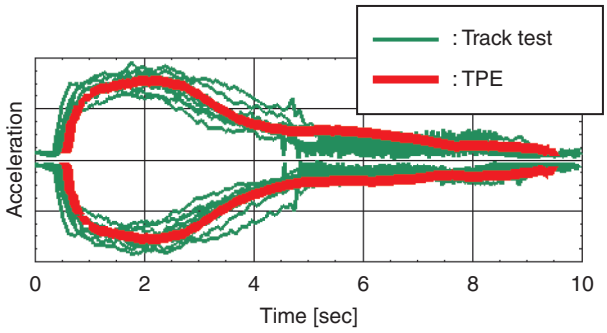


Fig. 5 Rotational acceleration: steering wheel comparison between track test and TPE

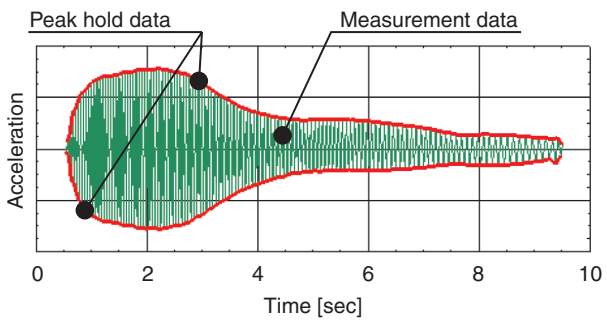


Fig. 6 Steering wheel acceleration: peak hold data

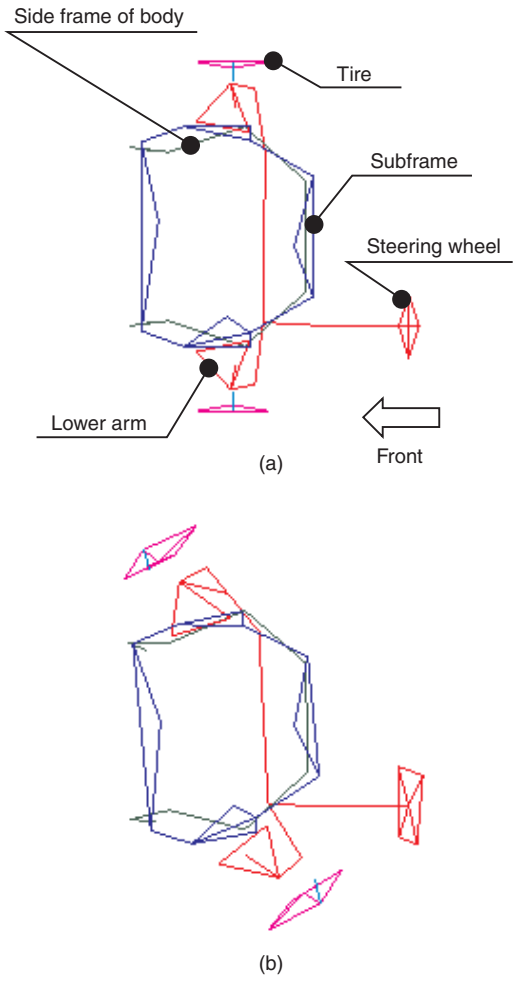


Fig. 7 Operational deflection shape at TPE (suspension, steering, subframe and side frame of body)

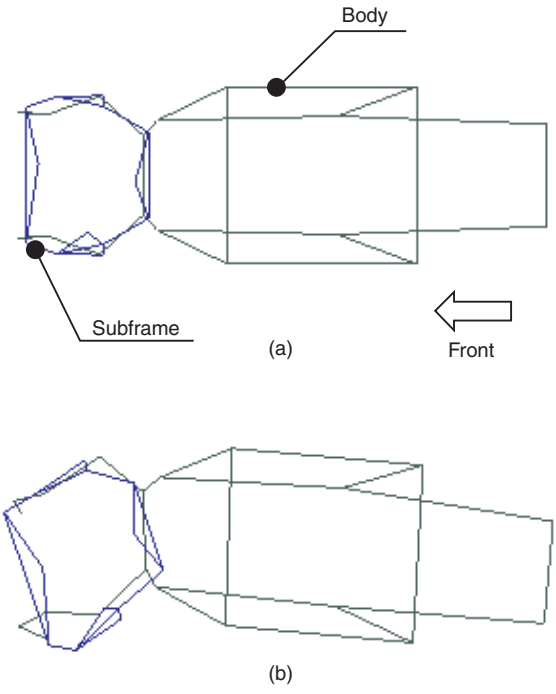


Fig. 8 Operational deflection shape at TPE (subframe and body)

The transfer path (1) of vibration, shown on the left side of the figure, is the conventionally known transfer path in which longitudinal vibration from the suspension - a main cause of brake judder - becomes rotational vibration about the king pin axis, and passes through the tie rod to become steering vibration.

In contrast, transfer paths of vibration (2) and (3) shown at center and the right side of the figure are the transfer paths related to vibration of the sub frame and body, newly clarified in this research. As a result of the generation of longitudinal vibration of the suspension, the sub frame that supports the suspension is excited in the lateral direction at the lower arm bushing point, and in the lateral and longitudinal directions at the compliance bushing point. As a result, the sub frame vibrates in the lateral direction while rotating slightly around the vertical axis of the vehicle. Concurrently, the housing of the gearbox mounted on the sub frame also vibrates in the lateral direction, more or less integrally with the sub frame, generating a relative displacement with respect to the rack, which becomes the rotational vibration of the steering. This is transfer path (2).

Vibration of the sub frame is also transmitted to the body, which supports it, and the body itself also vibrates in the lateral direction while undergoing lateral bending at the front from the cabin. This is transfer path (3), and is the mechanism of body vibration when brake judder occurs.

As a result of performing the abovementioned vehicle behavior analysis using multiple point analysis, it was determined that there are two transfer paths through which rotational vibration of the steering occurs, and it was possible to help elucidate the mechanism by which body vibration occurred.

In addition, vehicle behavior analysis was likewise carried out for multiple additional vehicles employing different types of front suspensions, and the abovementioned basic mechanism of brake judder was observed to be the same in each case.

4. Influencing Factors in the Transfer System

4.1. Study of Modification of the Sub frame and Body

When studying proposals for modification to the vehicle, it is possible to establish guidelines for such proposals by focusing attention on areas where major deformation and vibration occur, according to the operational deflection shapes in Figs.7 and 8. Here, attention was focused on the deformation of the mount bushing of the sub frame and the lateral bending deformation of the front end of the body.

In order to minimize deformation of the sub frame mounting part, a reinforcement patch equivalent to a rigid mount was added, and to suppress lateral bending deformation of the front end of the body, a reinforcement patch was added to each member of the body. When the shape of the reinforcement patch was being studied, the finite element method (FEM) was used to analyze each member's sensitivity to lateral bending deformation, and the reinforcement locations were thus determined. Figure 10 shows the results of comparing the stiffness levels on the body without the sub frame, with and without this reinforcement. It can be seen that lateral bending deformation has been reduced by about 17% due to the body reinforcement.

Regarding vibration transfer to the body, it is clear from the results of this vehicle behavior analysis that vibration is transmitted from the lower arm mounting point on the sub frame. Consequently, in order to evaluate change in stiffness level related to brake judder due to the reinforcement, a comparison of static deformation at the

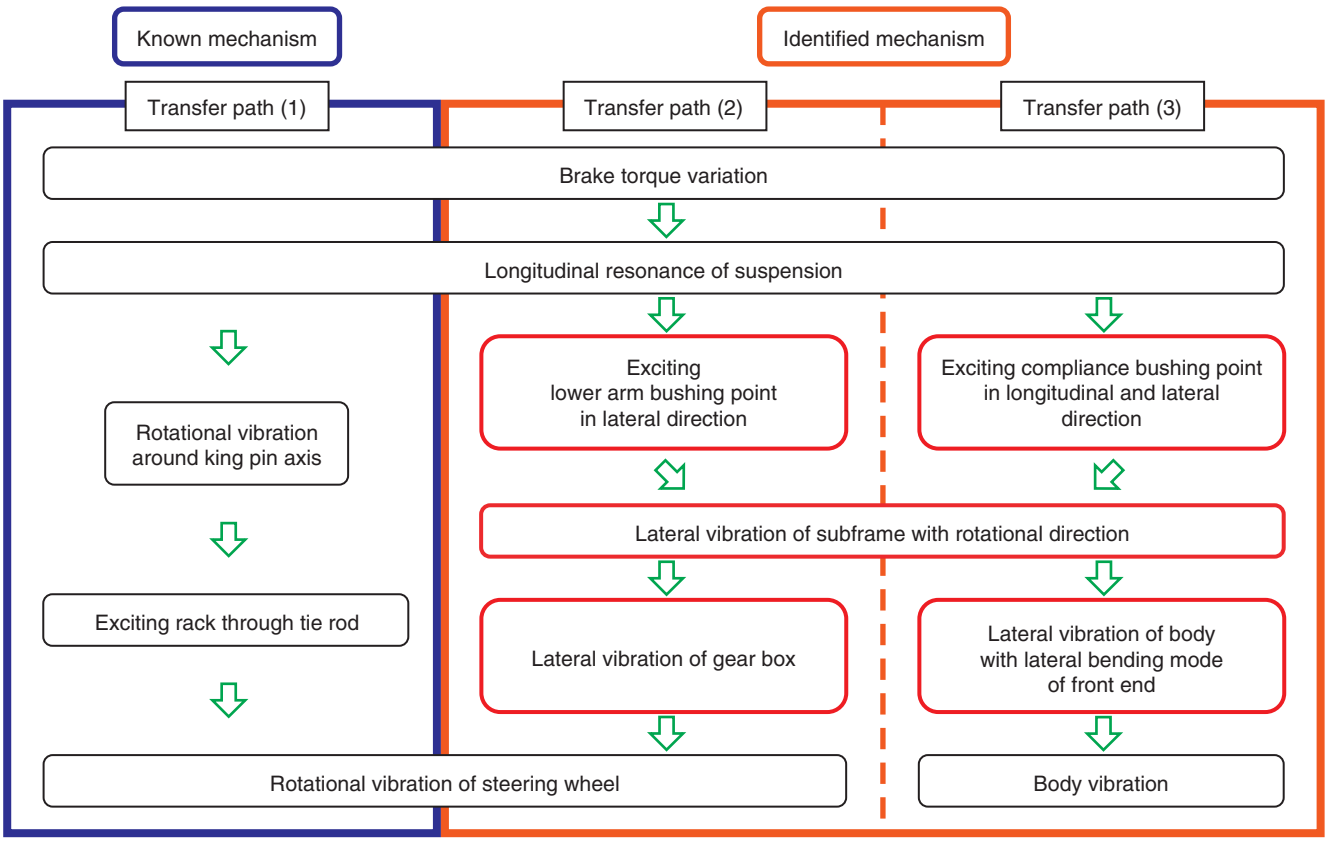


Fig. 9 Basic mechanism of brake judder

lower arm bushing point was performed. The results are shown in Fig. 11. For specifications under which a reinforcement patch was applied to the body alone, the stiffness of the lower arm bushing point remained almost unchanged. In contrast, for specifications under which a reinforcement patch was added to the sub frame mounting part as well as to the body, the deformation was reduced by about 64%. From this it can be confirmed that in the case where a vehicle has a sub frame mounted via a mount bushing, the increase in stiffness of the lower arm bushing point due to the body reinforcement alone is low.

As a result of performing track tests to evaluate these two modification proposals, it was confirmed that whereas no meaningful difference was found for body reinforcement alone, an enhancement of about 20% was obtained for specifications under which both the body and sub frame mounting parts were reinforced, which matches the case results of studying stiffness of the lower arm bushing part.

4.2. Effect of the Steering System

The steering system is the final path of vibration transfer containing the steering wheel from which the driver directly detects judder, and thus performs an important role. However, the vibration phenomenon is reduced mainly by increasing sliding resistance of the rack in the steering gearbox such as damper and friction, and there have been almost no cases of research into other factors carried out to date. In this research, attention was focused on the column shaft, and a study of its effect was carried out.

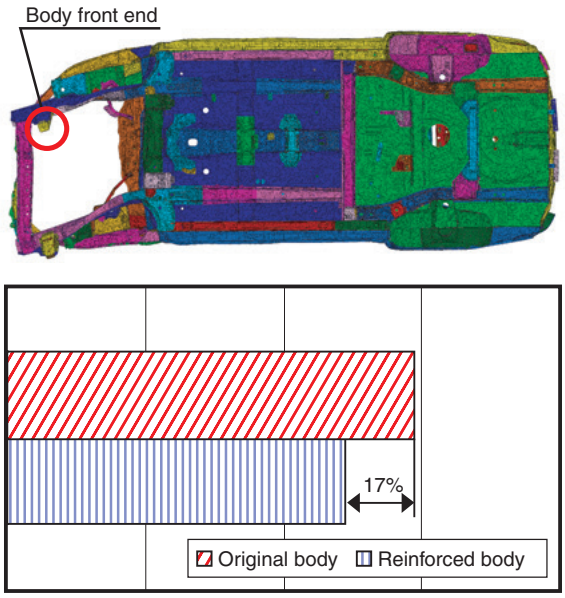
The column shaft comprising the steering system normally uses yoke joints due to the vehicle layout (Fig. 12). The shafts connected by these joints intersect at an arbitrary angle, causing the transfer characteristics to vary based on rotational position. Furthermore, the influence of friction at the yoke joints also changes along with the rotational position, so the total friction characteristics of the column shaft also change.

In order to check the way in which these characteristics affect brake judder, a track test of the yoke joint phase differences of the column shaft in a neutral position of the steering was carried out. Figure 13 shows the yoke joint phases at which measurements were performed, the rotational transfer rate fluctuations at each position, and the characteristics of rotational friction. Figure 14 shows a comparison of the steering rotational vibration results for each of these positions. In the case of this testing, it was confirmed that the maximum difference obtained was about 30%. Consequently, it was deemed necessary to take adequate consideration of these characteristics when performing brake judder studies.

In the case of steering systems with a tilt and telescopic mechanism, the shaft intersection angle changes along with the position of the steering wheel, which in turn causes the rotational transfer rate to fluctuate and the frictional characteristics to change. It is therefore important to select a yoke joint phase that is not readily affected by these factors.

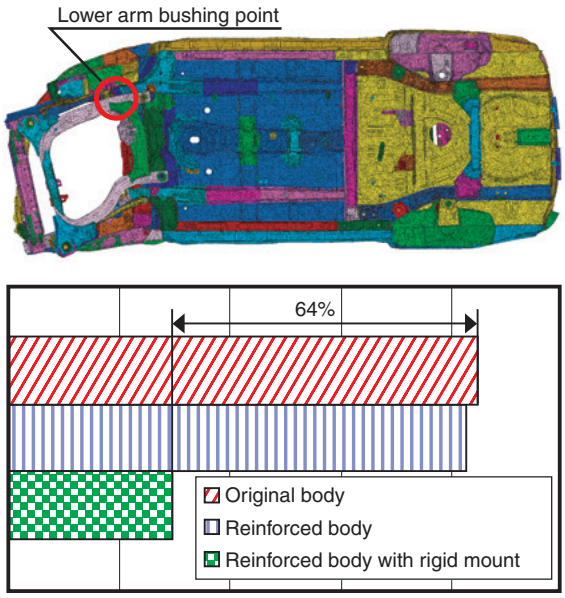
4.3. Degree of Contribution of Influencing Factors

Through actual cases of the abovementioned analysis, it was possible to help elucidate the contribution of influencing factors in the various components of the transfer system, including the steering system, sub frame and body. Accordingly, the influencing factors (including the steering damper, which has been conventionally used to suppress rotational vibration) have been set out below, in decreasing order of contribution.



Displacement: body front end

Fig. 10 Body stiffness level without subframe



Displacement: lower arm bushing point

Fig. 11 Body stiffness level with subframe

(1) Yoke joint phase
(2) Steering damper characteristics
(3) Sub frame mount

By thus extracting the factors influencing the transfer system and analyzing their contribution, it was possible to help identify the points of modification related to brake judder from various components and systems of the overall vehicle, including the excitation source and resonance system.

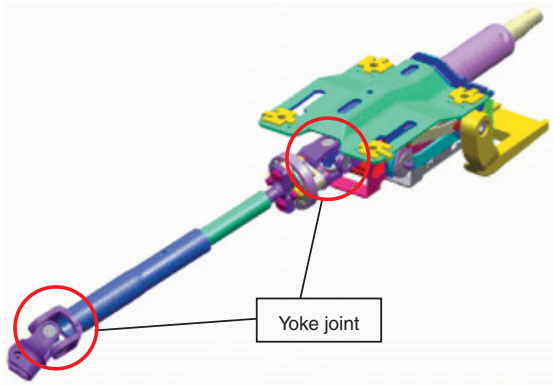


Fig. 12 Yoke joint: column shaft

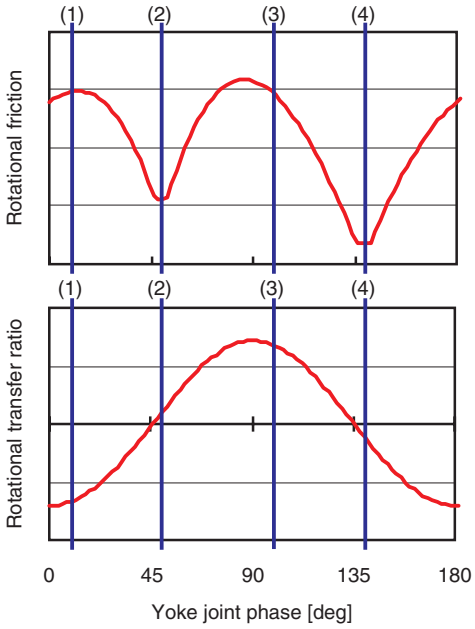


Fig. 13 Characteristics of column shaft

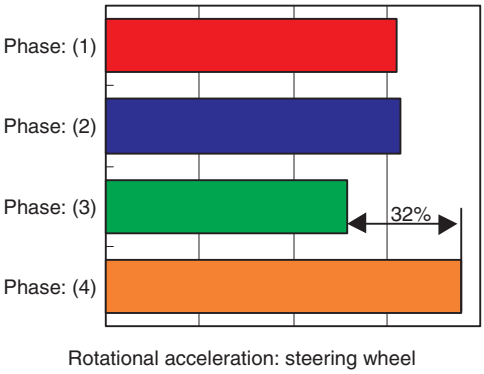


Fig. 14 Result of track test

5. Conclusions

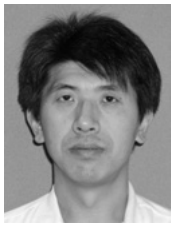
By using a bench testing system to excite vibration, it was possible to perform vehicle behavior analysis concerning brake judder, and also to analyze the component contributions to the transfer system, from which the following conclusions have been obtained.

(1) As a result of using a bench test employing TPE, it was possible to establish a test method that had high reproducibility, could stably generate the vibration phenomenon, and permitted vehicle behavior analysis to be performed efficiently.
(2) As a result of visualizing the vibration behavior when brake judder occurred, it was possible to obtain a grasp of the basic mechanism of vibration transfer from the brake to the steering wheel and body.
(3) It was found that the transmission characteristics changed greatly along with the rotational vibration of the steering wheel, depending on the yoke joint phase and the tilt and telescopic positions of the column shaft in a neutral steering position.
(4) It was possible to help elucidate modifications related to brake judder in relevant components and systems of the overall vehicle, including the excitation source and resonance system, by extracting each factor in the steering system and also the transfer systems in the sub frame and body, and analyzing the respective contributions.

References

(1) Doi, K. et al.: Brake Judder Reduction Technology- Brake Design Technology including Frictional Materials Formulation -, 1999 JSAE Annual Congress Proceedings, No. 100-99, p. 9-12 (1999)
(2) Abdelhamid, M. K.: Brake Judder Analysis Using Transfer Functions, SAE Paper 973018 (1997)
(3) Kim, M. G., et al.: Sensitivity Analysis of Chassis System to Improve Shimmy and Brake Judder Vibration on Steering Wheel, SAE Paper 960734 (1996)
(4) Gassmann, S., et al.: Excitation and Transfer Mechanism of Brake Judder, SAE Paper 931880 (1993)
(5) de Vries, A., et al.: The Brake Judder Phenomenon, SAE Paper 891329 (1989)
(6) Yamaguchi, T., Kobayashi, K.: Study of the Dynamic Characteristics of the Suspension as Related to Brake Judder Reduction, Honda R&D Technical Review, Vol. 13, No. 1, p. 99-104

■ Authors ■



Tetsuya YAMAGUCHI

Study on Combustion Monitoring System for Formula One Engines Using Ionic Current Measurement

Yuichi SHIMASAKI* Junko SAKAGUCHI* Hidetaka MAKI*
Hiroaki SUZUKI* Akira KATO* Kazutoshi NISHIZAWA*

ABSTRACT

A combustion monitoring system has been developed by applying ionic current measurement for malfunction diagnosis and combustion management of Formula One engines. In this system the spark plug's center electrode acts as an ion probe for ionic current measurement, which eliminates the need for additional sensors. The system allows the onboard monitoring of each of the cylinders for their combustion status under all operational conditions. The accuracy and reliability has ensured that the technology can be effectively used for the management of Formula One engines with car-to-pit communication carried out via telemetering. It is capable of various types of controls including detection of misfire, hesitation, detonation and the lean-burn condition. In addition to these points, this paper reports on the relationship between the spark plug center electrode configuration and the absolute quantity of ionic current.

1. Introduction

In recent years, passenger cars are using onboard diagnosis (OBD) systems in order to prevent air pollution due to the risk of large volumes of hazardous exhaust gas being emitted from malfunctioning vehicles. These systems include systems for high-rpm, high-power engines that detect misfiring by measuring ionic current. Figure 1 shows a vehicle that utilizes the ionic-current misfire detection system.

A Formula One engine, on the other hand, consists of the combination of a wider rpm range and larger bore diameter for high power. These features have posed a problem in achieving stable combustion throughout the wide rpm range. Additionally, in case a technical failure or malfunction should occur, the engine is required to detect the problem location and identify the cause with high accuracy and take the necessary measures in a limited period of time.

This paper reports on ionic current measurement technology for mass production vehicles being developed and used effectively in Formula One engines in order to resolve the issues mentioned above.



Fig. 1 Vehicle with ionic current measuring system

* Tochigi R&D Center

2. Mechanism of Ion Generation and Measuring Principle

It has been known for a long time that ions are generated during engine combustion. It is thought that ionic current is generated via two different generation processes explained below. As a result, the ionic-current waveform has two peak values (Fig. 2).

(1) One peak detecting relatively long-lived ions including $C_3H_3^+$ generated when the flame surface ends pass through the electrode during the initial stage of combustion.

(2) The other detecting the NO^{2+} ions generated as a result of thermal dissociation of N_2 in combustion gasses with a temperature of 2000K or higher.

Figure 3 shows the principle of ionic current measurement. An ion probe installed inside the combustion chamber is energized with positive electrical potential at approximately 300V. With the energization, ions of $C_3H_3^+$, CHO^+, NO^{2+} and others are generated due to the engine's combustion and these ions are captured. The center electrode of the spark plug is used as an ion probe and the ignition coil energy is stored in the condenser making use of the energy as a power source. This configuration, which ensures simplicity, is the one most commonly used. However, the system is not capable of measuring the current when discharge is taking place. In particular, when used in conjunction with a full transistor ignition system, which is characterized partly by a prolonged inductive discharge of approximately 1msec., measurement accuracy tends to deteriorate due to an overlap of induced discharge over the period of combustion. In the case of Honda's Formula One engine, the discharge process is completed in approximately 70 μ sec., which is achieved due to the incorporation of a condenser discharge ignition (CDI) system. This allows almost the entire combustion process to be monitored.

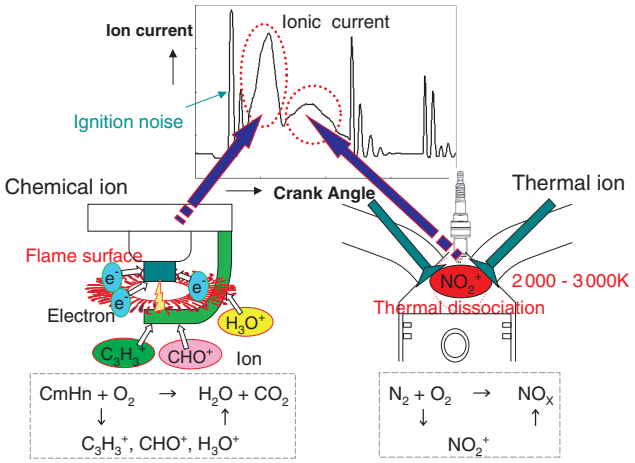


Fig. 2 Mechanisms of ionic current generation

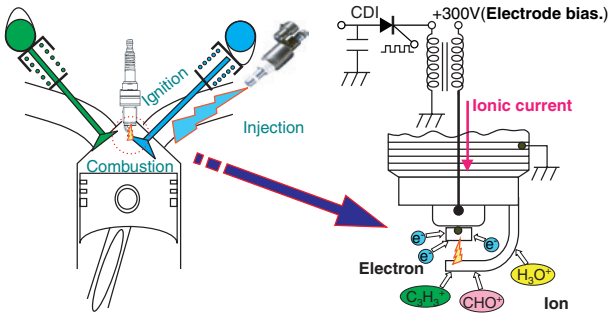


Fig. 3 Principle of ionic current measurement

3. System Configuration

With the CDI system incorporated, the energy stored in a large-capacity condenser of the CDI unit is led to the primary coil by the thyrister, generating high voltage at the secondary coil unit. This ionic current detection system regulates part of the energy outgoing to the ground due to ignition by means of a 300V zener diode. The energy thus regulated is then stored in a condenser, forming a part of the misfire detection system unit (MDS unit). This system was designed so that the energy stored at a voltage level of 300V would provide positive bias voltage to the spark plug center electrode after the completion of discharge. The reason why a positive voltage is applied is that it is thought that it is possible to detect greater amount of ionic current by capturing electrons instead of positive ions, which have larger mass per charge and move over shorter distances when an electric field is applied. Figure 4 depicts the relationship between the bias voltage direction and the ionic current detection amount [(1)]. It shows that capturing positive ions inside the combustion chamber with its relatively large surface area, and capturing electrons with the central electrode with its relatively smaller surface area results in detection of a larger amount of ionic current. This allows improvement in the signal-to-noise (S/N) ratio of the system and raises the detection precision.

Ionic current is detected as a voltage value according to the detection resistance (shunt), and then digitized via two operational amplifiers, one for integration and the other for resetting. Following this, the digital signal is transmitted to the engine control unit (ECU) either through pulse width modulation (PWM) or via high-speed serial communication and from there is used for engine control and for provision of information to the pit via telemetering. The configuration of the ionic current measurement system is shown in Fig. 5.

The MDS unit is compact in size and the case is made of magnesium alloy for reduced weight. Also, two Deutsche Auto Sport connectors are used, one for power supply and one for input/output, to ensure reliability. The MDS unit can be seen in Fig. 6.

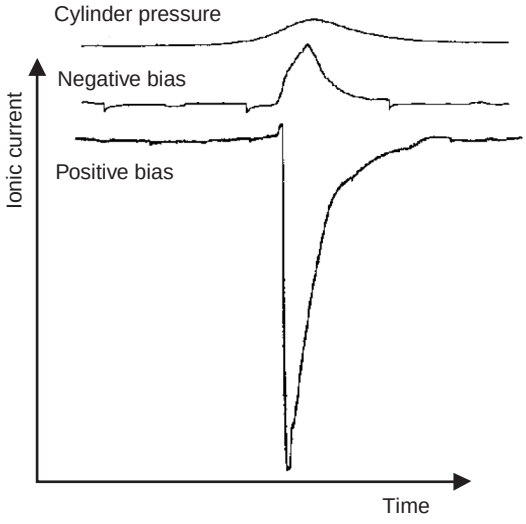


Fig. 4 Relationship between direction of bias voltage and amount of ionic current

The ignition coil uses an exclusive pin as an output terminal for measurement of ionic current in addition to two ordinary pins for the CDI input and ground. This makes the induction discharge time extremely short, about 70 μsec. Figure 7 is a picture of the ignition coil for ionic current measurement.

The MDS unit is located at the side of the body, close to the ECU. In order to minimize the negative effect of the stray capacitance of the wiring harness, a measure against noise was taken for the circuit and sealed wiring was eliminated. An example of the system installation on a vehicle is shown in Fig. 8.

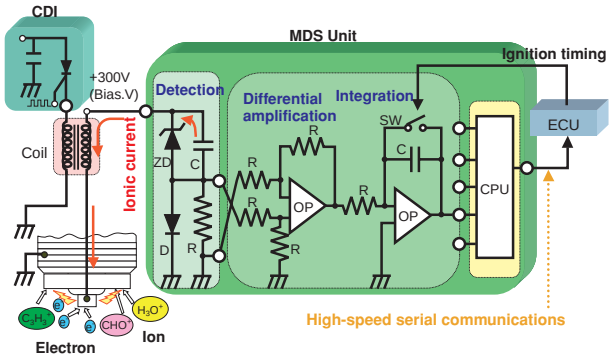


Fig. 5 Configuration of ionic current measuring system

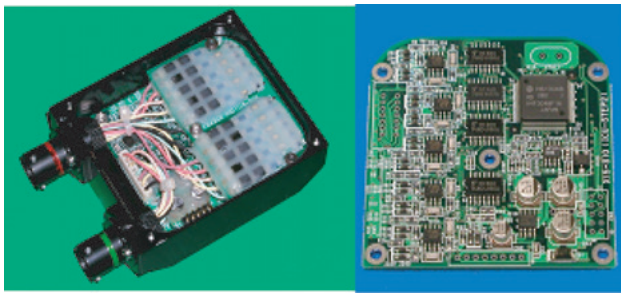


Fig. 6 MDS unit

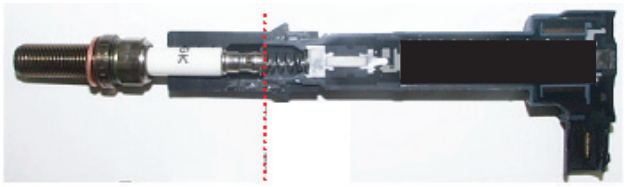


Fig. 7 Ignition coil for ionic current measurement



Fig. 8 Example of system installation

4. Misfire Detection System

The diagnosis system was so designed that it would provide a comprehensive detection of malfunctions in addition to misfire through synchronization with other sensors, to identify which component was displaying the failure, and measure the frequency of the failure and grasp the state of the malfunction in detail (Fig. 9).

As for the misfire detection flow, the ionic current is integrated in the designated area for gating. The system judges that misfire has occurred if the value is lower than a predetermined threshold. Furthermore, if the threshold is not satisfied for a specific number of times, the system determines that a malfunction exists. The gating range was set up to eliminate electric vibration occurring inside the ignition coil during and after discharge (Figs. 10 and 11).

Figure 12 shows the state of ionic current generation with and without a misfire. As can be seen from this figure, in the case that misfire occurs, no ions are generated by combustion, which results in a low ionic current integral value, whereas a large number of ions are generated during normal combustion and the difference between the two is very clear. The difference between the two is

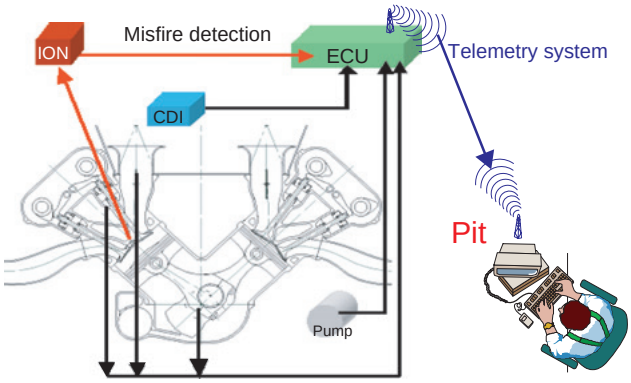


Fig. 9 Diagnosis system configuration

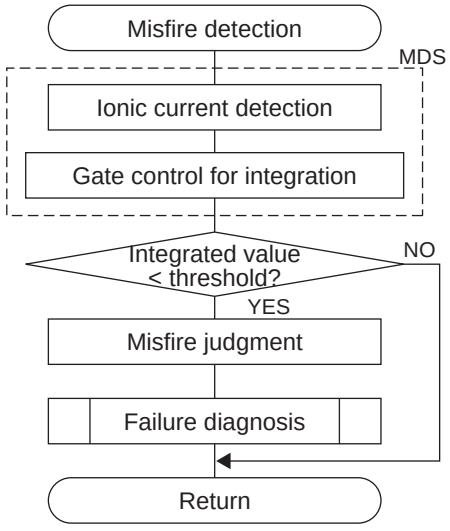


Fig. 10 Misfire detection flowchart

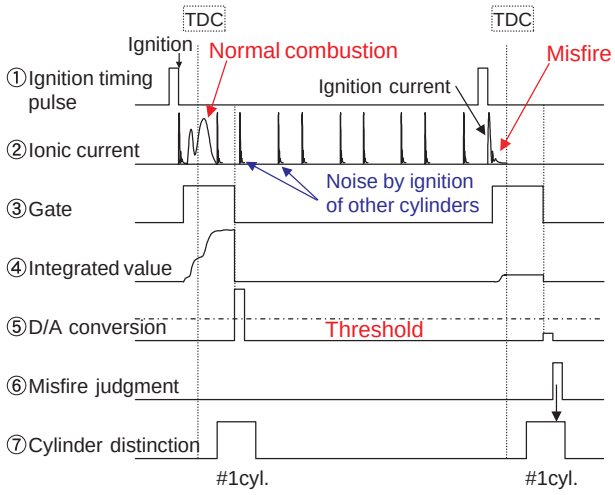


Fig. 11 Timing chart

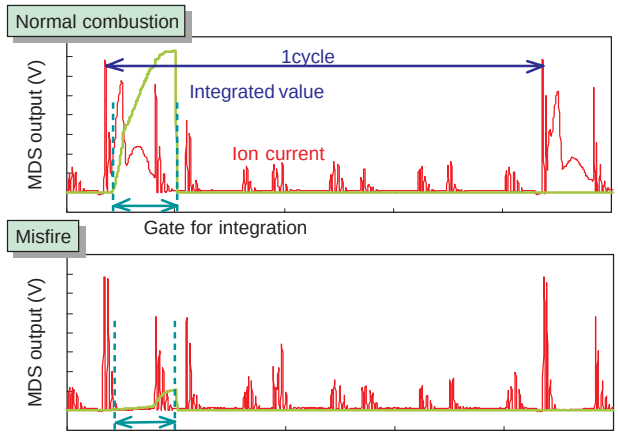


Fig. 12 Test results under misfire and normal combustion

so prominent that it can be judged that an appropriate S/N ratio is achievable. Also, misfire was detected during the actual vehicle test with fuel supply intentionally shut off. It was confirmed that a malfunction flag is set when a predetermined frequency threshold is exceeded (Fig. 13).

5. Lean Burn Controls

5.1. Ionic Current for Lean Combustion

In order to make clear the relationship between the air-fuel ratio and the ionic current, a universal exhaust gas oxygen (UEGO) sensor was used to measure the air-fuel ratio and verify its correlation with the ionic current. In general, a leaner air-fuel ratio improves fuel economy. However, if the lean limit is exceeded, the frequency of misfiring increases and fuel consumption actually increases (Fig. 14).

There is also a correlation between the air-fuel ratio and the ionic current and it has been verified that the generation of ionic current is lower during lean combustion (Fig. 15).

Looking at the relationship between air-fuel ratio and ionic current according to cylinder, it is confirmed that a cylinder presumed to be with a higher air-fuel ratio and indicated mean effective pressure (IMEP) generates a large amount of ionic current. These characteristics may be used for simple air-fuel ratio detection among the cylinders (Fig. 16).

5.2. Hesitation Detection

Hesitation is most likely to occur under acceleration when the air-fuel mixture ratio is set for lean in order to achieve improved fuel consumption. This has a negative effect on acceleration after exiting a corner. To control this phenomenon, the ionic current measuring system was applied. Hesitation occurs in the following process; an abrupt increase in the volume of air introduced to the injection system results in the mixture being leaner than the combustible limit. Then, IMEP is observed equivalent to that for misfire or the condition close to misfire, causing hesitation. A leaner air-fuel mixture results in less amount of ionic current and a longer

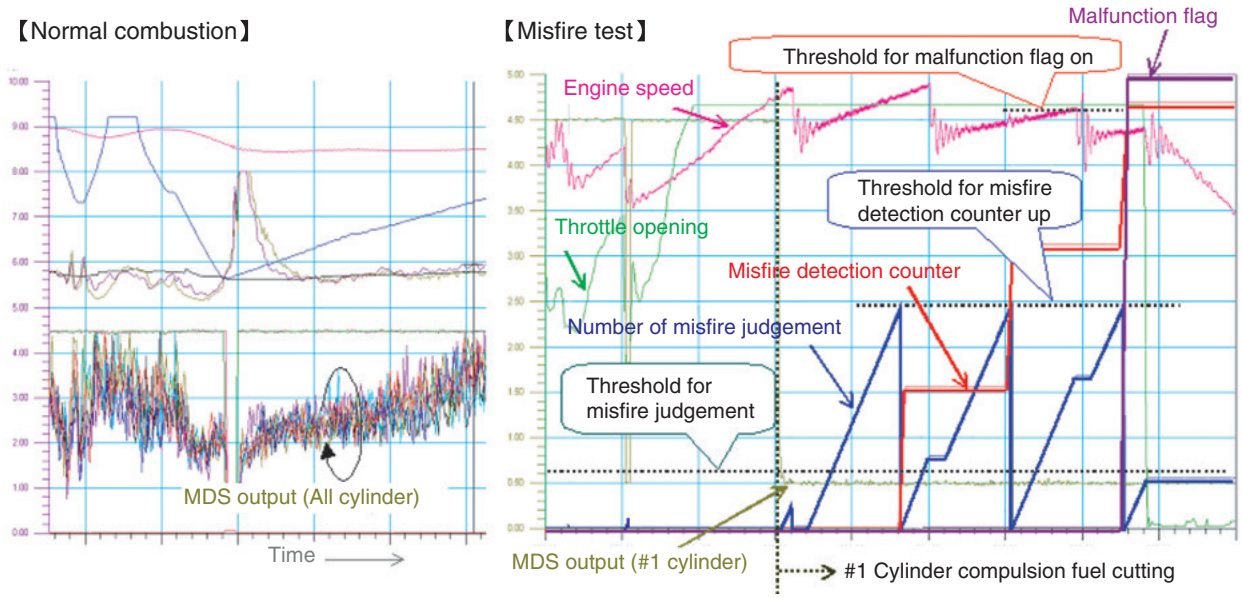


Fig. 13 Test results with actual vehicle

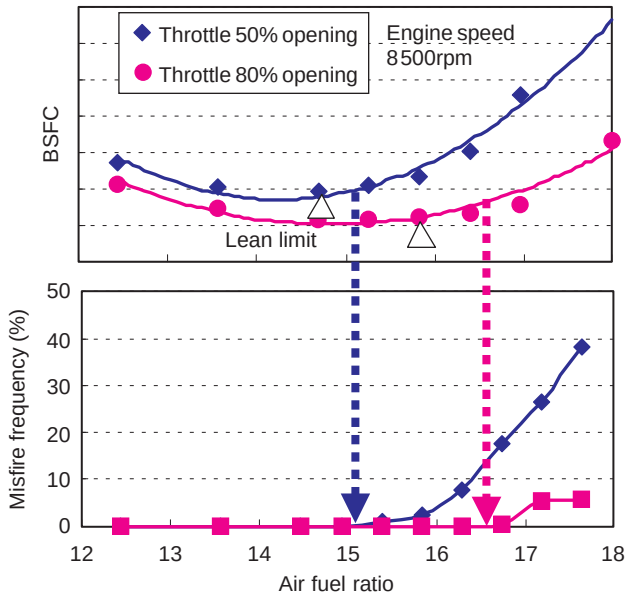


Fig. 14 Lean limit and frequency of misfire

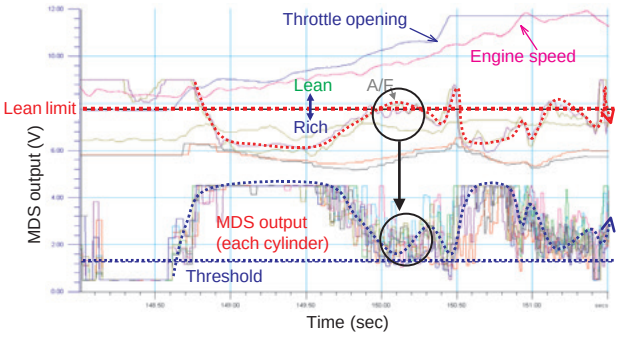


Fig. 15 Lean-burn test with actual vehicle

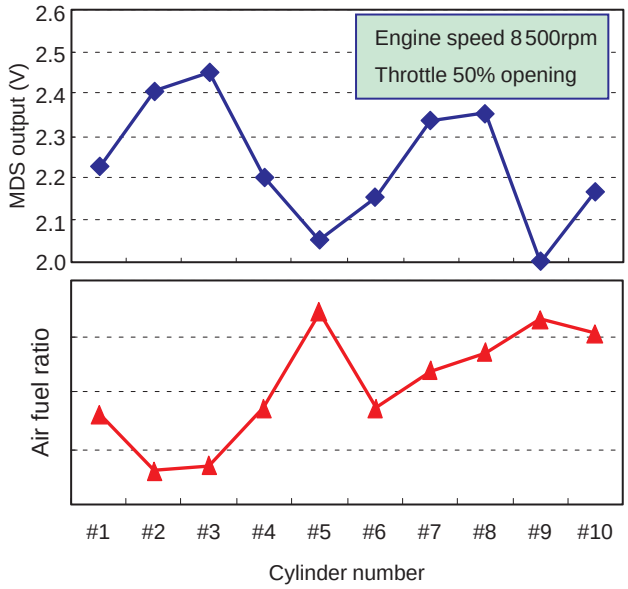


Fig. 16 Cylinder-to-cylinder variations of air-fuel ratio and ionic current generation

period of hesitation. The developed system detects hesitation in accordance with the principle mentioned above. The system flowchart can be seen in Fig. 17. Figures 18 and 19 show the measurements from dynamometer tests and from actual vehicle tests.

In the system flow the system identifies the period of time when the ionic current measurement is below the stipulated threshold. In case the condition is longer than the predetermined period, the system judges that an excessively leaner mixture is being supplied, which triggers a system command for a richer mixture ratio. If the period of time is shorter than the threshold, this means that there is available margin for making the mixture leaner and accordingly the system opts for a leaner setting in order to achieve improved fuel consumption.

As shown in Figs. 18 and 19, a leaner mixture ratio contributes to prolonged hesitation. Focusing on the signal from the UEGO

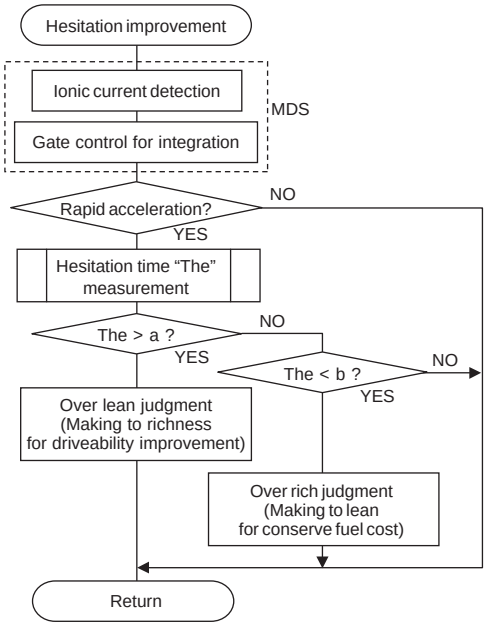


Fig. 17 System flow chart for Hesitation control

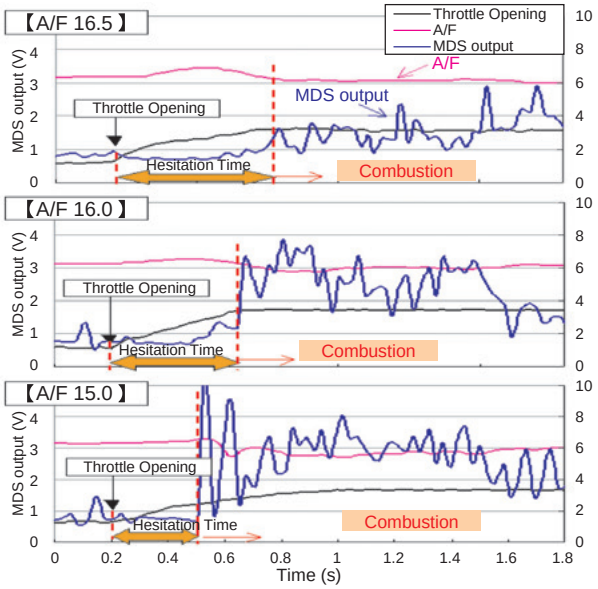


Fig. 18 Dynamometer measurement result about lean-burn condition

sensor, with a mixture set close to the stoichiometric ratio, the mixture becomes leaner under acceleration and then becomes richer, supporting acceleration. A similar phenomenon, however, cannot be observed under a condition close to the lean-burn limit. Because of the non-availability of the acceleration support effect, severe hesitation occurs. In the worst case, the period of time of hesitation may be prolonged by as much as three times.

6. Detonation Detection

It is well known that knocking, and pre-ignition and other forms of detonation, tend to occur under high-speed, high-load conditions with a lean air-fuel ratio.

Examples of detonations caused due to hot surface ignition are shown in Fig. 20. The cases shown in the top and middle rows in the figure were observed during a Formula One race whereas those shown in the bottom row are from detonations produced during reproduction tests in the lab. It could be clearly observed that the piston as well as the combustion chamber were thermally damaged. During the reproduction test, similar damage resulted from advancing the ignition timing under a lean mixture condition. Figure 21 shows the ionic current waveform in the detonation reproduction test.

It is verified during the preliminary test, that no knocking occurs even with the ignition advanced. Tests confirm that immediately after the mixture is ignited a large amount of ions is suddenly generated, reaching the highest measurement limit. The tests also verify that, with the passage of time, the combustion chamber walls reach high temperatures and detonation occurs. Ions are generated immediately after ignition without the ordinary delay in ignition. In the neighborhood of the in-cylinder pressure peak, combustion at high temperature occurs. Under this condition, a large number of ions are generated due to thermal dissociation. This phenomenon is thought to be hot surface ignition, which is similar to pre-ignition. Nevertheless, it is presumed that it should be regarded as a post-ignition phenomenon caused by hot surface ignition since there are no ions generated before ignition.

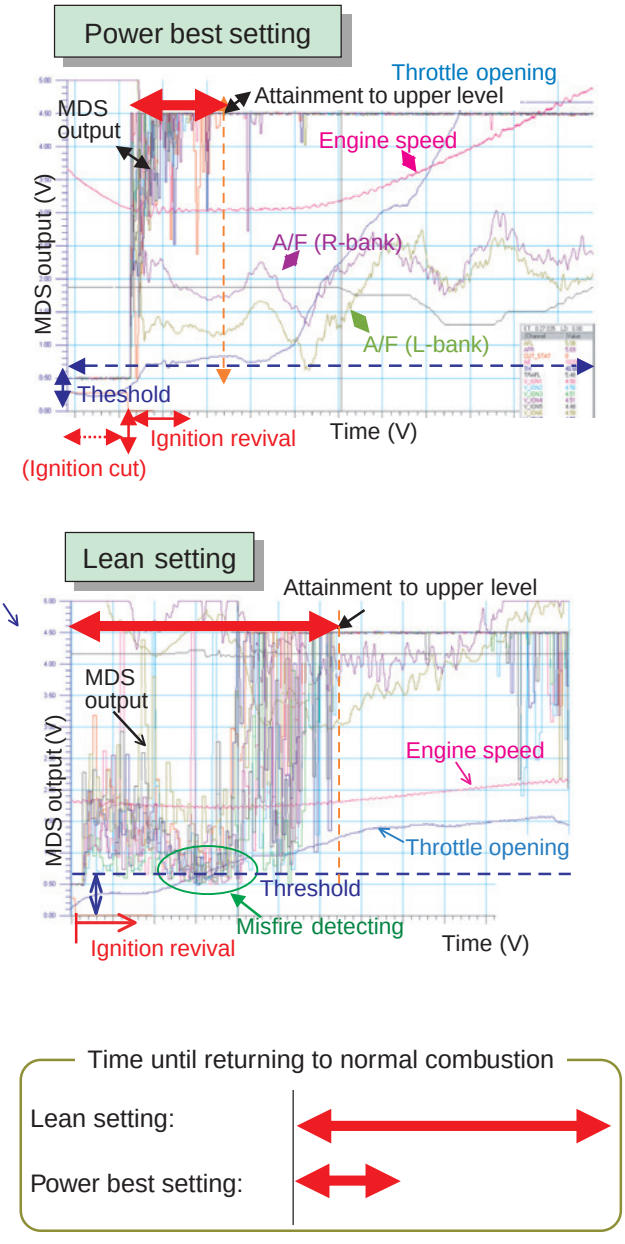


Fig. 19 Actual vehicle measurement result about lean-burn condition

7. Ionic Current Amount

7.1. Spark Plug Center Electrode Configuration and Ionic Current Amount

The amount of ions generated during combustion remains the same but the amount of ionic current varies depending on the measuring capacity of the system. The ionic current measuring

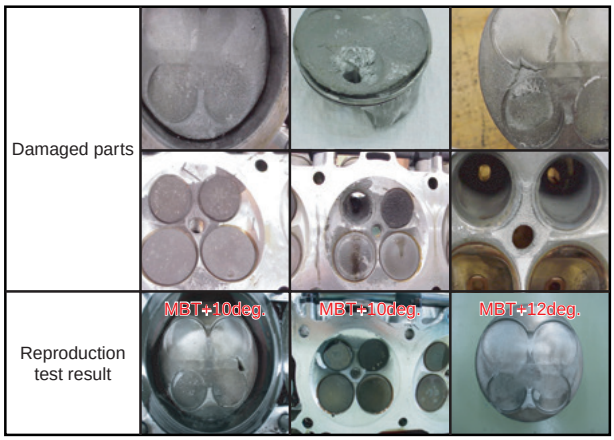


Fig. 20 Detonation caused by hot surface ignition

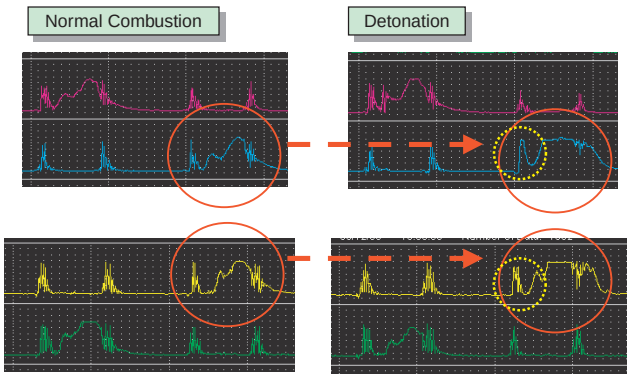


Fig. 21 Amount of ionic current during reproduction test

system used in the present research features a spark plug that also operates as the sensor. In other words, the spark plug serves as a measuring probe. The amount of ionic current detectable relies on the sensitivity that the probe offers.

Figure 22 depicts the relationship between the spark plug center electrode configuration and ionic current generation, while Fig. 23 shows the relationship between the configuration of the spark plug center electrode and cylinder-to-cylinder ionic current generation. In Fig. 22 the surface area of the center electrode is plotted in abscissa and the ionic current in ordinate. Given that the configuration of the spark plug is constant, the relationship between the surface area and ionic current is approximately linear and ionic current increases in proportion to the surface area. In a similar manner, as shown in Fig. 23, a comparison between cylinder-to-cylinder variations in terms of ionic current, reveals changes in the same ratio for all cylinders.

In Fig. 24 we can see the ionic current waveform measured with a spark plug electrode protrusion of 1.5mm. Figure 25 shows the relationship between the electrode protrusion and ionic current generation measured during actual vehicle tests. With the protrusion set at 1.5mm, it was confirmed that the waveform is large and that a satisfactory level of detection was provided. During the actual vehicle test, it was observed that the waveform output varies significantly depending on the amount of projection of the center electrode.

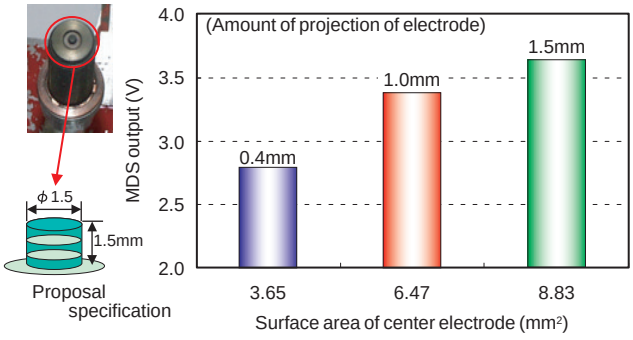


Fig. 22 Relationship between spark plug center electrode configuration and ionic current generation (detectable)

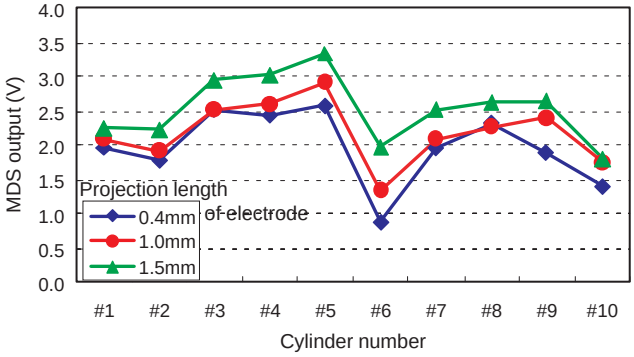


Fig. 23 Relationship between configuration of spark plug center electrode and cylinder-to-cylinder ionic current generation

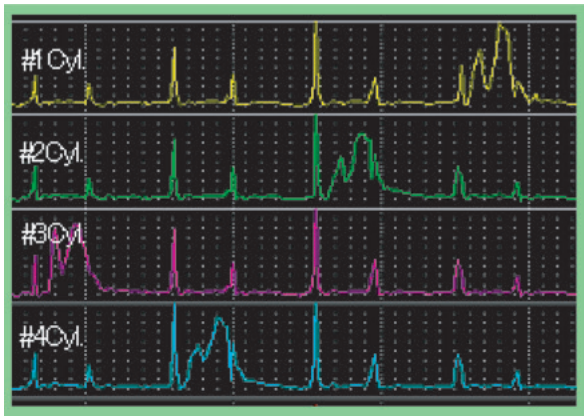
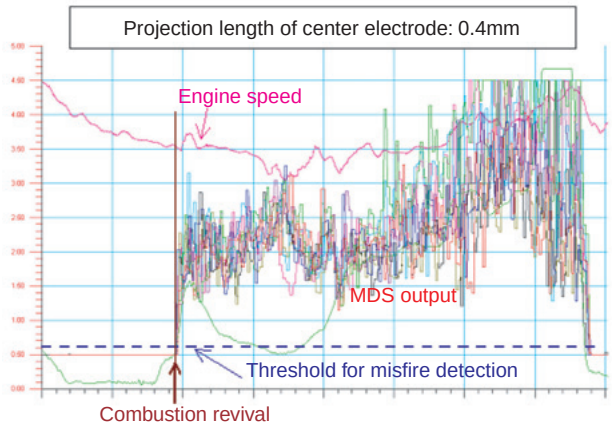


Fig. 24 Ionic current waveform measured with spark plug electrode protruding by 1.5mm

7.2. Detected Ionic Current Amounts

When spark plugs with a center electrode surface area of 3.65 mm² (0.4mm) are used, with the detection resistance is set at 18 kΩ, the voltage across that resistor at the chemical ion peak is 19 V. As Eq. (1) shows, the ionic current at this time is 1.06 mA. Also the integrated amount of ionic charge can be expressed by Eq. (2). The integrated amounts for chemical ions and thermal ions at 15000 rpm obtained using Eqs. (3) and (4) are both 0.19 μC. Therefore, as can be seen from Fig. 22, it can be inferred that as the surface area of the center electrode increases, the amount of ionic current captured increases as a linear function. Figure 26 shows the amount of ionic current when the chemical ions are at their maximum and Fig. 27 shows the amount of charge detected.



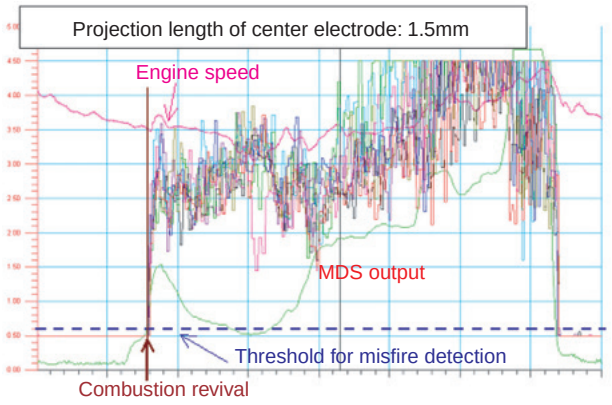


Fig. 25 Actual test results with different protrusions of sparkplug center electrode

$$I = \frac{V}{R} = \frac{19}{1.8 \times 10^4} = 1.06mA \quad (1)$$

$$Q = \int Idt \quad (2)$$

$$Qchemical = 0.19\mu C \quad (3)$$

$$Qthermal = 0.19\mu C \quad (4)$$

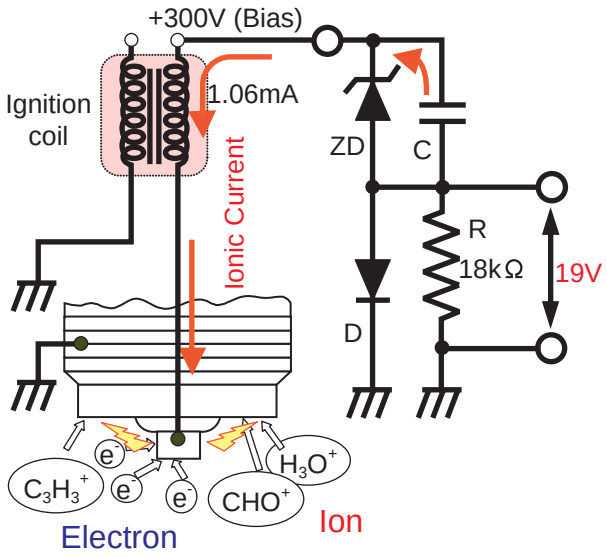


Fig. 26 Amount of ionic current at chemical ion generation peak

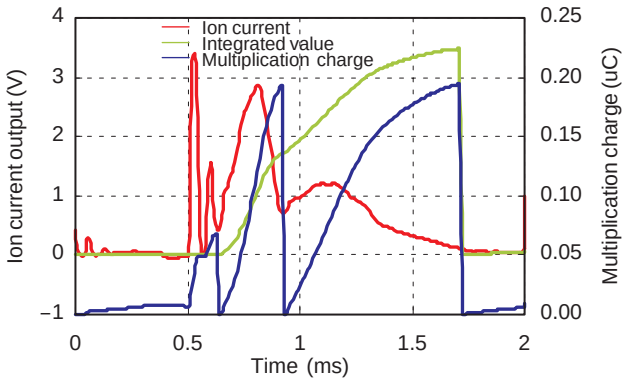


Fig. 27 Detected electric charge

8. Conclusions

A combustion state detection system featuring an ionic current measuring concept was developed in an attempt to apply it to a Formula One engine. During research and development, the following was learned;

(1) The spark plug center electrode had the dual function of serving as a measuring probe. This discharge energy was stored in the condenser, which was consequently used as the source of bias voltage. This ionic current measuring system, when used in conjunction with the CDI system, which is characterized by its short discharge time, provided a sufficient level of measuring accuracy throughout all engine speeds.

(2) The misfire detection system, using ionic current measurement, mainly consists of gating for the elimination of ignition noise, integration and a misfire frequency detection device. Utilizing these functions, the system diagnoses the engine to identify whether or not a malfunction occurs. It supports high detection accuracy throughout the revolution range.

(3) During lean combustion, the ionic current decreases. It is possible to utilize this to detect and control misfiring and detect the amount of reduction in IMEP from ionic current and to control lean burn combustion. This system can also provide simplified detection of relative differences in air-fuel ratios among cylinders.

(4) It is possible to control IMEP fall (hesitation) due to transient excessive lean air-fuel ratios by measuring the period of time during which ionic current falls. This system can be applied to air-fuel ratio setting tools and engine control.

(5) The system detects detonation including hot surface ignition that occur frequently under high-load operation by means of ionic current generation under these conditions. In the case of severe hot surface ignition that could lead to damage to the engine, the delay in ignition is cancelled, promoting flame propagation at the initial stage of combustion. In the neighborhood of the in-cylinder pressure peak, thermal dissociation caused by high-temperature combustion promotes the generation of ions, resulting in an increase in ionic current generation.

(6) The spark plug center electrode served as a measuring probe that detected ionic current. Provided that the configuration remains unchanged, the electrode surface area and the amount of ionic current detectable are directly proportional. The greater the protrusion of the center electrode, the higher the degree of sensitivity.

The developed system using ionic current measurement is being utilized effectively in current Formula One engines and other race engines and is becoming indispensable for dealing with malfunctions and for data logging. It is likely that in the near future it will be necessary to detect the combustion state in greater detail and control the engine. This ionic current detection system has the appropriate capacity as a forerunner and the authors are confident that it has succeeded in creating new value.

Acknowledgements

The authors wish to express their profound gratitude to the late Kenji Nakajima, who as a co-researcher left behind such valuable bench test results.

We would also like to take this opportunity to express our deep appreciation to Noriaki Kondo and Tatsunori Yamada of NGK Spark Plug Co., Ltd. for their cooperation.

References

(1) Shimasaki, Y., et al.: Spark Plug Voltage Analysis for Monitoring Combustion in an Internal Combustion Engine, SAE 930461
(2) Miyata, S., et al.: Flame Ion Density Measurement Using Spark Plug Voltage Analysis, SAE 930462
(3) Shimasaki, Y., et al.: Study on Combustion Monitoring System for Formula One Engines Using Ionic Current Measurement, SAE 2004-01-1921
(4) Shimasaki, Y., et al.: Study on Combustion Monitoring System for Formula One Engines (Report 1), SAE Proceedings No. 107-04, p. 175

■ Authors ■


Yuichi SHIMASAKI


Junko SAKAGUCHI


Hidetaka MAKI


Hiroaki SUZUKI


Akira KATO


Kazutoshi NISHIZAWA

Development of Transient State Model for CVT HILS

Hiroshi SAOTOME* Rei ITO*
Kenji HAGIWARA* Ko YODA*

ABSTRACT

HILS has been introduced to the CVT ECU development process in an attempt to increase efficiency. To create HILS, it was necessary to develop a CVT HILS model capable of simulating transient states in a CVT shift mechanism, including a hydraulic control system. The calculation burden of the model was required to be low enough to enable real-time simulation. The aim of this project was to develop an experimental model capable of calculating the transient characteristics of the pulley ratio on the basis of pulley ratio, the torque input to the pulley, and the speed of revolution of the pulley; in order to enable simulation of transient states, in particular in kick-down shift. Given the high calculation load of the hydraulic control system model, test data was employed to enable the higher order simultaneous equation model to be replaced by a lower order transfer function model. The newly developed HILS has been successfully introduced to the development process for CVT ECU, resulting in a 30% reduction in the number of procedures required for verification of functioning and setting parameters for programs.

1. Introduction

Honda has already applied the ECU development support technology Hardware In the Loop Simulation (HILS) to the development of AT ECU in order to increase efficiency, and the effectiveness of the technology has been reported[1]. The development project discussed in this paper attempted to introduce HILS to the CVT ECU development process. In the discussion below, the entire system is termed the CVT HILS system, while the CVT model employed to make the CVT HILS system function is termed the CVT HILS model.

The projected CVT HILS system was to be used in the development process to verify functioning in and set parameters for ECUs after alteration of their CVT control programs and electrical circuitry, prior to their being fitted in actual vehicles. This required a CVT HILS system possessing sufficient calculation accuracy to replace vehicle tests, which necessitated the development of a CVT HILS model capable of simulating transient states of ratio changing of the CVT. However, the calculation load for a model including a hydraulic control system is high[1], making it unlikely to provide sufficient accuracy in real-time simulations using existing Digital Signal Processors (DSP). In addition, while a report on a simulation of CVT transient state ratio changing does exist in the literature[2], it was not possible to provide sufficient calculation accuracy with respect to the effect of differences in vehicle speed and engine output conditions using the pulley ratio factors employed in that study, in particular when calculating the rate of change of the pulley ratio during sudden shifts such as kick-down shift. It was therefore necessary to obtain factors for the pulley input torque and pulley input speed.

This paper will provide details of the development of a CVT HILS model which possesses sufficient calculation accuracy while enabling real-time simulation.

2. Configuration of CVT HILS System

As Fig. 1 shows, the CVT HILS system is composed of five elements: A host computer, a DSP system, an interface box, a relay box and an ECU for CVT control.

The host computer downloads the model to the DSP system and sets the parameters for simulation data, and displays and analyzes the results of the simulation.

* Tochigi R&D Center

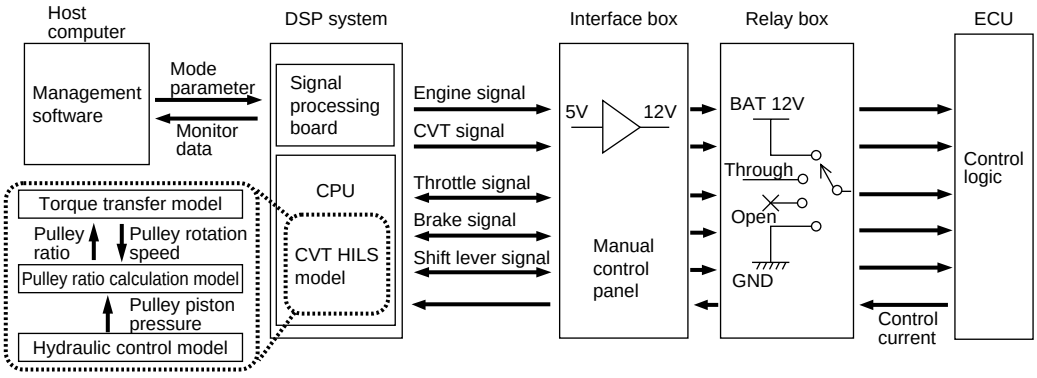


Fig. 1 HILS system configuration

The DSP system is made up of a CPU for model calculation and I/O processing, and a signal processing board, which conducts real-time simulations. The CVT HILS employs multi-rate modeling, with a minimum and maximum calculation frequency of 200 μsec and 1 msec respectively.

The interface box conducts the signal processing required for electrical connection between the input and output signals of the DSP system and the signals from the ECU corresponding to conditions in an actual vehicle. The relay box shorts and disconnects the electrical circuits.

The ECU receives the signal from the DSP after it passes through the interface box and the relay box, and conducts shift control at a frequency of 10 msec, sending the results back to the DSP via the relay and interface boxes.

3. CVT HILS Model

3.1. Configuration of the CVT HILS Model

The CVT HILS model discussed above in section 2, which is downloaded to the DSP, is basically made up of three models, as shown within the dotted lines in Fig. 1.

(1) A torque transfer model; including the engine, CVT, and vehicle body
(2) A hydraulic control model, which outputs the piston pressure for the two pulleys that control shifting
(3) A pulley ratio calculation model, which changes the speed of the pulleys in response to the pulley piston pressure output by the hydraulic control model

These three models will be discussed in detail below.

3.2. Torque Transfer Model

The torque transfer model is shown in Fig. 2. Engine torque is input via an input shaft, which is directly connected to the drive pulley, and is transferred to the driven pulley by means of a steel belt. The torque is then transferred to the drive shaft by the start clutch via the final gear[5]. Torque transfer and the speed characteristics of each shaft are solved by commonly used numerical integration methods, of which the Runge-Kutta method is a representative example[1]. The mathematical model is as follows:

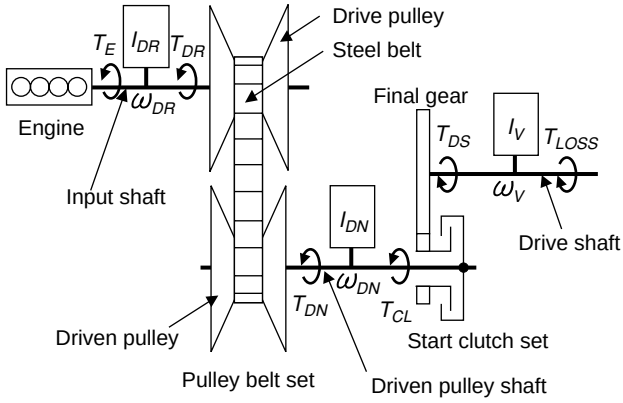


Fig. 2 Torque transfer model

Input shaft	$T_E - T_{DR} = I_{DR} \cdot (d\omega_{DR}/dt)$	(1)
Pulley belt set	$T_{DR} \cdot i = T_{DN}$	(2)
Driven pulley shaft	$T_{DN} - T_{CL} = I_{DN} \cdot (d\omega_{DN}/dt)$	(3)
Start clutch	$T_{CL} = \mu \cdot n \cdot r \cdot (P_{CL} \cdot A_{CL} - F)$	(4)
Final gear	$T_{CL} \cdot GR_F = T_{DS}$	(5)
Drive shaft	$T_{DS} - T_{LOSS} = I_V \cdot (d\omega_V/dt)$	(6)

Nomenclature

- I : Inertia
- i : Pulley ratio ($i = \omega_{DR}/\omega_{DN}$)
- GR : Gear ratio
- ω : Speed
- T : Torque
- μ : Clutch disk friction coefficient
- n : Number of clutch disks
- r : Clutch disk effective radius
- P : Hydraulic clutch pressure
- A : Hydraulic clutch piston bearing area
- F : Clutch return spring load

Subscripts

- E : Engine
- DR : Drive pulley set (Pulley input)
- DN : Driven pulley set (Pulley output)
- CL : Start clutch
- F : Final gear
- V : Body
- $LOSS$: Running resistance

3.3. Hydraulic Control Model

As shown in Fig. 3, the CVT hydraulic control model consists of a line pressure control section and a drive and driven pulley piston pressure control section[5].

In the line pressure control section, the supply pressure generated by the oil pump is regulated to match the line pressure by the regulator valve. Line pressure is reduced by the linear solenoid valves operated by the control current of the electronic control unit (ECU) and the pulley control valves in the pulley piston pressure control section, thus enabling the pulley piston pressure on the drive and driven sides to be controlled.

Two issues were encountered in developing a hydraulic control model.

The first was the fact that the mechanism generating the time lag in pulley piston pressure response to ECU hydraulic pressure commands in transient states was unclear.

The second was that transient states necessitated a higher-order hydraulic control model with a high calculation load.

Figure 4 shows the results of a vehicle test in which the accelerator pedal was suddenly depressed from a fixed vehicle speed of 40 km/h (kick-down shift). The shaded sections in Fig. 4 show a considerable time lag in pulley piston pressure response to the ECU hydraulic pressure command.

An actual vehicle was employed in tests conducted using the setup shown in Fig. 5 in order to analyze the cause of this phenomenon for modeling.

These tests used a multipurpose ECU to provide patterned hydraulic control commands for pulley piston pressure. The ECU was programmed to increase the pressure command to the driven side in steps at specific engine speeds. The pressure command to the drive side was maintained at a fixed value. The multipurpose ECU was fitted in the vehicle, and the line pressure, pulley piston pressure, engine speed, and pulley ratio were measured at different engine speeds. Figures 6 and 7 show the results of measurements at 1 000 and 2 500 rpm respectively.

The change in pulley ratio between 1 and 2 seconds was focused on in both sets of results.

In the first frame of the graphs it can be seen that the pressure of the driven pulley piston, to which oil is flowing, is lower than the hydraulic pressure command. In the second frame of the graphs, it can be seen that the pressure of the drive pulley piston, from which oil is flowing, is higher than the hydraulic pressure command. Changes in the volume of the pulley piston are known to be a factor generating such changes in pressure with the flux and efflux of oil[2].

The effect of the oil supply capacity of the oil pump was studied, with consideration of these changes in volume. A comparison of the first frames of the graphs shows that at 1 000 rpm (Fig. 6) the change in ratio is gentler than at 2 500 rpm (Fig. 7). Despite the minimal influence of a change in volume of the driven pulley piston, the piston pressure is significantly less than the hydraulic pressure command and the line pressure and piston pressure are equivalent,

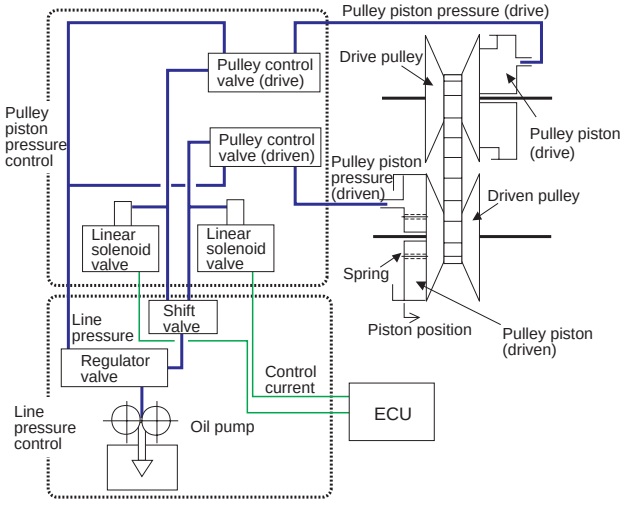


Fig. 3 Schematic drawing of CVT system

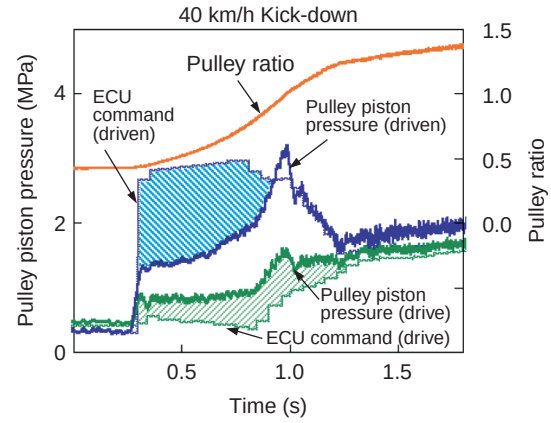


Fig. 4 Vehicle test results

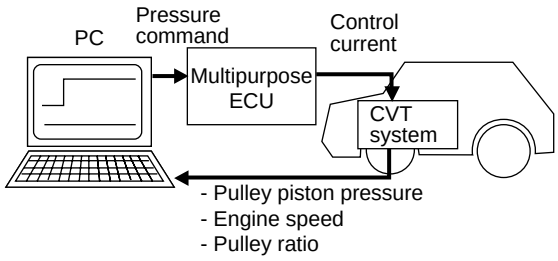


Fig. 5 Schematic drawing of test equipment

indicating that factors other than piston volume change are at work. This effect was believed to be due to the inability of the oil pump to respond to the ECU pressure command, which was increased in steps.

The hydraulic control model, as shown in Fig. 8, was constructed on the basis of these considerations. In addition to a hydraulic response paragraph, based on a standard oil inertia[3] derived from hydrodynamics, and a piston volume change paragraph which takes into account changes in the volume of the pulley piston, the hydraulic control model contains an amount of flow from oil pump paragraph, in which the oil supply capacity of the pump is considered. These paragraphs determine the pulley piston pressure, but the method of calculation can be switched according to the type of shift being conducted by the CVT. For slow shifts the pulley piston pressure is determined by the hydraulic response and piston volume change paragraphs; for rapid shifts such as kick-down shift, when the pulley piston pressure generated by the amount of oil flow from oil pump paragraph drops below the pulley piston pressure generated by the sum of the piston volume change paragraph and hydraulic response paragraph, the amount of oil flow from oil pump paragraph is selected.

The method of modeling the three paragraphs will now be discussed in more detail.

The hydraulic response paragraph is a model which calculates the pressure drop due to oil inertia, assuming no change in the volume of the pulley piston. The model was created by identification from vehicle tests. Specifically, a frequency response test was conducted to identify the relationship of pulley piston pressure to the hydraulic pressure command in order to identify the effect of oil inertia. As a result, it was determined that it could be approximated by a secondary-order time-lag transfer function. The transfer function is shown as Eq. (7).

$$\frac{1}{\alpha Ts^2+\alpha s+1} \tag{7}$$

Here, α represents the model parameter and T the time constant. Figure 9 shows the results of pulley piston pressure calculated using the transfer function and the results of vehicle measurements for the same hydraulic pressure command. There is a good correlation between the two sets of results, which demonstrates the validity of the hydraulic response paragraph.

The piston volume change paragraph is a model which calculates changes in pressure with the flux and efflux of oil due to changes in the volume of the pulley pistons. Because hydraulic response could be approximated with a second-order time-lag transfer function, as discussed above, and the continuity equation expressing the relationship between the amount of oil flow from the control valve (Qv) and the pulley piston pressure is a first-order function[2], linear transformation of the relationship between the spool operation power for the pulley control valve (Fv) and Qv is possible using a first-order time-lag function, as shown in Fig. 10.

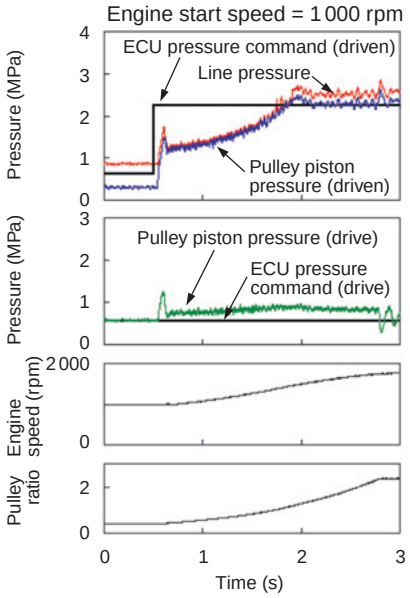


Fig. 6 Step shift test results at low engine speed

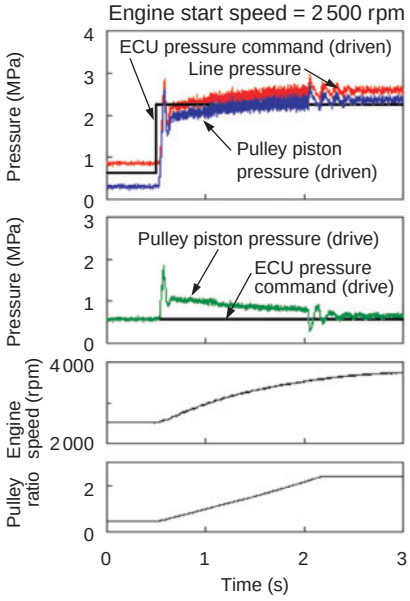


Fig. 7 Step shift test results at high engine speed

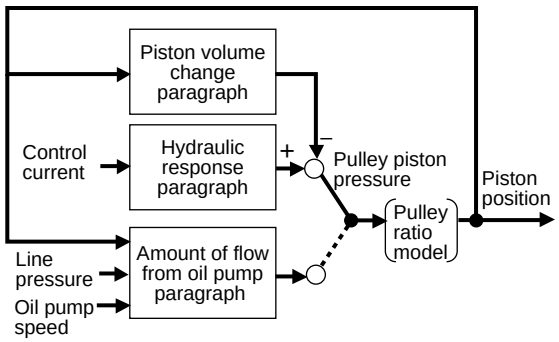


Fig. 8 Hydraulic control model

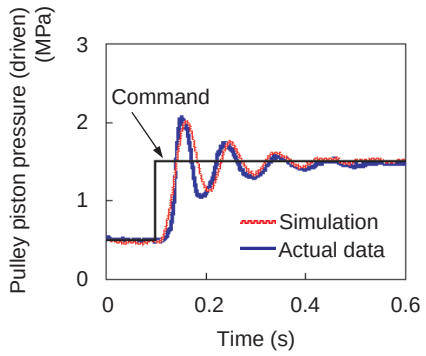


Fig. 9 Simulation results of hydraulic response paragraph

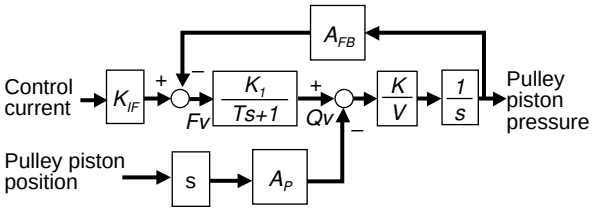


Fig. 10 Hydraulic response and piston volume response function

Here,

V : Pulley piston volume
A_P : Area of pulley receiving pressure
A_{FB} : Area of pressure circuit feedback
K_{IF} : Current-electromagnetic power gain
K_1 : Spool operation power-flowing quantity gain
T : Spool operation power-flowing quantity time constant
K : Modulus of elasticity of volume
Fv : Spool operation power for pulley control valve
Qv : Quantity of flow through pulley control valve

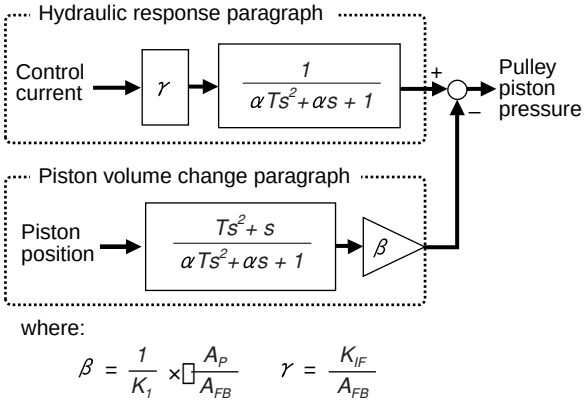


Fig. 11 Hydraulic response and piston volume response paragraph

Figure 11 shows the model generated by consolidating the model in Fig. 10 with model parameters α and time constant *T*.

The piston volume change paragraph in the model shown in Fig. 11 can be modeled as the second-order transfer function shown below (Eq. 8).

$$\frac{Ts^2 + s}{\alpha Ts^2 + \alpha s + 1} \tag{8}$$

The results of vehicle tests and simulations employing conditions like those shown in Fig. 7, with high oil flow from the oil pump at high engine speed, demonstrated the validity of the piston volume change paragraph. To verify the validity of the hydraulic control model as a whole, results from vehicle tests were employed for the pulley ratio time series characteristics, one of the input parameters employed in the simulation. Figure 12 shows the results of the simulation and vehicle tests. The good correlation between the two sets of results demonstrates the validity of the piston volume change paragraph.

The amount of flow from oil pump paragraph is determined by the difference between the rate of flow from the oil pump (supply capacity) and the amount of pulley piston volume change against the hydraulic pressure command. When the rate of flow is less than the amount of volume change, the pulley piston pressure cannot change to match the hydraulic pressure command. In the model, when this is the case, pulley piston pressure is determined by the amount of flow from oil pump paragraph. The model is shown in Fig. 13.

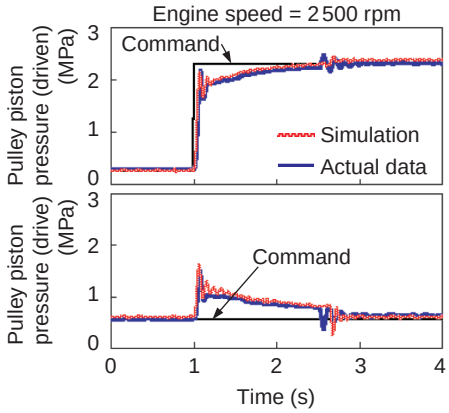


Fig. 12 Simulation results of piston volume change paragraph

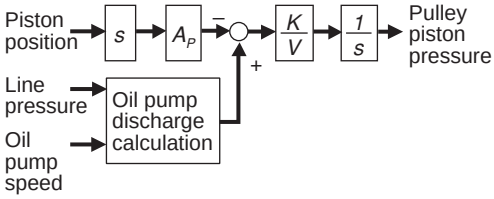


Fig. 13 Amount of flow from oil pump paragraph

The results of vehicle tests and simulations employing conditions of low oil flow from the oil pump at low engine speed, like those shown in Fig. 6, demonstrated the validity of the model used in the amount of flow from oil pump paragraph. As was the case in tests of the validity of the piston volume change paragraph, vehicle test results were used for the pulley ratio time series characteristics in the simulation. Figure 14 shows the results of the simulation and vehicle test. The good correlation between the results demonstrates the validity of the amount of flow from oil pump paragraph.

Having confirmed the validity of the hydraulic response paragraph, the piston volume change paragraph, and the amount of flow from oil pump paragraph, they were employed as a hydraulic control model.

3.4. Pulley Ratio Calculation Model

As Fig. 3 shows, in a CVT shift mechanism a steel belt is clamped by a drive and a driven pulley. The clamping force is the total of pulley piston pressure, centrifugal pressure force and the force generated by the springs in the pulley pistons[4]. The total force clamping the belt is called total thrust, and the ratio of total thrust of the drive to the driven sides is called the total thrust ratio. The ratio between the maximum torque that can be applied without causing the steel belt to slip on the pulleys and the torque input to the pulleys is called the torque ratio[5].

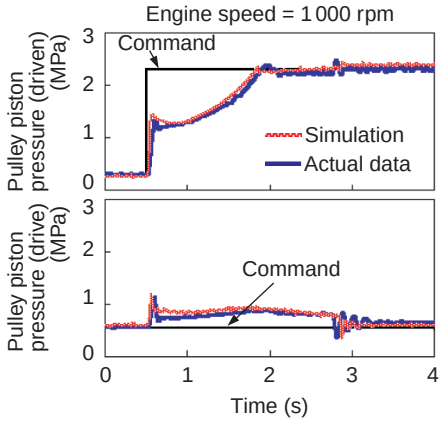


Fig. 14 Simulation results of amount of flow from oil pump paragraph

A method of calculating CVT pulley ratio has been discussed several times in the literature to date[2),(5)]. In this method, the pulley ratio calculation model consists of a steady state part, which calculates conditions of equilibrium in which the pulley ratio does not change, and a transient part, which calculates the rate of change in the pulley ratio when disequilibrium occurs in the system. The remainder of this section will discuss the steady state and transient parts in more detail.

In the steady state part, the pulley ratio is in a state of equilibrium and does not change. Tests have indicated that the total thrust ratio that produces this state can be unambiguously defined by torque ratio and pulley ratio. Pulley piston pressure, pulley input speed and pulley input torque are entered in the model and the degree of discrepancy between the induced total thrust and the total thrust in a state of equilibrium is calculated. This is called the thrust for shift. The thrust for shift causes the pulley ratio to change until the next state of equilibrium is reached.

The factor that determines the rate of change in the pulley ratio generated by the thrust for shift is calculated in the transient part. A factor for pulley ratio that can function as an argument for calculation of this factor is known[2]. However, use of this factor for pulley ratio alone does not enable the rate of change of the pulley ratio to be calculated with a high degree of accuracy, particularly when analyzing sudden shift transient states such as kick-down shift in an actual vehicle. This was hypothesized to be due to changes in the friction between the pulley and the steel belt with torque input to the pulley and changes in the centrifugal load on the steel belt due to changes in the pulley input speed. Figure 15 shows the pulley ratio calculation model.

To test the hypothesis mentioned above, the test equipment shown in Fig. 16 was constructed to measure the torque input to the pulley in an actual vehicle. The measurement equipment employed the flywheel. The friction plate and filled grease, which

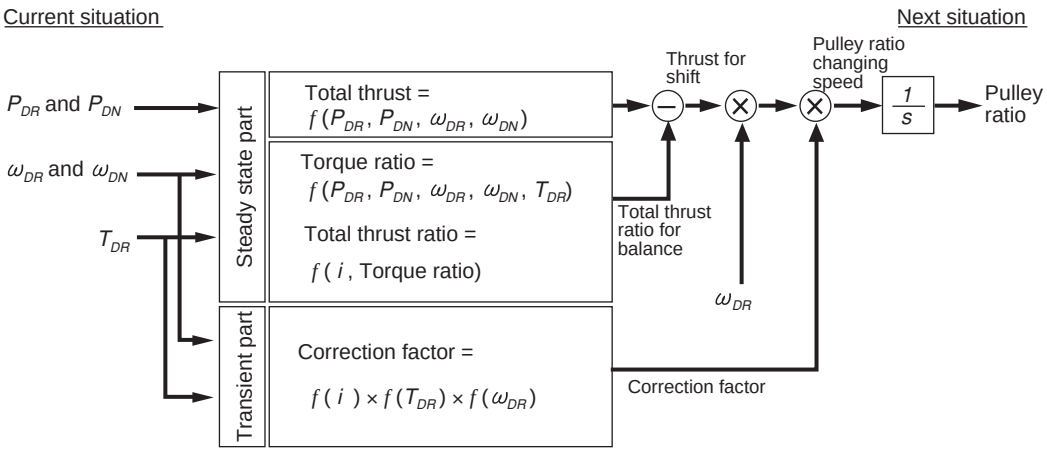


Fig. 15 Pulley ratio calculation model

acted as damping elements, were removed from the flywheel. And the flywheel was grooved on the input and output side to measure turn pulse. The phase difference between the input and output pulses was then determined. A torsional angle converter was employed to determine the torsion angle of the flywheel from this phase difference. The torsion angle was then converted to torque using previously measured data on the flywheel torsion angle and torque characteristic. By this means, a factor was obtained enabling calculation of the rate of change of pulley ratio in sudden shift transient states such as kick-down shift.

The results of these measurements are shown in Figs. 17 and 18. Figure 17 shows a plot of the factor for pulley input torque and Fig. 18 a plot of the factor for pulley input speed. The factor which is shown on the vertical axis is an integrating factor for the rate of change of pulley ratio, as discussed above. When it is greater than one, it shows a high rate of change, and when it is less than one it shows a low rate of change. That is, the rate of change of the pulley ratio becomes higher as input torque increases, and becomes lower as the pulley input speed increases. This characteristic indicates the validity of the hypothesis discussed above.

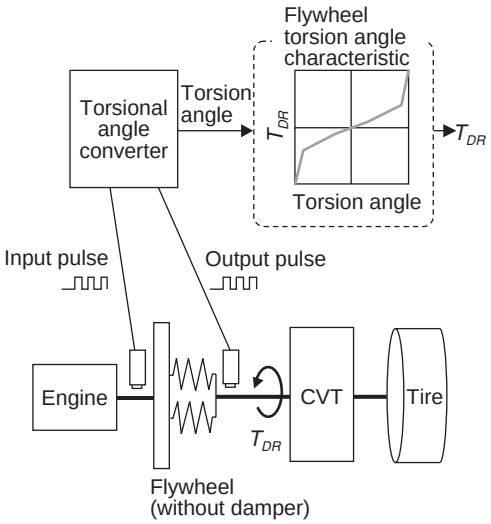


Fig. 16 Schematic drawing of test equipment

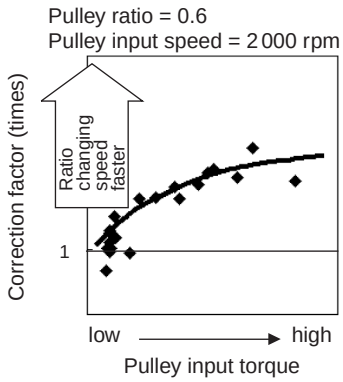


Fig. 17 Newly developed factor for pulley input torque

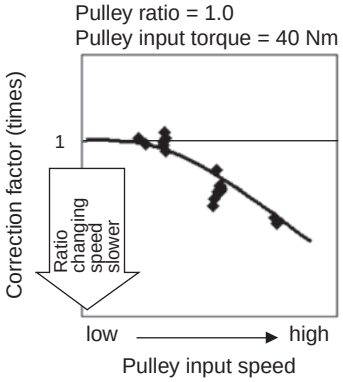


Fig. 18 Newly developed factor for pulley input speed

3.5. Accuracy of the CVT HILS Model

Figure 19 shows vehicle test results and the results of simulations employing the CVT HILS model (Fig. 1) composed of the torque transfer model, hydraulic control model and pulley ratio calculation model discussed above.

Good correlation is displayed between vehicle test and simulation results for pulley piston pressure and rate of change of pulley ratio, demonstrating the achievement of a level of calculation accuracy in the simulation of CVT shift transient states enabling them to replace vehicle tests. The employment of the newly developed hydraulic control model and pulley ratio calculation model has enabled the creation of a CVT HILS model with a calculation burden low enough for real-time simulation with existing DSP.

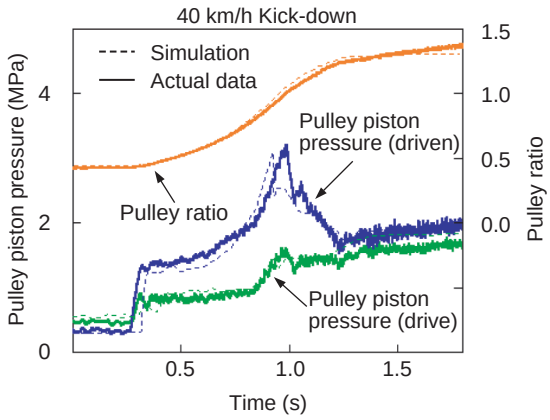


Fig. 19 Simulation results

4. Results of Application of Model

The time required for initial performance verification and parameter setting for CVT control programs in the newly developed ECU when employing the newly developed CVT HILS system was compared with the conventional process employing an actual vehicle.

Despite the fact that preparation of the CVT HILS system, including input of the design specifications of the target vehicle and connection of the ECU and interface box, required one day, performance verification and parameter-setting on the desktop required 30% less time than when a vehicle is employed.

5. Conclusion

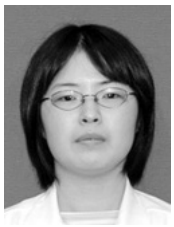
(1) Test data has been employed to enable the higher-order simultaneous equation model conventionally used for the high calculation load hydraulic control model with a lower-order transfer function model, in order to allow real-time simulation using existing DSP. This has resulted in the creation of CVT HILS model with a calculation burden that does not exceed the processing capacities of existing DSP.
(2) The employment of an experimental model that calculates the transient characteristics of the pulley ratio on the basis of pulley ratio, pulley input torque, and pulley input speed has enabled the creation of a CVT HILS model capable of simulating transient states in a CVT shift mechanism.
(3) Initial performance verification and parameter-setting of new ECU can now be performed using the CVT HILS system prior to vehicle testing, reducing the time required by 30%.

References

(1) Takeda, Y., Yoda, K., Terayama, S., Hagiwara, K., Saito, Y., Kamiyamaguchi, T.: Application and Utilization of HILS for the Development of an Automatic Transmission Control System, Honda R&D Technical Review, Vol. 14, No. 2, p. 99-106
(2) Ide, T., Udagawa, A., Kataoka, R., Uchiyama, H.: A Study on a Response of a Metal V-Belt CVT, SUBARU TECHNICAL REVIEW, Vol. 22, p. 50-55 (1994)
(3) Ishikawa, K., et al.: The Development and Utilization of ACTASS, AVEC'94, p. 224-229 (1994)
(4) Osono, K., Aoki, T.: Development of Full-electronic Control Metal Belt CVT, HONDA R&D Technical Review, Vol. 8, p. 21-33
(5) Ohta, S., Kunii, H., Sumi, M., Fujimoto, S., Yamaguchi, T.: Development of a Compact CVT for a Hybrid Car - Insight, HONDA R&D Technical Review, Vol. 12, No. 2, p. 61-70

■ Authors ■


Hiroshi SAOTOME


Rei ITO


Kenji HAGIWARA


Ko YODA

Development of Electronically Controlled Belt CVT "Honda S MATIC" for Motorcycles

Michio ASUMI* Hideo ISHIKAWA*
Kazuhiko MORI* Naotada MATSUDAIRA*

ABSTRACT

World's first electronically controlled belt CVT System (hereinafter referred to as Honda S MATIC) for 250 cm^3 class scooters has been developed in FORZA 2004 model. Honda S MATIC employed a rubber belt with a high friction coefficient and pulleys made of aluminum alloy. It was placed inside the unit-swing type engine, which is the same type as conventional scooters. For shift changing, pitch circle diameter of the driving pulley was adjusted by a motor. Preparing several selectable shift modes, suitable shifting characteristics could be obtained at flat road or mountain road. Furthermore, because of the elimination of ratio change due to aging, Honda S MATIC provides several advantages such as little reduction in maximum speed, no change in shifting characteristics, and no change in clutch connection point. Exceeding the conventional CVTs, Honda S MATIC has simultaneously satisfied low fuel consumption, low emissions, low noise and excellent engine performance.

1. Introduction

Demands for reduction in exhaust emissions, lower fuel consumption, and low noise, which offer a feeling of superior quality, are growing year after year, as part of the measures to cope with global environmental issues. Some of these demands tend to be in direct conflict with enhancing the power performance. The conventional belt CVT had its limitation in that it was capable of only one shifting characteristic. The electronically controlled belt CVT system (hereafter called "Honda S Matic system") capable of setting shifting characteristics freely, was developed in response to these demands. The engine equipped with the Honda S Matic system is an unsprung unit swing type engine similar to the engine in conventional scooters, and is designed as a lightweight and compact engine without reducing its maneuverability.

This paper describes the technology of the Honda S Matic system used in the 2004 year model FORZA 250-cm^3 class scooter.

* Asaka R&D Center

2. Conventional Belt CVT Technology

The belt CVT with a good overall balance of weight, performance, and cost has been used in scooters with the goal for realizing easy-to-drive performance. Figure 1 shows the structure of the conventional belt CVT. The conventional belt CVT generates centrifugal force in the weight roller of the drive shaft because of engine rotation, and converts this force to thrust force that acts to move the movable drive face in the axial direction. The belt pitch diameter changes and shift change occurs according to the balance between the thrust force on drive pulley, the spring load of driven pulley, and the thrust force on driven pulley generated by the torque cam. The shifting characteristics were decided primarily by these mechanical elements, and to freely set the ratio corresponding to each throttle opening was a challenging issue. Although low engine speed is beneficial to achieve exhaust emissions reduction, low fuel consumption and low noise, the power performance decreases.

When the travel distance increases, the belt wears and the belt width decreases. As a result, the pitch diameter of drive pulley becomes small, the pitch diameter of driven pulley becomes large, and the ratio changes over to the low speed range, therefore, the maximum speed decreases.

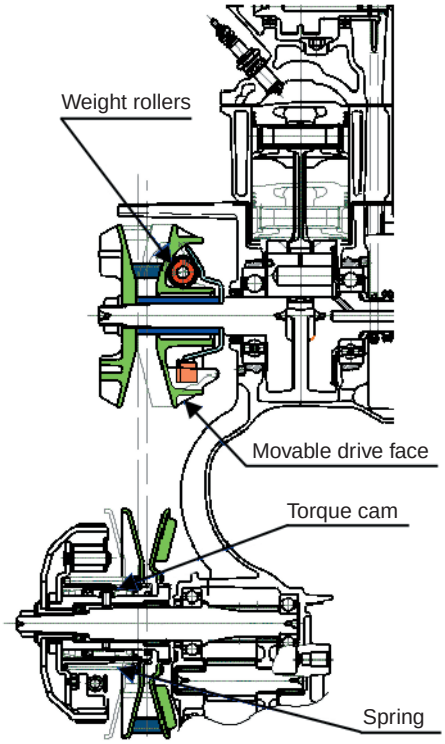


Fig. 1 Structure of conventional belt CVT

3. Basic Structure and Requirements for Development Goals

The goals of development of the Honda S Matic system are as follows.

(1) To achieve lightweight and compactness
(2) To enable shifting characteristics that fuel consumption, exhaust emissions, and low noise are compatible with driveability.
(3) To adopt a simple operation system.

In the 2004 model FORZA, three modes are provided including two automatic modes and one manual mode. The rider can press the switch and freely select the desired mode. This arrangement contributes to a fun to ride. Figure 2 shows the overview of this system. Various sensors are provided for detecting drive speed, driven speed, pulley position, vehicle speed, and throttle opening. The ratio control unit decides the control objectives from the data from these sensors and switches, and it controls the pulley position by the motor drive based on these data. Figure 3 shows the cross section of the S Matic mechanism. Figure 4 shows the shift change mechanism on the drive side.

The control current flows into the motor, which rotates and transmits the torque to the movable gear through the reduction gear. The internal part of the movable gear contains a feed screw, which converts the transmitted torque to axial force, moves the movable drive face, and performs the shift change. The guide key is used as the mechanism that transmits the engine torque while the movable drive face slides. Because the shift change drive unit is not lubricated, a plastic gear was used in a part of the unit considering both gear wear reduction and weight reduction. The guide key and the feed screw are lubricated by grease to ensure their moveability.

Outside air is introduced to lower the temperature in the belt chamber considering the belt durability. Measures to prevent intrusion of water or dust have also been adopted. The structure on the driven side is basically similar to that of the conventional belt CVT, but a rotor for detecting the pulley speed has been provided

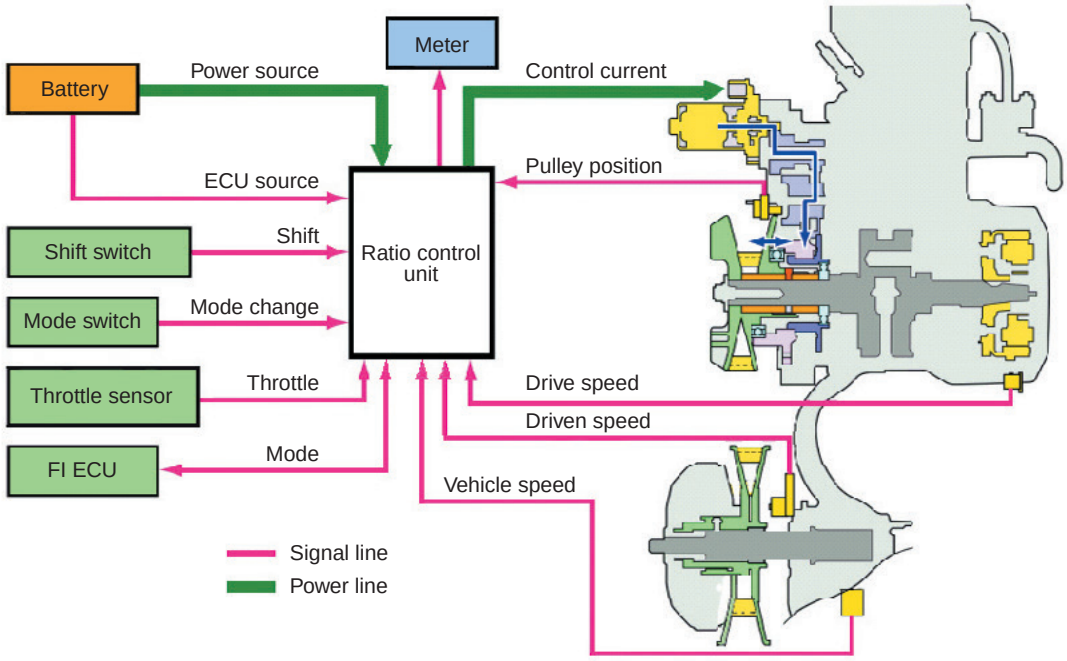


Fig. 2 Diagram of Honda S MATIC system

additionally. The scooter generally has an unsprung unit swing type engine, but since the engine weight affects the maneuverability adversely, a lighter weight engine is desired. To maintain the compact and lightweight features, which are the advantages of the conventional belt CVT, rubber belt was used and the pulley was made of die cast aluminum alloy. The movable drive face consisted of the boss made of steel and cast into the aluminum alloy pulley with the pitch diameter restricted to a small value to obtain a wide ratio.

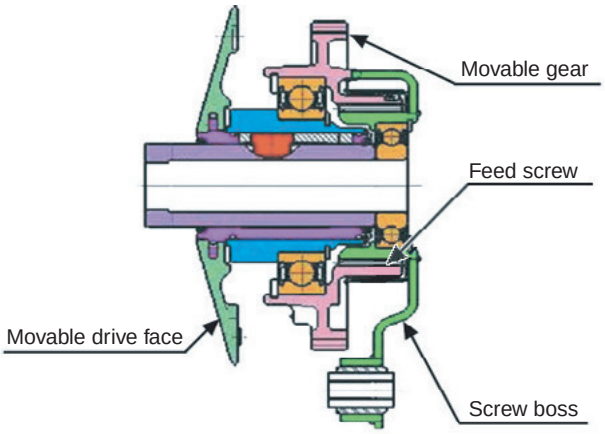


Fig. 4 Shift mechanism of drive side of Honda S MATIC

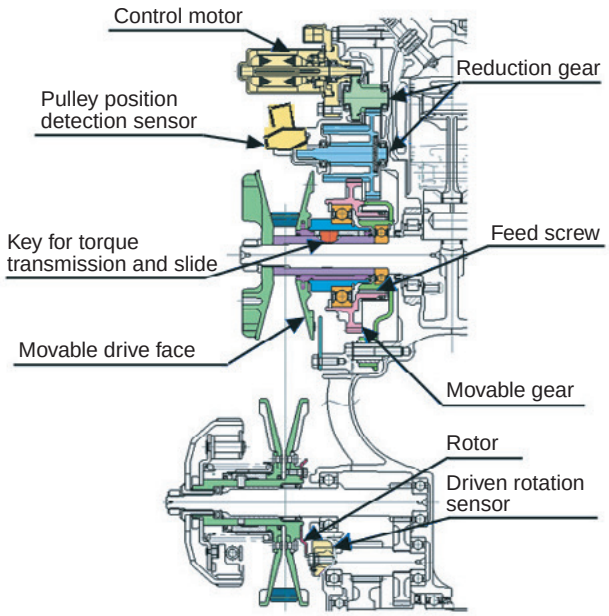


Fig. 3 Sectional view of Honda S MATIC mechanism

4. Setting of Specifications for Each Part and Performance

4.1. Selection of Drive Belt Suitable for Ratio Control

The material of the drive belt, which is a rubber belt with a high coefficient of friction and lightweight, is essential to achieve light weight and compactness. However, the slip ratio of the conventional rubber belt is large. Because the difference in ratio between no load and full load is very large, it was important to minimize the slip ratio of the rubber belt to ensure ratio control in the Honda S Matic system. Table 1 shows the comparison of the drive belts of the 2000 model FORZA and the 2004 model FORZA. Figure 5 shows the external view of the drive belt.

As shown in Table 1, the drive belt of the 2004 model FORZA were enhanced mainly three points shown below.

(1) Change in the cog shape: Change from a single cog to a double cog

Table 1 Comparison of drive belt specifications

		2000 Model FORZA	2004 Model FORZA
Material of component	Upper canvas	Cotton canvas	Without canvas
	Upper rubber	Chloroprene rubber with thread	Chloroprene rubber with thread*
	Core wire	Polyester	Aromatic polyamide
	Bonding rubber	Chloroprene rubber	Chloroprene rubber
	Lower rubber	Chloroprene rubber with thread	Chloroprene rubber with thread*
	Reinforcements	With reinforcement	Without reinforcement
	Lower canvas	Polyamide canvas	Synthetic fabric mixed cotton canvas
Shape	Cog shape	Single cog	Double cog
	Upper width	Approximately 23 mm	Approximately 25 mm
	Thickness	Approximately 10.5 mm	Approximately 12.5 mm
	Angle	Approximately 30 degrees	Approximately 30 degrees
Ratio range		2.95	3.13

* : New compounded rubber which has two times strength of rubber elasticity rate for single cog

(2) Change in the core wire: Change from polyester to aromatic polyamide
(3) Change in the upper and lower rubbers: Change to compounded rubber with enhanced lateral pressure strength

Figure 6 shows a comparison of slip ratio of the drive belt in the typical LOW ratios and TOP ratios. In the 2000 model FORZA, the slip ratio in the LOW ratio of the single cog belt is more than approximately 8%, and the slip ratio in the TOP ratio is more than approximately 2%. Compared to the 2000 model FORZA, the pitch diameter for LOW ratio on the drive pulley of the 2004 model FORZA is reduced, and the ratio range has been widened by approximately 10%. Therefore, it is inappropriate for reducing the slip ratio. However, by using new forms of belt composed of new materials, slip ratios of approximately 4.5% in the LOW ratio and approximately 1% in the TOP ratio have been obtained, and realized a belt suitable for ratio control.

4.2. Shift Control

The 2000 model FORZA employs a belt CVT (Hyper V Matic system). By changing the shift change timing to two stages, the connection from the medium-speed area to the high-speed area has been enhanced compared to previous models of the scooter.

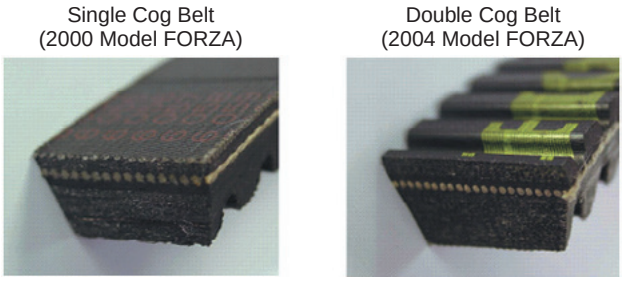


Fig. 5 External view of drive belt

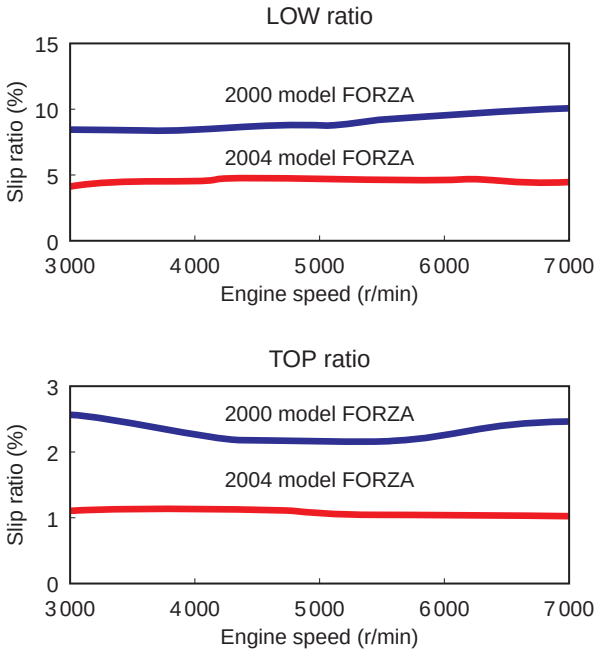


Fig. 6 Comparison of slip ratio of drive belt

As the result, comfortable driving performance was obtained by smooth acceleration. Figure 7 shows the shifting characteristics.

Furthermore, by setting the automatic D mode and S mode, and the manual M mode shifting characteristics in the 2004 model FORZA, the range of usable engine speeds increased, and smoother running was realized. The features of each mode are described below.

(1) D mode

In the D mode, engine speed in the shift area was lowered, and fuel consumption, exhaust emissions and noise enhanced. For obtaining smooth acceleration, the shift area adopted characteristics of which engine speed increases in conjunction with increase of vehicle speed. Figure 8 shows the shifting characteristics. In the D mode, the ECE40 mode fuel consumption was enhanced by approximately 10% compared to the 2000 model FORZA. In exhaust emission levels, half in CO and less than one-third in HC of the regulation value in Japan were attained. Figure 9 shows the fuel consumption and exhaust emission data during the D mode driving. Low noise characteristics were enhanced compared to the 2000 model FORZA by reducing the engine speed at partial throttle opening.

(2) S mode

The shift area in the S mode also adopted characteristics of which engine speed increases in conjunction with increase of vehicle speed, as well as D mode. As shown in Fig. 10, the LOW ratio in S mode for shifting characteristics has been set larger than that in the D mode. As a result, the acceleration performance has been enhanced, as shown in Fig. 11, compared to that of the 2000 model FORZA. By setting the ratio to a lower speed during deceleration, the engine braking effect can be obtained compared to that of the conventional scooter.

(3) M mode

As shown in Fig. 12, the M mode is a manual mode that enables six shift ratios to be fixed. The rider can freely select a fixed ratio, thus acceleration during hill climbing and also during high-speed running was enabled easily. Engine braking can also be used by shifting to low gear.

Considering ease of use for riders, the automatic shift down and shift limitation functions have been provided. The automatic shift down is a function that enables automatic shift to a proper low gear ratio for comfortable running at low vehicle speeds. It helps eliminate the uncomfortable feeling in riders. The shift limitation function has two functions for restricting the shift down and the shift up by riders. When the rider attempts to shift gear in the condition which driving comfort will be lost, this function does not permit the shift. The LCD part of the meter flashes to notify the user that the shift operation has been restricted.

4.3. Ratio Change

Even if the belt or the pulley surface wears out, the pulley position is changed proportionally and control is performed such that the ratio becomes equal to the preset ratio. As the result, the belt pitch diameter does not change, and the ratio does not change provided there is some margin in the range of pulley operation.

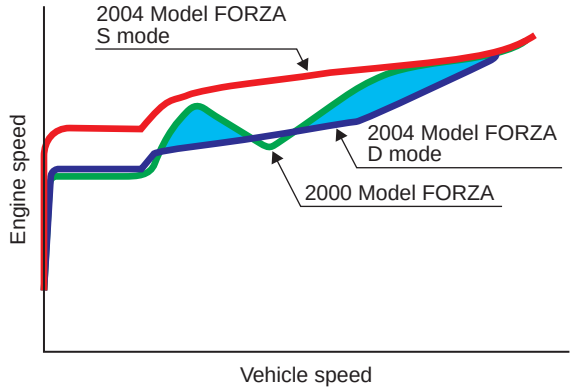


Fig. 7 Shift speed characteristics of HYPER V MATIC system

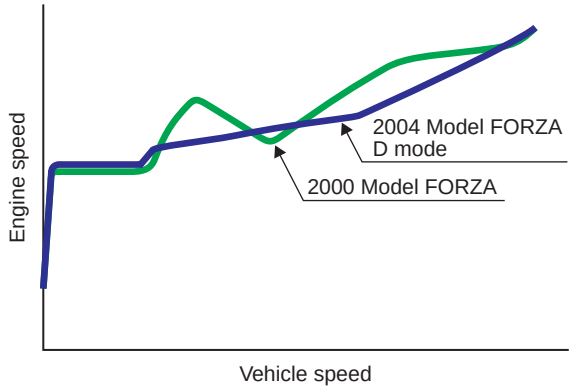


Fig. 8 Shift characteristics of D-mode

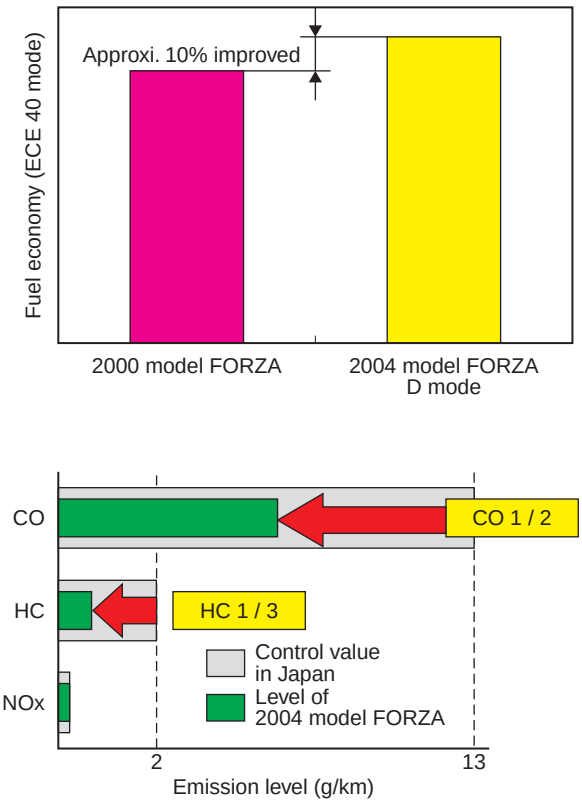


Fig. 9 Fuel consumption and exhaust emission during D-mode use

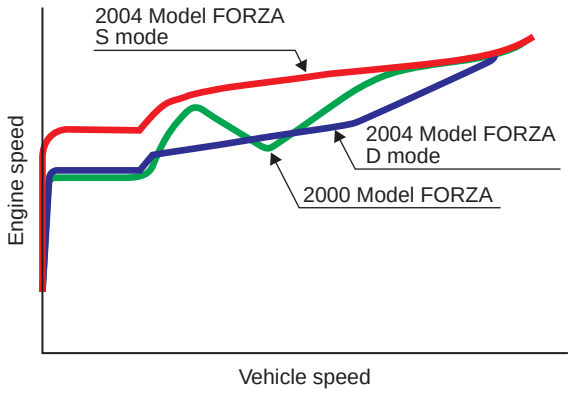


Fig. 10 Shift characteristics of S-mode

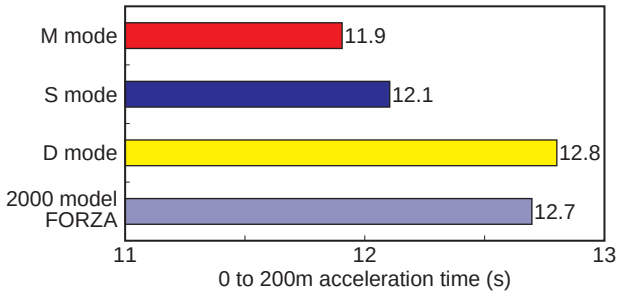


Fig. 11 Comparison of acceleration performances

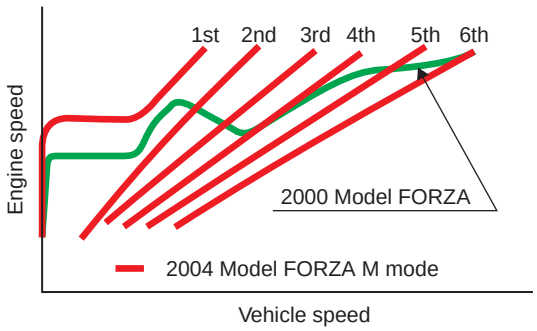


Fig. 12 Shift ratio of M-mode

4.4. Control Specifications

4.4.1. Overview of control

The basic primary control flow starts with the calculation of target drive rotation from the throttle opening, its displacement speed, and the driven rotation. Next, the difference between this value and the present drive rotation is calculated. The electric current control for the motor is implemented after deciding the motor control command value from this difference. The indicator lamp of the meter lights up to indicate the specific shift change mode, and the shift position during the M mode is also shown in the LCD display.

Optimized fuel injection and ignition controls are implemented to suit the aims of each shift change mode. Therefore, the function of notifying the FI ECU the present shift change mode from the ratio control unit is also provided. A pulley position sensor is also used to identify the movable range of the drive pulley. Figure 13 shows the overview of the control system.

4.4.2. Selection of shift mode

When selecting the shift mode, for instance, when changing over from D mode to S mode resulting in an abrupt ratio change, a noticeable speed change shock is generated. To help eliminate such shocks, the ratio control unit performs control so that the ratio is changed gradually and smoothly during mode selection. Figure 14 shows the overview of control during shift mode selection.

4.4.3. Change from automatic to manual mode

The function of automatic selection of optimum ratio is provided when changing over from D mode or S mode to M mode.

4.5. Honda S Matic Control Switch

Controls such as switch, levers, and pedals are normally operated close at hand or close at foot, but the switches for controlling the Honda S Matic have all been arranged on the handlebar close at hand considering operability and comfort near the foot.

Switches required for operating the Honda S Matic include the push button mode switch for selection of "Automatic and Manual" modes, the see-saw type shift switch for "High or Low Gear" during the M mode and for selection of the "D Mode and the S Mode." This arrangement of switches easily brings out the appeal of the Honda S Matic System. Figure 15 shows the operation when a switch is pressed.

The arrangement of the switches is such that they are always in the field of view of the rider during driving. The shift switch is arranged on the left side considering ease of operation simultaneously with the right hand throttle operation. As shown in Fig. 16, the mode switch is arranged on the right side considering the balance of operation with the shift switch. This arrangement enables ease of operation of the S Matic switches without losing the ease of operation of existing switches such as the direction indicator switch. It has also enabled the external form of the handle switches to be made the same size both on the left and right sides, thereby enhancing the design around the handle grip.

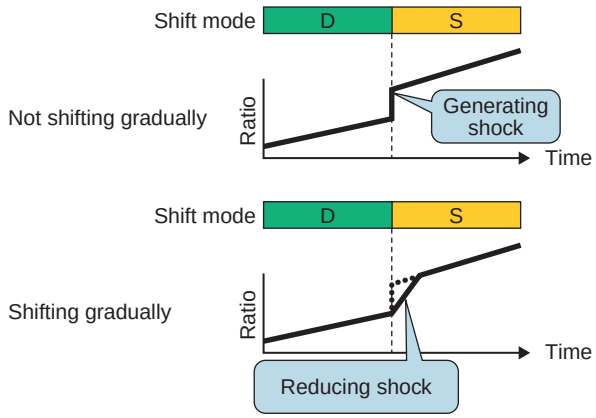


Fig. 14 Control concept of shifting modes

Modes	+ Button	– Button
Automatic	To “D mode”	To “S mode”
Manual	Shift up	Shift down

Changed by mode switch

Fig. 15 Explanation of shift switch operation

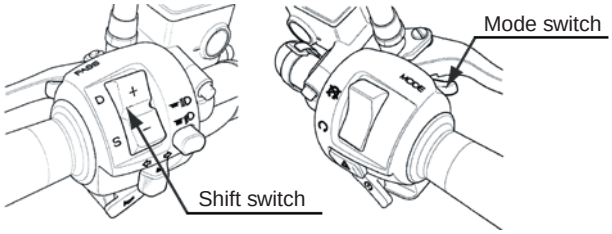


Fig. 16 Location of shift switch

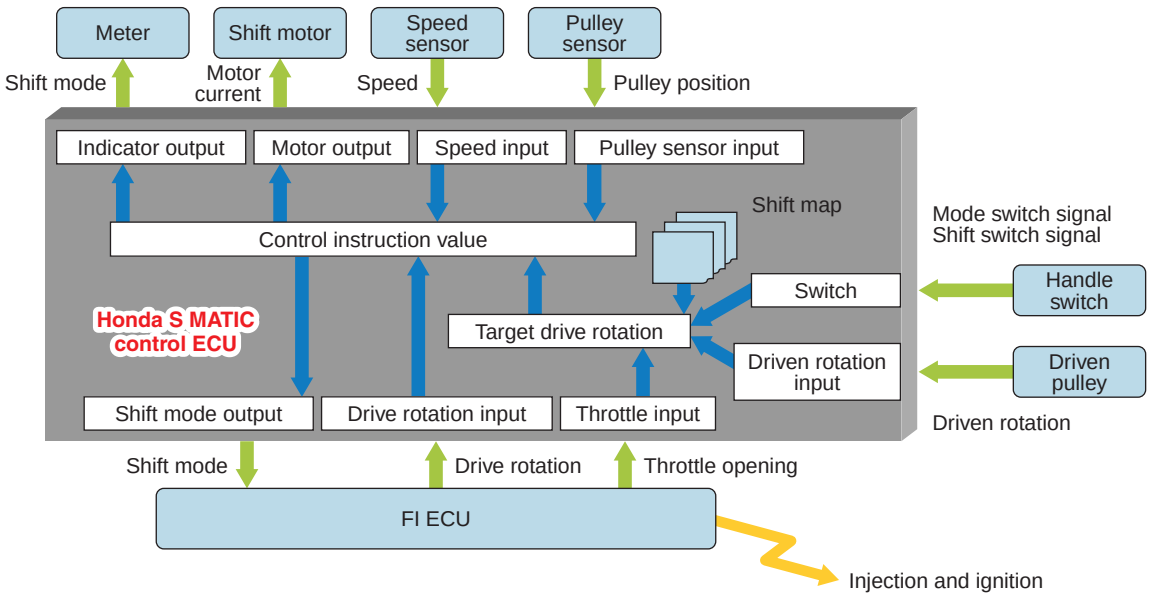


Fig. 13 Diagram of Honda S MATIC control flow

5. Conclusion

A lightweight electronically controlled belt CVT system was developed for use in the unsprung unit swing type engine of the same type as used in conventional scooters.

(1) Riders can select shifting characteristics according to the condition by setting any of the two automatic modes for electronic control of the belt type CVT, thereby realizing a good balance between fuel consumption, exhaust emissions, low noise on the one hand and power performance on the other hand.
(2) Acceleration performance and engine braking performance not available in conventional scooters have been achieved by providing a manual mode that can fix the shift change ratio.
(3) A simple and easy-to-operate system was developed enabling selection of running mode and shift operations to be performed easily and close at hand.

Acknowledgements

The authors are grateful to the staff members of the Bando Chemical Industries, Ltd., for their cooperation in providing the drive belt essential for developing this system.

■ Authors ■


Michio ASUMI


Hideo ISHIKAWA


Kazuhiko MORI


Naotada MATSUDAIRA

Study of Inspection Technology for Gear Surface using Self-organizing Map

Junji EGUCHI* Manabu MURAKAMI*
Takanao UCHIDA* Kinya FUJIWARA*

ABSTRACT

Research was carried out on inspection technology for gear surface imperfection inspection that has the same degree of accuracy as that of a human inspector. Regarding the surface of the tooth which is the object of inspection, over-detection resulting from the extraction of uneven brightness other than that due to imperfections was an issue. For this reason, the features of imperfections that permit imperfections to be discriminated from non-imperfections were set based on visual observation. In addition, a self-organizing map which is a kind of neural network was employed as a method whereby these features are used to identify imperfections in the same way as a human inspector. By using this map to teach the inspection system the features of multiple imperfections and also uneven brightness and dirt on the surface of the gear, it was possible to recognize imperfections to the same degree of accuracy as that of a human inspector. Technology constructed using this imperfection recognition method enabled the work of visual inspection to be reduced to about 10% of that previously necessary.

1. Introduction

Automotive transmissions are composed of a large number of gears, and the quality level of these gears is known to have an effect on driving comfort[1]. Tiny raised areas on the interlocking surfaces of gears caused by scratches and the like generate noise, which can cause discomfort to vehicle occupants. Therefore, gear tooth surfaces are visually inspected. However, visual inspection places a significant burden on the inspectors, and individual differences in the accuracy with which imperfections are detected may cause variations in quality, making automation of the inspection process desirable. This paper discusses the development of a method of detecting imperfections on gear tooth surfaces and of the inspection system in which it is employed.

* Tochigi R&D Center

2. Outline of Research

2.1. Goal

The goal of this research project was to develop a technology for the detection of imperfections on gear surfaces possessing an equivalent level of accuracy to visual inspection. Imperfections occurring on gear tooth surfaces can be classified into dents, chips and scratches, as shown in Fig. 1. If a method in which potential imperfections are identified by conventional image analysis is employed to inspect for these imperfections, accuracy can be reduced by instances of over-detection, in which uneven brightness, dirt, etc. is recognized as imperfections. Over-detection occurs for the following reasons:

- Difficulty in ensuring uniform illumination: As Fig. 1 shows, the gear surfaces are curved, and therefore there are differences in the intensity of illumination at different points.
- Recognition of a variety of different imperfection types: Because the system must be able to detect a variety of different imperfection types, criteria for recognition are complex, and establishing system settings is therefore difficult.

By contrast, over-detection rarely occurs in visual inspection, because the inspector recognizes imperfections based on a concept of what constitutes an imperfection and his or her memory of past experiences in detecting them. The following research goals were therefore established to enable the development of a method possessing equivalent accuracy to visual inspection:

(1) Development of a technique of defining the features of imperfections (Image analysis).
(2) Development of an ability to recognize imperfections using features of sections of captured images
(3) Development of a learning ability to increase the accuracy of recognition

2.2. Development of Imperfection Detection Technology

This development project employed the following three element technologies to create an imperfection detection technology with equivalent accuracy to visual inspection:

(1) Imperfection recognition technology
The ways in which inspectors discriminate between imperfections and dirt, etc. during visual inspection were analyzed to enable the new system to recognize imperfections with an equivalent level of accuracy to visual inspection. Multiple features defining the appearance of an imperfection were established on the basis of this analysis.

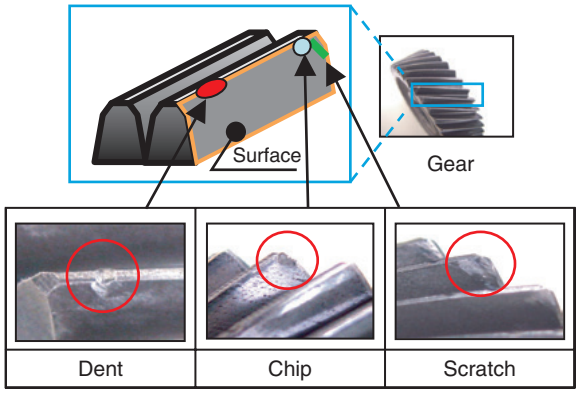


Fig. 1 Imperfection samples

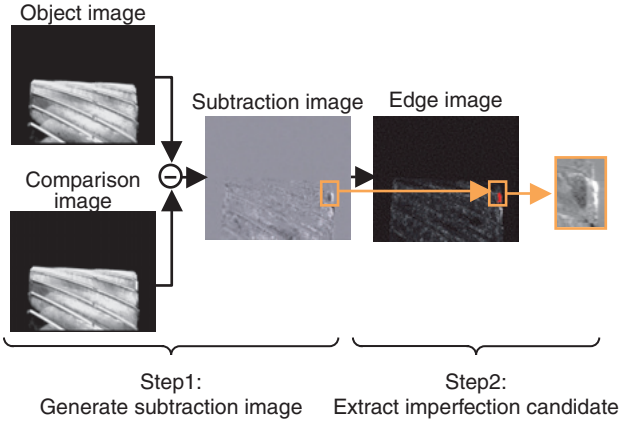


Fig. 2 Image processing to extract imperfection candidate

(2) Practical application of imperfection recognition technology
A data classification method employing a self-organizing map (a type of neural net) has been employed to recognize imperfections. This enabled the formulation of a table grouping together similar data concerning previously detected imperfections, and over-detection elements such as uneven brightness on the surface. When an area which might be an imperfection ("imperfection candidate" below) is extracted by image analysis, the table is used to determine whether the candidate is most similar to an imperfection or an over-detection element, i.e. it enables recognition of imperfections by judgment on the level of similarity of a candidate to an imperfection.
(3) Increased accuracy in recognition of imperfections
A learning function adds details of the imperfections, and over-detection elements encountered in inspections to date to the table, enabling the accuracy of imperfection recognition to be increased when required.

2.3. Extraction of Imperfection Candidates by Image Analysis

This section will discuss the technique used for extracting imperfection candidates, which formed the backbone of this development project. In this technique, an image of the gear tooth surface under inspection (object image) is compared with an image of another gear tooth surface (comparison image), and any area of difference is extracted as an imperfection candidate. The gear tooth surfaces are compared using a subtraction image generated according to the following formula (Fig. 2: Step 1):

Subtraction image = Object image – Comparison image

The area of difference between the original two images, in which the potential imperfection is located, becomes an area differing in brightness on the subtraction image. An edge image in which this area of differing brightness is emphasized is generated and compared with the original subtraction image, enabling the area to be extracted from the image (Fig. 2: Step 2). This becomes the imperfection candidate. Over-detection elements such as dirt and areas of uneven brightness are included among imperfection candidates; the priority in this method is to ensure that no imperfection is overlooked.

The following discussion will focus on the method of recognizing imperfections by means of classifying the features of imperfection candidates.

3. Development of Imperfection Recognition Technology

3.1. Methods Used in Visual Inspection

Multiple parameters relating to features of the external appearance of imperfection candidates have been input to the system, and these are used to recognize imperfections. The features that inspectors focus on to recognize imperfections in visual inspections were used as a reference in selecting these features. Figure 3 shows imperfections and over-detection elements (surface dirt, etc.) isolated from subtraction images. Our research suggested that human inspectors use the shape of an imperfection and the pattern of distribution of brightness around the imperfection to discriminate imperfections from dirt, areas of uneven brightness, etc. Therefore, the development team focused on the following features to ensure the achievement of an equivalent level of ability in recognizing imperfections as that of visual inspection:

(1) Geometric features of imperfections
(2) Features of distribution of brightness around imperfections

3.2. Determining Features of Imperfections

1: Geometric features of imperfections

In visual inspection, the geometric features that define the external appearance of an imperfection are size (area), direction (angle) and shape (circularity). These features were therefore employed as parameters in the inspection system (Fig. 4).

(1) *SA*: Area

(2) *θA*: Angle

(3) *CA*: Circularity (*CA* = *SA*/*C*, where *C* is the area of a circumscribed circle of the imperfection)

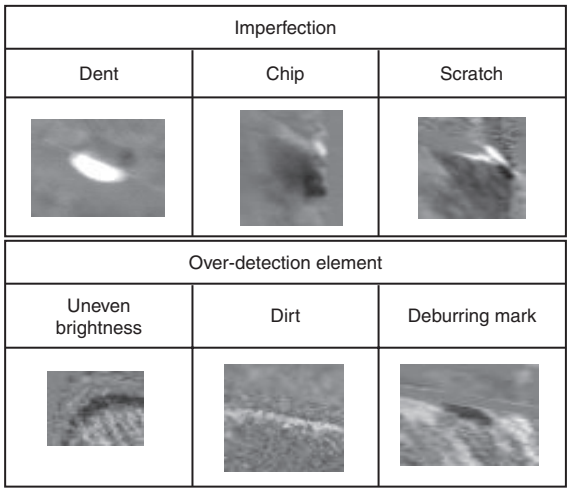


Fig. 3 Images of imperfections and over-detection elements

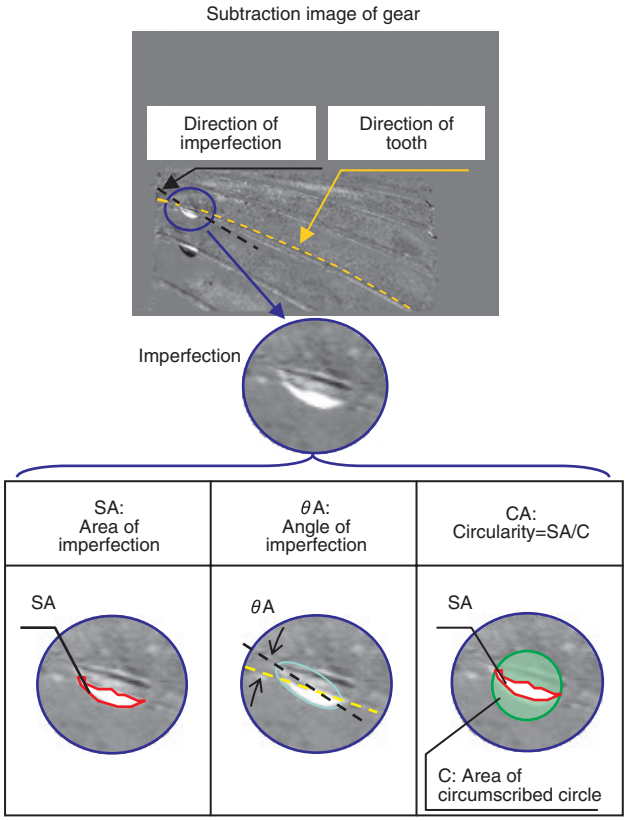


Fig. 4 Geometrical features of imperfection

2: Features of distribution of brightness around imperfections

Features of the pattern of distribution of brightness around imperfections were similarly employed as parameters. These were the messiness of the image (entropy), the symmetry of the distribution of brightness (anisotropy) and the change in brightness (average brightness of the edge image).

(4) *entB*: Messiness (entropy)

(5) *AnsB*: Symmetry (anisotropy)

(6) *edgB*: Change in brightness (average brightness of edge image)

By this means, the external appearance of imperfections was defined by a feature vector which imparted directionality to the six individual features. The feature vector, *x*, can be expressed mathematically as:

$$x = (SA, \theta A, CA, entB, ansB, edgB).$$

3.3. Feature Vector Example

Figure 5 shows feature vectors for an imperfection (a dent) and an over-detection element (uneven brightness) as an example of the extraction of feature vectors from imperfection candidates. When these are compared, significant differences are observed in *CA* (circularity), *entB* (messiness) and *edgB* (change in brightness). These features enable an imperfection to be discriminated from an over-detection element. This indicates the successful development of a technique for defining the features of imperfections, to enable imperfection candidates to be accurately judged as imperfections.

4. Practical Application of the Technique

Having developed a technique for defining the features of imperfections, it would be possible to recognize imperfections by comparing the feature vectors of imperfection candidates with existing data on imperfections and over-detection elements. A recognition table was constructed by means of the two-dimensional map shown as (a) in Fig. 6 to enable this. Images of dents, etc. and the feature vectors discussed above were imported to each node of this table (shown as (b) in Fig. 6). Judgments on whether these were imperfections or over-detection elements were also entered. This enabled the achievement of an equivalent level of accuracy in judgment of an imperfection candidate as an imperfection or an over-detection element to that achieved in visual inspection.

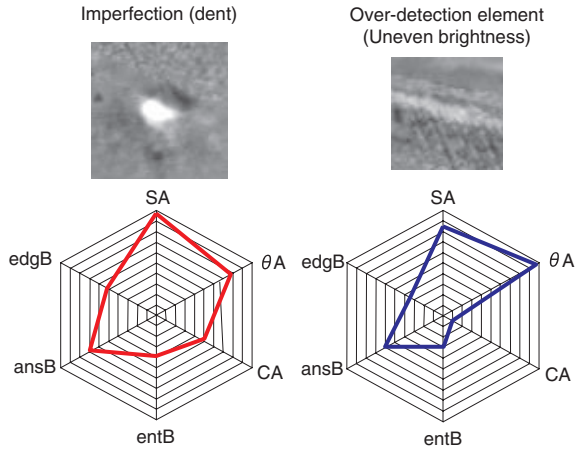


Fig. 5 Feature vector

4.1. Creation of Recognition Table

A self-organizing map[2], a type of neural net, was employed in creating the recognition table. A self-organizing map is one method of classifying multi-dimensional data. It is an algorithm that gathers and groups similar items in multiple pieces of data. On the basis of the features delineating the external appearance of imperfections defined in section 3, this enables pieces of data (dents, dirt, etc.) with a high level of similarity to be grouped together on the two-dimensional map, as shown in Fig. 7. Imperfections are judged during inspection by determining which group the imperfection candidate resembles.

However, there are elements among the data which confuse the ability to recognize imperfections, for example dirt that resembles chips. Therefore, if a self-organizing map alone is used, there is a possibility that data that is close to the boundaries of groups will be inaccurately classified into a group. In addition, at this stage the data showing similarities was only grouped, and no judgments on imperfections had been added to the recognition table. Therefore, visual recognitions on whether the imperfection candidate was an imperfection or an over-detection element were entered for all the data composing each group to correct inaccurate groupings. Therefore, the judgment in each group matched visual inspection values. This resulted in the creation of a recognition table equaling the accuracy of visual inspection.

As shown in Fig. 7, the recognition table was created by means of the following steps:

(1) Calculation of similarity levels between different data
(2) Grouping of similar data utilizing self-organizing map
(3) Input of visual recognition

4.1.1. Calculation of similarity levels between different data

The level of similarity between data on the recognition table can be determined by the distance between their feature vectors. The smaller the distance between the feature vectors, the closer the component values of the vectors, and the higher the level of similarity. As shown below, the distance d_{ij} between the feature vector of an imperfection candidate, X (shown here as (1)) and the feature vector of a node coordinate i and j, X_{ij}, shown as (2), can be calculated using the equation shown as (3).

$$X = (SA,\ \theta A,\ CA,\ entB,\ ansB,\ edgB) \quad (1)$$

$$x_{ij} = (SA_{ij},\ \theta A_{ij},\ CA_{ij},\ entB_{ij},\ ansB_{ij},\ edgB_{ij}) \quad (2)$$

$$d_{ij} = \sqrt{(SA - SA_{ij})^2 + \ldots + (edgB - edgB_{ij})^2} \quad (3)$$

4.1.2. Grouping of similar data utilizing the self-organizing map

Data with a high level of similarity are grouped together on the two-dimensional map by the self-organizing map by means of the following steps.

Step 1: Selection of the node expressing the similarity relationship of the data

The closest node (best match node below) at that point in time is selected to express the relationship of similarity between data on the two-dimensional map. The best match node is the node possessing the feature vector most similar to a particular piece of data (Fig. 8: Step 1).

Step 2: Grouping the data

The feature vectors of the best match node and surrounding nodes are revised to ensure similarity with the various pieces of data. The amount of revision at this time is greater the closer the node is to the best match node, and smaller the further away the node is. As

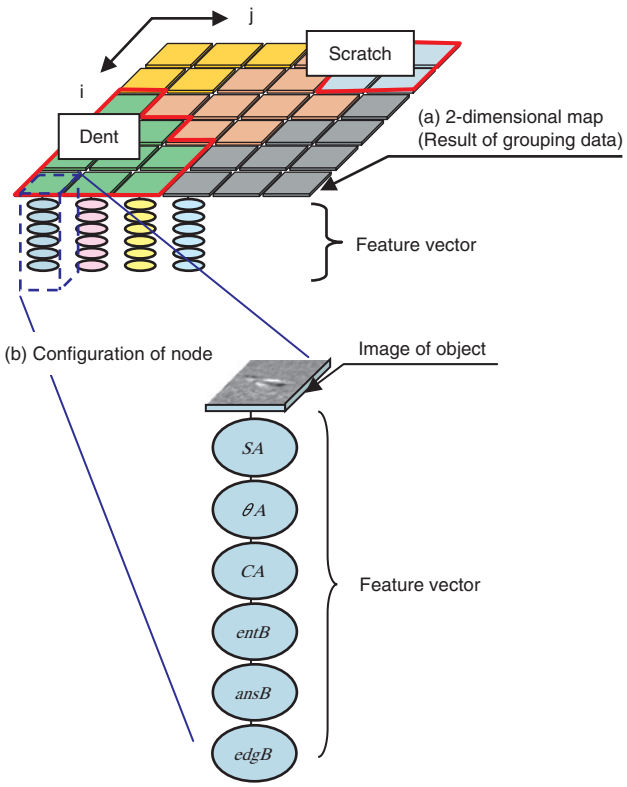


Fig. 6 Construction of recognition table

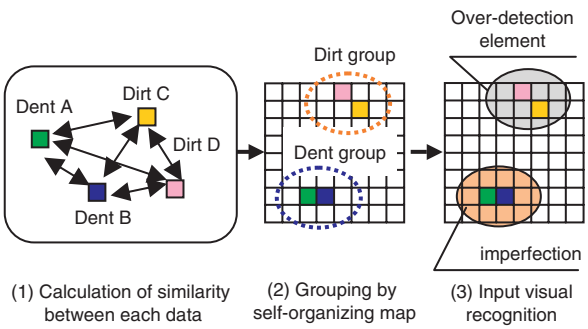


Fig. 7 Sequence of making recognition table

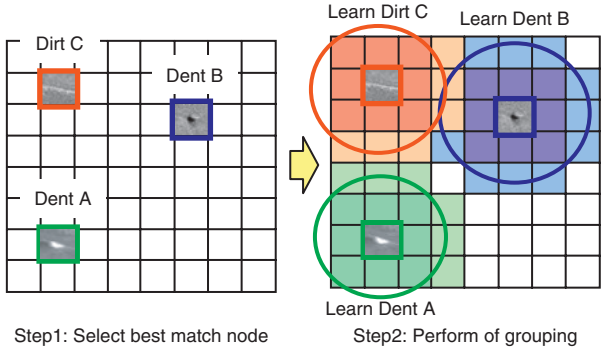


Fig. 8 Grouping data by self-organizing map

classification proceeds, the range of nodes which are revised becomes increasingly smaller. By this means, node areas are created possessing feature vectors similar to the various pieces of data (Fig. 8: Step 2).

The repetition of steps 1 and 2 ensures that the best match nodes for data with a high level of similarity are clustered closely together. By this means, as Fig. 9 shows, the level of similarity between the different data groups is expressed by the relationship between the positions of the node areas possessing feature vectors most similar to them.

(1) When there is a high level of similarity between data
The node areas of dent A and dent B which has a high level of similarity to it are generated close together, and therefore form a single group.

(2) When there is a low level of similarity between data
The node areas of dents A and B and the node area of dirt C, which has a low level of similarity to them, are generated in positions far apart, and dirt C therefore forms a separate group.

The shape of the node area for each piece of data and the boundaries with other node areas are automatically determined by the positional relationships of the best match nodes.

4.1.3. Input of visual recognition

To ensure that each of the groups on the recognition table match with standards for recognition in visual inspection, previous visual recognition of imperfections and over-detection elements are input for each node area forming a group. Because input is conducted for node areas, it is not necessary to input for each node, and the procedure can therefore be carried out in a short period of time.

4.1.4. Recognition table features

Figure 10 shows the recognition table formulated using the method discussed thus far. This table groups 100 pieces of data by means of 1600 (40 X 40) nodes. It is clear that the initial aim has been achieved, and that the table is composed of groups of data for dirt, dents, etc. possessing similar features.

The recognition table offers the following advantages.

(1) Human judgment
The self-organizing map enables multiple pieces of multi-dimensional data to be grouped on the basis of relationships of mutual similarity with no requirement for prior knowledge. This enables the possibility of a form of recognition close to human intuition[3].

(2) Stable imperfection recognition
Expressing data as node areas makes it possible to fill in the gaps between each group. This enables stable recognition of a diverse range of imperfection candidates, even with comparatively low numbers of data.

(3) Visual representation of relationships of data similarity
It is difficult for humans to intuitively grasp relationships of similarity between multi-dimensional data. This method enables these relationships to be represented visually on a two-dimensional map, thereby making them easy to grasp.

The next section will explain the method of recognizing imperfections employing the recognition table shown in Fig. 10.

4.2. Recognition of Imperfections Using the Recognition Table

Imperfections are recognized using the recognition table by comparing imperfection candidates and nodes with similar feature vectors. To ensure accuracy, the imperfection candidates are compared with multiple, similar feature vectors. To enable this, match node areas are established from multiple pieces of recognition data possessing similar features to the imperfection candidate, and judgment on whether the candidate is an imperfection or not is made on the basis of these areas.

4.2.1. Calculation of match node areas

The following two elements define match node areas.

(1) Size (Number of nodes)
The size of the match node area varies with the imperfection candidate. If the match node area is excessively large, there is

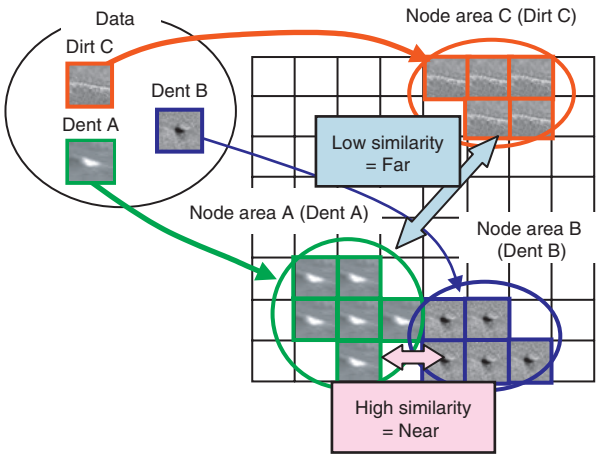


Fig. 9 Result of data grouping

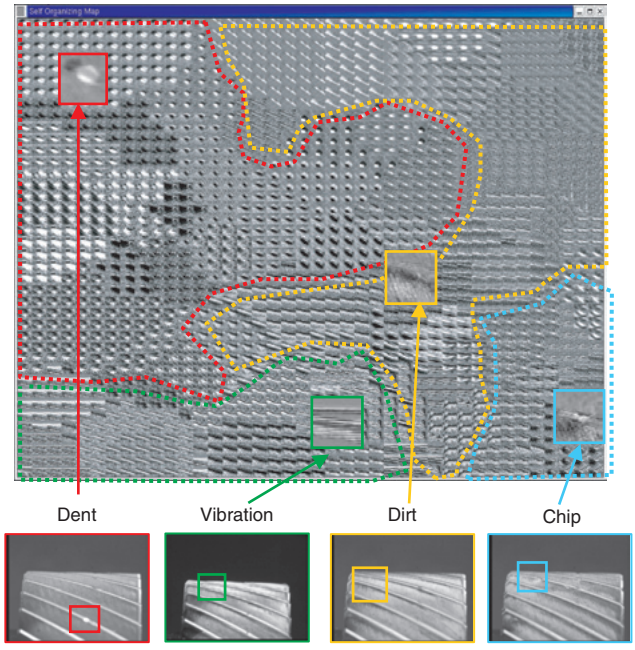


Fig. 10 Groups of data on recognition table

the possibility of an error in recognition. Therefore, an upper limit has been set for the size of the match node area. If the number of nodes in the match node area exceeds the upper limit, only the nodes with the highest level of similarity are allowed. The upper limit for the number of nodes in each area on this recognition table is 100.

(2) Distance between the feature vector of imperfection candidate and feature vector of nodes

The match node areas are the areas in which the distance between the feature vectors of the imperfection candidate and the nodes falls below the value set as a threshold. The distribution of the number of nodes, which is the distance d between feature vectors, is calculated for the feature vector of the imperfection candidate, X, and the feature vectors of all nodes, x, as shown in Fig. 11. Threshold value (a) is set as 50% of the minimum distance (c) (best match node) from the average distance between feature vectors (b). Node areas (d) with distances between feature vectors smaller than this are taken to be the match node area (e).

4.2.2. Imperfection recognition processing

A candidate is judged as an imperfection on the basis of the percentage of nodes recognized as imperfections (imperfection nodes), including those falling within the match node areas, as shown below.

- Imperfection node ratio: F = Number of imperfection nodes / Number of nodes in match node area
- Imperfection recognition threshold value: D

When F ≧ D, the candidate is recognized as an imperfection; when F < D, the candidate is recognized as an over-detection element. D has been set at 0.5 in this table.

Figure 12 shows an example of the recognition of an imperfection, in this case a dent. The composition of the 80 nodes making up the match node area was as follows:

- Imperfection nodes: 79
- Non-imperfection nodes: 1

This generates an imperfection node ratio (F) of 0.99. F is therefore ≧ D, fulfilling the condition for recognition as an imperfection.

4.3. Increasing the Accuracy of Imperfection Recognition

To increase the accuracy of the recognition of imperfections, the existing recognition table is able to learn the relationships of similarity between newly acquired data (new data below) and existing data, and generate a new table reflecting these relationships. As Fig. 13 shows, this processing is conducted off-line, unlike imperfection recognition processing.

To explain this processing in greater detail, feature vectors for imperfection candidates obtained during inspection (new data) are added to the existing recognition table, and the self-organizing map regroups the data. By this means, similarity between the new data and the existing data is determined and the data is realigned.

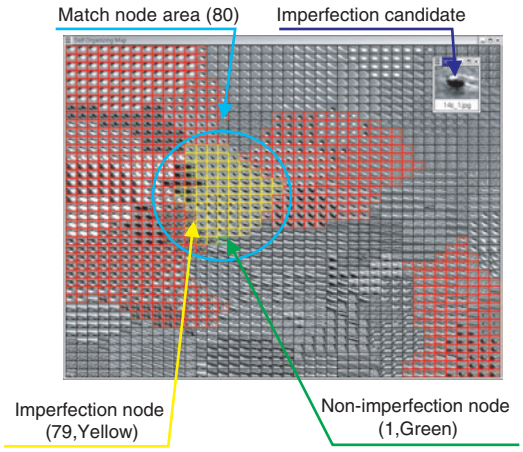


Fig. 12 Result of imperfection recognition

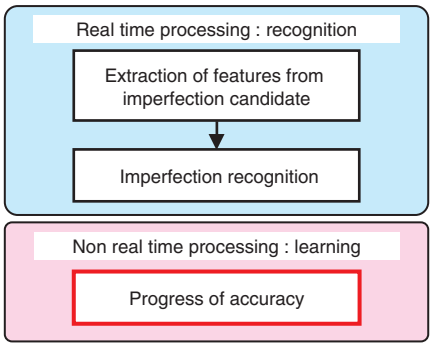


Fig. 13 Sequence of inspection for imperfection candidate

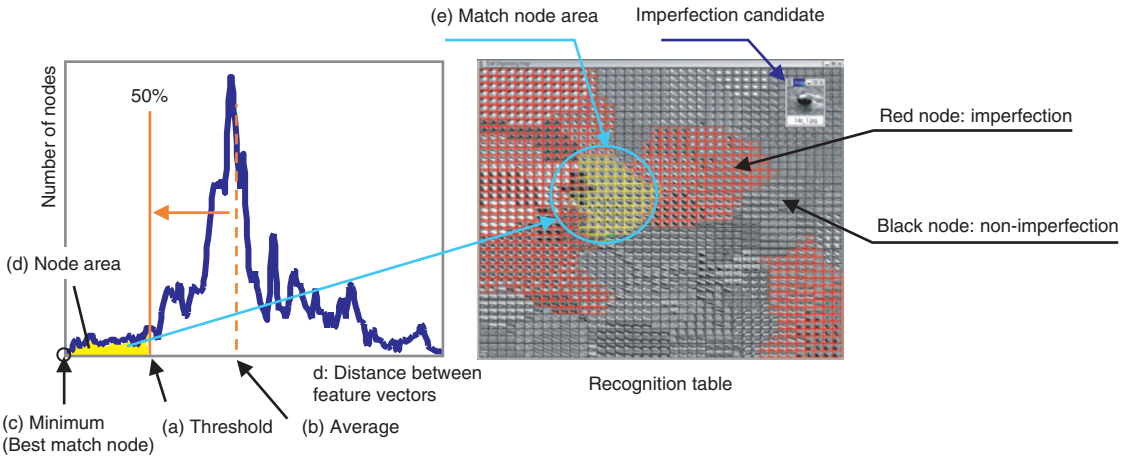


Fig. 11 Distribution of distance between feature vectors

Figure 14 shows an example of the revision of a recognition table with the addition of ten types of new data. After the revision, node areas for new data have been added to the table.

5. Inspection System

An inspection system was constructed to put the imperfection recognition method discussed thus far into practical operation. As shown in Fig. 15, the major components of this inspection system were (a) a rotation table to position the gear tooth surface being inspected, (b) a wide dynamic range CMOS camera to image the gear[4], and (c) an LED illuminator. The system also employed a PC.

6. Test Results

This section will discuss the results of tests conducted to verify the accuracy of the inspection system. Table 1 shows a comparison of inspection accuracy for one gear when the new recognition processing system is used (b) and when it is not used (a). In both cases, accuracy in recognizing imperfections was equivalent to that of visual inspection. However, there is a 40:1 difference in the rate of over-detection between cases b and a. This result indicates that there will be a difference in inspection accuracy of 180:1 per gear between case (d) on the table, when the new system is applied, and case (c), when it is not applied, assuming 40 teeth on a gear. Using the new processing system will therefore ensure correct judgment in 90% of cases (d). The remaining 10% of cases in which it is difficult to recognize an imperfection should be reinspected visually.

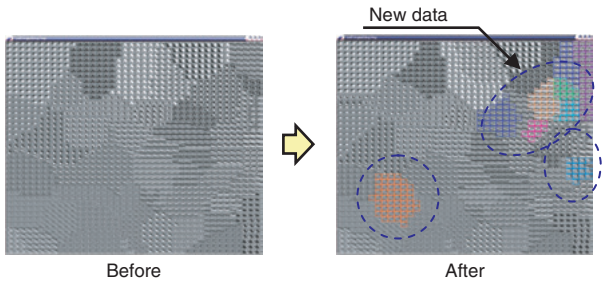


Fig. 14 Add new data to recognition table

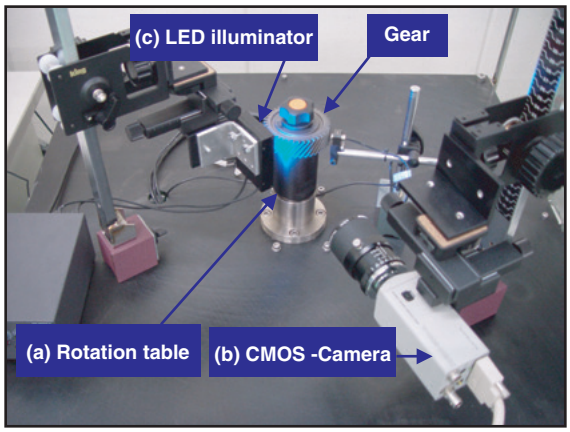


Fig. 15 Gear inspection setup

Table 1 Inspection accuracy

Recognition	Rate of over-detection: α	Inspection accuracy for one gear: A $A=100\cdot(1-\alpha/100)^N$
No use	12.4% (a)	0.5% (c)
Use	0.3% (b)	90% (d)

N : Number of teeth on one gear
$N = 40$

The results discussed above demonstrate that the inspection technology developed in this project equals visual inspection in terms of ability to recognize imperfections. The use of the system will reduce the burden on human inspectors.

7. Conclusion

A variety of new technologies have been developed for the inspection of gear tooth surfaces.

(1) A technology has been developed to define the features of imperfections on gear tooth surfaces and enable them to be recognized. This technology can identify imperfections with an accuracy equivalent to visual inspection.

(2) The development of a recognition table which “learns” the features of existing imperfections and over-detection elements has reduced the ratio of gears requiring visual inspection to approximately 10% of the former level.

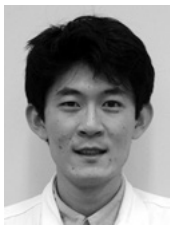
(3) Revision of the recognition table on the basis of feature vectors of imperfections and over-detection elements found during inspection has increased the accuracy of imperfection recognition.

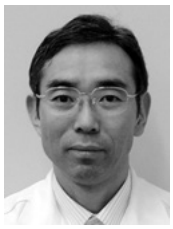
The application of these technologies has enabled the production of an inspection system which both reduces the burden of visual inspections on human inspectors and enables an increase in gear quality.

References

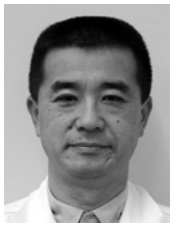
(1) Komori, M., Kubo, A., Takahashi, T., Tanaka, T., Ichihara, Komiyama, M.: Failures of Involve Gears Due to Contact of Side Edge and Creat of Tooth (1st Report, Chipping of Side Edge of Tooth and Progress to Tooth Breakage), Transactions of Japan Society of Mechanical Engineers(C), Vol. 69, No. 685, p. 273-280 (2003)
(2) Kohonen, T.: Self-Organizing Naps, Springer-Verlag (1995)
(3) Kamomoto, N., Wang, B., Omatu, S.: Quality Test of Interphones Using Two kinds of Neural Networks, Transactions of Institute of Electrical Engineers of Japan, Vol. 122-C, No. 10 (2002)
(4) Seki, H., Nakajima, A., Ohtsuka, K., Arai, H.: Observation of Welding Phenomena by Wide Dynamic Range Camera, Journal of the Japan Welding Society, Vol. 70, No. 7, p. 8-11 (2001) (in Japanese)

■ Authors ■


Junji EGUCHI


Manabu MURAKAMI


Takanao UCHIDA


Kinya FUJIWARA

Prediction of Braking Distance Temperature Dependence through Bench Test

Ayao KAWAKAMI* Hiroyuki HASE* Tetsuya MIZONE*

ABSTRACT

The temperature of the road surface is known to affect vehicle braking distance. This study demonstrated that the variation in wet braking distance with road temperature is affected by the viscoelastic properties of the tread rubber of the tires. Consequently, a study was carried out focusing on the friction and viscoelasticity of the tire tread rubber. Based on the results of this study, a method of predicting the braking distance over a wide range of road surface temperatures was established from the results of a viscoelastic characteristics bench testing of the tire tread rubber and also the results of a braking distance test performed using an actual vehicle at arbitrary road surface temperatures.

1. Introduction

Braking distance performance is an important measure of active safety performance. The results of braking distance performance have been publicized in Japan New Car Assessment, and preparations for testing are being carried out in the U.S. and Europe as well.

Also, braking distance is evaluated independently in automobile magazines throughout the world, and the results of these evaluations are of interest to consumers.

The factors shown in Fig. 1 are considered to have a major effect on the braking distance[1].

Some of these impacting factors, including the method of human operation, the measuring system, the vehicle specifications and the road profile can be maintained constant to some extent by controlling the test method. However, in order to understand the effect of the road surface temperature condition on the braking distance, it is necessary to perform an actual vehicle test from a low temperature range to a high temperature range.

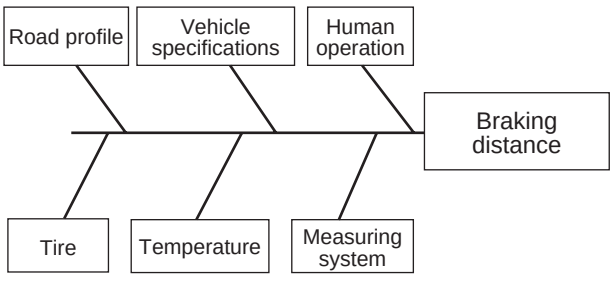


Fig. 1 Cause and effect diagram for braking distance

In order to understand the effect of the road surface temperature on the braking distance, it is necessary to perform multiple tests using an actual vehicle over a long period of time, so it is difficult to make an evaluation within a limited period.

In this research, attention was focused on the viscoelastic characteristics of the tire tread rubber under bench test conditions, and a method of predicting the braking distance which varies with the road surface temperature from the minimum test results obtained using an actual vehicle was developed in order to provide a method of more readily evaluating the performance of the tires.

2. Dependence of Braking Distance on Road Surface Temperature for Different Tires

Figure 2 shows the change in the braking distance with change in temperature of a dry road and a wet road. As shown here, with some tires the braking distance varies with the road surface temperature, so it is not possible to cover all conditions of use in the market by simply evaluating the tires in a certain temperature region.

The tests were carried out on the Multipurpose Track of the Honda R & D Tochigi Proving Ground, and the test method used was based on Japan New Car Assessment Program (J-NCAP: an automobile assessment published by the automobile accident countermeasure organization of an independent administrative corporation). Regarding the road surface temperature, however, tests were also performed at temperatures that exceeded the J-NCAP

* Tochigi R&D Center

upper and lower limit values. The test vehicle used was an FF (front engine, front wheel drive) 2.0 L minivan.

Figure 3 shows the braking distance results obtained for a wide range of road surface temperatures using the same vehicle, in order to confirm the dependence of braking distance on road surface temperature for different tires on a wet road surface. Also, the tires used in the test are shown in Table 1.

The tests shown in Fig. 3 were carried out on the Multipurpose Straight Track of the Japan Automobile Research Institute, and the test method used was based on J-NCAP. Regarding the road surface temperature, however, tests were also performed at temperatures that exceeded the J-NCAP upper and lower limit values. The test vehicle used was an FF 1.5 L passenger vehicle.

From these results, it was confirmed that the dependence of braking distance on road surface temperature tends to vary from one tire to another.

The braking distance with respect to road surface temperature for tire A is short at low temperature, and increases in the high temperature region. On the other hand, the variation in the braking distance with respect to road surface temperature for tire B is less than that of tire A, but the braking distance increases in both the low temperature region and the high temperature region. Tire C is ranked mid-way between tires A and B. Like tire A, the braking distance increases in the high temperature range, however this tendency is less than that of tire A.

Test track: Honda R&D.,Ltd Tochigi Proving Ground
Test method: J-NCAP (with change to specified road surface temperature)
Test vehicle: FF 2.0L Minivan

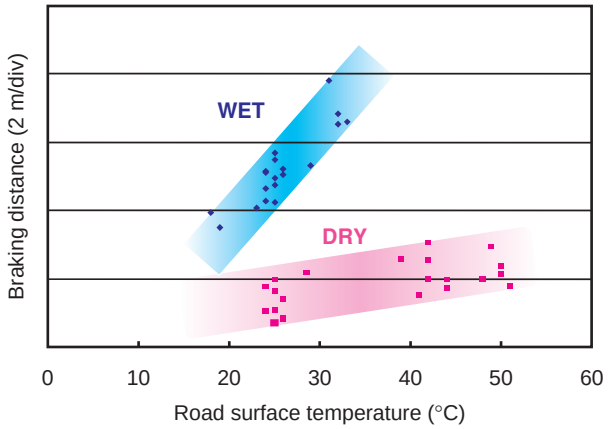


Fig. 2 Wet and dry braking distance vs road surface temperature

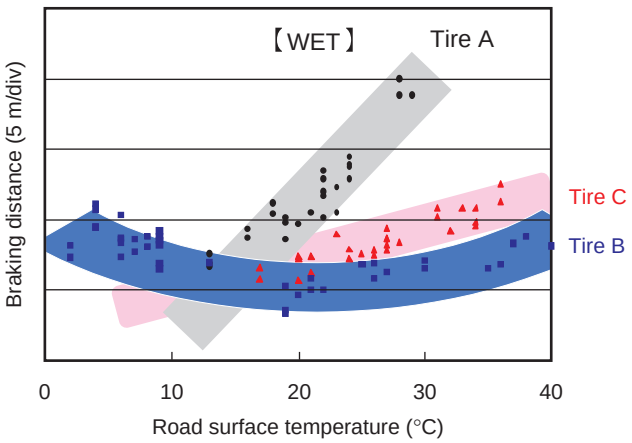


Fig. 3 Road temperature dependence of braking distance by tire

Table 1 Tire characteristics

	Tire A	Tire B	Tire C	Tire D	Tire E
Tread compound	1	2	3	4	5
Construction	a	b	c	d	d
Tread pattern	Ⅰ	Ⅱ	Ⅲ	Ⅳ	Ⅳ
Tire size	185/70 R14	185/70 R14	185/70 R14	185/70 R14	185/70 R14

The three types of tires shown in Fig. 3 differ from each other in tread rubber, construction and pattern. In order to determine which of these elements has an effect on the dependence of braking distance on road surface temperature, braking distance tests were performed using tires of different tread rubber, tires of different construction, and tires of different patterns.

As a result of performing braking distance tests on an actual vehicle, it was found that differences in tread rubber had the effect on the dependence of braking distance on road surface temperature.

Figure 4 shows the braking distance results for tires D and E, which were of the same pattern and size but differed only by tread rubber.

Tires D and E, which differed only in tread rubber, exhibited different dependence of braking distance on road surface temperature, and it was found that the temperature dependence of braking distance varied with the type of tread rubber used.

Consequently, it was confirmed that the tread rubber had an effect on the temperature dependence of braking distance.

3. Examination of Mechanism

3.1. Friction and Viscoelasticity of Tread Rubber

The friction force of the tire is expressed as the sum of the friction force by hysteresis of the tread rubber F_H and the friction force by adhesion F_A (Fig. 5).

The hysteresis friction force F_H is the friction force due to the energy loss generated when the rubber undergoes relatively large deviation due to irregularities in the road surface. The larger the phase delay (hysteresis loss: tan δ) due to deformation of the rubber, the greater is the hysteresis friction force F_H.

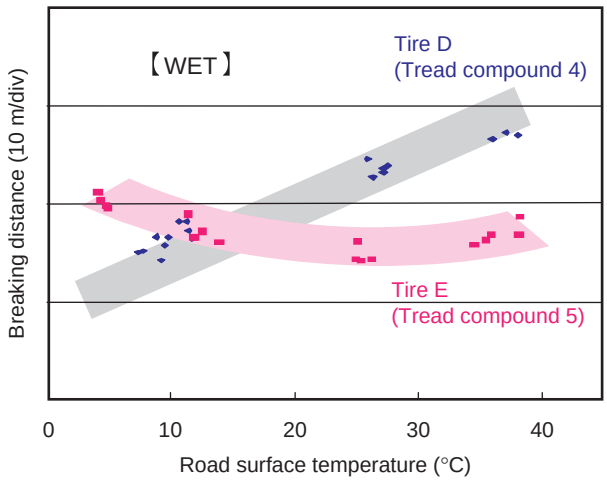


Fig. 4 Road temperature dependence of braking distance by tread compound

Because the braking distance is inversely proportional to the braking force, it is possible to assume that following equation holds, where the braking distance due to the friction force by hysteresis F_H is defined as X_H.

$$X_H \propto 1/F_H \propto 1/\tan\delta \quad (1)$$

The adhesion friction force F_A is generated by energy loss resulting from adhesion between the tread rubber and the road surface aggregate (intermolecular force).

Consequently, the adhesion friction force F_A increases in proportional to the actual area of contact of the tire[2].

Adhesion friction force $F_A = M$ (Contact area) • S (Tread rigidity per unit area)

From a microscopic viewpoint, the contact area M is considered to be related to the modulus of elasticity E^* of the rubber material in a micro-deformed state that follows the surface irregularities of the road surface aggregate (Fig. 5), and in the low temperature region the actual contact area changes in inverse proportion to the increase of E^*. Therefore, if the braking distance due to the adhesion friction force F_A is defined as X_A, it can be assumed that the following equation holds in the low temperature region.

$$X_A \propto 1/F_A \propto 1/M \propto E^* \quad (2)$$

3.2. Prediction Equation

As a result of studying the relationship between braking distance and tread rubber friction, an equation for predicting the dependence of braking distance on road surface temperature was determined.

It is possible to express the change of braking distance with road surface temperature ΔX as the sum of the change of braking distance ΔX_H due to the change in the hysteresis friction force F_H with road surface temperature and the change of braking distance ΔX_A due to the change in the adhesion friction force F_A with road surface temperature.

$$\Delta X = \Delta X_H + \Delta X_A$$

In addition, from previous investigation[3] it is known that the braking distance on a wet road is related to tan δ in the vicinity of 0 °C from the tire tread rubber viscoelasticity characteristics test.

This means that the greater the value of tan δ in the vicinity of 0 °C in the viscoelasticity test, the larger is the hysteresis friction force F_H, and the shorter is the braking distance on a wet road.

Concerning the road surface temperature dependence of the braking distance, it was considered that the increase in the braking distance in the high temperature region was due to the effect of the temperature gradient of tan δ in the vicinity of 0 °C in the viscoelasticity test, and thus the following equation was assumed.

$$\Delta X_H = f(t) \times a \quad (3)$$

Where,
a: Gradient of tan δ in the vicinity of 0 °C
f(t): Linear expression of road surface temperature t

f (t) was assumed to be a linear expression with respect to road surface temperature t because the braking distance showed a tendency to increase in proportion to the increase of road surface temperature.

Next, it was considered that the magnitude of the modulus of elasticity E^* in the vicinity of 0 °C was a factor that caused the braking distance to increase in the region of low road surface temperature, and the following equation was assumed.

$$\Delta X_A = g(t) \times b \quad (4)$$

Where,
b: E^* in the vicinity of 0 °C
g(t): Expression of 1/t

Also, g(t) was assumed to be the function 1/t with respect to road surface temperature t because of the fact that the braking distance increases in inverse proportion to the road surface temperature in the low temperature region.

Consequently, if the braking distance to be predicted at road surface temperature ta is defined as X_a, it can be expressed by the following equation in which the change in the braking distance due to the road surface temperature is added to the reference braking distance X_c at road surface temperature t_c.

$$X_a = \Delta X_H + \Delta X_A + X_C \quad (5)$$

Here, it was assumed that the reference braking distance X_c was measured using an actual vehicle because it varies depending upon the vehicle specifications and tire size. In other words, it can be expressed using the following equation.

$$X_a = f(t) \times a + g(t) \times b + Xc \quad (6)$$

3.3. Relationship between Road Surface Temperature Dependence and Viscoelasticity Characteristics

In order to verify the trend of tan d and E^* of tire D and tire E used in Fig. 4, test pieces were cut from the tread rubber, and the viscoelasticity characteristics were measured using a spectrometer (Fig. 6).

The results of the viscoelasticity test are shown in Fig. 7 and Fig. 8.

In the case of tire D shown in Fig. 4, the braking distance increases more or less in proportion to the increase in the road surface temperature. It is thought that this is because, as shown in Fig. 7, tan δ in the vicinity of 0 °C which has a correlation relationship with the hysteresis friction force F_H of tread rubber (4) falls as the temperature rises from the vicinity of 0 °C.

The braking distance of tire D increases more than that of tire E when the road surface temperature is between 20 °C and 30 °C. This is considered to be due to the fact that the slope of tan δ in the vicinity of 0 °C in the case of tread rubber (4) is greater than that of tread rubber (5).

On the other hand, the braking distance of tire E shown in Fig. 4 increases in inverse proportion to road surface temperature, particularly in the low temperature region.

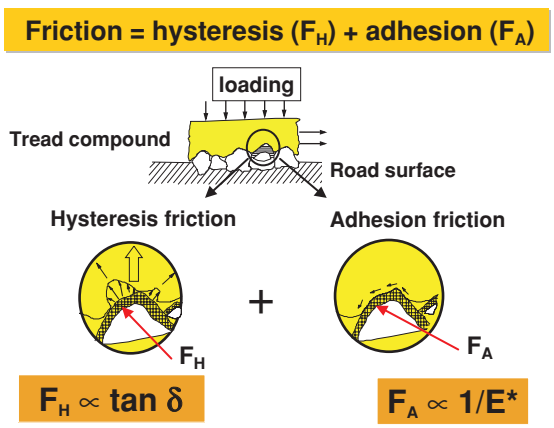


Fig. 5 Friction of tread compound

It is thought that this is because although the tread rubber maintains a stable contact area in the region where the road surface temperature is at least a certain value, the E^* of the tread rubber rises as the temperature falls, decreasing the contact area and causing the adhesion friction force to decrease, as shown in Fig. 8.

It is also considered that the tendency for the braking distance of tire E to increase in the low temperature region is greater than that of tire D because of the fact that E^* in the low temperature region in the case of the tread rubber (5) is greater than that of tread rubber (4).

Using the braking distance results obtained for tires D and E and also tan δ and E^* of tread rubbers (4) and (5) obtained using the bench viscoelasticity spectrometer, multiple correlation analysis using the method of least squares was performed. From these results, the coefficients for the prediction equation were set, and the prediction equation was determined.

By using the resulting prediction equation, the correlation between results of predicting the braking distance on road surface temperature for other roads based on the braking distance obtained using an actual vehicle at a road surface temperature of 10 °C for tire D and tire E, and the actual braking distance, was confirmed (Fig. 9 and Fig. 10). From these results, the proposed equation for predicting the temperature dependence of braking distance based on tread rubber viscoelasticity characteristics was verified.

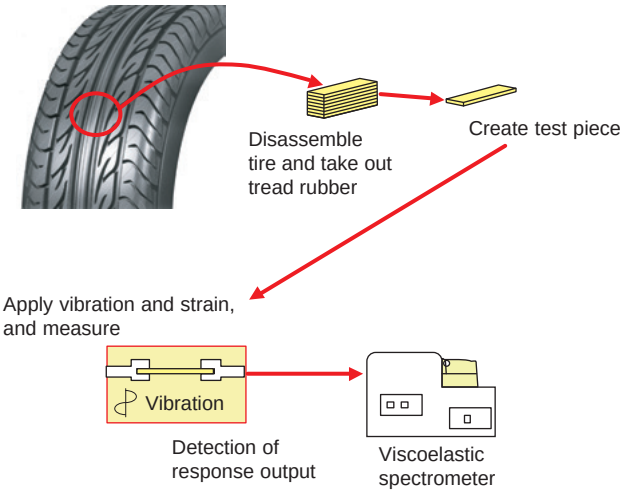


Fig. 6 Measurement method for viscoelasticity of rubber

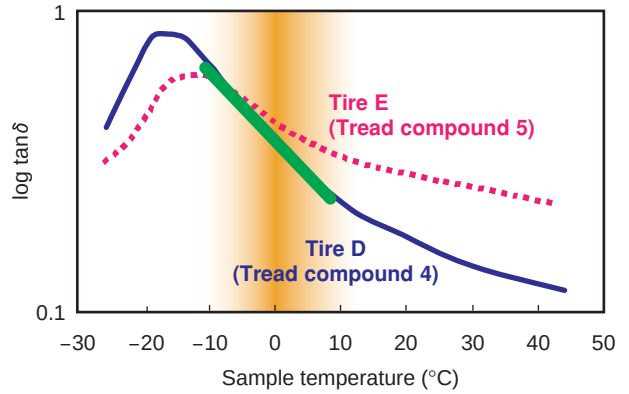


Fig. 7 Viscoelasticity measurements for Tires D and E

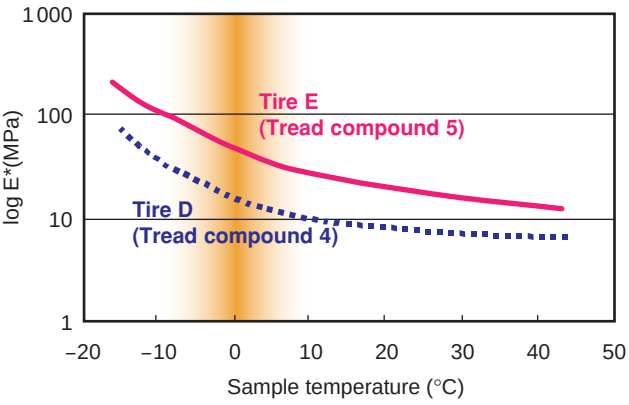


Fig. 8 Viscoelasticity measurements for Tires D and E

4. Results of Application of the Prediction Method

In the development of the prediction equation, two kinds of tread rubbers were used. A verification concerning the prediction for a different rubber compound was carried out.

A verification concerning prediction with regard to the tread pattern, vehicle, and tires (size and construction) was also performed.

The test conditions are shown in Table 2.

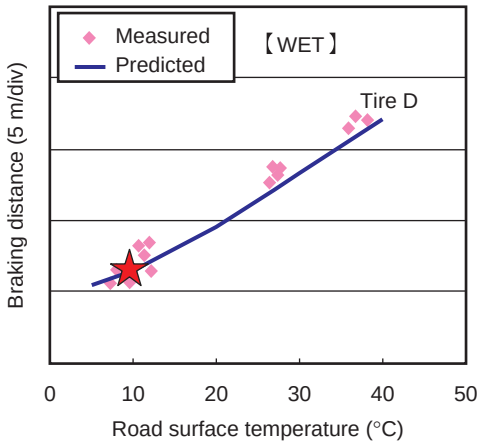


Fig. 9 Road surface temperature dependence of Tire D Prediction based on results of measurement at 10°C

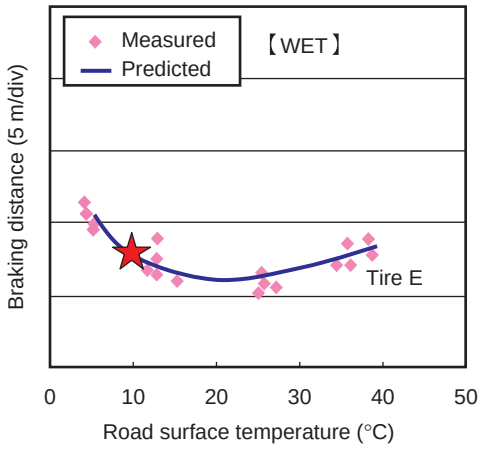


Fig. 10 Road surface temperature dependence of Tire E Prediction based on results of measurement at 10°C

Table 2 Tire characteristic

	1	2		3	
	FF 1.5 L Passenger	FF 1.5 L Passenger	FF 1.5 L Passenger	FF 0.66 L Passenger	FF 2.4 L Minivan
	Tire F	Tire G	Tire H	Tire I	Tire J
Tread Compound	6	4	5	7	8
Construction	d	d	d	e	f
Tread pattern	Ⅳ	Ⅴ	Ⅴ	Ⅵ	Ⅶ
Tire size	185/70R14	185/70R14	185/70R14	155/65R13	215/60R16

4.1. Verification According to Differences between the Tread Rubbers

Tire F, which consists of tire D with the tread rubber alone changed to (6), was fabricated.

Figure 11 shows the results predicted from the actual vehicle test with Tire F for a road surface temperature of 10 °C and the results of testing the temperature dependence on an actual vehicle.

Thus, there is good agreement with the results obtained using an actual vehicle, even when the tread rubber is changed.

4.2. Verification According to Difference in Tread Pattern

Tires G and H, which consist of tires D and E with the tread pattern alone changed, were fabricated.

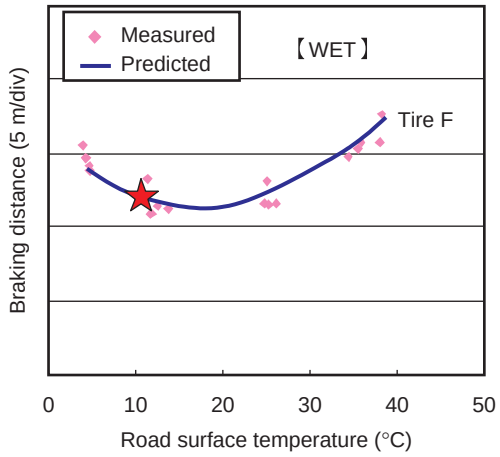


Fig. 11 Road surface temperature dependence of Tire F Prediction based on results of measurement at 10°C

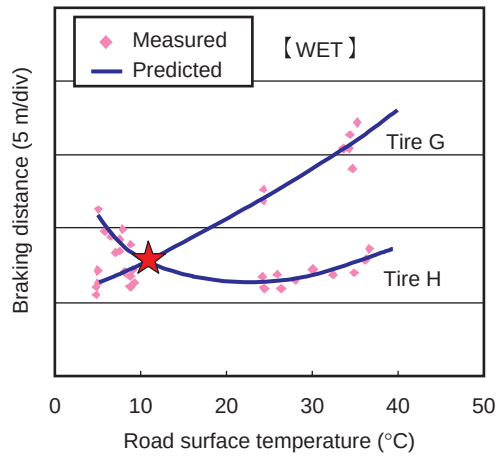


Fig. 12 Verification of accuracy by varying tread pattern Prediction based on results of measurement at 10°C

Figure 12 shows results predicted from the results of the actual vehicle test with Tire G and H for a road surface temperature of 10 °C and the results of testing the temperature dependence on an actual vehicle.

Thus, there is good agreement with the results obtained using an actual vehicle, even when the tread pattern is changed.

4.3. Verification According to Differences between Vehicles and Tires

Finally, a vehicle verification was performed using an FF minivan and an FF light passenger vehicle.

Figures 13 and 14 show the results predicted from the results of the actual vehicle test for a road surface temperature of 10 °C and the results of testing the temperature dependence on an actual vehicle.

Thus, there is good agreement with the results obtained using an actual vehicle, even for different tires (tread rubber, construction, pattern and size).

In the above way, in the verification of the differences between tread rubbers, tread patterns, vehicles and tires (size and construction) as well, it was found that the results of the braking distance test performance using an actual vehicle agreed with the predicted results from the viscoelasticity characteristics of tread rubbers, thus verifying the versatility of the prediction equation.

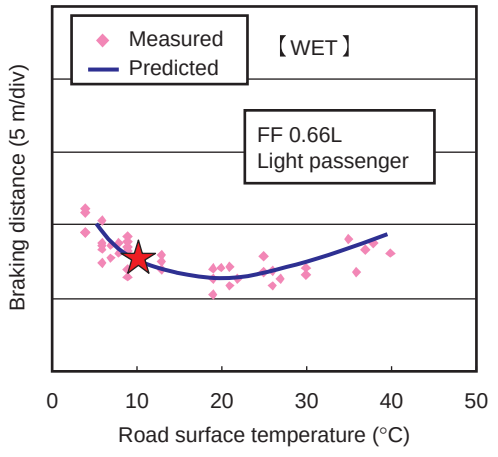


Fig. 13 Verification of by varying tires and vehicles Prediction based on results of measurement at 10°C

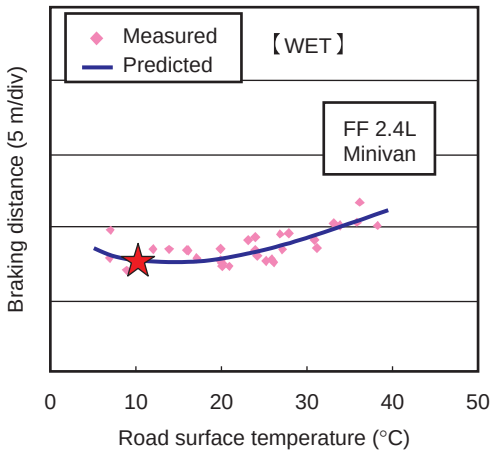


Fig. 14 Verification of by varying tires and vehicles Prediction based on results of measurement at 10°C

5. Conclusion

The following facts were established as a result of the foregoing research.

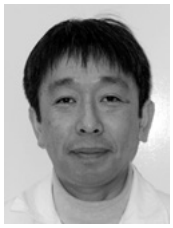
1) As a result of measuring the braking distance according to tire difference over a wide range of road surface temperatures using the same vehicle, it was possible to prove that the dependency of the braking distance on road surface temperature differed from one tire to another. In addition, it was found that the tire tread rubber was the dominant factor that determined the road surface temperature dependence of the braking distance.
2) A method of predicting the braking distance over a wide range of road surface temperatures was established from the results of a viscoelastic characteristics bench testing of the tire tread rubber and also the results of a braking distance test performed using an actual vehicle at arbitrary road surface temperatures.

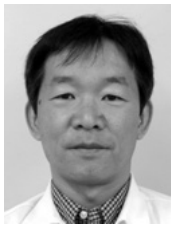
References

(1) Japan Automobile Research Institute: Brake Seinousiken ni Eikyou wo Ataeru Youin ni Kansuru Chousa, p. 1-9 (1999) (in Japanese)
(2) Kamo, S., Sakurai, M., Awabi, I., Mitsubashi, K., Amino, S., et al.: Karyuu Gomu no Katasa Sokuteiji niokeru Hyoumen Hizumi to Masatsu no Kanrensei, Collected Works of the 51st Rheology Conference, p. 309 (2003) (in Japanese)
(3) Muraoka, K.: Viscoelastic Properties of Rubber Compounds for Tire Application, Journal of The Society of Rubber Industry, 74, p. 6 (2000) (in Japanese)

■ Authors ■


Ayao KAWAKAMI


Hiroyuki HASE


Tetsuya MIZONE

Study of Fuel Tank Sloshing Noise Prediction

Tohru WAKO*

ABSTRACT

The development of technology to predicting sloshing noise from a fuel tank was approached from the aspects of simulation and experiment. First, an acceleration and deceleration from a vehicle was applied to a bench-mounted fuel tank containing fuel to generate a sloshing noise, and the physical parameters that were closely correlated with the sloshing noise were extracted. Next, computer simulation using an explicit transient solution method was performed to reproduce the fluid motion behavior in the tank, and a study was performed whether or not the physical parameters obtained from the experiment was useful for predicting sloshing noise. As a result, it was confirmed that the sloshing noise was caused by fuel striking localized areas of the inside wall of the tank. It was found that the occurrence of sloshing noise could be predicted by analyzing the impulsive pressure rise at the inside wall of the tank. A comparison of the computer simulation results with the experimental results showed that the experimentally observed impulsive pressure rise could be accurately reproduced by simulation as well, thus enabling the occurrence of fuel sloshing noise to be predicted.

1. Introduction

In order to enhance quietness inside a passenger vehicle, it is important to address noise reduction of all the relevant functional parts, including the fuel tank. For this reason, demands for reduced fuel sloshing noise are increasing year by year.

The conventional fuel tank made of steel sheet has baffles spot-welded to it for reducing sloshing noise. The specifications of the tank were determined by trial and error through evaluation using an actual vehicle. However, along with the increasing use of plastic fuel tanks that are difficult to install with baffles, it has become necessary to consider the basic profile of the tank that minimizes the occurrence of sloshing noise, at the initial stage of development. In addition, efforts are being made to reduce the number of prototype vehicles and shorten the development period by using a computer, so simulation technology for predicting the occurrence of fuel sloshing noise is being increasingly demanded.

In order to predict sloshing noise, it is necessary, first of all, to reproduce the fluid motion behavior of the fuel in the tank using a computer. This was previously considered to be extremely challenging because the behavior of the fluid is complicated. However, along with the evolution of analysis technology in recent years, several analysis codes which can handle the behavior of a fluid that has a free surface have become commercially available, and there are also reports of cases of analysis[(1),(2)]. These reports state that by using simulation to visualize the flow inside the tank it is possible to acquire general guidelines for reducing sloshing noise. However, there is little mention of technology for directly predicting the occurrence of noise by simulation. The reason for this is that because the understanding of the phenomenon is insufficient, the mechanism whereby the motion of the fuel in the tank generates sloshing noise has not been adequately investigated. In this research, first a bench test was performed to extract the physical parameters that are closely correlated with the generation of sloshing noise, and then these physical parameters were

* Tochigi R&D Center

reproduced by computer simulation, and finally the two sets of results were compared with each other in order to develop technology for predicting the occurrence of sloshing noise by computer simulation.

2. Mechanism of Generation of Sloshing Noise

The following two hypotheses concerning the mechanism of generating of sloshing noise are conceivable. One is that the air in the fuel tank vibrates due to agitation of the fuel, generating noise which passes through the wall of the tank to the outside, and the other is that the surface of the inside wall of the tank vibrates when struck by the fuel, causing noise to be generated. Both of these phenomena coexist, however, from the viewpoint of simulation it is very important to establish which of them is dominant. If the former is dominant, it is necessary to simulate the process where the fluid is agitated causing the air in the vicinity to vibrate. In this case, however, it is difficult to predict the vibration of the air due to the interaction between the air and the liquid. Conversely, if the latter is dominant, it is possible to perform simulation by calculating the pressure rise when the fuel in the tank strikes the wall of the tank.

3. Bench Test

3.1. Test Equipment

A bench test was carried out to determine which of the above two phenomena has the greater effect. Figure 1 shows the concept of the test equipment.

Microphones were installed at a point 300 mm above the tank and also inside the tank, in order to compare the level of the noise inside and outside the tank. In addition, pressure sensors were installed at 10 points inside the tank in order to measure the pressure when the fuel in the tank strikes the tank wall, and also acceleration sensors were installed on the outside of the tank in order to measure the vibration of the wall surface.

The test equipment for applying motion to the tank consisted of a frame made of steel pipes suspended by a wire. The tank was mounted on this frame and rocked back and forth. Figure 2 shows the overall construction of the equipment.

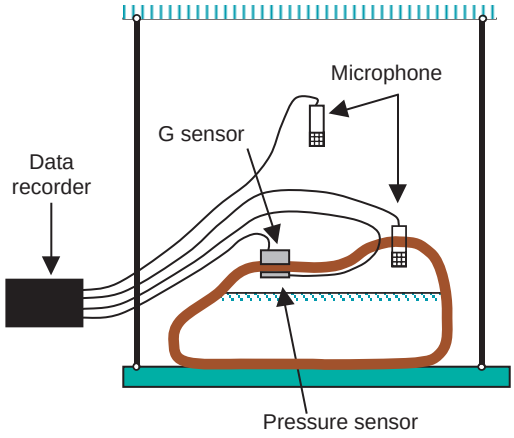


Fig. 1 Concept of equipment

The following procedure for applying acceleration and deceleration to the tank was set. First, the tank is pulled to the rear until it touches the stopper of Fig. 3, and is then left motionless until the surface of the liquid in the tank comes to rest. Next, the tank is released, causing it to move forward while accelerating. It continues to move forward past the bottom center position. A rope is tied to the rear of the frame supporting the tank in order to regulate the stroke of the frame. Consequently, when the tank moves forward and exceeds a certain limit, this rope becomes taut, applying a deceleration to the tank. When the rope is stretched to its limit, the tank starts to move backward. The length of the rope has been adjusted in advance so that the maximum deceleration reaches 0.3 G, enabling the same deceleration to be generated repeatedly.



Fig. 2 Laboratory equipment

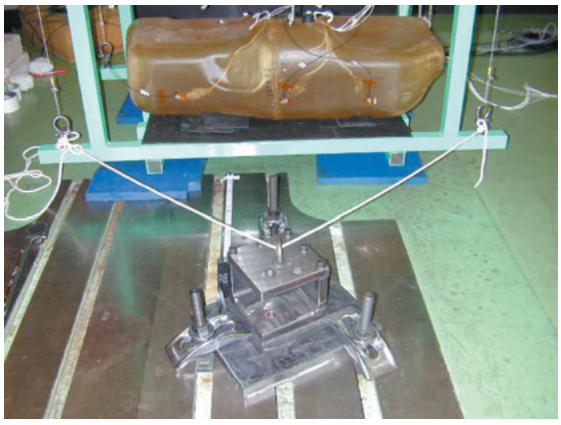


Fig. 3 Stopper

3.2. Test Results

Figure 4 shows a graph of the noise measured from a height of 300 mm above the tank (hereafter called “evaluation point noise”). The level of the fuel in the tank at this time is 40 liters. The graph has five large peaks that correspond to the timing at which the surface of the sloshed fuel alternately reaches the front and rear walls of the tank.

Here, a detailed study of one of these peaks is carried out. Figure 5 shows the evaluation point noise, Fig. 6 the noise inside the tank, and Fig.7 the vibration of the tank wall at the location nearest the evaluation point. In each of these graphs, attention is focused on the instant at which the peak rises, and the time axis is indicated in enlarged form. In all three graphs, one graduation along the horizontal axis is 0.05 second. By comparing these three graphs with each other, it can be seen that there is strong correlation between the evaluation point noise and the vibration of the surface of the tank wall, but that there is no correlation between the noise inside the tank and the other two graphs. For this reason, it can be considered that the noise inside the fuel tank has little effect on the evaluation point noise. In the case of both of the hypotheses mentioned in Section 2, noise generated due to vibration of the inside of the tank wall is ultimately transmitted to the evaluation point, so it follows as a matter of course that there is correlation between wall surface vibration and the evaluation point noise. However, because no correlation with the noise inside the tank can be seen, it can be considered that the cause of vibration of the tank wall surface lies elsewhere.

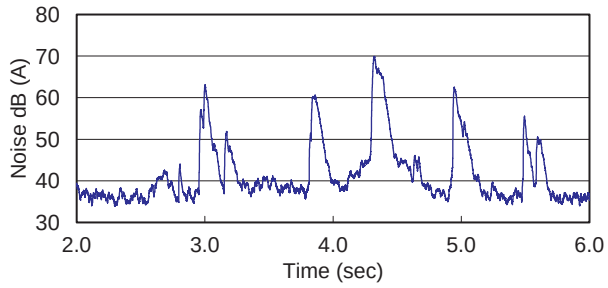


Fig. 4 Sloshing noise at evaluation point

Next, attention is focused on the relationship between the pressure at the inside wall of the tank and the evaluation point noise. Figure 8 shows a comparison of the time history of the evaluation point noise and the wall surface pressure at each point. This figure shows that the pressure on the inside wall of the tank rises abruptly when the evaluation point noise rises. From this fact,

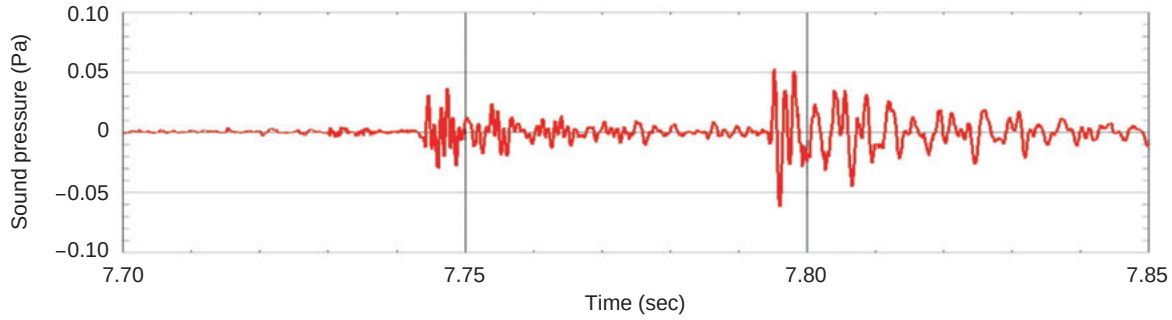


Fig. 5 Sound pressure (Outside of tank)

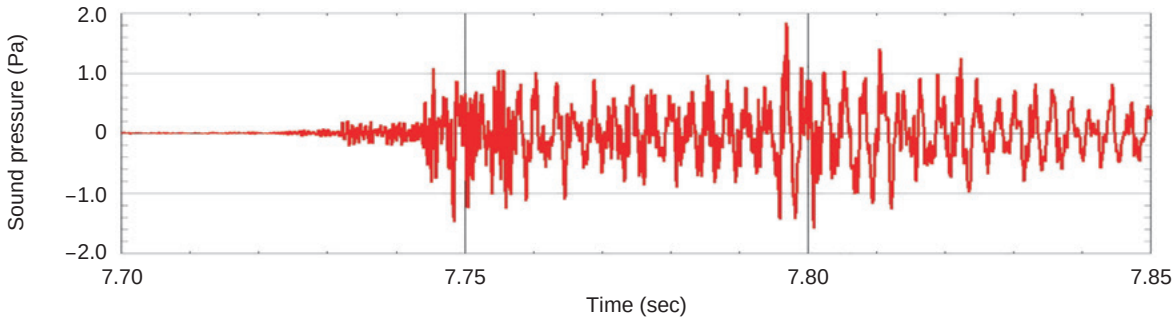


Fig. 6 Sound pressure (Inside of tank)

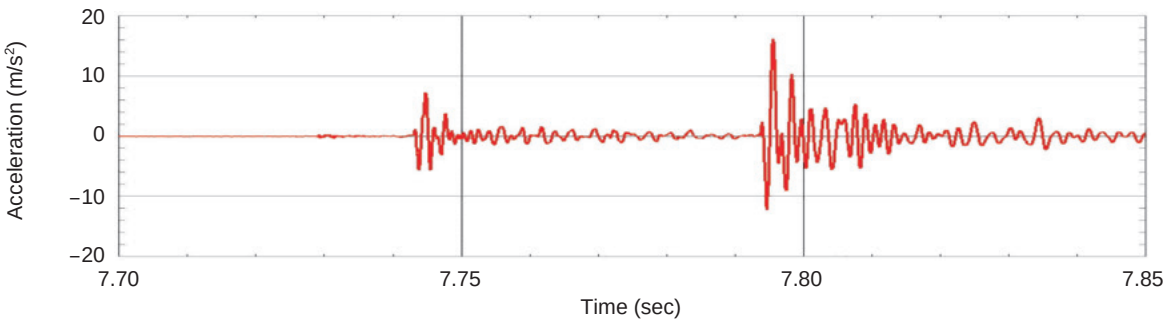


Fig. 7 Vibration (Tank surface)

it can be inferred that evaluation point noise occurs when the tank wall surface is vibrated as a result of the liquid in the tank striking the wall surface. The difference in the detected pressure rise from one measurement point to another indicates that the phenomenon whereby the liquid strikes the inside wall of the tank is extremely localized. In the simulation, when the motion of the liquid surface is visualized, permitting a detailed observation of the points where the pressure rise at the wall surface can be conducted, it is possible to verify the phenomenon whereby the fuel strikes the wall surface, thus bearing out the above inference. When the pressure inside the

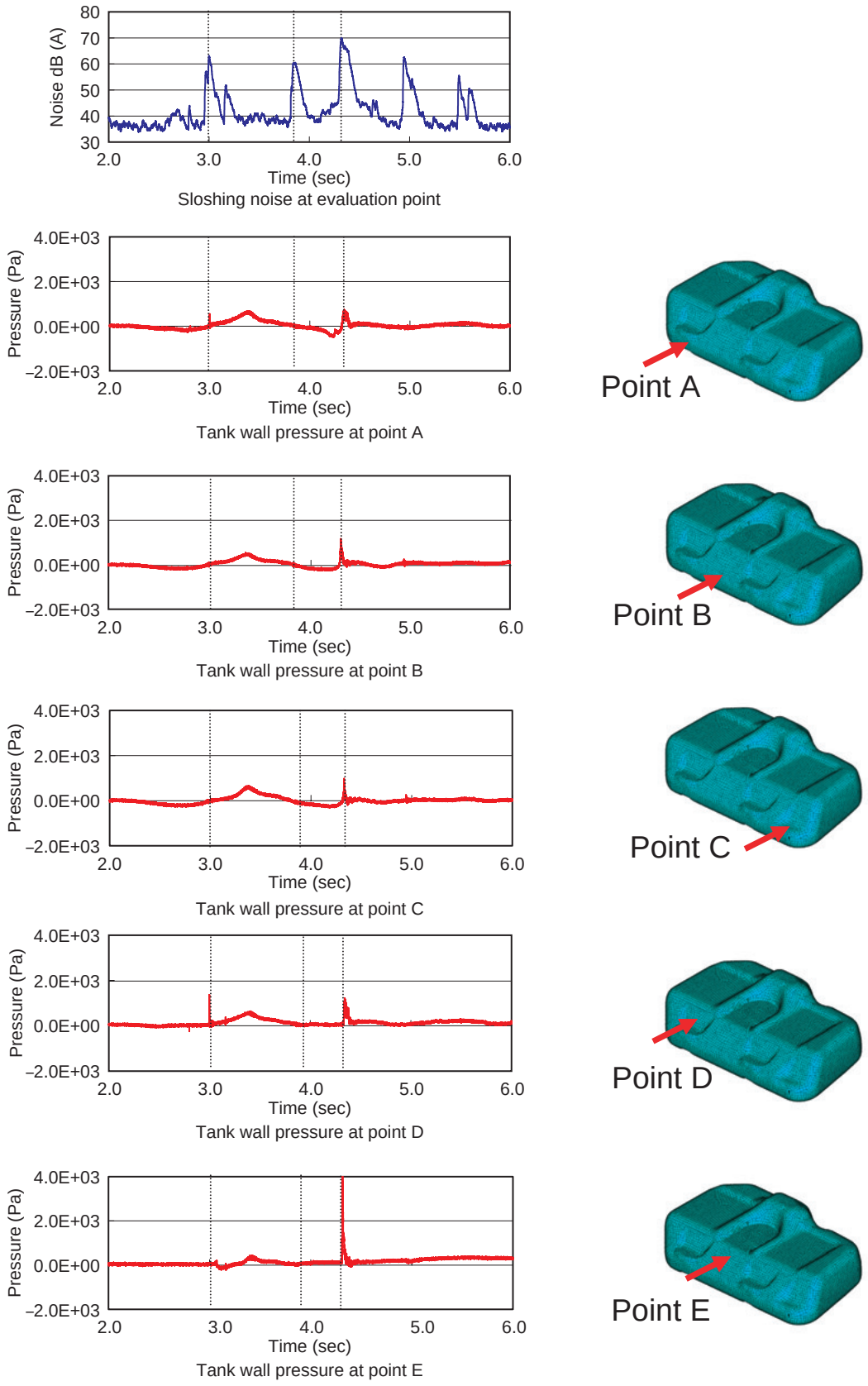


Fig. 8 Measured tank wall pressure

tank rises slowly, the phenomenon whereby the evaluation point noise reaches a peak corresponding to the pressure rise is not seen, so it can be considered that the sloshing noise is generated only when the pressure rises impulsively over a short period. Incidentally, a pressure peak, such as that corresponding to the second noise peak, sometimes fails to appear at any measurement point whatever when the evaluation point noise is generated. It is thought that this is due to the occurrence of a pressure rises at a point other than the measurement point.

4. Computer Simulation

Generally, the entire internal volume of a fuel tank of an automobile is not filled with fuel, but instead is always occupied simultaneously by air and liquid. Therefore, in order to simulate the sloshing of the fuel in the tank, it is necessary to reproduce the behavior of a fluid that has a free surface. Also, because both a structure (tank) and a fluid (fuel) exist in the system, and exert an effect on each other, it is necessary to perform structure-fluid interaction analysis. In this research, MSC Dytran, which enables analysis of a fluid that has a free surface and also permits structure-fluid interaction analysis, was used.

4.1. Making a Model

In the structure-fluid interaction analysis, an Euler element was applied for the fluid part, and a Lagrange element for the structural part, and a method in which they were superimposed on each other was used. Here, an Euler element is a type of element that is fixed in a space and contains the object that moves through it. It is suitable for analyzing fluids. A Lagrange element, on the other hand, is a type of element that undergoes deformation motion according to the deformation motion of the object. It is suitable for analyzing a structure. These types of elements are coupled to each other by a method called General Coupling by MSC Dytran. This method defines each of the Euler and Lagrange elements entirely independently of each other, and then superimposes them on each other. Regarding the coupling between the Euler and Lagrange elements, the Lagrange element functions as a wall that separates the fluid, as seen from the Euler element, and the reaction from the fluid is transmitted to the structure via this boundary surface, as seen from the Lagrange element[3].

Figure 9 shows an example of a finite element model that was used in this research. When the initial liquid surface height is specified in this finite element model, a fluid is defined in the region surrounded by the tank and the initial liquid surface, and it is possible to reproduce the way in which the liquid moves along with the motion of the tank, which constitutes the boundary surface with the fluid. By assigning the motion of the tank as time history data of the motion velocity, it is possible to reproduce any arbitrary motion.

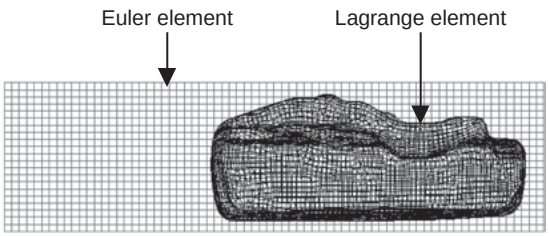


Fig. 9 Finite element model

4.2. Confirmation of Reproducibility

In order to confirm that the simulation could reproduce the motion of an actual liquid surface, the tank was made of transparent acrylic plastic to render it visible inside, and the motion of the liquid surface obtained from simulation was compared with that obtained experimentally. The results are shown in Fig. 10. It can be seen that the motion of the liquid surface can be reproduced extremely well by simulation.

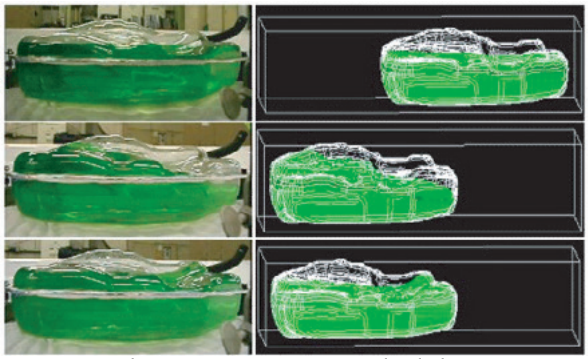


Fig. 10 Liquid surface behavior

5. Comparison with Experimental Results

A comparison of whether or not the pressure peaks observed at the inside wall of the tank during the bench test could be observed in the simulation was performed. In order to accurately reproduce the condition of the bench test, the value of the tank velocity measured during the bench test was used as the input value for the simulation. The tank inside wall pressure was output at the same points as those to which pressure sensors had been applied for the bench test, and the values obtained were compared with the measured values for the bench test. Figure 11 shows a comparison of the measured time history waveform and the results of simulation with the evaluation point noise when pressure is applied to the tank wall surface. It was found that the simulation results at point D agreed closely with the measured results, and also that the sharp pressure peak that appeared during the bench test could be observed using simulation as well. In addition, even at a point, such as point F, where no pressure peak was observed in the bench test because there were no measurement points, the pressure peak corresponding to the evaluation point noise was observed in the simulation, thus proving that the hypotheses were correct. In the simulation, it is possible to set many more measurement points within the range of the computer's ability compared to when performing actual measurement. Consequently, by appropriately allocating the measurement points, it is possible to reproduce all of extremely localized pressure peaks. This means that it is now possible to accurately predict the occurrence of sloshing noise by simulation.

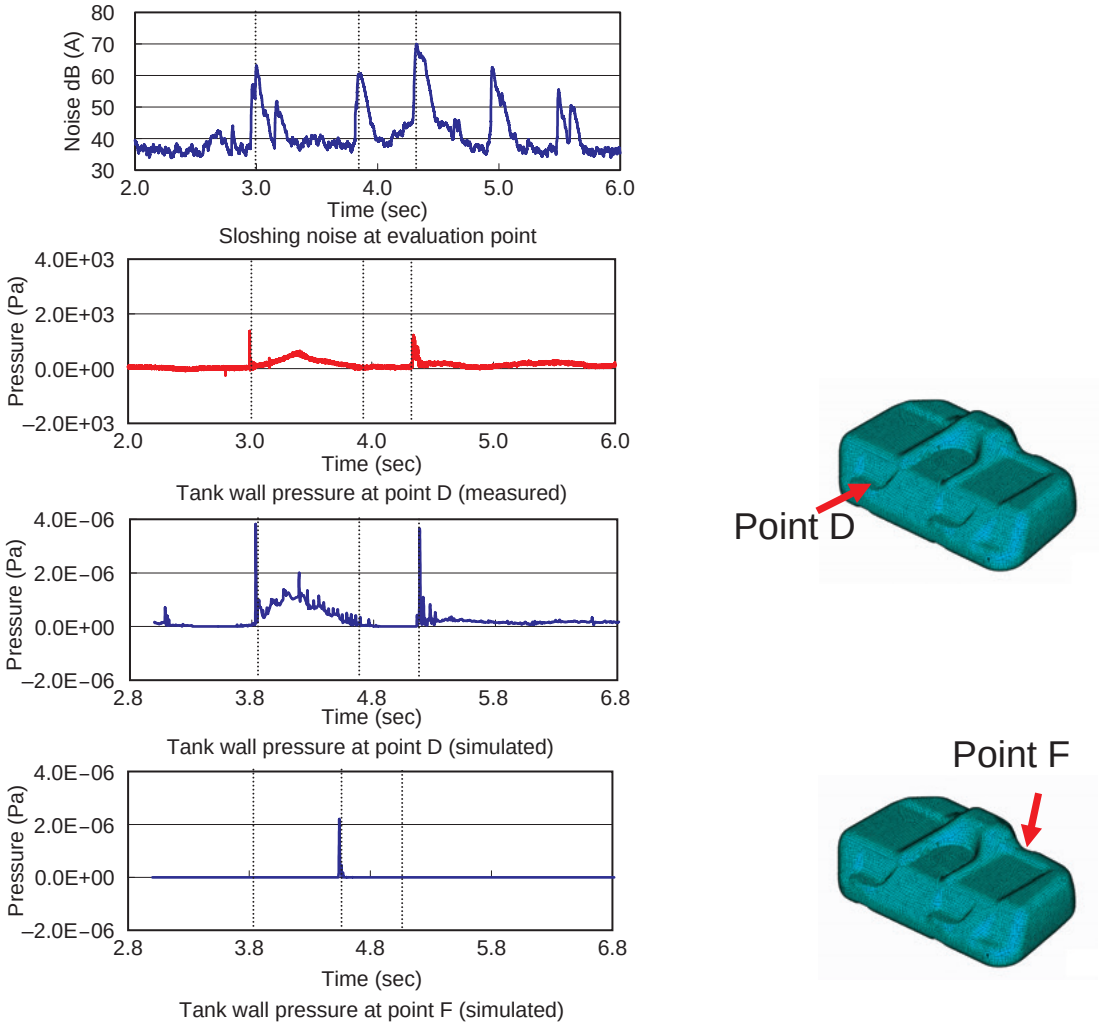


Fig. 11 Comparison between simulation and experiment

6. Conclusion

In order to develop technology for predicting sloshing noise by simulation, an experiment for extracting the physical parameters that are closely related to the occurrence of sloshing noise was performed, and the results compared to those obtained by simulation. As a result, the following facts were established.

(1) Sloshing noise occurs as a result of the fuel striking the inside wall of the tank over a localized area.
(2) When this happens, the pressure at the inside wall of the tank rises impulsively in a short time.
(3) In the simulation, this sharp pressure peak could be reproduced, enabling the generation of sloshing noise to be predicted.

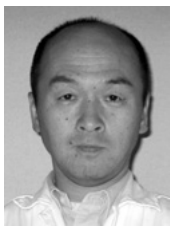
Acknowledgements

Finally, the author wishes to express his deep appreciation to all of the related personnel at ESTECH Corporation who provided valuable cooperation in the promotion of this project.

References

(1) Kamiya, K., Yoshida, Y., deVries, E.: Simulation studies of sloshing in a Fuel Tank, SAE Paper 2002-01-0574
(2) Kamiya, K., Suzuki, K.: Visualization of fuel tank sloshing and noise estimation, MSC. Software solution forum 2000 proceeding
(3) MSC. Dytran USER'S MANUAL Version4.7, MSC. Software, p. 100-106(1999)

■ Author ■



Tohru WAKO

Research on Prediction of Cooling Air Flow in Small Air-cooled Utility Engines

Toshiro KIURA* Takashi KUSHIBIKI* Kazuyuki SHIOMI*

ABSTRACT

This report describes research on the prediction of the cooling air field for air-cooled engines using Computational Fluid Dynamics (CFD). The design of the cooling air field is very important for engine cooling, a factor which has a significant effect on engine performance, fuel consumption, noise, reliability, etc. However, the flow field is very complex because it is developing turbulence caused by a large number of components are located in the flow passages and the cooling air is generated by a centrifugal fan. In order to understand this flow field, calculations were performed using CFD and measurements were taken in an actual engine.

Given practical considerations such as computing time, modeling time, correlation between calculation and test results, formulation of a database, etc., the fan P-Q (pressure vs. volume flow rate) characteristics curve and the flow field were calculated separately when adopting CFD. In addition to visualization using Particle Image Velocimetry (PIV), pressure measurements and measurements of the P-Q characteristics of the cooling fan were done to measure the flow field in the actual engine. The correlation between the results of CFD calculations and measurements was studied. Almost suitable prediction results were achieved by setting the P-Q characteristics at the boundary surface of the rotational area, as obtained from the calculation of P-Q characteristics, as a fan boundary condition for CFD analysis of the cooling air field. This research has enabled the qualitative and quantitative prediction of the cooling air flow of air-cooled engines.

1. Introduction

Small utility engines are used as power sources for construction machinery, agricultural machinery, industrial machinery and so on. It is estimated that approximately 35 million units of spark ignition engines alone are annually produced around the world (according to Honda's survey). They are required to be compact, lightweight and easy to install, and most of them are air-cooled single-cylinder engines. In the industry of utility engines, approaches to environmental issues have also come under closer scrutiny just as they have with engines for automobiles and motorcycles. As a result, a change from 2-stroke to 4-stroke engines has become widespread[(1)-(3)]. The mainstream of valve driving systems has also evolved from SV to OHV or OHC, resulting in greater power output per unit displacement volume.

The cooling system of these engines must be of simple and lightweight structure. Mainly for this reason, a forced air-cooling system with a rotational fan mounted on a crankshaft is commonly

* Asakahigashi R&D Center

adopted. It is, however, hard for this design to appropriately distribute the required air quantity into various parts of an engine. If the size of a fan were enlarged just to increase the air quantity for cooling, it would result not only in the increase in mechanical loss and the decrease in power output and fuel efficiency, but also in the increase in aero-acoustic noise. Therefore, a more efficient cooling system is required.

Engine cooling capability, namely, heat transfer, is an extremely complex phenomenon which consists of heat conduction, heat transfer and heat radiation. They are due to physical properties, structure and geometry of cylinders and cylinder heads, cooling flow field and surface treatment of die-cast respectively. Moreover, the cooling air rises from a centrifugal fan, whose geometry is restricted by engine performance, design, and other limitations, through a flow passage in which many components in a variety of forms are located, resulting in a flow field with developing turbulence. As the phenomenon is extremely complex as mentioned above, a greater part of the development of a new engine depends on designing based on experimental knowledge and performance tests of prototype engines. It is obvious that the prediction of the cooling capability of air-cooled engines at the design stage would be an effective technique in the development of engines.

Some experiments have been carried out using CFD to clarify the cooling capability of water jackets for automobiles[4] or cooling air flow in engine compartments of working vehicles[5] in order to assist in the development of engines. The advantages in applying CFD is the ability to analyze in detail the flow field or heat transfer in locations that have been difficult to measure by the conventional method, and the possibility to provide a guideline for design.

However, there have been relatively a small number of reports on efforts to use CFD to predict the flow field in forced air-cooling systems for small utility engines.

So, the object of this research is to create a design technique that can predict air cooling capability and to optimize engine structure. To achieve this aim, CFD was applied to quantitatively predict cooling flow field of small air-cooled utility engines and measurements were taken to verify the adequacy of such predictions.

2. Calculation Method

2.1. Calculation of Fan P-Q Characteristics Curve

To achieve the calculation of fan P-Q characteristic, the calculation space has to be discretized and at its each element, the conservation laws for the mass and momentum are satisfied, and the moving boundary problem for rotating region has to be solved. SCRYU/Tetra (Software Cradle Co., Ltd.), which is unstructured grid computational fluid dynamics software, was used for this calculation.

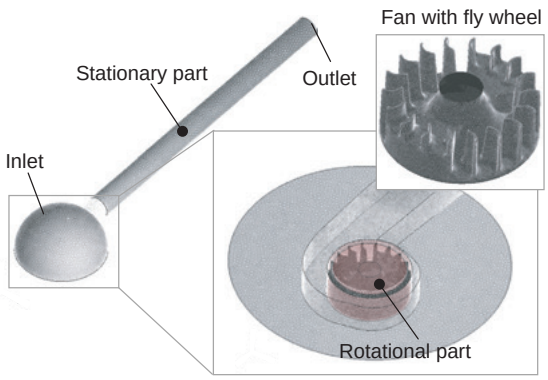


Fig. 1 Model geometry and mesh for calculation of fan P-Q characteristics

The simulation geometry is shown in Fig.1, which is modeled three-dimensionally to the internal geometry of measurement equipment (refer to section 3.1.) based on JIS Standards[6]. There are two differences between the simulation model and the real measurement equipment. One difference is the inlet. This part is modeled as the finite section instead of the space open to the atmosphere, which is a hemisphere space with an enough length of diameter compared with fan diameter. The other difference is the outlet. This part is replaced with the butterfly valve located at the outlet of pipe with the pressure boundary condition. Therefore, the model produces as a form up to the front of the valve. As for the grid making, triangle meshes of a size appropriate to each region were adopted on the model surface. Then prism meshes were applied for the near wall regions and tetra meshes were applied for the inner space of the model, respectively (see Fig. 1). The purpose of applying this prism mesh is to adjust the wall function parameters (y^+ value). The number of cells were determined to be not more than 1 million cells and as small as possible. This is due to the time limitations of fan performance calculation for practical development.

The phenomenon was regarded as steady state, and Arbitrary Lagrangian Eulerian (ALE) was adopted as the calculation method of the moving boundary problem for the rotating motion of the fan. The model consisted of two parts: the static region and the rotating region. Additionally, the standard k-ε model and wall function was adopted as the turbulent model from the viewpoint of convergence, which is based on the turbulence kinetic energy k and the rate of the turbulence energy dissipation ε. Pressure boundary conditions were used for both the inlet and the outlet. In actual measurements, the P-Q characteristics curve was measured by raising the fan backpressure using the butterfly valve located at the pipe outlet, while in calculation, the rise of back pressure is treated as the increase of input pressure boundary value.

Calculations were done by use of the above-mentioned models, grids and boundary conditions. To evaluate the calculation results, the values, which are static pressure and flow rate, obtained from measurements and calculations were directly compared. From the results of evaluation, a method was constructed to make the calculation results asymptotically closer to the measured results by controlling the wall function parameters (y^+ value) and adjusting the thickness of prism mesh.

2.2. Calculation of Flow Field

To calculate the flow field, the calculation space has to be discretized and at its each element, the conservation laws for the mass and momentum have to be satisfied, and the moving boundary problem for the rotating region has to be solved. VECTIS (Ricardo plc), which is commercially available structured grid computational fluid dynamics software, was used for this calculation. This is because one of the important abilities of CFD software in the engine development are to ensure to read and modify directly the 3-D model used at the design. This software has higher potential compared with other software for importing geometry, and Cartesian grids make it easy to control the cell size locally.

For calculation of the flow field, the three-dimensional model of an actual engine was used as shown in Fig. 2. A point that the model is different from the measurement equipment was the fact that the outer space open to the atmosphere was modeled on the

finite section (a rectangular parallelepiped that has a sufficient area against the size of the engine). The meshes consisted of a required minimal number of meshes, and the sizes are determined to be able to sufficiently express the geometry of the engine, and in other external spaces, gradually larger mesh sizes were applied.

Steady state condition was applied for this calculation. At the fan part, a fan model was adopted, which could produce a suitable swirl flow by inputting the P-Q characteristics curve. Calculations were performed by substituting the P-Q characteristics curve on the boundary surface of the rotating region, which was obtained from the previous calculation, for this fan model. For the turbulent model, the standard k-ε model and wall function were adopted.

Calculations were done based on the above-mentioned models, mesh, and boundary conditions. Additionally, verification was done by use of both the velocity vector obtained from flow visualization via PIV (refer section 3.3.) and the value of total pressure measuredÅA as supplementary data (refer section 3.4.).

3. Measurement Method

3.1. Measurement of Fan P-Q Characteristics Curve

Figure 3 shows the measurement equipment. It consists of a motor, a fan, a scroll, a pipe, a butterfly valve, a volumetric flow rate meter, and a static pressure measurement point. Specifications of the measurement equipment are shown in Table 1.

Measurements were taken constantly set at 3 000 rpm continually. The fan P-Q characteristics curve was measured by adjusting backpressure with the butterfly valve installed at the outlet of the pipe. Each point of data was measured when the pressure and flow rate became stable.

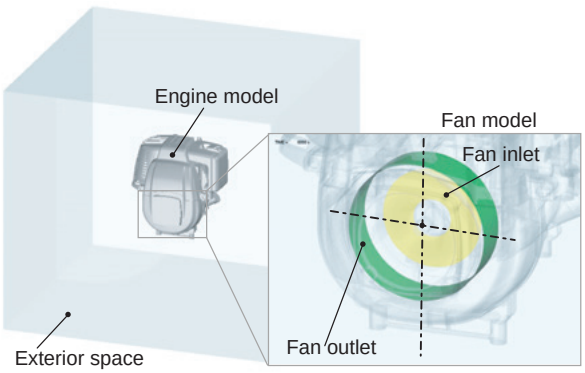


Fig. 2 Model geometry for flow field

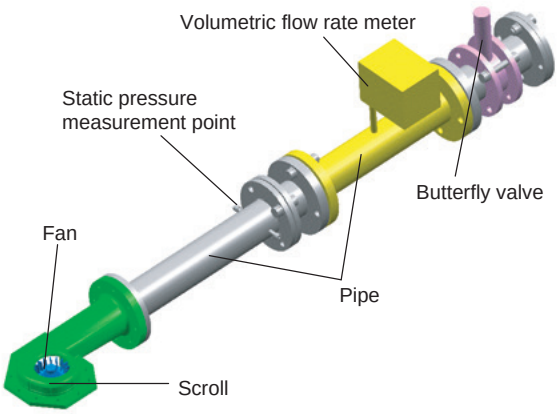


Fig. 3 System for measurement of fan P-Q characteristics

Table 1 Measurement system specifications

Measurement standard	JIS B 8330
Motor	ORIENTAL MOTOR VEXTA FBLM 5120
Pipe	JIS B2238 80A
Volumetric flow rate meter	Japan Flow Control FOX 10A (Range: 15 - 300 Nm³/h (Accuracy ±2%))
Pressure meter	YOKOGAWA JP208

Table 2 Test engine specifications (GX22)

Engine type	4-stroke single cylinder (OHV) spark ignition
Bore × Stroke (mm)	33 × 26
Displacement (cm³)	22.2
Dry weight (kg)	3.3
Dimensions L × W × H (mm)	210 × 251 × 249

3.2. Test Engine and Drive Unit

As the test engine, a small air-cooled utility engine, GX22 (Fig. 4) was selected. This engine was developed as the world's first 4-stroke spark ignition engine capable of freely inclining 360 degrees, and as a power source for handheld tools with clean emissions and superior economical efficiency. The engine specifications are shown in Table 2. The testing equipment is also shown in Fig. 5. As the object of this test is only to measure the flow field, the output shaft of this test engine is driven by a battery-powered motor, and a transparent cover through which laser beams



Fig. 4 Test engine (GX22)

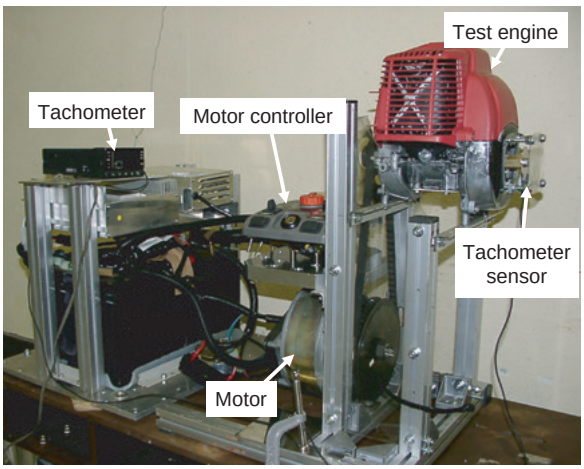


Fig. 5 Test engine bench

can pass is provided. The drive unit consists of a driving motor, a control unit, batteries and an optical rotational sensor.

3.3. Measurement of Flow Field

The flow visualization for the cooling flow field was performed by PIV system. PIV technique uses two special instantaneous images, captured at quite short intervals, of the flow field illuminated by laser. Cross-correlation of the images resulting from two shots was analyzed to calculate the length and direction of displacement of the seeding particles. To obtain two images, two independent laser units, a CCD camera, a synchronizer, and a seeding generator are needed. As an illuminant, two coaxial laser units are used. These laser beams are expanded in a sheet form through the cylindrical lens mounted on the oscillating unit outlet, and they are pulse-emitted twice by controlling the pulse separation (interval of double pulses). Laser oscillation is synchronized with the CCD camera through the synchronizer. In addition to the equipment, "Frame-Straddling", which is a technique to position the two laser pulses on sequential CCD frames, is adopted for capture at quite short intervals. Seeding particles, which are mixed into the flow upstream, are captured on two images. Spatial velocity vectors of instantaneous flow field are obtained by analyzing with cross-correlation, for each displacement of particles on the pair of images. The specifications of the measurement equipment used are shown in Table 3.

In this experiment, several visualization windows were created on the engine cover (fan blowing area and exhaust side) in order to visualize the flow within the cover. Figure 6 shows the three PIV sections. All the measurements were taken at 3 000 rpm continually. 100 pairs of captured images were taken and each spatial velocity vector of instantaneous flow field was used for averaging. The frame straddling interval was set at 10 μs and cross-correlation was performed on the interrogation area with 32 pixels in size. To enhance the precision, images captured at PIV measurement section A shown in Fig. 6, were divided into four parts and combined to one flow field after calculation of averaging.

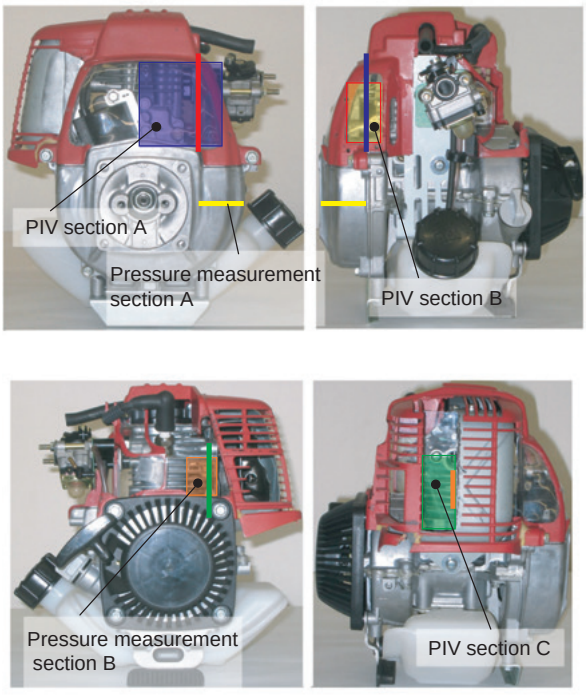


Fig. 6 PIV and pressure measurement sections

Table 3 PIV system specifications

Camera

TSI PIVCAM 10-30 Cross/ autocorrelation CCD Camera	
Light sensitive pixels	1 008 (H) × 1 018 (V)
Frame rate (MAX) (frame/s)	30
Frame straddling time (MAX) (μs)	0.4

Optional system components

TSI LASERPULSE™ Y12-15	
Energy (per pulse) (mJ)	12
Repetition rate (max.) (Hz)	15
Wavelength (nm)	532

Others

Seeding generator	DLR Seeding Generator LSG-500 (Particle diameter 1μm)
Analysis software	INSIGHT™ TSI

Table 4 Pressure measurement system specifications

Pressure probe

Diameter (internal/external) (mm)	0.8/1.2

Pressure transducer

YOKOGAWA JP208	
Range (Pa)	0 - 100 (Accuracy ±1%)

3.4. Measurement of Pressure

As it is related to an inside flow of a small utility engine, the area where PIV measurements can be adopted is restricted spatially. For this reason, pressure measurements were performed at two positions, which are the scroll outlet and the space between exhaust fins shown in Fig. 6, as the supplementation for PIV measurements.

For the measurements, a total pressure probe, a traverse unit and a differential pressure transducer were used. Their specifications are shown in Table 4. The engine operating conditions here were the same as those of the flow field measurements.

4. Results

4.1. Fan P-Q Characteristics Curve

Figure 7 shows the results of the fan P-Q characteristics curves at 3 000 rpm obtained from calculation and measurement. The fan P-Q characteristic curve expresses the relationship between static pressure values and volumetric flow rates of the fan. The solid lines in the figure show the values at the measurement points shown in Fig. 3; the black one shows the measured results and the red one shows the CFD results. The broken line shows the CFD results relationship between the pressure drop between the inlet and the outlet boundary of the rotational region (see Fig. 8), and the flow rate. The latter P-Q characteristics curve is adopted as the input data for the flow field calculation. As an example of the results of P-Q characteristics curve calculations, Fig. 8 shows the velocity vector at the center section of the blade height and pressure distribution on the boundary surface between the rotational and statistic region at 80 Pa of backpressure.

According to Fig. 7, the calculation results correctly predict the measurement results within the low to medium backpressure range (pressure 0 – 90 Pa). This is because the relationship between the wall function parameters (y^+ value) and the wall friction loss is examined in advance, in the solver. Based on the pre-examined results, the thickness of boundary layer mesh has been controlled to make calculation results became asymptotically closer to the measured results. In actual practice, 30 to 100 were aimed as the target of the y^+ value, and the suitable thickness of prism mesh was locally determined. In addition, the same mesh was used on all backpressure conditions of this calculation.

On the other hand, Fig. 7 shows that the difference of each result tends to expand at the high back pressure range, this is due to imbalance of pressure between the backpressure set at the outlet and the pressure generated with the fan as increasing the backpressure. Under such imbalanced conditions, the backward flow against the normal vector occurred locally on both the inlet and outlet. And finally the calculation convergence and stability got decrease resulting in lowering in accuracy. This is a limitation of applying this simulation model. Generally, the application range of backpressure for centrifugal fans is within the low to medium, which is highly efficient. Thus this method can be applied for the prediction of fan P-Q characteristics curves.

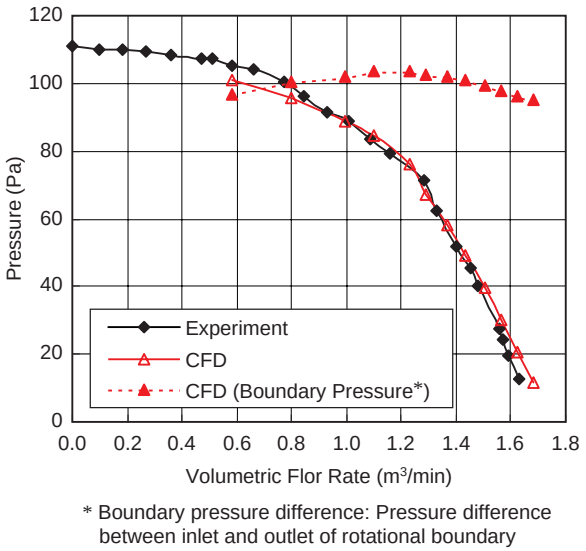


Fig. 7 Results of calculation and measurement of P-Q characteristics curve (3 000 rpm)

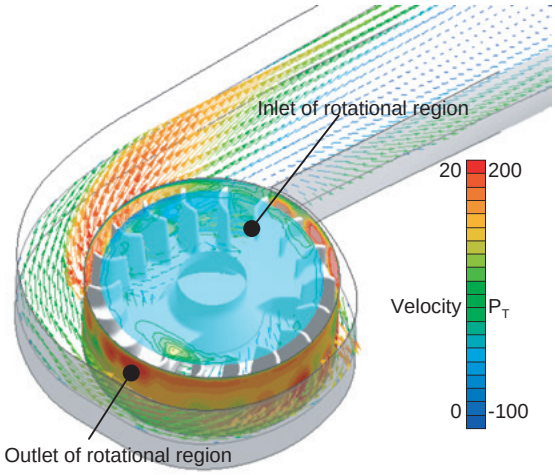


Fig. 8 Velocity vector at 80 Pa of back pressure

4.2. Flow Field Visualization Results

Figure 9 shows the comparison between the flow fields visualized with PIV and calculated with CFD under the same condition, in two sections inside the fan cover and in one section vertical to the cooling fins on the exhaust side.

According to Fig. 9, the comparison at each section shows that the CFD qualitatively predicts the flow field well. While the quantitative comparison of the flow field has a difference of approximately 10% in terms of the absolute velocity, it is considered to be that one of the main reasons is that it was affected twice by the geometry of fan scroll in the fan P-Q characteristics curve analysis and the flow field analysis. In this way of analysis, this difference is unavoidable. Thus there is room for more work to be done in this area.

4.3. Flow Field Pressure

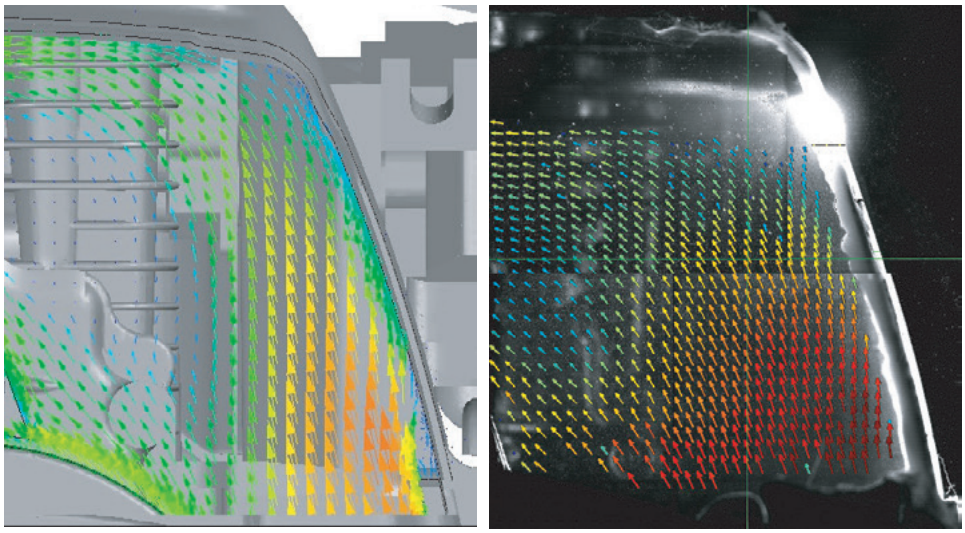
Figures 10 and 11 show the comparison of total pressure results which were obtained from the measurements and CFD. These comparisons are done at the sections indicated in Fig. 6 as the pressure measurement section A and B respectively (fan blowing area and exhaust side).

According to Figs. 10 and 11, in comparison of pressure field, CFD made an accurate forecast of pressure distribution of each section in the same way. However in terms of the absolute values, a difference of about 10% occurred in the same manner as in the flow field.

5. Discussion

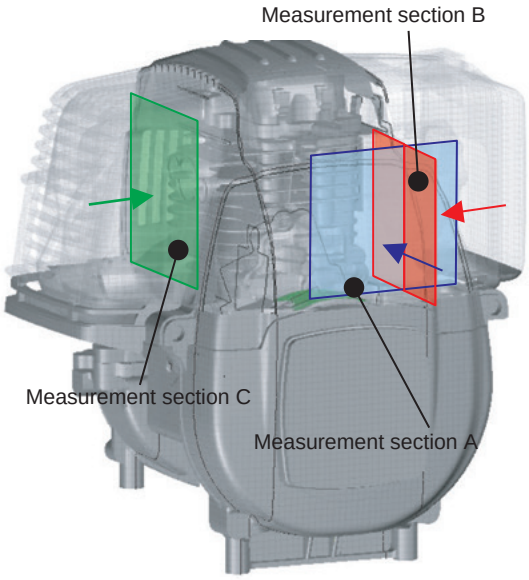
The cooling fan for the test engine dose not have cyclic symmetric geometry for each of the blades, because the fan is united within the flywheel, magnet and the counterweight. The configuration of the fan produces the unsteady and intermittent flow with cyclic tendency depending on the angular position of fan. In addition, it is assumed that the complex cooling air passage induces flow separation in various areas, and develops the turbulence of the flow field. For such strongly fluctuated and fully developed turbulence as this, PIV performed space-averaging in the inspection area and time-averaging for a certain period of time in its measurement method and processing. In addition, in CFD, an assumption of steady state was applied for flow field and a time-averaged formula, which is Reynolds Averaged Navier-Stokes Equation (RANS), was used as the turbulent model. Thus it can be easily presumed that many delicate issues are involved in the correlation between this experiment and the calculations. It is, however, highly significant that these phenomena established a generally good correlation both qualitatively and quantitatively in the numeric calculations.

On the other hand, the predictions, which are the fan P-Q characteristics curve, the flow around the fan and the flow in the cooling air passage, make it possible to analyze the flow field for the reduction in the mechanical loss of the fan and in aero-acoustic noise etc. Also, it goes without saying that additional consideration needs to be given to the heat transfer issue at the viewpoint of predicting the cooling capability. Prediction of temperature and radiation of heat from the surface still remains to be ascertained, it

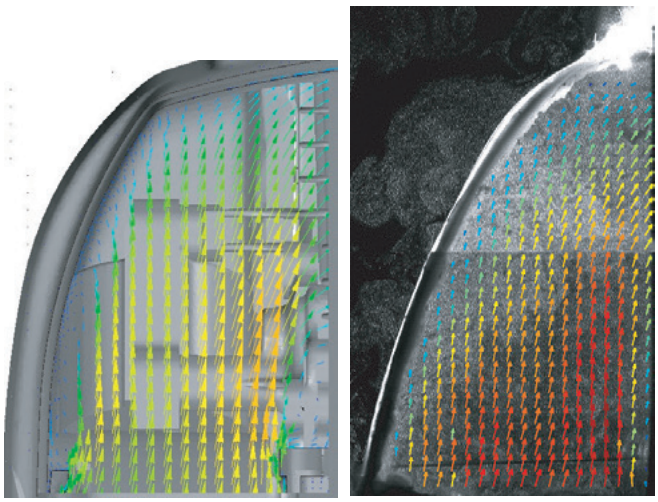


CFD PIV

(a) Results on section A (velocity range 0-10 m/s)

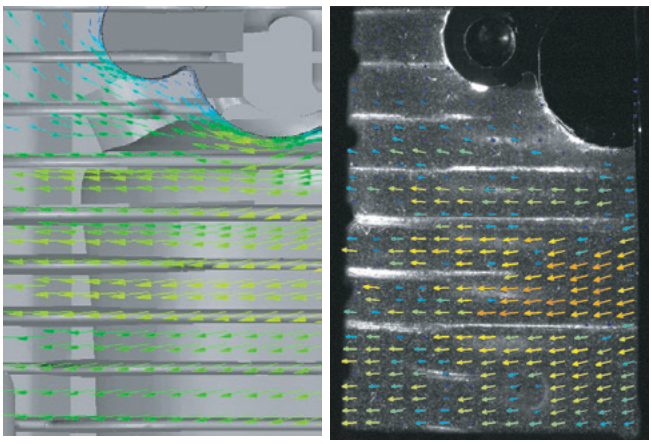


Arrows show direction of view



CFD PIV

(b) Results on section B (velocity range 0-10 m/s)



CFD PIV

(c) Results on section C (velocity range 0-7 m/s)

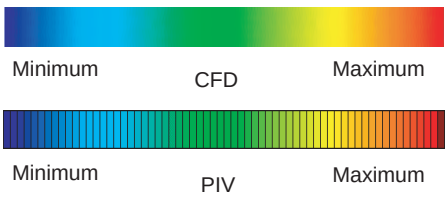
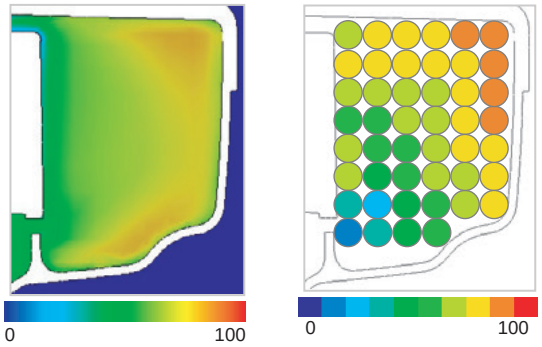
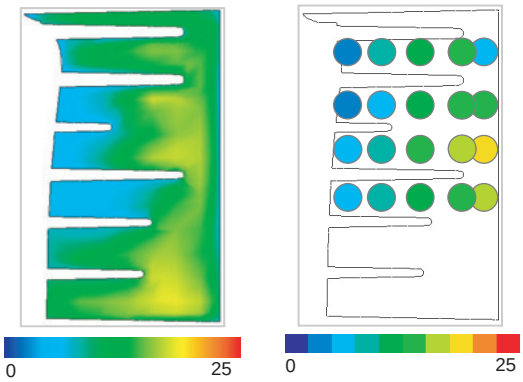


Fig. 9 Comparison of CFD and PIV results for cooling air flow



(a) CFD (b) Measurement

Fig. 10 Pressure distribution at pressure measurement section A (fan - scroll outlet)



(a) CFD (b) Measurement

Fig. 11 Pressure distribution at pressure measurement section B (Exhaust fins)

is clear that more research is necessary to establish the technique which can predict the heat flux distribution from in-cylinder.

6. Conclusions

The object of this research was to create a design technique capable of predicting the engine cooling capability and optimizing engine structure. As a first step, the technique of predicting the flow field of the cooling system of an air-cooled engine qualitatively and quantitatively using CFD was studied by using a small utility engine for hand-held power equipment as test engine. The following were learned from these results:

(1) In the calculation of the fan P-Q characteristics curve, a calculation method to make the calculation results closer asymptotically to the measured results was established. By using the calculation, it became possible to examine the performance of a fan unit only.

(2) A good coincidence was regarded as the results of the flow field obtained with CFD, and of the measurements by PIV etc. In this calculation method, first, the P-Q characteristics curve of the fan alone was calculated. And the calculations for flow field were performed by substituting the P-Q characteristics curve on the boundary surface of the rotating region which was obtained from the previous calculation, for this fan model.

(3) It became possible to qualitatively and quantitatively predict and calculate the cooling flow field using the technique created through this research.

It writes in addition that the calculation method created here has been put into practical use in the subsequent development of air-cooled engines; for example, it has enhanced the accuracy of prediction made at the design stage, and contributed to enhancing the development quality.

Acknowledgements

The authors would like to thank Dr. Yasuaki Kohama and Mr. Fukuo Ohta of Tohoku University Institute of Fluid Science, Dr. Satoshi Kikuchi of Gifu University Faculty of Engineering Department of Mechanical and Systems Engineering, and all other related persons. They assisted us in the flow visualization using PIV.

References

(1) Shiga, M., Nishida, T., Ryu, Y., Tsugekawa, T., Higashi, K.: Development of Multipositional Small Four-stroke Engine, HONDA R&D Technical Review, Vol. 9, p. 44-50 (1997)

(2) Ito, K., Ryu, Y., Yoneda, S., Warashina, M., Edamatsu, S.: Development of GX25 4-Stroke Engine for Handheld Equipment, Honda R&D Technical Review, Vol. 14, No. 2, p. 1-8 (2002)

(3) Maeda, T., et al.: Development of All Position-Operable Small Four-Stroke Engine, Small Engine Technology Conference '97, 972104, (1997)

(4) Xin, J., et al.: Theoretical Consideration to Improve Engine Cooling and Application of Coupling 3D Combustion Simulations with Heat Transfer in Water Jacket and Components, Honda R&D Technical Review, Vol. 15, No. 2, p. 117-126

(5) Saito, M., et al.: Development of Low Noise Working Machine based on CFD Technique, Small Engine Technology Conference 2002, 20024295, 2002-32-1802, (2002)

(6) JAPANESE INDUSTRIAL STANDARD B 8330:2000 Testing methods for turbo-funs, Japanese Standards Association, (2000)

■ Authors ■


Toshiro KIURA


Takashi KUSHIBIKI


Kazuyuki SHIOMI

Corrosion of Zinc Coated Steel: An Atomic Force Microscopy Study of Galvanised and Galvannealed Steels

M. F. Fitzpatrick* Y. Nakazawa* J.E. Castle**

ABSTRACT

Over the past 20 years the automotive industry has constantly improved vehicle corrosion behaviour by exploiting the benefits of zinc coated steels. The application of zinc coated steel, however, does have considerable impact on processes within the automotive industry, the choice of coating type, therefore, can differ between OEM. Using the surface sensitive technique of Atomic Force Microscopy (AFM) the local corrosion behaviour of galvanised steel (GI) and galvannealed (GA) has been compared. Three sample models have been exposed to 5 wt% sodium chloride solution, for different times, to simulate cut edge, stone chipping and galvanic coupling corrosion behaviour. AFM was used to determine the volume of material loss for each time interval which could then be related to an absolute measure of corrosion rate. By converting corrosion rate to current density values the degree of electrochemical activity of the GI and GA systems were compared. For all experimental models GA showed lower corrosion densities compared to GI. The cut edge specimens show GI to have up to 7 times the current density of GA after 256 minutes. The coupled samples magnify this difference further with almost no material loss to the GA coating but a greatly increased corrosion rate for GI. This study has confirmed that, by using the specialised technique of AFM in an innovative way, GA outperforms GI, where the zinc coating has been damaged, with its coating sacrificially corroding at a slower rate.

1. Introduction

Steel has always been the major material of use in the automotive industry. In recent times, where there has been a demand for increased safety, weight reduction and reduced fuel consumption, steel has demonstrated its versatility by offering a range of high strength yet formable new products. Steel, however, is essentially unstable and can react immediately with its environment, when exposed. The corrosion of steel in the automotive industry can have a catastrophic impact on safety critical parts and result in unwanted cosmetic defects that are unacceptable to the customer. Rust has twice the volume of steel and once the corrosion process has been initiated protective paint coatings are destroyed allowing damaged areas to grow rapidly[1].

* Honda R&D Europe (UK)

** University of Surrey, Guildford, UK

In an effort to hinder the corrosion of vehicle Body In White (BIW) and closure panels zinc coated steels are being increasingly employed by the Original Equipment Manufacturer (OEMs) on a global scale. The aim is to reduce weight with no sacrifice to performance, safety and cost[2]. These targets have led to design changes allowing reduction in steel sheet thickness and growth of materials such as galvanised steel (GI) and galvannealed steel (GA). Zinc coatings offer protection to steel in two ways: firstly, zinc acts as a barrier since, being more corrosion-resistant than steel, it separates the steel from any possible aggressive environment; secondly, zinc is less noble than steel and, when coupled together in the presence of an electrolyte, will sacrificially corrode to protect the steel. The latter form of protection is particularly important where a coated substrate has been mechanically deformed and the integrity of the zinc coating broken, leaving the steel substrate exposed, as for example at a cut edge or stone chip area.

The application of a zinc coating, whilst improving corrosion resistance, can have a deleterious effect on other critical aspects of vehicle manufacturing, for example stamping, welding, painting and cost. Depending on the desired performance and quality, there are many different coating compositions and processes that can be employed by the steel mill. GI and GA have emerged over the past 10-15 years as the dominant coated substrates within the automotive sector[3]. Traditionally electro plated zinc (EG) was used, offering a class A paint finish, however, improvements in GI and GA as well as cost implications have seen a decline in the use of EG. Current trends in the automotive application of coated steel indicate that European OEMs tend to utilise GI where as Japanese OEMs favour GA.

It is fundamentally understood that the iron-zinc alloy coating of GA, provided all other factors were equal, would sacrificially corrode at a slower rate compared to the conventional pure zinc coating of GI. Previous studies have obtained average area corrosion data based on a macroscopic scale that may not be relevant to the usual forms of damage observed on BIW for example, stone chips and cut edges. This investigation seeks to rectify this deficiency by comparing the local corrosion behaviour of GI and GA on a microscopic scale using Atomic Force Microscopy (AFM). Three experimental models, cut edge, stone chip and galvanic couple, have been developed to simulate possible on vehicle electrochemical scenarios. It is intended that the models help further the understanding of the impact of anode/cathode ratio on coating composition. AFM offers the ability to analyse surface at atomic level and, with this degree of spatial resolution, unique experiments can be carried out at the coating/substrate interface. AFM, in the contact mode, has been used to obtain quantitative corrosion data which can improve knowledge of the local corrosion at the coating/substrate interface for GI and GA.

2. Hot Dipped Zinc Coating of Steel

2.1. Advances in Coating Quality

Hot dipped galvanising of steel is by far the most common of the zinc coating processes and has existed for over 200 years[4]. Most sheet product is made on a Sendzmir type hot process continuous line, Fig. 1. After uncoiling, the strip is cleaned, to remove oils and other surface contamination, before entering the heat treatment furnace. The annealing furnace heats the strip in a reducing atmosphere, usually a Nitrogen / Hydrogen mix, above the recrystalisation temperature at about 700 °C, removing further contamination from the strip. As the strip leaves the furnace it is cooled, by gas jets, to approximately 450 °C, similar to the zinc pot. Next, the strip enters the zinc pot, the rate of coating tends to depend on the steel type with thickness controlled by immersion time and gas wipers at the pot exit, which remove excess material. Roller levelling, temper rolling, inspection, oiling and recoiling complete the production process.

In the automotive industry, as already discussed, GI and GA have been increasingly employed over the past couple of decades. The growing demands for these products have subsequently coincided with improved coating quality, properties and processing know how from steel suppliers. Modernisation of galvanising lines such as the implementation of automated surface control devices, greater control of temperature and atmosphere during annealing

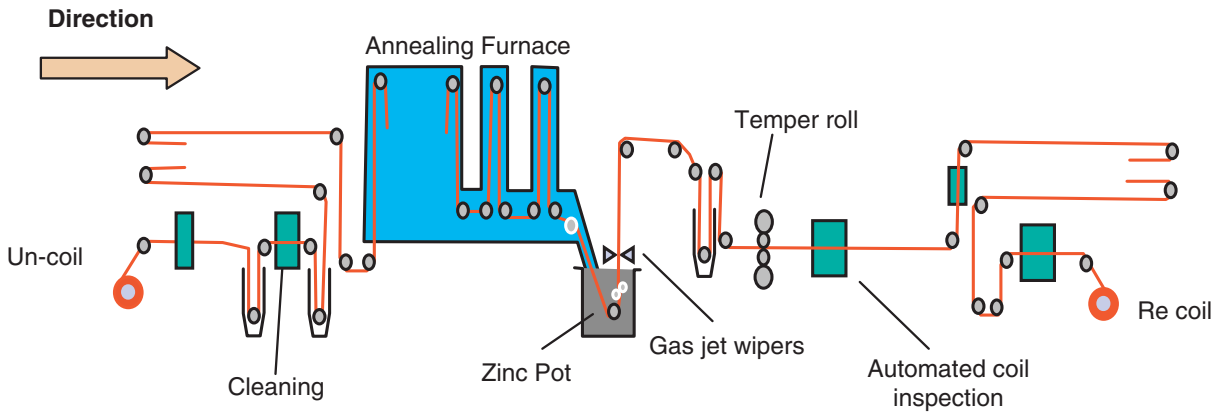


Fig. 1 Schematic of a Sendzimir continuous galvanising line

and the optimisation of strip cleaning have led to a more consistent product with tighter tolerances. Zinc pot control has improved, increasing pot life and reducing costs. The wiping and solidification area is enclosed in a nitrogen atmosphere avoiding and reducing surface defects. The purpose of this review is not to detail the advances in modern hot dip galvanising but to demonstrate that zinc coated products available to the automotive industry are constantly changing and are of a higher quality now than at any time in the past.

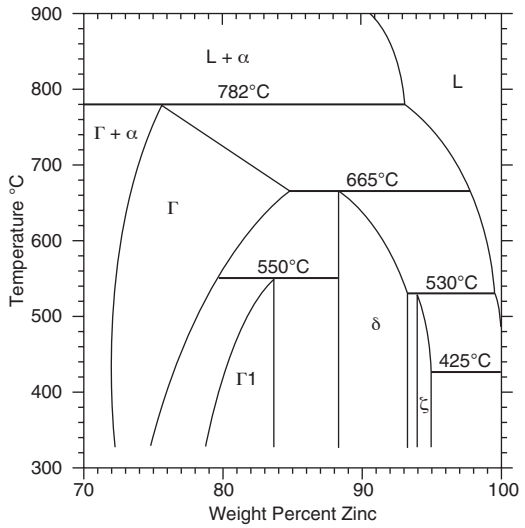


Fig. 2 Zinc rich end of Fe-Zn phase diagram

2.2. Gavanised and Galvannealed Steel

GI and GA are both hot dipped zinc coated steels. As the steel strip passes though the zinc pot several specific iron/zinc intermetallics can form. The iron/zinc system is well understood and has been reported in great detail previously. The possible phases formed by the hot dipping processes can be found by examining the zinc rich end of the iron/zinc equilibrium phase diagram, Fig. 2[5]. The composition of the coating depends on several factors; immersion time and speed, the influence of alloying elements and the application of a post annealing stage.

The processing route for GI is, essentially, the same as described in section 2.1. The microstructure of the coating is almost completely pure zinc, Fig. 3. Aluminium (0.2 wt%) is typically added to the zinc pot to prevent the formation of brittle iron-zinc intermetallics at the coating/substrate interface. The aluminium reacts preferentially with the steel forming a thin $Fe_2Al_5(Zn)$ inhibition layer, suppressing any iron/zinc alloying. In the case of GA, however, the growth of iron zinc phases is controlled and encouraged by passing the strip through an annealing tower after zinc pot exit, Fig. 4. As the freshly coated strip passes through the furnace, iron/zinc phases grow due to thermal diffusion. A coating

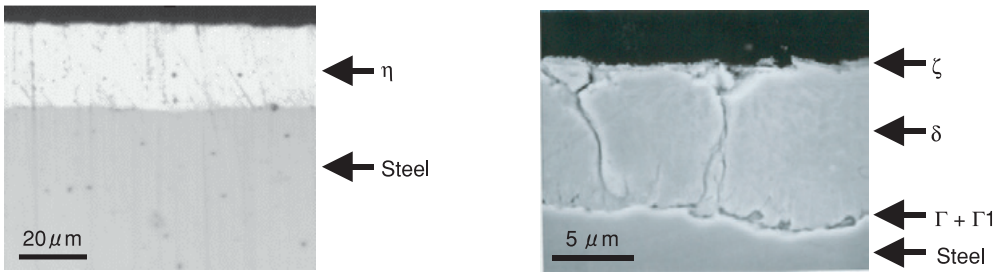


Fig. 3 Micrographs of the microstructure of (a) conventional GI and (b) typical GA found in the automotive industry

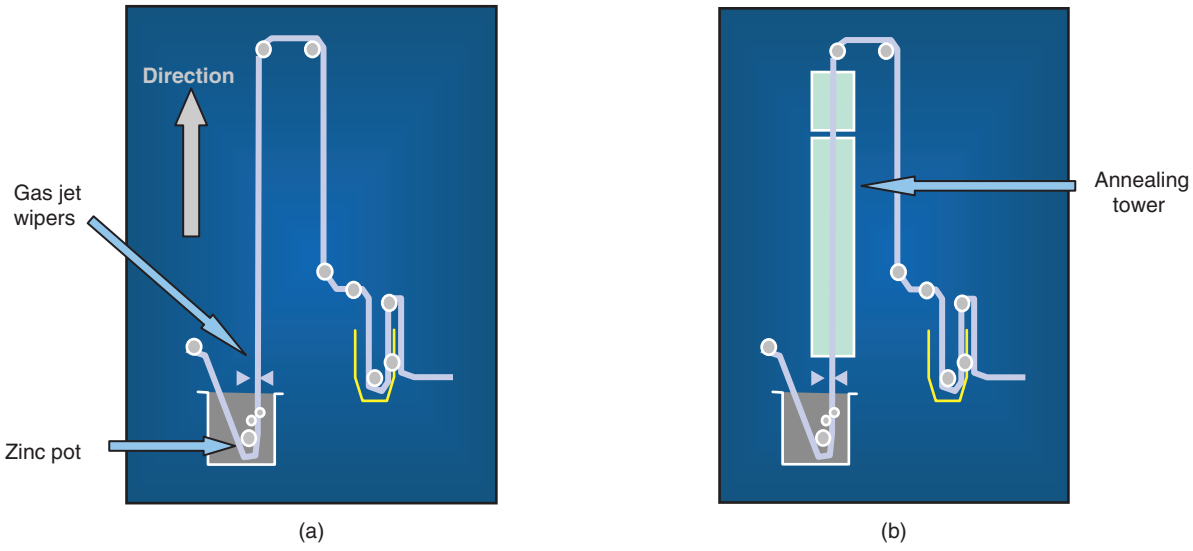


Fig. 4 Schematic highlighting process differences between (a) GI and (b) GA steel (with annealing tower)

mainly consisting of d-phase is preferred by the automotive industry because of optimum weld, powdering and corrosion properties[6], [7].

The iron/zinc alloy coating offers improved weldability and, due to a corrosion potential closer to the steel substrate than GI, enhanced corrosion protection. Traditionally GA has also offered better paintability to the automotive industry because of a higher surface roughness, although since the advent of surface texturing the paint appearance of GI has improved. The harder coating of GA however, poses powdering and drawing concerns. Finally, as steel competes more and more with the lightweight technologies offered by the use of light metals and carbon composites in the automotive industry, there have been great steps made in the development of High Strength Steel (HSS). This has been accompanied by an increase in the complexity of metallurgy, for example TRansformation Induced Plasticity (TRIP) steel, which can potentially be effected by the elevated temperature of the GA annealing tower[8].

3. Experimental Work

3.1. Sample Preparation

3.1.1. Experimental models

In galvanic protection, zinc is less noble or anodic to steel in ambient conditions and will sacrificially corrode to protect steel. The corrosion rate, according to the Catchment Area Principle, is influenced by the proportion of the exposed zinc (anode) compared to the exposed steel (cathode). Taking into consideration different anode/cathode ratios, samples were prepared in different ways related to possible scenarios that could occur on a vehicle. Three experimental models for GI and GA were prepared, Fig. 5:

(1) Cut Edge Simulation - Samples were mounted in cross-section resulting in a high iron exposed area (cathode) to small zinc area (anode). Estimated anode/cathode ratio = 1:1000.

(2) Stone Chipping Simulation - A more specific laboratory developed method yielding a smaller exposed iron area compared to the exposed zinc. Stone chipping damage can be very random in its nature; however, some situations will result in a large anode to small cathode scenario. Estimated anode/cathode ratio = 24:1.

(3) Galvanic Coupling Simulation - GI and GA were mounted together in the same epoxy and galvanically coupled (samples were touching). The resin block was then cut and polished so that their individual cut and polished edges were simultaneously exposed to the electrolyte.

To prepare the large anode to small cathode sample a specific laboratory preparation method was developed, as mentioned above. 15 mm discs were cut from the steel sheet. The discs were then punched into dome shapes, described in Fig. 6. The overall aim of this work is to compare the behaviour of GI and GA, therefore reproducible sample shape was critical. A custom made tool was designed for the “dome” punch procedure, Fig. 7. Using the tool

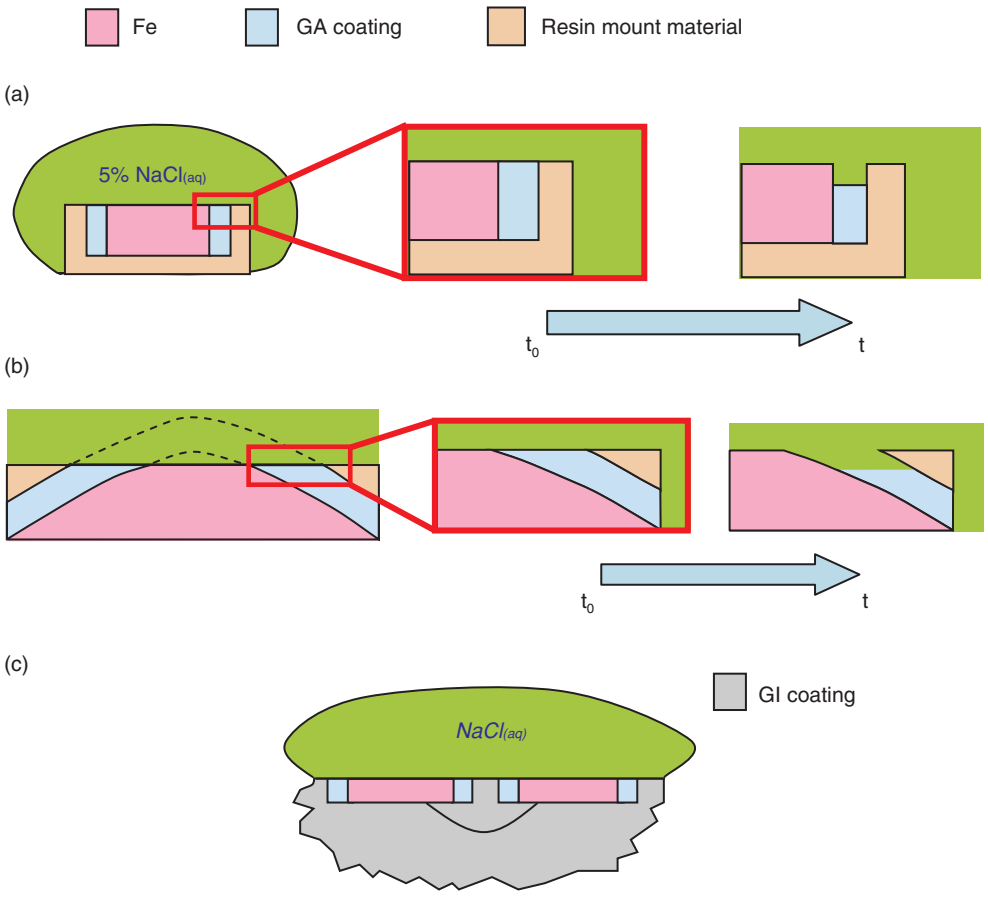


Fig. 5 Schematic diagrams of (a) the cut edge sample (b) the stone chip sample and (c) the galvanic sample. For (a) and (b) examples of the expected effect of exposure after a given time, t.

an 8 mm ball forms the disc into a dome shape to a fixed height, 0.8 mm in these experiments. The domes were then mounted in resin and ground to 4000 grit paper. The grinding process removed the top of the dome thus exposing an iron cathode surrounded by zinc, Fig. 6. The samples were polished to a 1 µm finish and washed in a water free environment. The grinding and polishing stage was controlled for each sample to give a tolerance in the diameter of the exposed material to ±0.05 mm.

3.1.2. Ex-Situ aqueous corrosion treatments

GI and GA material (0.8 mm gauge) was supplied from three industrial suppliers, samples A, B and C. Samples were cut and mounted in epoxy resin. The mounted specimens were first ground with successive silicon carbide papers, from 320 to 4000 grit, and then polished to a 1 µm finish to give a highly smooth and flat surface. Specimens were usually ultrasonically cleaned in ethanol, not rinsed in water to avoid initiating corrosion. Finally the epoxy resin mount was machined to an appropriate size for AFM analysis

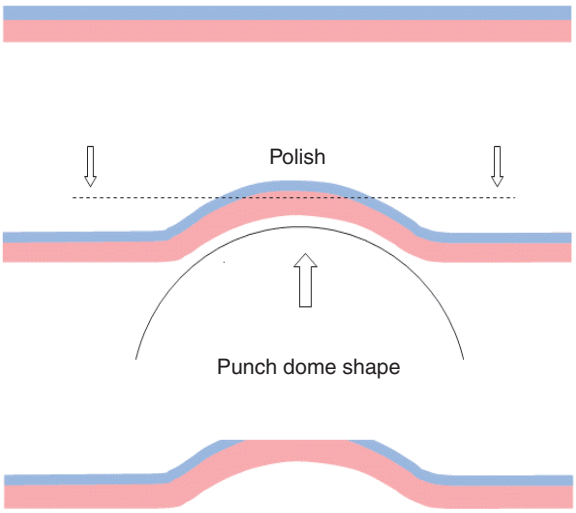


Fig. 6 Schematic diagram describing the production of the stone chip sample

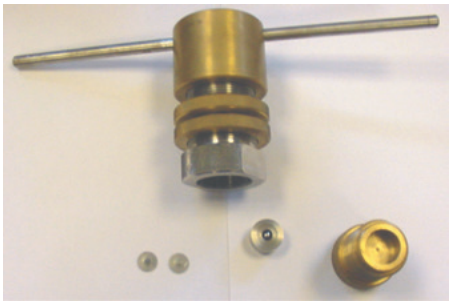


Fig. 7 Photograph of the custom made tool to make the stone chipping samples

All samples were treated using a 5 wt% NaCl aqueous solution for test periods of 1, 4, 8, 16, 64 and 256 minutes. The treatment was carried out at room temperature and ambient pressure in plastic aerated containers. After each treatment samples were washed using six baths of de-ionised water and ultrasonically washed in ethanol.

3.2. Atomic Force Microscopy Analysis.

3.2.1. Atomic Force Microscopy

In AFM a sharp stylus, mounted on a cantilever, is scanned across the surface of the sample under investigation. The technique differs from the 'Talysurf' type of profilometer, widely used in industry, only in the sensitivity of the cantilever and the miniaturisation of the scanning system. In AFM the cantilever deflects towards, or away from the surface under the influence of interatomic forces and the scanning system, equally, has a resolution of atomic dimensions. The deflection of the cantilever, as it traverses the surface, is measured by a laser beam acting as an optical lever. The system provides an accurate representation of the surface with full x,y,z co-ordinates for each position and a resolution of around 1nm. The surface can be interrogated in many ways to provide measurements of roughness and other relevant surface profiles.

3.2.2. Analysis modes

(1) Height analysis

The simplest quantitative display is the height profile, which shows the elevation of the features along a line. The line need not coincide with an original scan line, but can be an arbitrary line on the image. Measurements of differences in surface elevation, horizontal distance between points, and slopes were possible with the image processing program, Nanoscope III Digital Imaging 5.12.

(2) Bearing analysis

The word "bearing" characterises the relative roughness of a surface in terms of high and low areas. The bearing ratio curve is the integral of the surface height histogram and plots the total percentage of the surface above a reference plane as a fraction of the depth of that plane below the highest point in the image. By utilizing bearing analysis it is possible to determine what percentage of the surface lies above or below any arbitrarily chosen height (the "bearing ratio"). For example, bearing analysis is frequently used in studies of surface wear and friction and in silicon etching procedures to observe changes in etched features over an interval of time. In qualitative terms, the bearing ratio gives a measure of how "jagged" a surface is. In this study, etching of zinc in zinc coated steel is being considered, where zinc works as a sacrificial anode. The protected iron may so be used as a height reference from which to compute the bearing volume which will then coincide with the amount of removed zinc. In practice, the volume is measured over an area defined by a rectangle placed over the image on the screen. This area is used by the software to return the bearing volume in the form of volume per unit area. This has the units of depth and is the mean depth of the zinc removed by corrosion over the area selected. This value can be processed to give a corrosion rate in more conventional units.

3.2.3. Local area analysis.

To establish the rate of coating loss it was imperative that the exact same sample location was revisited after each exposure time. With small localised areas of interest, 20 μm^2, a simple but effective method to recognise analysis areas easily was developed, Fig. 8.

3.3. Quantitative Electrochemical Calculation of AFM Data

Bearing analysis of the AFM data gives a measure of the removed volume of material per unit area for a given exposure time. This measure needs to be corrected by subtraction of the initial bearing volume arising from the natural roughness of the as-polished surface, Fig. 9. This correction value was determined for the reference area before exposure. The rate of material loss is an absolute measure of corrosion rate but can be related to the values often obtained by electrochemical measurements. Corrosion is essentially an electrochemical process that relies on the flow of electrons from an anode to a cathode. It is possible to convert known material loss volumes to current densities, which reflect the degree of electrochemical activity of a system, in the following manner.

The corroded mass per unit area after a time t, is given by

$$m = (V_t - V_o)\,\rho_{Zn} \quad (1)$$

Where V_t is the bearing volume, expressed as volume per unit area after time t and ρ_{Zn} is the density of zinc.

The mean corrosion rate is then

$$dm/dt = (V_t - V_o)\,\rho_{Zn}/t \quad (2)$$

at any given time t.

This corrosion rate can be converted to electrochemical current by the use of Faraday's laws. First express the rate in the form of mols of zinc per unit area per unit time

$$dM/dt = 1/M \cdot dm/dt \quad (3)$$

Where M is the atomic weight of zinc

The total electrochemical current, i, is then given by

$$i = (AnF/M) \cdot dm/dt \quad (4)$$

Where n electrons are associated with the formation of a zinc ion (Zn^{2+}) and nF coulombs are released by the dissolution of the anodic zinc and A is the total area of zinc exposed to the electrolyte. Thus the current density is given by

$$i/A = (nF/M) \cdot (V_t - V_o)/t\,\rho_{Zn} \quad (5)$$

Whilst the assumption that the coating is 100% zinc is not true for the GA calculations it does not actually change the assumption that all removed material is related to corrosion rate dm/dt. Automotive grade GA is predominantly d-phase which has a composition of about 90% zinc and 10% iron. The final location

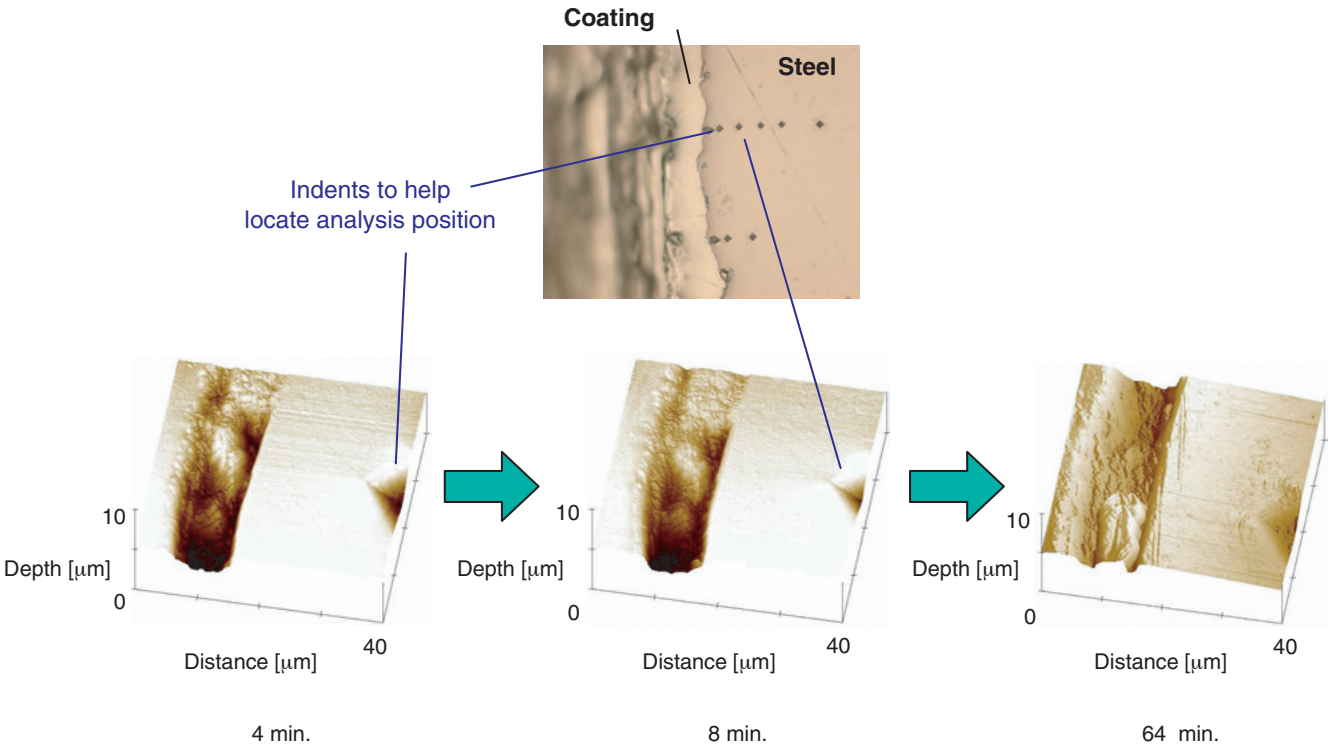


Fig. 8 AFM Images showing the use of Vickers hardness tester indents used to locate sample analysis position

of the removed iron is not known, back deposited or left behind on the coating surface as mobile species are possible outcomes. In any case, the volume of material removed, as measured by AFM, relates exactly to the electrochemical current flowing. The net effect of the iron contribution in the coating on the calculation is relatively small, appearing only in the molecular mass and the density terms of Eq. (3). For the purposes of this study this small correction has been neglected.

4. Results

4.1. Cut Edge Samples

Fig. 10 shows a graph of removed volume against time for GI cut edge samples. The plot of removed volume against time is representative of corrosion rate. Following the sequence of calculations described in Section 3.3. all the removed volume values can be converted to charge, for each respective time intervals, Fig. 11. Graphs of charge against time make inferences about current density for a particular system. Using the values plotted for each time interval, however, only indicates the average current density to the respective point in time. Taking the tangent of the graph at a point in time will give the instantaneous current density, as if measured by the electrochemist using conventional methods. As can be seen the value is essentially constant after about 100 minutes. It is these values taken at 256 minutes, which are shown in Table 1 and compared against GA values.

For a GA sample the rate of loss of coating was much slower than for GI. Taking into account experimental tolerances only data at 256 minutes could be used. The data for GA values at 256 minutes, therefore, is representative of instantaneous current density values, Table 1.

Table 1 Current density values for GI and GA for cut edge samples

Current density (μA / cm^2)			
Sample	A	B	C
GI	36.8	27.6	11.0
GA	8.4	6.1	5.9

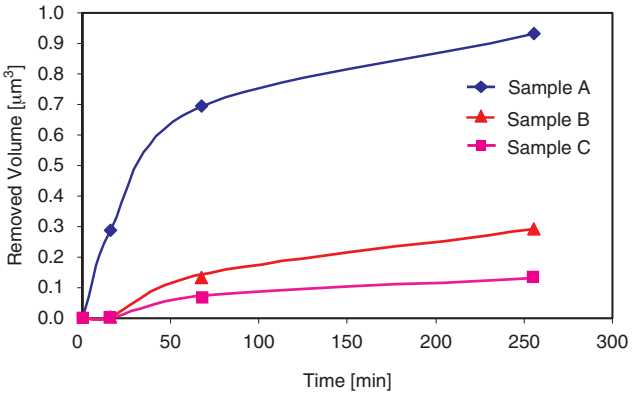


Fig. 10 Removed volume [μm^3] against time [min] for cut edge GI samples

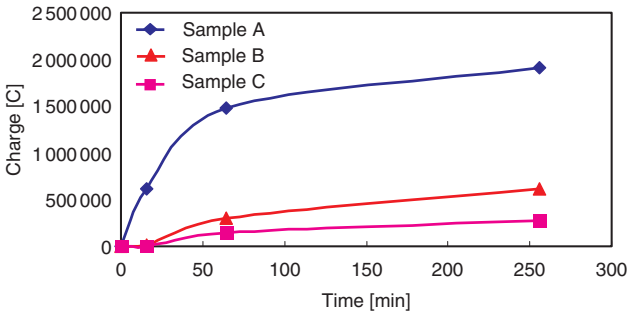


Fig. 11 Charge [C] against time [min] for cut edge GI samples

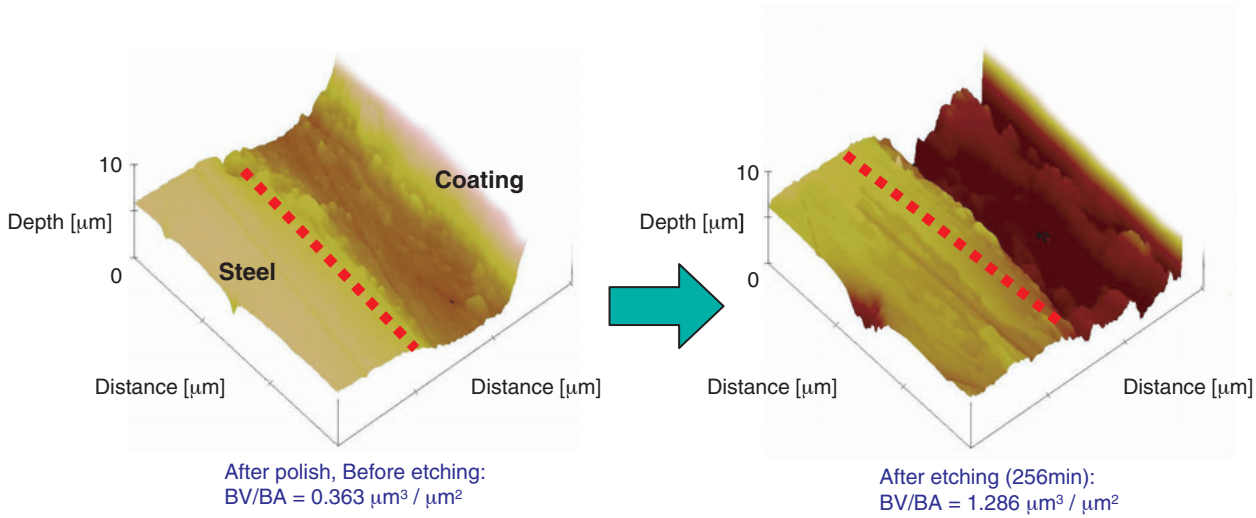


Fig. 9 AFM Images of zinc/steel coating interface at (a)t_0 before exposure and (b) t_{256} after 256 minutes exposure

4.2. Stone Chipping Samples

It is not the intention of this study to compare material across different suppliers and for this reason only sample B was analysed for the stone chipping (and galvanically coupled) model. Previous results have shown sample B to offer data in between the other samples and so would offer representative data for GI and GA. The calculated charge data for the stone chipping model for GI is shown in Fig. 12. In order to take into account the whole data set and reflect that the zinc coating has been sacrificially removed an average current density has been shown. The instantaneous current density at 256 minutes is so small that its value could mistakenly be thought to indicate that little or no coating loss has taken place. This was the case with the GA sample hence no data is given.

4.3. Galvanic Couple Sample

No significant loss of GA coating was observed on the galvanic coupled sample. The current density values calculated for the GI coating, however, were significantly higher than previously observed. An instantaneous current density value of 85.6 μA/μm^2 was calculated at 256 minutes. Fig. 13 shows a graph comparing the GI values for a cut edge sample and a galvanic coupled sample.

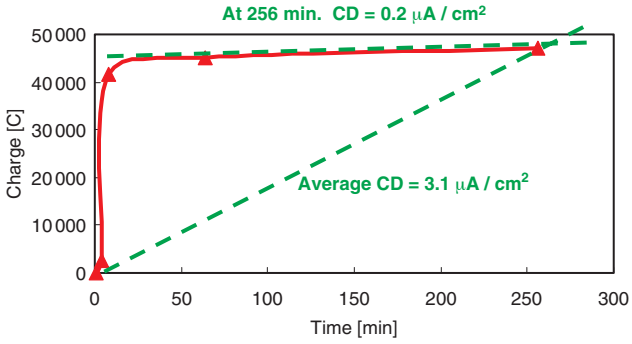


Fig. 12 Charge [C] against time [min] for stone chipping sample (Sample B only)

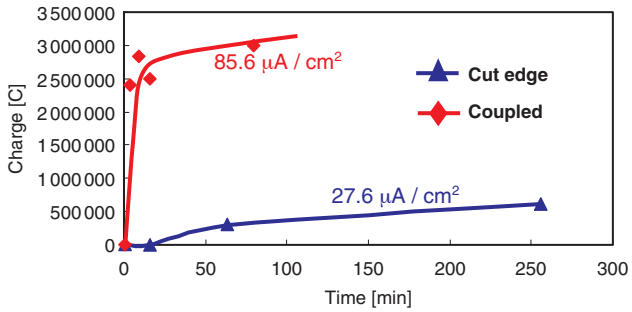


Fig. 13 Comparison of charge [C] vs time [min] curves for GI coupled and GI cut edge sample from sample B

5. Discussion

The local corrosion behaviour of zinc coated steel at the coating/substrate interface has been studied. The performance of GI and GA has been compared in different situations, in the context BIW exposure, taking into consideration different anode/cathode ratios and the galvanic coupling of the different substrates. This study has taken advantage of the high spatial resolution AFM offers, to develop a novel method for the study of local corrosion activity at an interface. Current density values for the different substrates and experimental models have been calculated from raw data measured by AFM.

It is already understood that, due to its zinc/iron alloy coating, GA is expected to sacrificially corrode at a slower rate than GI. In two of the experimental models investigated corrosion of the GA coating was so small that it could not even be measured by AFM. Only analysis of the cut edge samples gave quantifiable results for both GI and GA. The GI results, shown in Fig. 10, indicate quite a large variation between samples. The GA values, whilst much lower, show less variation possibly suggesting that GA offers a more stable corrosion protection coating. One explanation, considering the process route differences, could be that the annealing furnace for GA has a stabilising effect on the coating across all suppliers.

The initial corrosion rate of the GI samples is almost linear before slowing with time. This indicates a change in the local corrosion behaviour with time due to concentration polarisation; as zinc corrodes and becomes deeper relative to the steel corrosion slows. There is also variation in the rapidity of initial corrosion of GI with sample A having much higher values than samples B and C. The instantaneous current density values of GI are considerably higher than those for GA. The current density values for GA were so low in the initial stages of corrosion that only a value at 256 minutes could be calculated. Cut edge protection is a critical area for vehicle BIW. Often paint protection at a cut edge can be at its thinnest and coupled with poor burring properties can act as site for the early onset of corrosion. From the results in this study it has been confirmed that GA offers improved substrate corrosion protection. For some OEMs, however, the cosmetic red corrosion product of GA is not acceptable, resulting in the selection of a coated substrate to be determined by performance priorities, opinions and experience.

The stone chipping model exposure tests resulted in corrosion rates and current density values that were significantly lower. For GA samples no quantifiable coating loss was measured. Even for GI the current density values were much lower; indeed the instantaneous value at 256 minutes was as low as 0.2 μA/cm^2. The initial corrosion rate, once again, is much higher and an average value at 256 minutes is shown in Fig. 12. The lower current density values were expected, as a result of the reversal of the anode/cathode ratio from 1:1000 to 24:1. The large drop off in rapidity of corrosion was not so expected, but can be explained by sample geometry. The stone chip sample, to all intense and purposes, is a polished dome. If a sequence of AFM height analysis curves is considered, Fig. 14, the etching of the zinc can clearly be observed on the right hand side of the figure.

After punching and grinding, the coating/substrate interface is not perpendicular to the surface but is sloped, Fig. 6. The local depth of the underlying iron determines the maximum depth to which the zinc can be etched. These geometric limitations could at some point cause a rapid drop off in the corrosion rate and explain the results shown in Fig. 12. Another reason for the drop in

corrosion rate could possibly be that in the early stages of corrosion a thin oxide layer protects large areas of the coating surface, thus reducing the size of the effective anode. As this oxide dissolves so the area of exposed metallic zinc increases changing the anode/cathode ratio and slowing the rate of corrosion.

Consideration of the galvanic couple results shows no attack to the GA coating. There is, however, a relatively high current density value for the GI sample. The instantaneous current density value of 85.6 μA/cm^2 is considerably higher than the cut edge sample. The corrosion rate of the GI in the galvanic sample is due, as the name would imply, to the fact that it galvanically protects not just its own substrate but the whole of the GA sample as well. This affects the anode/cathode ratio greatly with corrosion rate increased. Even though the GA coating is in direct contact with its respective steel substrate, the composition difference between the d-phase and the pure zinc of GI is sufficient for a large galvanic effect between the two substrates when connected by an electrolyte. For vehicle BIW that are predominantly GA the introduction of GI, for example for cost benefit, should be considered carefully. Other concerns such as joining methods may have been countermeasured but if galvanically connected and exposed to an aggressive environment the corrosion to the GI part would be significantly accelerated.

For the first time local current density values for a metallic coating/substrate system have been obtained. The areas analysed and volumes measured could only have been examined using AFM. The benefit of local values ensure that no external influence, such as coating defects, affect the analysis. As with any small area analysis technique a certain amount of caution must be employed when considering results as representative of a larger area. The method developed in this paper is not limited to GI and GA coatings. Metallic coatings play an important role in the automotive and other high profile industries. The measurement of coating loss and subsequent conversion to electrochemical data can help further understanding and development of other coated materials, applications and systems.

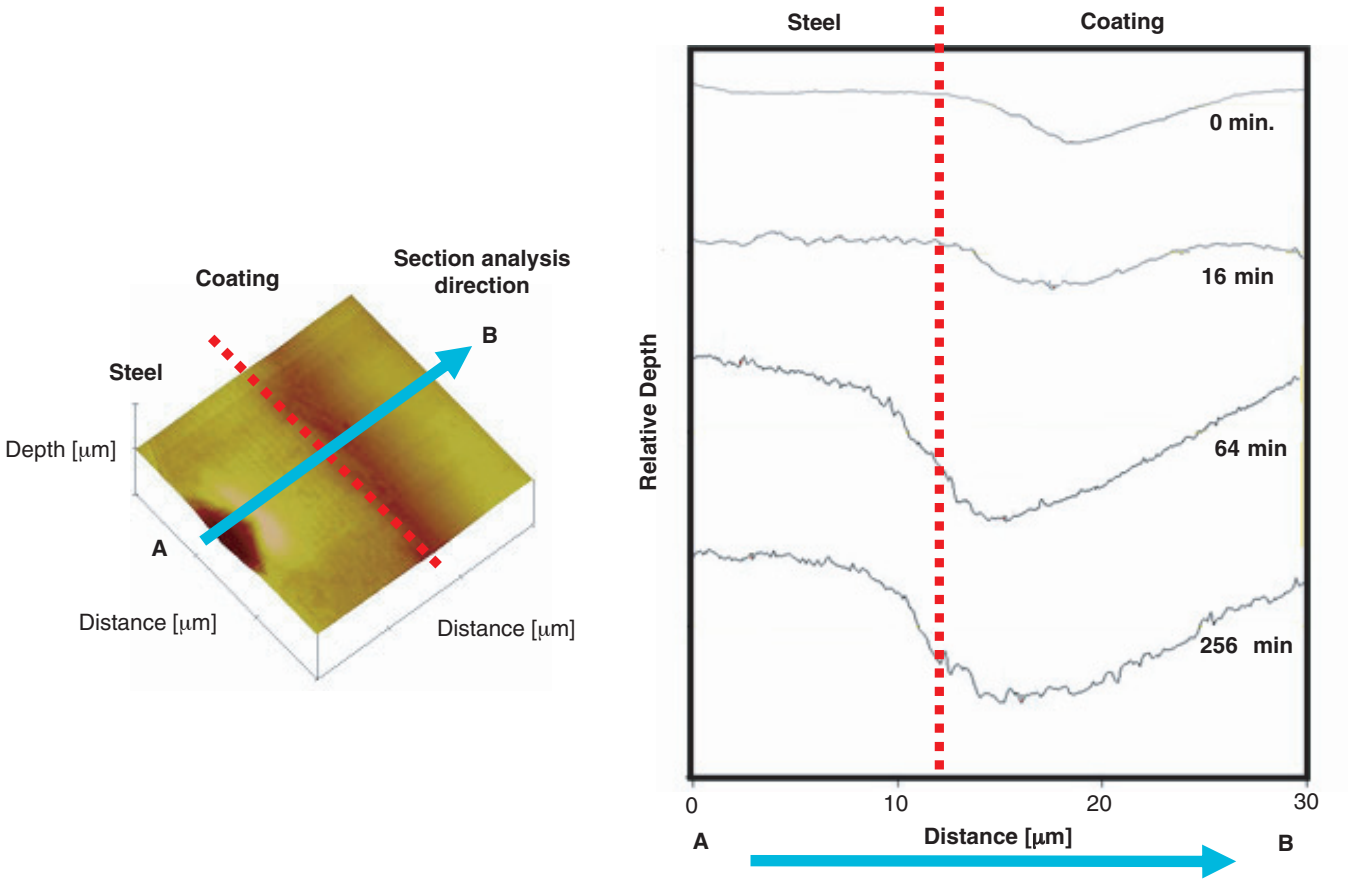


Fig. 14 AFM Height analysis curves describing the corrosion evolution of a GI sample from 0 minutes to 16, 64 and 256 minutes exposure.

6. Conclusion

(1) This investigation has studied and compared the local corrosion behaviour of GA and GI at the coating/substrate interface by using AFM.
(2) Three experimental models have been developed to simulate different possible BIW corrosion scenarios; cut edge, stone chipping and galvanically coupled.
(3) Electrochemical activity of the different coating systems has been compared as a result of controlled corrosion experiments. Mass loss data, measured by AFM, offers an absolute corrosion rate, these values have been converted to current density values permitting conclusions to be made concerning the coating systems corrosion performance.
(4) For each experimental model the GI coating corrodes at a faster rate than the GA coating. The initial corrosion rate for GI is greatly accelerated, and, as demonstrated by the cut edge samples exhibits a larger variation in corrosion performance compared with the more stable GA data. As expected the anode/cathode ratio has a significant effect on corrosion behaviour.
(5) For the stone chipping model, steel remains cathodic to the coating however, corrosion is slowed significantly (for GA, material loss is almost zero).
(6) By galvanically coupling the two systems, GI sacrificially protects all exposed metal. The change in anode/cathode ratio therefore greatly increases the GI coating corrosion rate.
(7) For the first time a method has been developed to study the local electrochemical activity at a coating/substrate interface. The novel use of AFM has allowed the corrosion behaviour of GI and GA to be compared.

Acknowledgements

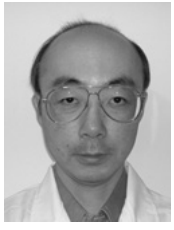
The authors would like to thank Damien Deforge for the AFM work carried out in this study as part of an overseas research placement at the University of Surrey. Thank you also to Dr. Peter Zhdan, University of Surrey, whose expert supervision of the practical work allowed the project to run smoothly.

References

(1) Porter, F. C. : Corrosion Resistance of Zinc and Zinc alloys, Marcel Dekker Incorporation (1994)
(2) Davis, R. E. and Fay, P. : Durability of Bonded Coated Steel Joints, International Journal of Adhesion and Adhesives, Vol. 13, No. 2, p. 97-104 (1992)
(3) Shrier, L. L. : Corrosion George Newnes Ltd. (1999)
(4) Marder, A. R. : Metalurgy of Zinc Coated Steels, Progress in Materials Science, No.45, p. 191-271 (2000)
(5) Massalski, T. B. : Phase diagram, ASTM Metals Handbook, No.3, p. 206 (1992)
(6) Jagannathan, V. : The Influence of Coating Characteristics on the Powdering and Corrosion resistance of Galvannealed Coated Steel Sheet, Galvatech 92, p.127-131 (1992)
(7) Mercer, P. D. : Factors which Affect the Alloy Growth Rate in Galavannealed coatings, Galvatech 92, p. 204-208 (1992)
(8) Tanae, T. and Kaneko, K. : Development of 590 and 780 MPa Grade High-Ductility Steel Sheets, Honda Technical Review, Vol. 16, No.2, p. 183-190 (2004)

■ Authors ■


M. F. Fitzpatrick


Y. Nakazawa


J.E. Castle

Development of Hexavalent Chromium-free Surface Treatment

Kazunori TAKIKAWA* Tsutomu MIYADERA* Toshiaki OHTSUKA*
Atsushi SHIRAKAWA* Mitsuo TAKASHIMA* Youji MATSUOKA*

ABSTRACT

A hexavalent chromium-free surface treatment has been developed for automotive parts which provides a coating possessing equivalent anti-corrosion performance and friction characteristics to conventional chromate layers containing chromium(VI). The treatment forms a passivation layer of trivalent chromium and metallic chelates at the interface with the zinc, while uniformly covering the surface with a protective zinc layer. It is an unusual feature of this process that a single procedure is able to form a double layer. Optimization of the amount of silica added has enabled the achievement of friction characteristics equivalent to those of conventional chromium(VI) chromate layers. The new surface treatment has resulted in a reduction in the amount of hexavalent chromium used in the production process and in finished parts.

1. Introduction

Demands for the reduction of the amount of environmental load substances used in automobiles are increasing with a growing focus on global environmental issues. Annex II of the EU End of Life Vehicle (EU-ELV) Directive bans the use of hexavalent chromium, employed in automotive applications as a rust inhibitor, from 1 July 2007[(1),(2)]. This makes the development of a hexavalent chromium-free surface treatment as a substitute for chromate conversion coatings containing hexavalent chromium (referred to as hexavalent chromate coatings below) an urgent issue.

2. Development Goals

The purpose of the project discussed in this paper was to develop a substitute for hexavalent chromium in order to reduce the environmental load associated with scrapping and recycling vehicle parts at the end of vehicle life. Hexavalent chromate is often used as a coating on zinc in fasteners, where its corrosion resistance and clamping performance (friction properties) fulfill an important function, making the development of a substitute particularly important.

2.1. Issues Associated with Conventional Technologies

The following treatments have recently been adopted as substitutes for hexavalent chromium:

(1) Molybdate-phosphate coatings[(3)], triazinthiol coatings, tannic acid coatings
(2) Chromate coatings containing trivalent chromium compounds to which metallic salts have been added (termed trivalent chromate coatings below).
(3) Organic and inorganic compound silicate coatings applied by dip-spin and baking

However, these methods generate a number of issues.

The cost of the materials for the substances listed in (1) is high, and they do not offer an equivalent level of corrosion resistance to hexavalent chromate coatings, due to the lower coating thickness. The reactivity of the substances listed in (2) in terms of coating formation is low. High temperatures (more than 50 °C) and long

* Tochigi R&D Center

periods of time (more than 60 secs) are required to increase reactivity, making productivity low compared to hexavalent chromate coatings, which only require 15-30 secs at room temperature. In addition, the differences in chemical composition (low level of hydrates in the coatings, etc.) tend to have a high coefficient of friction, necessitating the addition of an extra coating treatment to adjust the coefficient of friction for the fastener. The coatings listed in (3) tend to generate a higher film thickness within the screw threads, leading to torque and fit concerns. Other issues associated with these substances include the high baking temperatures required to ensure that the coatings adhere, making it difficult to process in conventional plating processes.

Given these issues, the following goals were established for the development of a substitute:

(1) From the environmental perspective, elimination of hexavalent chromium, lead, cadmium and mercury, which have become the targets of legislation.
(2) From the performance perspective, the achievement of identical corrosion resistance and friction characteristics to those displayed by hexavalent chromate coatings.
(3) From the production perspective, the achievement of an identical level of productivity to hexavalent chromate coatings while using the same production facilities.

2.2. Design and Development of Materials

2.2.1. Enhancement of corrosion resistance performance

Hexavalent chromate coatings are thick (0.2-1.0 μm) inorganic coatings composed of complex salt hydrates of soluble hexavalent chromium and trivalent chromium. Hexavalent chromium produces a shielding effect to prevent damage from external sources; when the coating is damaged by a scratch, a passivation film is formed by the reduction of the soluble hexavalent chromium to trivalent chromium. This shielding effect and self-healing characteristic of the coating gives it a high level of corrosion resistance performance[4),(5)]. Corrosion resistance performance therefore declines greatly when hexavalent chromium is not contained in the coating. The achievement of both a shielding effect and self-healing characteristic is important in ensuring an equivalent level of corrosion resistance performance in a replacement material. Self-healing ability in particular is essential, due to the likelihood of damage to the coating when fasteners are tightened and when gravel chipping contacts the coating during vehicle operation.

While reports concerning various development projects for hexavalent chromate replacements exist in the literature[(6)], few report development of a replacement possessing both a good shielding effect and self-healing ability. The project discussed in this paper therefore attempted to design a coating which would combine two materials which each guaranteed one of these characteristics in a single production process.

The top layer of the projected material would be a silica layer with colloidal silica as the main component. Silica has superior shielding properties compared to conventional trivalent chromate coatings and it also possess good coating formulation properties. The bottom layer, which is in contact with the zinc-coated substrate, would act as an inhibitor via the chelating effect of trivalent chromium salt and metallic salts and could be expected to display self-healing properties. The coating is shown in Fig. 1.

2.2.2. Control of friction properties

Sufficient attention to the friction properties produced by the surface treatment is important in ensuring that the axial tension acting on the bolt when the fastener is tightened as close as possible to the design value. Because it is not practical to directly measure the axial tension on the bolt, a calibrated wrench method, which measures tightening torque, is generally employed for tightening control. The torque produced by tightening and the axial tension generated are proportional; in the calibrated wrench method, the torque coefficient is read from the gradient of the torque-tension line. The relationship between torque and axial tension in this range of elasticity[(7)] is shown by Eqs. (1) and (2). Figure 2 shows a typical example of a torque-tension line.

$$T_f = T_s + T_w = K \cdot F_f \cdot d \tag{1}$$

$$K = \frac{1}{2d}\left(\frac{P}{\pi} + \mu_s d_2 \sec\alpha + \mu_w D_w\right) \tag{2}$$

[T_f: Tightening torque T_s: Screw torque T_w: Flange torque
K: Torque coefficient F_f: Axial tension d: Nominal diameter
P: Screw pitch μ_s: Screw surface friction coefficient
d_2: Effective diameter of screw μ_w: Flange friction coefficient
$sec\alpha$: Flank angle of thread
D_w: Equivalent diameter of friction torque on flange]

The equations above are used to convert friction coefficient to torque coefficient. Torque coefficient varies according to the characteristics of the surface treatment. If a new surface treatment with a higher torque coefficient is used, tightening with identical torque will produce less axial tension, possibly leading to the fastener dropping out due to looseness or loss of function due to stress fractures and the like. The replacement substance is therefore required to possess a similar torque coefficient to the existing surface treatment.

This development project focused on the upper corrosion-preventing silica layer. The concentration and properties of the colloidal silica added to the chromate treatment solution were studied to enable the achievement of an equivalent torque coefficient to that of hexavalent chromate coatings[(8),(9)].

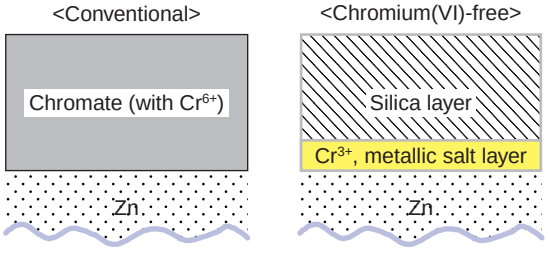


Fig. 1 Chromate layer

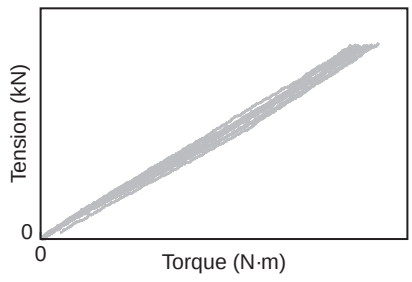


Fig. 2 Example of torque-tension line

3. Composition of Newly Developed Coating

To apply the newly developed coating (trivalent chromate coating below), first a uniform mixture of chromium nitrate, metal chelate salts and a dispersed solution of colloidal silica is created. This is applied to a zinc coating in an immersion treatment at 30-40 °C for 15-40 seconds. Glow discharge spectroscopy (GDS) was used to analyze the concentration of elements in the depth direction. The results are shown in Fig. 3.

The analysis confirmed a two-layer structure, with silicon present in the silica component at a depth of 100-150 nm from the surface layer and chromium and metallic elements derived from the metal chelate salts in a 50 nm-thick layer observed at the zinc interface.

A cross-section of the coating was also studied using scanning electron microscopy (SEM). SEM images are shown in Fig. 4. Observation under the SEM showed microscopic particles of silica distributed throughout the entire surface layer.

The results show a trivalent chromium and metal chelate salt layer deposited at the zinc interface and a uniform distribution of silica throughout the surface layer, indicating the achievement of a two-layer structure in the trivalent chromate coating. Figure 5 shows a diagram of the structure of the trivalent chromate coating.

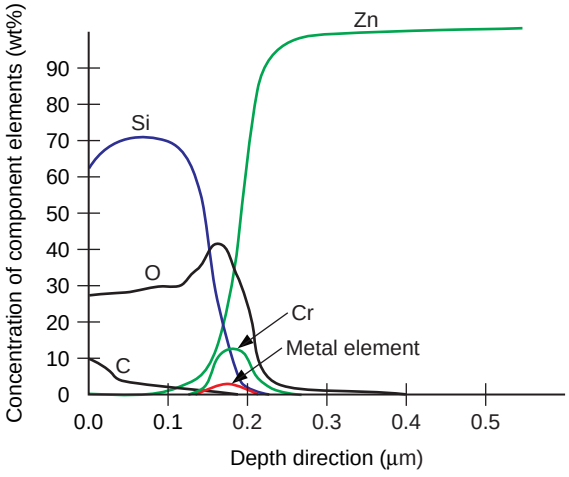


Fig. 3 Depth profile of element concentration in chromium(VI)-free chromate on zinc

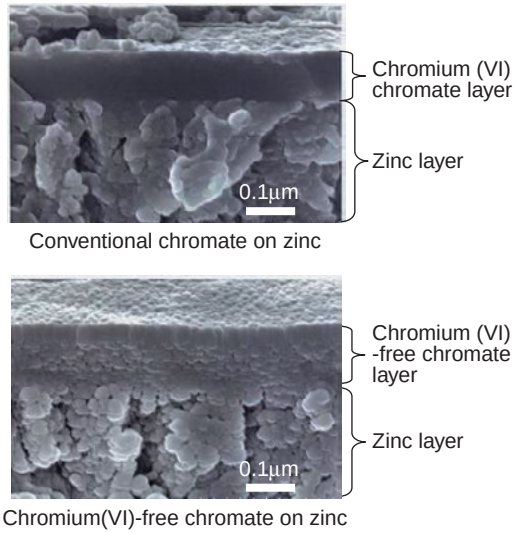


Fig. 4 Surface cross-sectional structure of chromium(VI)-free chromate on zinc

The formation mechanism of the trivalent chromate coating is believed to be as follows:

(1) Dissolution and activation of the surface of the zinc by the acid components
(2) The pH rises at the boundary between the zinc and the treatment solution
(3) Formation of chromium hydrate compounds and complexes of metal chelate salts and zinc at the zinc interface, together with deposition of colloidal silica and film formation in the upper layer
(4) Fixing of the coating by drying

4. Characteristics of Components of Newly Developed Coating

4.1. Contribution of Silica to Corrosion Resistance Performance

The corrosion resistance performance of the silica layer was evaluated to verify the shielding effect. Figure 6 shows the relationship between the silica content of the trivalent chromate treatment solution and the thickness and corrosion resistance performance of the coating, as measured in a saltwater spray test (SST).

In addition to making the coating thicker, the addition of silica has enhanced the corrosion resistance performance. The results of the tests can be assumed to indicate that the silica has produced a shielding effect.

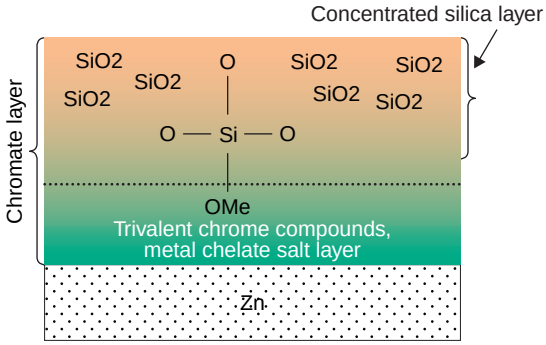


Fig. 5 Diagram of structure of chromium(VI)-free layer on zinc

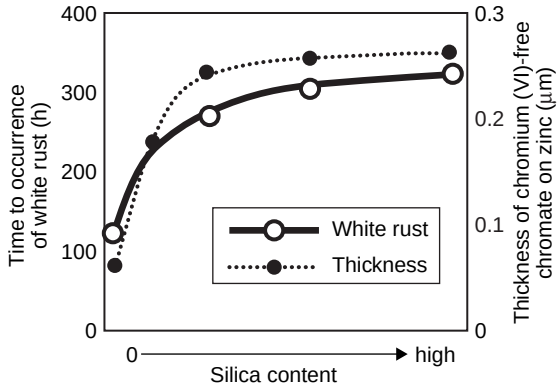


Fig. 6 Relation between amount of silica added and time to occurrence of white rust

4.2. Contribution of Metal Chelate Salts to Corrosion Resistance Performance

To test the effectiveness of the metallic salts in producing a self-healing characteristic, trivalent chromate coated test pieces were produced with and without the added metallic salts. Scratches reaching to the substrate were generated on these test pieces, after which they were subjected to combined cyclic corrosion tests (CCT) to evaluate corrosion resistance. Figure 7 shows external views of corrosion after 7 and 22 test cycles.

The addition of metal chelate salts was shown to have increased corrosion resistance performance at the scratch site to a level equivalent to or greater than that displayed by a hexavalent chromate coating. These results can be assumed to indicate that the addition of metal chelate salts produces a self-healing characteristic and generate a passivating effect.

The following tests were further conducted to verify the passivating effect:

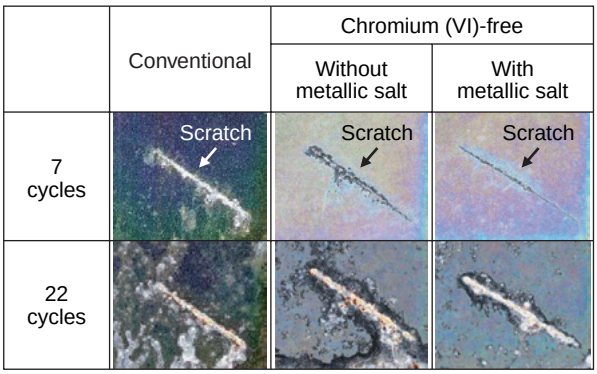


Fig. 7 Corrosion resistance of chromate on zinc with metallic salt around scratch (CCT)

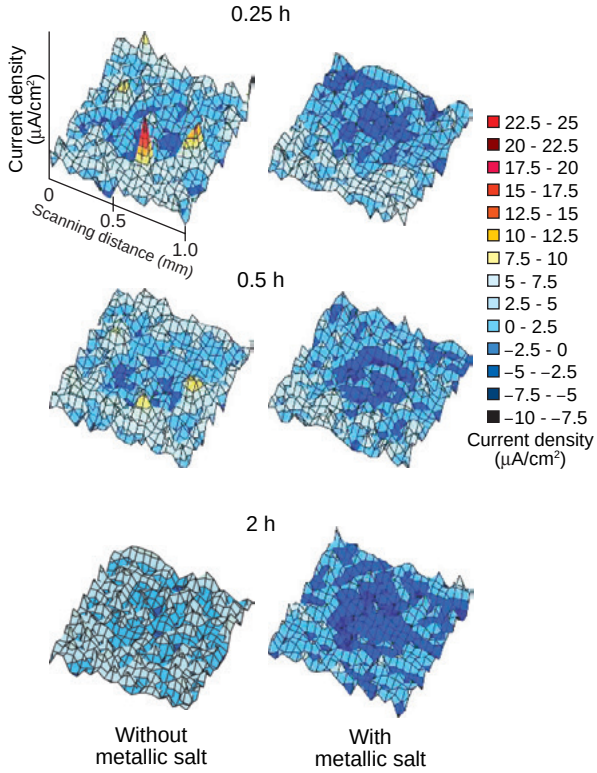


Fig. 8 Time variation of corrosion current density around micro-hole on zinc chromate

(1) Scanning vibrating electrode technique (SVET)[10]

Micro-holes of 1 mm in diameter were artificially produced on test pieces, after which the test pieces were immersed in a 10 ppm NaCl solution and the density of the corrosion current around the hole was measured. Figure 8 shows the corrosion current density at 0.25 hr, 0.5 hr and 2 hr from immersion.

Immediately after immersion, a local cell, in which the center of the hole acted as a cathode and the surrounding area as an anode, was formed on the test piece coated without the addition of metallic salts, producing a maximum current of 20 μA/cm^2. As a result of the protective effect of substances formed in a reaction between the dissolved zinc, trivalent chromium and silica, the corrosion current decreased with immersion time, until it was virtually nonexistent at 2 hr.

By contrast, despite the fact that the center of the hole formed a cathode on the test piece with a coating containing metal chelate salts, a distinct anode section could not be identified, and the maximum corrosion current density was 5 μA/cm^2, indicating the occurrence of a passivation effect at the damaged section of the coating.

(2) Measurement of polarization

When polarization measurements were conducted using the same test pieces, a passivation potential range (–1.1 –1.0 V) was recorded on the anode section of the test piece with a coating containing metallic salts (Fig. 9). These results indicate that a passivation effect and self-healing characteristic like that occurred by a hexavalent chromate coating can be achieved through the addition of metallic salts[11].

The results discussed above enable the mechanism of corrosion resistance in the trivalent chromate coating to be theorized as follows:

(1) Corrosion prevention by shielding effect

The surface silica layer prevents the corrosion promoters H_2O, O_2 and Cl- from contacting the zinc layer, and the trivalent chromium at the boundary with the zinc layer functions as a passivation coating. This prevents penetration of the corrosion promoting anion Cl^- from an external moist environment, in addition to preventing fluxion of cations (Zn^{2+}) from the zinc layer.

(2) Corrosion prevention by self-healing characteristic

At the scratch site, where the zinc layer is exposed to the atmosphere, corrosion first produces a dissolution reaction in the zinc.

$Zn \rightarrow Zn^{2+} + 2e^-$

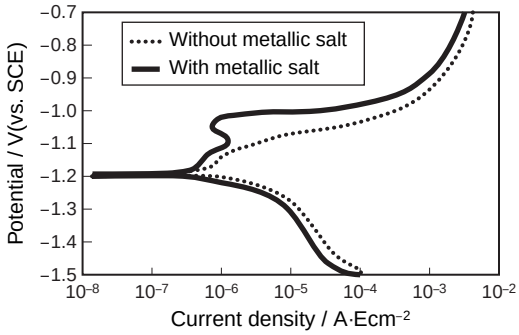


Fig. 9 Polarization curves of chromate on zinc with metallic salt

At the same time as reducing the dissolved metal ions (M^{m+}), the e- produced by the dissolution reaction of the zinc reacts with the unreacted chelates in the metallic salts (X) to form insoluble metallic salts.

$$M^{m+} + ne^- \rightarrow M^{(m-n)+}$$
$$X^{(m-n)-} + M^{(m-n)+} \rightarrow MX$$

The dissolution reaction of the zinc raises the pH at the zinc coating interface, and the presence of unreacted trivalent chromium in the coating causes deposition of complex ions of trivalent chromium, forming a film. This self-healing characteristic produces a passivation reaction.

$$Cr^{3+} + 6H_2O \rightarrow 2Cr(OH)_3 + 3H_2$$

4.3. Heat Resistance

Due to the high quantity of hydrates in hexavalent chromate coatings, cracks tend to occur at temperatures of 80 °C and above, causing corrosion resistance performance to decline. Figure 10 shows the surface property of trivalent and hexavalent chromate coatings after heating at 80 °C and 120 °C.

The trivalent chromate coating contains less hydrates than the hexavalent chromate coating, and therefore virtually no cracks caused by evaporation of the moisture content were observed.

Figure 11 shows the results of an SST conducted after heating. The corrosion resistance of the hexavalent chromate coating drops rapidly at 80 °C, while the trivalent chromate coating displays only a gentle decline, demonstrating that the trivalent chromate coating possesses high heat resistance.

5. Effect of Processing Conditions on Corrosion Resistance Performance

A saltwater solution test (SST) was used to evaluate the effect of processing temperature and processing time on corrosion resistance, in order to establish optimum processing conditions for the trivalent chromate coating. Figures 12 and 13 show the relationship demonstrated between processing temperature and corrosion resistance and dipping time and corrosion resistance respectively.

The results showed that film thickness increases with an increase in processing temperature and dipping time, and there was a consequent increase in corrosion resistance. This indicated that good performance could be achieved with the trivalent chromate coating at low processing temperatures and with short dipping times.

6. Control of Torque Coefficient by Variation of Amount of Added Silica Content

Torque coefficient was measured in zinc plated nuts and bolts coated with trivalent chromate coatings containing varying concentrations of silica. The results are shown in Fig. 14.

The measurements showed that the torque coefficient became lower as the silica content was increased, and indicated the existence of an optimum range of concentration enabling the achievement of an equivalent torque coefficient to that displayed by hexavalent chromate coatings. However, if silica was added in excess quantities, the torque coefficient was observed to increase again.

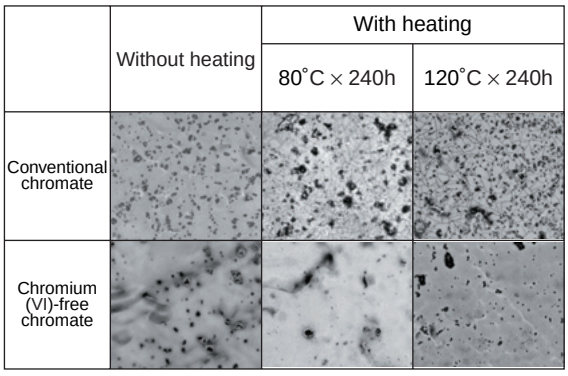


Fig. 10 Surface property of chromate after heating

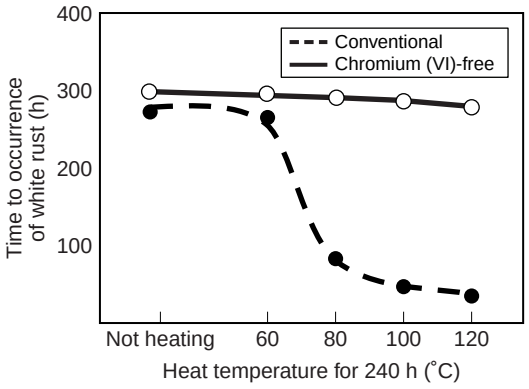


Fig. 11 Heat resistance of chromium(VI)-free on zinc (SST)

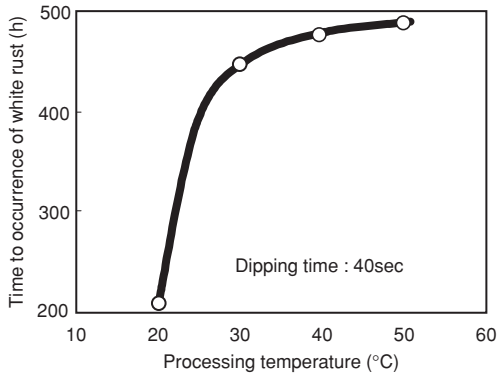


Fig. 12 Relation between processing temperature and time to occurrence of white rust (SST)

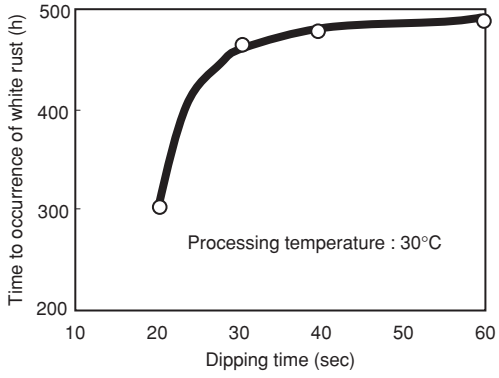


Fig. 13 Relation between dipping time and time to occurrence of white rust (SST)

This is believed to be caused by coagulation of the excess silica in the trivalent chromate surface layer, causing the surface to become rough.

This indicated the necessity of achieving a uniform distribution of silica within the treatment solution. There is a possibility of significant variations in torque coefficient being produced because of the surface roughness caused by silica flocculation.

7. Productivity

The occurrence of variations in corrosion resistance and torque coefficient in trivalent chromate-coated bolts produced in a mass-production coating facility was studied. Random samples of fasteners were taken from consecutive barrels. Figure 15 shows the results of SST of corrosion resistance and Fig. 16 shows measurements of torque coefficient.

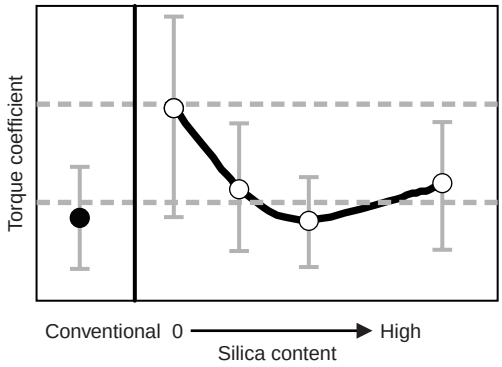


Fig.14 Relation between amount of silica added and torque coefficient

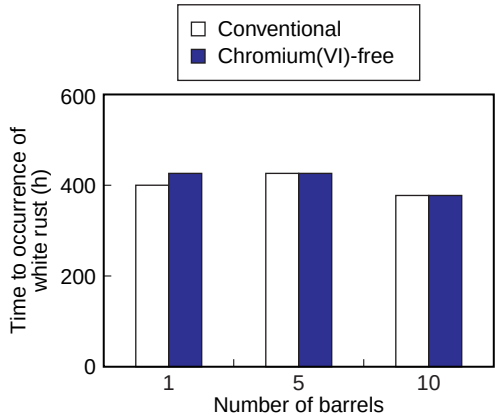


Fig. 15 Corrosion resistance of 10 consecutive barrels in facility

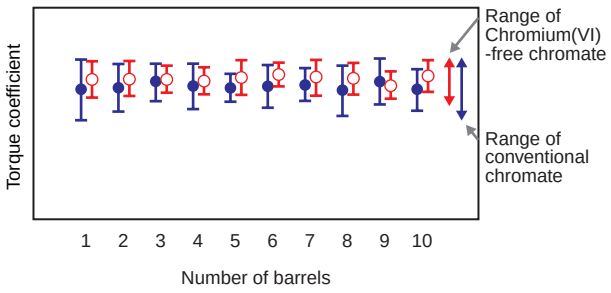


Fig.16 Torque coefficient of 10 consecutive barrels in facility

The trivalent chromate-treated bolts showed an equivalent range of torque coefficient as displayed by hexavalent chromate-treated bolts.

The results of measurements confirmed the achievement of a level of corrosion resistance and torque coefficient equal to those shown by hexavalent chromate coatings.

8. Evaluation of Durability in Actual Vehicles

Trivalent chromate-coated parts were fitted into a vehicle and put through comprehensive durability testing in corrosion-promoting environments to evaluate the durability of the new coating. For purposes of comparison, hexavalent chromate-coated parts were used in the right side of the vehicle and parts coated with the new trivalent chromate coating were used in the left side. Figures 17-19 show external views of the parts after testing.

The corrosion resistance of the trivalent chromate coatings was equivalent or superior to that of the hexavalent chromate coatings, and no impairment of fastener function was displayed in the course of testing.

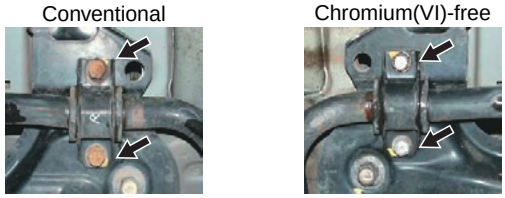


Fig. 17 Attachment bolt for stabilizer (front)

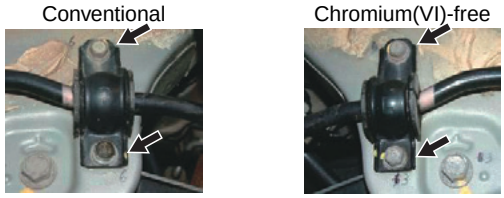


Fig. 18 Attachment bolt for stabilizer (rear)

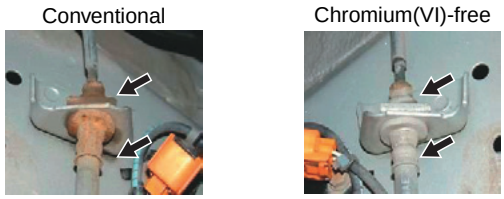


Fig. 19 Brake hose attachment nut (front)

9. Conclusion

A trivalent chromate coating possessing equivalent corrosion resistance and friction properties to conventional hexavalent chromate coatings has been developed a substitute for hexavalent chromate coatings. The following are the salient points of this development:

(1) In the new coating, silica shields the substrate from corrosion inducement factors in the external environment and metal chelate salts form a passivation coating, enabling the achievement of an equivalent level of corrosion resistance to the conventional hexavalent coating.

(2) The new coating has a two-layer structure: trivalent chromium and metal chelate salt layer at the boundary with the zinc coating, and a silica surface layer. These two layers are formed in a single production process.
(3) An equivalent range of torque coefficient (friction coefficient) to that of hexavalent chromate coatings has been achieved by optimizing the added silica content.
(4) Tests carried out on the production line to determine the suitability of the new coating to mass production demonstrated that the trivalent chromate coating process produced equivalent corrosion resistance and friction properties to the existing hexavalent chromate coating process.
(5) Durability tests of trivalent chromate-coated fasteners conducted in a vehicle, operating within a corrosion-promoting environment showed equivalent or superior corrosion resistance to hexavalent chromate coatings. There were no issues associated with clamping performance or function.

10. Afterword

The newly developed coating discussed in this paper has been applied on parts used in the 2005 model year LEGEND. For reference, Table 1 shows a list of other technologies employed in the new LEGEND and the main parts to which they have been applied.

Table 1 Application of chromium(VI)-free materials and relevant parts

Base materials	Conventional chromium(VI)	Chromium(VI)-free development	Application
Zn plating	Yellow chromate	Chromium(III) white chromate	Fastener Pipe
	Black chromate	Chromium(III) black chromate	Caliper
Zn-Ni plating	Yellow chromate	Chromium(III) white chromate	Brake pipe Fuel pipe
Sn-Zn plating	Yellow chromate	Chromium(III) white chromate	Hose metal parts
Zinc Aluminum composite coating	Chromate binder	Silicate binder	Fastener Stay
anti-corrosion primer	$SrCrO_4$ pigments	Epoxy resin Mg pigments	Brake pipe Fuel pipe
Aluminum	Chromate	Zirconium salt Titanium salt	Al wheel
		Anode oxidation	Wiper arm
Magnesium	Chromate	Zirconium salt	Engine head cover Oil pan

References

(1) Community legislation in force: Directive 2000/53/EC of the European Parliament and of Council of 18 September 2000 on end-of-life vehicles, Official Journal of the European Communities, L269, p. 34 (21/10/2000)
(2) Commission decision of 27 June 2002, amending Annex II of Directive 2000/53/EC of the European Parliament and of the Council on end-of-life vehicles, Official Journal of the European Communities, L170, p. 81-84 (2002)
(3) Suzuki, M.: Bousei Kanri, 40, p. 1(1996) (in Japanese)
(4) Suda, S., Ogino, M., Tanaka, N.: Tetsu to Hagane, 77, p. 1042 (1991) (in Japanese)
(5) Suda, S., Asari, M.: Zairyo to Kankyo, 46, p. 95-102 (1997) (in Japanese)
(6) Aoe, T.: Hyomen Gijyutsu, 49, p. 211 (1998) (in Japanese)
(7) Yoshimoto, I.: Neji Teiketsu Sekkeitai no Pointo, Gijyutsu Saakuru, Japanese Standards Association, p. 167-178 (2002) (in Japanese)
(8) Nishida, Y.: Zairyo to Kagaku no Kougaku, 41, p. 9 (2004) (in Japanese)
(9) Koudo, M. et al.: Hyoumen Gijyutsu, 54, p. 806 (2003) (in Japanese)
(10) Ishikawa, Y.: Hyoumen Gijyutsu, 44, p. 660 (1993) (in Japanese)
(11) Karube, T., Sako, R.: Hyoumen Gijyutsu, 53, p. 66 (2002) (in Japanese)

■ Authors ■


Kazunori TAKIKAWA


Tsutomu MIYADERA


Toshiaki OHTSUKA


Atsushi SHIRAKAWA


Mitsuo TAKASHIMA


Youji MATSUOKA

Development of Aluminum Alloy Rear-wheel Hub with Lightweight and High Strength for Off Road Motorcycles

Masaki AGATA* Mikio UCHIYAMA*
Yasuki ITO* Kyo TAKAHASHI*

ABSTRACT

A rear-wheel hub with lightweight and high strength that satisfies the needs for motocross riding and contributes considerably to the vehicle mass reduction has been developed. To reduce material, a hollow structure is used in the thick section of the flange on the sprocket side of the wheel hub, which transmits driving force. The thin-wall design is employed in the straight, cylindrical section of the hub. To maintain necessary strength of the structural part, the die-casting method, which is most suitable for a thin-wall product, is applied. With regard to the casting, the inner structure quality is ensured by applying a molten metal treatment, reducing the amount of gas by evacuating the cavity and providing a squeezing function after plunger ejection. As for the material, an Al-Si-Mg alloy is employed and T5 heat treatment is applied. Thus, the yield strength is improved by 27% and the tensile strength is increased by 30% compared to the conventional material.

1. Introduction

Off road motorcycles for motocross-competitions run on uneven roads with jump sections and tight turns. Therefore, the motorcycles require light handling and high run-through performance. Large impacts, such as jumps when riding, are applied to the suspension parts, which require high strength that can carry these shocks. At the same time, weight reduction is also important in enhancing road-holding ability by reducing unsprung mass. The wheel hub sprocket side flange of off road motorcycles transmits the driving force, so this section is subject to high loads. Therefore, reducing weight by employing a hollow shape for the thick section of the flange has been considered challenging. This development employed a new material with enhanced mechanical properties, an optimized casting design and casting conditions to allow the use of a hollow shape for the thick section of the sprocket flange side, and thin-walled straight cylindrical section. This resulted in a weight reduction of approximately 10%. Figure 1 shows the appearance of a motocross motorcycle applied to this new technology, and the developed wheel hub. This paper describes the material specifications, casting design, and casting conditions.

* Asaka R&D Center



Fig. 1 Appearance of CRF450R and developed wheel hub

2. Development Goals

The two main development goals were as follows:

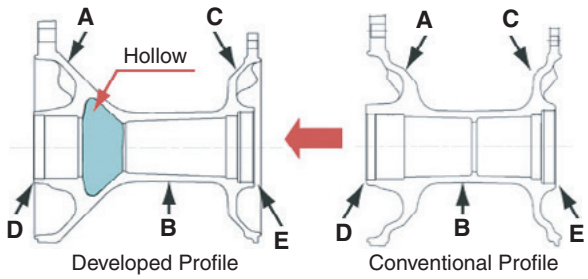
(1) Reducing weight by 10% or more, to provide weight reduction effects compared to conventional specifications.

(2) Provide endurance and reliability equivalent to wheel hubs manufactured using conventional manufacturing methods.

3. Technical Elements for Development

3.1. Part Structure

Rear wheel hubs manufactured by integrated molding using the aluminum die cast method are comprised of a cylindrical hub part through which the wheel axle passes, and a brake disk side flange and sprocket side flange, located on either end of this cylinder hollow in the axial direction. The sprocket side flange transmits the driving force, so it is subject to high loads and is normally thicker than the brake side flange on the opposite side. This thick section tends to increase the hub mass, so using a hollow structure for the thick section on the inside of the flange is an effective means of reducing the weight. Figure 2 shows the shapes of the conventional specification hub and the developed wheel hub. In the developed wheel hub, the section of the tapered part connecting the sprocket side flange and the straight cylindrical section has been increased and hollowed out by machining to form a large hollow structure. In addition, the straight cylindrical section uses a thinner new shape to reduce weight.



Profile	Thickness (mm)				
	A	B	C	D	E
Convention profile	4.8	5	6.2	6.3	3.5
Developed profile	3.4	4.75	4.4	4.2	2.5

Fig. 2 Comparison of developed profile and conventional profile

3.2. CAE Analysis

CAE is an effective method of early evaluations of function and performance, utilizing a three-dimensional CAD model, prior to manufacturing prototype parts. Stress analysis was performed by inputting a load to the new shape reduced weight wheel hub model under the assumption of use in an actual motorcycle. Figure 3 shows an example CAE analysis result. The shapes of the locations where high stress occurred were modified based on these results, and the required material strengths of the new shape were then obtained. These requirements were a yield strength of 185 MPa or more (15% increase over the conventional material) and a minimum tensile strength of 250 MPa (20% increase over the conventional material).

3.3 Manufacturing Method

The die cast method, which has high productivity and allows high accuracy for a thin part, was used as the manufacturing method for the developed wheel hub. However, the die cast method consists of injecting molten metal into a cavity at high speed, so gas inclusions occur more frequently than with gravity die casting (GDC) and low pressure die casting (LPDC). The developed wheel hub machines excess material away from the thick sections. This requires the hub to have higher internal quality compared to conventional parts, thus the following technologies were applied.

3.3.1. Molten metal treatment

(1) Oxides were eliminated using flux to help achieve and ensure the molten metal quality. Figure 4 shows some oxide confirmation samples made by the K molding method. Here, no oxides were confirmed on the fracture surface.

(2) Hydrogen gas was reduced by bubbling nitrogen gas, with the flow and time controlled. Figure 5 shows vacuum solidification samples produced under reduced pressure after bubbling. This enabled a reduction in the hydrogen gas level to 0.3 cm^3 or less.

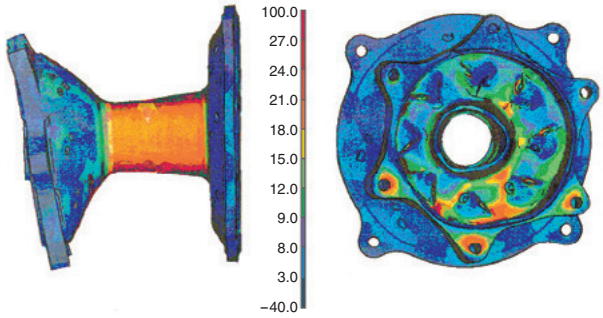


Fig. 3 Stress analysis result of wheel hub



Fig. 4 K-mold sample

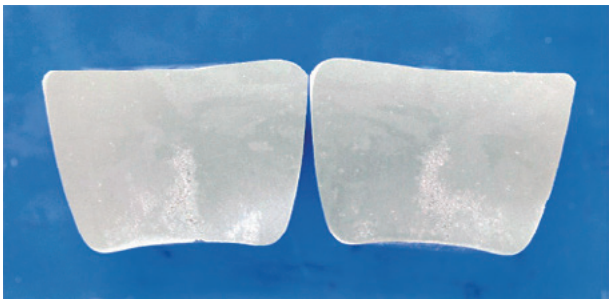


Fig. 5 Vacuum solidification sample

3.3.2. Casting technology

(1) The injection sleeve used a ceramic sleeve with superior insulating properties, and the temperature was controlled using a heater to prevent rupture chill crystals. Injection sleeve lubrication used a powder lubricant with high molten metal heat insulation characteristics when compared to water soluble lubricants. This prevented a drop in the molten metal temperature.

(2) The inside of the cavity was depressurized at the same time the die close operation was completed. This negative pressure enhanced the molten metal filling performance and prevented air inclusions when filling. Figure 6 shows the vacuum die casting system configuration.

(3) The die design, which includes overflow positions, gate positions, gate area, and filling time, and casting conditions were optimized using casting simulations. Figure 7 shows the simulation results. Simulations of the molten metal flow were performed to investigate designs that resulted in an even filling pattern along the overflows. Simulations of gas inclusion were performed to create designs where the gas was driven into the overflows. Simulations of the molten metal temperature were used to determine the casting design and casting conditions that produced no misruns.

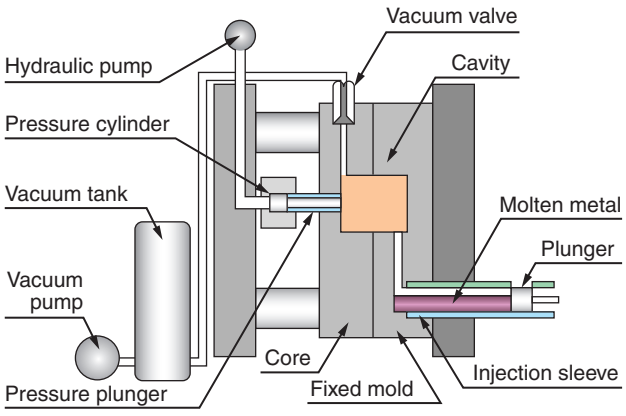


Fig. 6 Outline of vacuum die casting system

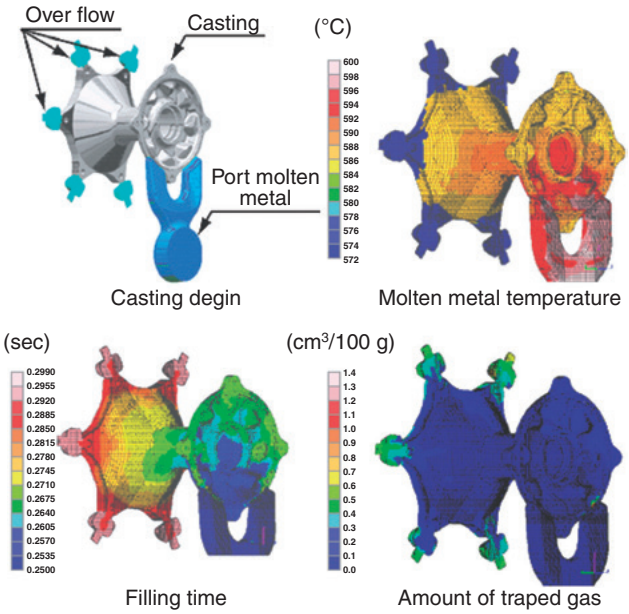


Fig. 7 Simulation of molten metal flow

(4) The thick section of the sprocket side flange was squeezed after plunger ejection. This effectively pressurized the molten metal before solidification and reduced the occurrence of shrinkage cavities, blowholes and other casting imperfections.

3.4. Materials Specifications

New materials that specified the component ranges of alloys added to an Al-Si-Mg base were used to satisfy the required material strength of a lightweight wheel hub. Table 1 shows a comparison of the chemical composition.

Contents of additive compositions were as follows.

(1) The Si content was set at 9.5 to 11.5% mass to provide good casting performance.

(2) Fe is an effective element for preventing seizure to the metal die, but crystallizes acicular Al-Fe-Si compounds, which is a factor that impedes ductility. Therefore, the Fe content was set at 0.15% mass or less.

(3) Mn 0.5 to 0.8% mass content was included to prevent metal die seizure due to the reduction in the Fe content.

(4) Sr 0.01 to 0.02% mass content was included to refine the eutectic Si. Refinement of the eutectic Si is an effective means of enhancing elongation properties.

(5) Adding Mg can increase the material strength by precipitating Mg_2Si during the aging treatment. Increasing the Mg content increases the yield strength but deteriorates ductility. Therefore, the Mg content was set at 0.4 to 0.5% mass in consideration of the balance between the yield strength and ductility required for a wheel hub.

Table 1 Chemical composition

(%)

	Si	Fe	Cu	Mn	Mg	Zn	Ti	Sr	P	Sn	Ni	Other
Developed alloy	9.5 - 11.5	≦0.15	≦0.03	0.5 - 0.8	0.15 - 0.50	≦0.07	0.04 - 0.15	0.010 - 0.015	≦0.001	–	–	≦0.10
Conventional alloy	8.5 - 11.0	≦1.0	1.0 - 2.5	≦0.3	≦0.2	≦1.0	–	–	–	–	≦0.3	–

Figure 8 shows the metallic structure of the developed alloy. The eutectic Si has been refined, and there are no acicular intermetallic compounds.

3.5. Heat Treatment

T5 heat treatment was used to obtain the necessary yield strength. In order to obtain the maximum effects with T5, quenching should be performed from high temperatures to create a super-saturated Mg solid solution and large amounts of Mg_2Si should be precipitated by artificial aging. Figure 9 shows the aging curves. Water quenching was used and the aging time conditions were set at 170 °C x 7 hours to obtain the maximum strength. Figure 10 shows the yield strength properties produced by the different quenching methods after casting. When aged at the same temperature, 170 °C, water quenching increased the yield strength by 10% compared to air quenching. This is thought to be because the rapid cooling during quenching increased the Mg solid solution amount, which provided effective age hardening. Compared to the F material, the yield strength increased 25% by using the water quench method. Figure 11 shows the relationship between time after removal from the die until water quenching and the yield strength. The yield strength was high when quenching was performed shortly after removal from the die, and decreased as time until quenching increased. This is because the work temperature drops as time passes. In order to obtain the required strength, water cooling was performed within 10 seconds after removal from the die. The quenching tank was controlled to a temperature of 60 °C or less at all times in order to reliably obtain the required strength.

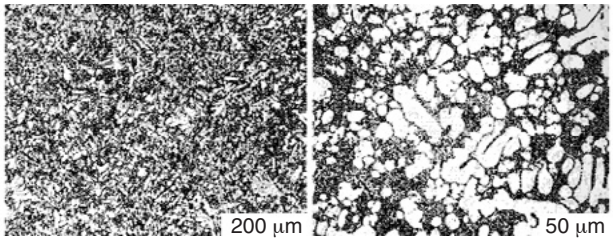


Fig. 8 Microstructure of developed material

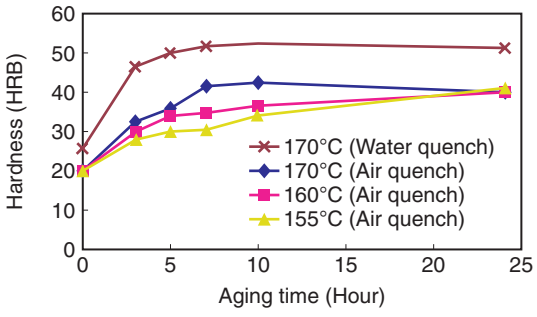


Fig. 9 Aging curve of developed material

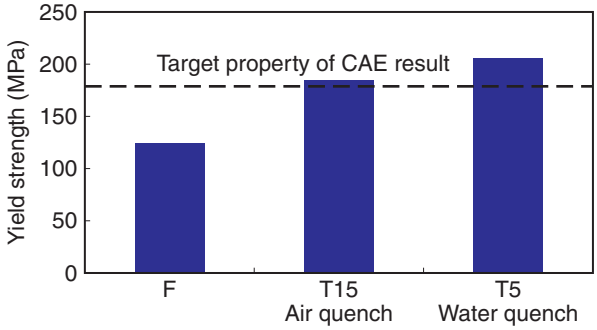


Fig. 10 Yield strength of each quench method

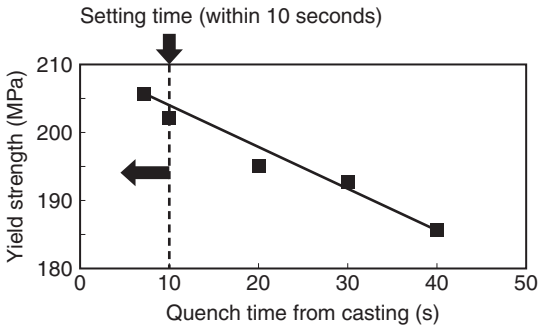


Fig. 11 Relationship between yield stress and quench time from casting

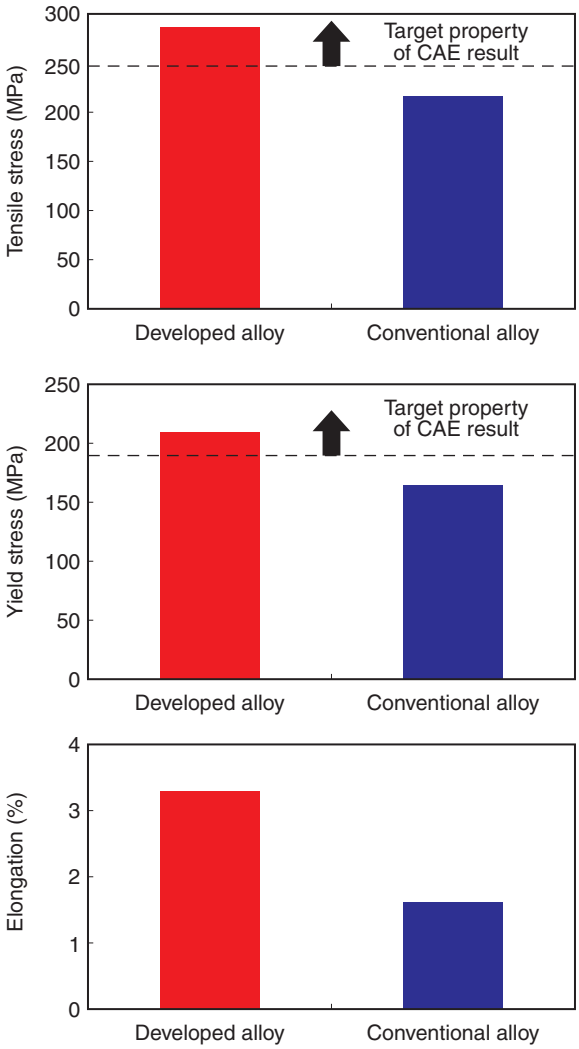


Fig. 12 Mechanical properties of developed alloy and conventional alloy

4. Test Results

Adopting the new shape reduced the mass from 1 065 grams for the conventional material, to 957 grams, for a weight reduction of 10.1%.

4.1. Mechanical Properties

Figure 12 shows the mechanical property results obtained. The developed material with the above specified heat treatment applied was able to achieve a yield strength of 206 MPa, a tensile strength of 286 MPa, and an elongation of 3.3%, which are increases of 27%, 30%, and 106%, respectively, when compared to the conventional material.

4.2. Internal Quality

Figure 13 shows internal quality of the wheel hub material. The internal quality obtained was the same high level as that of conventional die cast parts, including the thick section of the sprocket side flange and the straight cylindrical section.

4.3. Bending Fatigue Strength

Figure 14 shows fatigue curves for the developed and conventional materials. In motocross competitions the wheel hub receives a large load from jump landings on an order of 10^3 times, and the total over the life of a racing motorcycle is thought to be 10^5 times or less. The developed material shows a 10 to 15% increase in fatigue strength compared to the conventional material for a number of cycles from 10^3 to 10^6 times. Thus, the developed material provides sufficient performance as a wheel hub for motocross motorcycles.

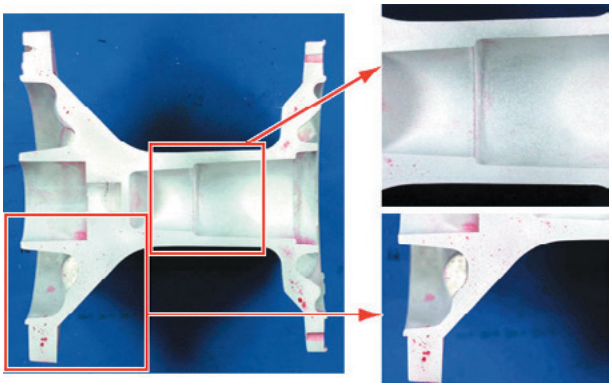


Fig. 13 Internal quality of wheel hub

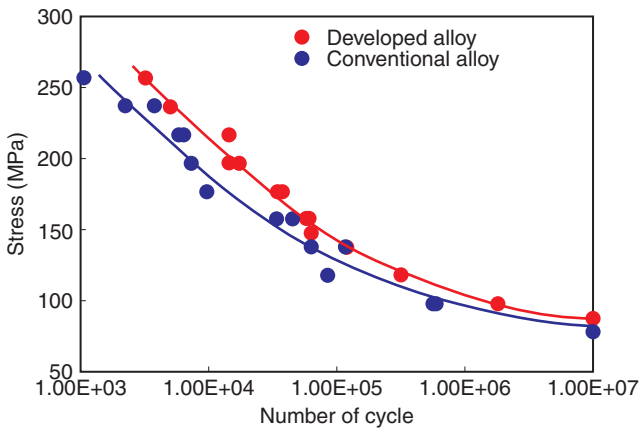


Fig. 14 Fatigue strength of dveloped alloy and conventional alloy

4.4. Torsional Endurance Test

Discrete torsional endurance tests to evaluate the number of cycles to fracture were conducted by fixing the sprocket with the spokes, wheel rim and sprocket attached to the wheel hub, and then applying a certain torque to the rim. As shown in Fig. 15, the number of cycles attained until the wheel hub fractured was approximately 70% higher for the developed material than for the conventional material.

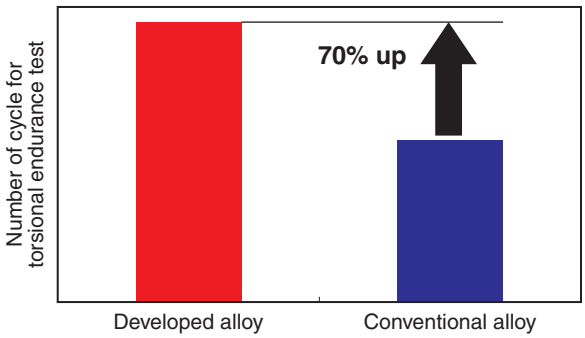


Fig. 15 Comparison of torsional endurance test results

5. Conclusion

(1) A reduction in the thickness of various wheel hub sections was achieved utilizing new materials, optimizing the heat treatment conditions and making use of the increase in strength.

(2) Optimization of the casting design and casting conditions helped to realize good internal quality in the thick sections of the wheel hub, which allowed a hollow-machined shape. This enabled the development of a rear wheel hub with lightweight and high strength that achieved a weight reduction of 10.1% (-108 g) compared to the conventional part.

Acknowledgements

The authors wish to express their deep thanks to Kyushu Yanagawa Seiki Co., Ltd. for their help in promoting this development.

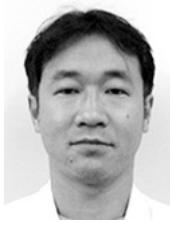
References

(1) Watanabe, S.: Jidousya Buhin you Kou Ensei Daikasuto Goukin no Kaihatsu, Al-aru, Dec, p. 13-17 (2002) (In Japanese)

(2) Handbook of Advanced Aluminum Technology, Light Metal Publishing Co., Ltd

(3) Kenkyu Houkoku 74 Daikasuto no Tyuzou Kekkan to Taisaku, Japan Foundry Engineering Society (1996) (In Japanese)

■ Authors ■



Masaki AGATA



Mikio UCHIYAMA



Yasuki ITO



Kyo TAKAHASHI

Development of Low-cost Material for Engine Exhaust Valve Seat

Hiroyuki OKETANI* Ryushi TSUBOTA* Masao ISHIDA*

ABSTRACT

A low-cost material for engine exhaust valve seats has been developed with the aim of a positive use of an oxide layer. A cost reduction of more than 40% has been attained while maintaining the same or better anti-wear characteristics and machinability as current materials by the optimum designation of density, the optimum addition of secondary hard particles and the special consideration given to the basic iron powder shape for microscopic vacancy without using a special molding method such as repressing and resintering (2P2S), copper infiltration, resin impregnation, nor using a high cost material such as Cr-Mo-Co, Co, or Ni powder to enhance the generation of an oxide layer.

1. Introduction

The main type of engine valve seat in use today is an iron sintered material insert type because of its material flexibility, low cost and abrasion resistance. Additionally, because the practical air fuel ratio is getting closer to the stoichiometric air fuel ratio in order to save fuel and meet ever stricter exhaust emissions regulations, combustion products are unlikely to provide buffering effect, so sintered valve seats (hereinafter referred to as valve seats) should provide enhanced abrasion resistance, which includes tolerance of higher exhaust temperatures[1] and increasing combustion pressure. To achieve abrasion resistance, valve seat materials undergo special production techniques such as repressing and resintering (hereinafter referred to as 2P2S) and copper infiltration as well as the addition of expensive metal powders like Co base alloy powder (Cr-Mo-Co-based) or Co or Ni powder. These are leading to great increases in the cost of valve seats.

In this research, the generation of an oxide layer (triiron tetroxide) that occurs when the engine is running was the focus, and by actively using this layer, an exhaust valve seat material with low cost and excellent abrasion resistance was developed. This paper reports on the content of this research.

* Asaka R&D Center

2. Development Goals

Figure 1 shows the raw material costs and the abrasion resistance results of a unit rig test of exhaust valve seat materials presently used in Honda motorcycles.

This development was to realize low cost and high abrasion resistance, and the red area shown in Fig. 1 was set as its goal. Specifically, abrasion resistance is equal to current materials, the cost reduction is more than 30% compared with current materials.

3. Establishment of Unit Abrasion Test Correlating with Actual Engine Endurance Test

Before starting the development, a compatibility test was performed to use a valve seat material that had been previously developed for automobiles (herein after referred to as diversion material) as a possible low cost valve seat material for motorcycle engines. As shown in Fig. 2, however, contrary to the unit abrasion results, actual engine endurance result was inferior to current materials.

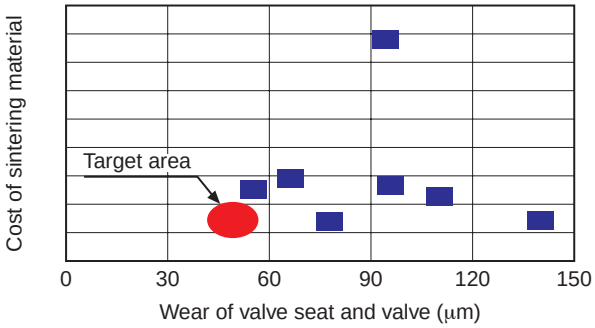


Fig. 1 Target of development

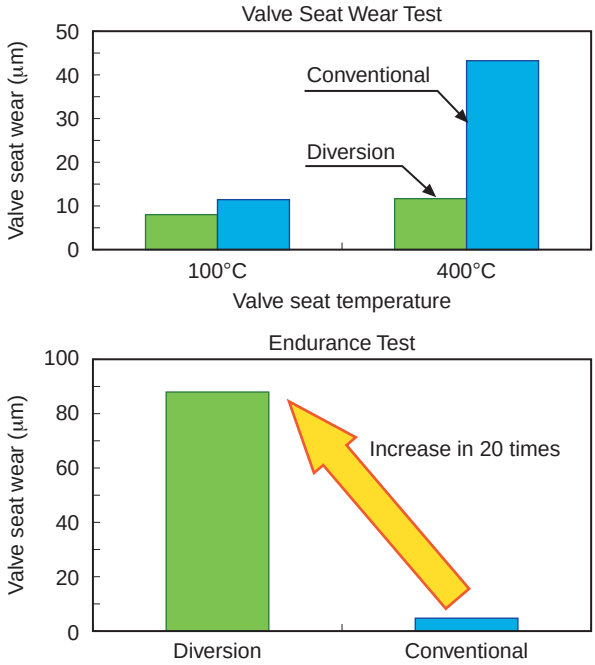


Fig. 2 Result of valve seat wear test & endurance test

3.1. Analysis of Components after Actual Engine Endurance Test

An examination of diversion material components that underwent high speed actual engine endurance testing and in which wear occurred found that, as Fig. 3 shows, there was metal contact, with no combustion products on the valve seat face and no generation of oxide layer. Further, it was found that initial wear occurs at the high running speeds characteristic of motorcycles (10 000 r/min and higher) because of insufficient fit with the valve.

3.2. Verification of Correlation of Unit Abrasion Test and Actual Engine Endurance Test

Figure 4 shows the unit abrasion testing machine and the test conditions. In the past, unit abrasion tests have been performed with an air fuel ratio of 8 - 9, with the results showing much buildup of combustion products on the valve seat face, so that the conditions of the evaluation were favorable for abrasion resistance. After tests, significant combustion product, carbon, was found on the valve seat face. This aspect is very different from what is seen on components after actual engine endurance testing.

The air fuel ratio was, therefore, changed to 13 - 14, and the amount of combustion products on the valve seat face was decreased. In addition, cam speed was increased from the former 3 000 r/min to 4 500 r/min, to increase valve contact load. This aim achieved a load level similar to that of an actual engine. These changes yielded results similar to those from actual engine endurance tests, as shown in Fig. 5. As shown in Fig. 6, combustion products and surface oxidation on the valve seat face were not detected after actual engine endurance testing by using the diversion material with much wear for the conventional material. These conditions were adopted as the standard conditions for the unit abrasion test.

4. Material Specifications

4.1. Materials Concept

Figure 7 shows the valve seat temperature and amount of wear of valve seat and valve face from the unit rig test performed under the conditions shown in Fig. 4. For the medium temperature range, valve seat wear increases relative to temperature, but the amount

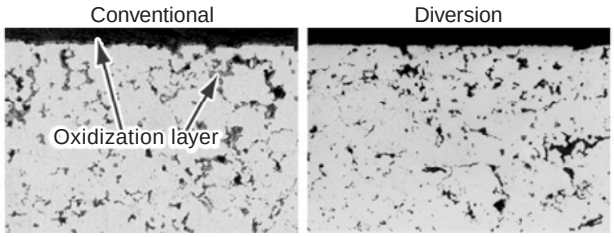
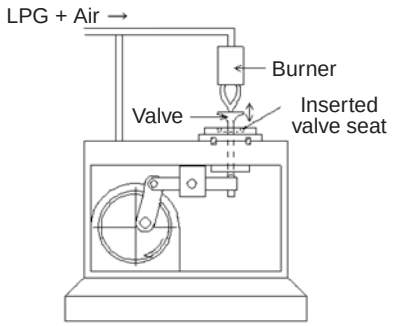


Fig. 3 Microstructure after endurance test



Test conditions

	Conventional	Improvement
Cam revolution	3 000 r/min	4 500 r/min
Valve revolution	10 r/min	10 r/min
Test time	4.5 hr	9 hr
Valve material	45% Ni	45% Ni
Air fuel ratio	8-9	13-14

Fig. 4 Valve seat and valve wear testing machine

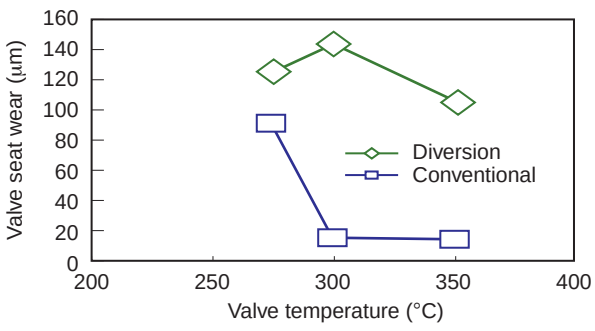


Fig. 5 Result of improvement valve seat wear test

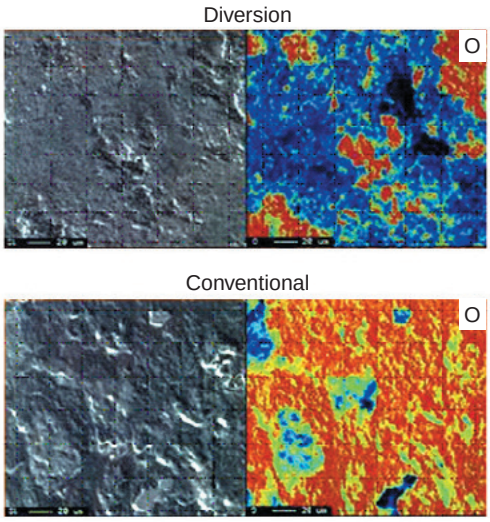


Fig. 6 Surface analysis (EPMA)

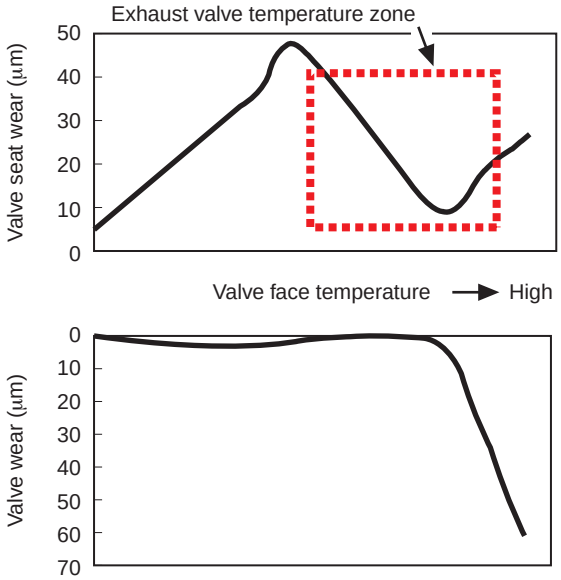


Fig. 7 Valve seat wear of temperature dependability

of wear tends to decline from a certain temperature. It is believed that the amount of wear decreases due to the low coefficient of friction and adhesion proof effect of the oxide layer (triiron tetroxide). As the temperature continues to increase, the high temperature hardness balance between the valve seat and valve face starts to decay, resulting in wear of the valve face.

In motorcycle engines, it has been identified from past data that the area within the broken red line of Fig. 7 is the range of temperatures at which exhaust valve seats are used.

Since running conditions in actual vehicles vary and the atmosphere around the valve seat varies greatly by driving conditions, it is believed that an early generation of a good oxide layer is important to ensure stable abrasion resistance. The concept of this developed material was to realize a low cost production method and to ensure a generation of oxide layer by using metal powders.

4.2. Examination and Selection of Base Material

Heteromorphic iron powder that has irregular shape with large surface area was used instead of spheroidal iron powder as the base iron powder in order to promote oxidation of the base material. Results of an oxidation test by heating showing oxidation properties is shown in Fig. 8, and a photograph of the internal microstructure after the test is shown in Fig.9. The developed material using heteromorphic iron powder has many microscopic cavities compared to the spheroidal iron powder. By above-mentioned reason, it is believed that good results of oxidation test by heating were shown.

Next, the alloying for the base material was examined to enhance heat resistance under high temperatures. Co powder, which is in heavy usage, is widely beneficial for generating good oxide layers, but its cost as a powder is high. Furthermore, it was excluded as an addition metal powder candidate for environmental reasons. Ni powder has similarly been removed as a candidate because of cost increases and environmental issues, so an addition metal powder was selected from the various steel alloy powders. Oxide layer generation and diffusion during sintering properties were emphasized, powder cost, hardness, and machinability were considered for steel alloy powder selection. Ultimately, Ni-Cu-Fe partial diffusion iron alloy powder was chosen.

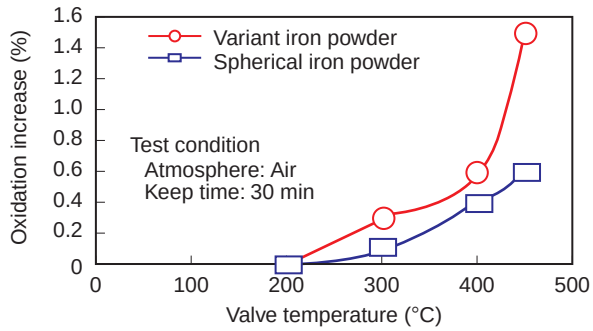


Fig. 8 Oxidation test of base iron powder

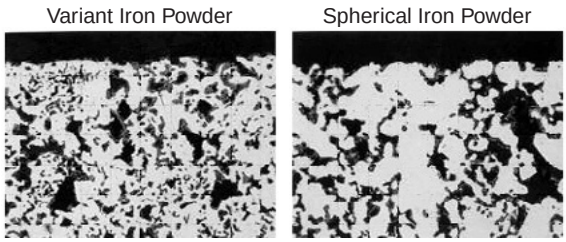


Fig. 9 Microstructure after oxidation test

4.2.1. Selection of hard particle material

Hard particles, which greatly affect the abrasion resistance of valve seat, are the base constituent of iron sintered valve seat material. In order to select materials for hard particles, coefficient of friction, oxide layer generating property, diffusion with the base material, fracture toughness, and powder cost were examined. Figure 10 shows results of lubricity tests of major hard particles.

In terms of the coefficient of dynamic friction and scuff load assessment, Mo-Ni-Cr-Co hard particle powder proved better than C-Cr-W-Co stellite powder and Fe-Mo ferroalloy powder and had characteristics next to Co base alloy powder Cr-Mo-Co.

The diffusion to the base is also an important factor for preventing defluxion of hard particles and for forming a high alloy phase of base material. Mo-Ni-Cr-Co powder showed better diffusion properties than stellite powder or ferroalloy powder, as shown in

Fig. 11. Mo-Ni-Cr-Co powder was selected by combined judgment, including fracture toughness and powder cost, as the hard particles for this developed material. Although Cr-Mo-Co powder has excellent abrasion and adhesion resistance, it is also costly and was excluded from application to the developed material, because cost reduction was the aim. Figure 12 shows the relative cost of hard particles, where the cost of Cr-W-Co material is defined as 1.

4.2.2. Examination of hard particle additive amount

The optimum addition amount of Mo-Ni-Cr-Co powder was examined. Figure 13 shows the results of unit abrasion tests in actual engines and under simulated conditions on the relationship between the amount of hard particles added and the amount of wear. The amount of valve seat wear decreases as the amount of hard particles increases, but this effects tends to saturate when amount of hard particle additive exceeds 20%. On the other hand, the amount of valve face wear tends to increase from 20% in addition amount. Based on the above test results and the cost consideration, the amount of hard particles to add in the developed material was set at 20%.

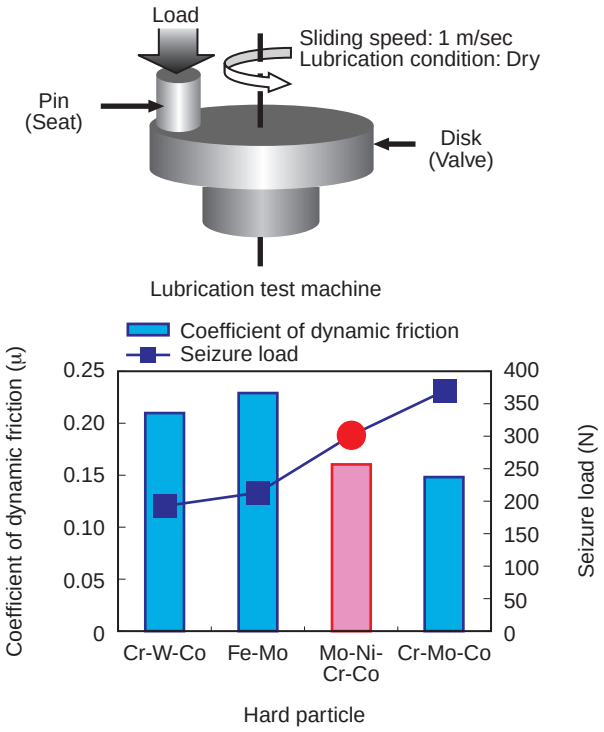


Fig. 10 Lubricity of hard particle

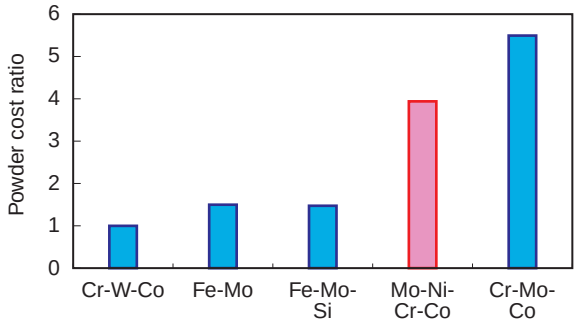


Fig. 12 Cost of hard particle

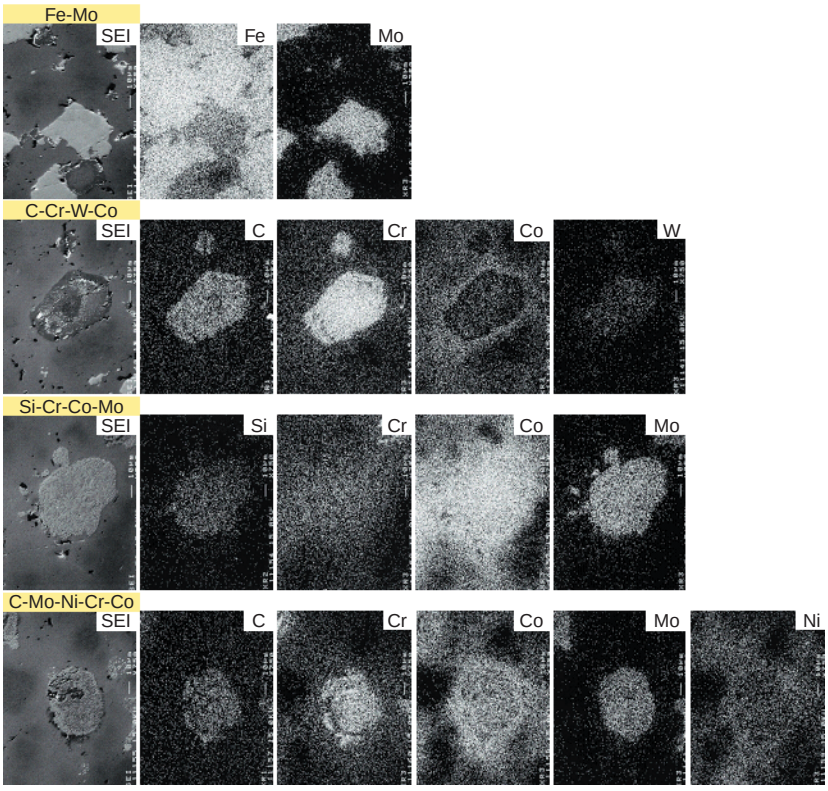


Fig. 11 Surface ultimatic analysis development (EMPA)

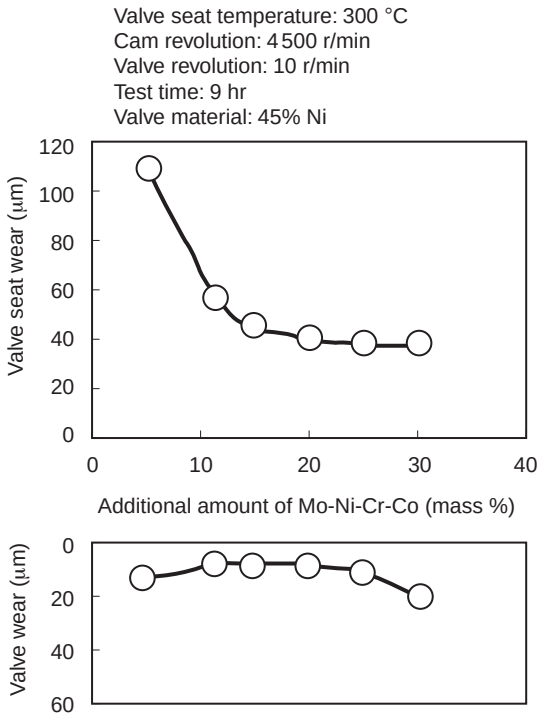


Fig. 13 Effects of hard particle amount for wear amount

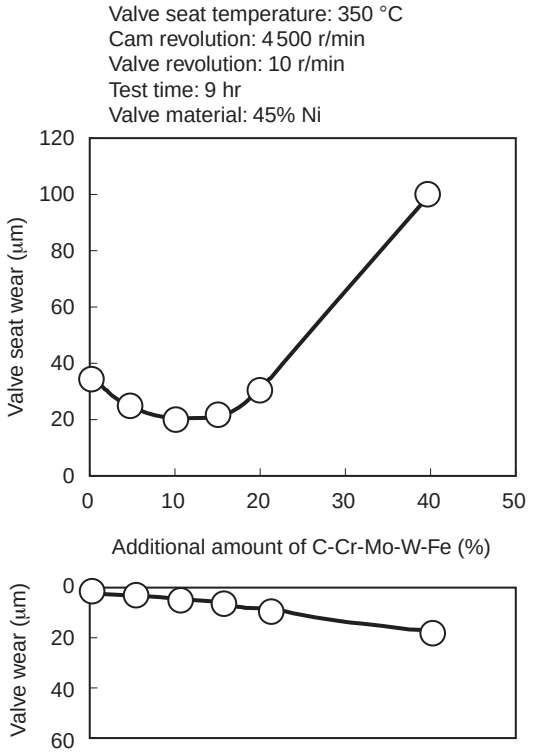


Fig. 14 Effects of fine carbide amount for wear amount

4.3. Examination of Secondary Hard Particle Additive Amount

In order to control initial wear before generating an oxide layer, in addition to the main hard particles, the optimum amount of secondary hard particles made of microscopic powder was examined. The type of hard particle selected was C-Cr-Mo-W-V-Fe powder, used in high-speed tool steels, by considering hardness, powder cost, and overseas availability. The amount of this additive was decided based on generation properties of oxide layer and abrasion resistance. Heteromorphic iron powder and Ni-Cu-Fe partial diffusion iron alloy powder were used for the base material iron powder. The addition amount of secondary hard particles was changed variously based on valve seat material that included the 20% addition of the main hard particle powder, Mo-Ni-Cr-Co. Figure 14 shows result of unit abrasion test on the relationship between the amounts of secondary hard particles added and the amount of wear. Wear was lowest at 10% and tended to increase even when increasing and decreasing the amount of additive.

Figure 15 shows the result of a valve seat material oxidation test by measuring the oxidation increase, and Fig. 16 shows the result of a radial crushing strength test. The oxidation increase tends to decline in inverse proportion to the amount of C-Cr-Mo-W-V-Fe powder added. In contrast, radial crushing strength tended to increase in proportion to the amount added. Based on these results, it is conjectured that excessively adding C-Cr-Mo-W-V-Fe powder reduces the generation of oxide layer and affects abrasion resistance. Considering the radial crushing strength and the oxide layer generation property, the amount of high-speed tool steel powder (secondary hard particles) to add was set at 10%.

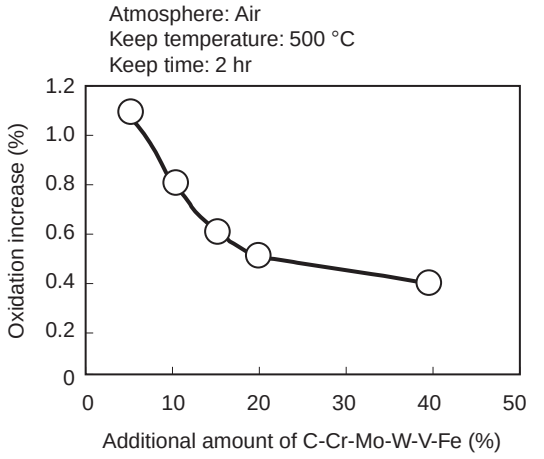


Fig. 15 Effects of fine carbide amount for oxidation increase

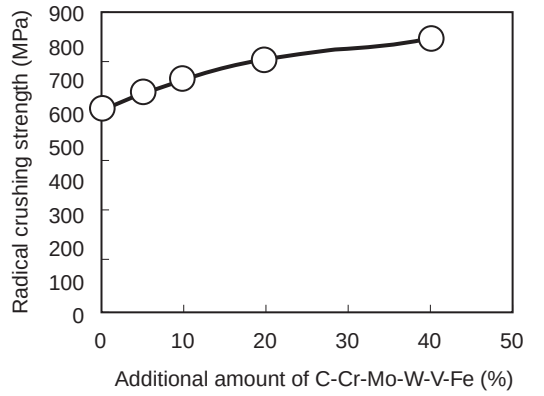


Fig. 16 Effects of fine carbide amount for radical crushing strength

4.4. Examination of Optimum Density

An abrasion resistance test with varying densities was performed; the results are shown in Fig. 17. Regarding the abrasion resistance of valve seat materials, it is generally known that abrasion resistance increases as density increases, but it was identified that an optimum density for abrasion resistance exists in the developed material.

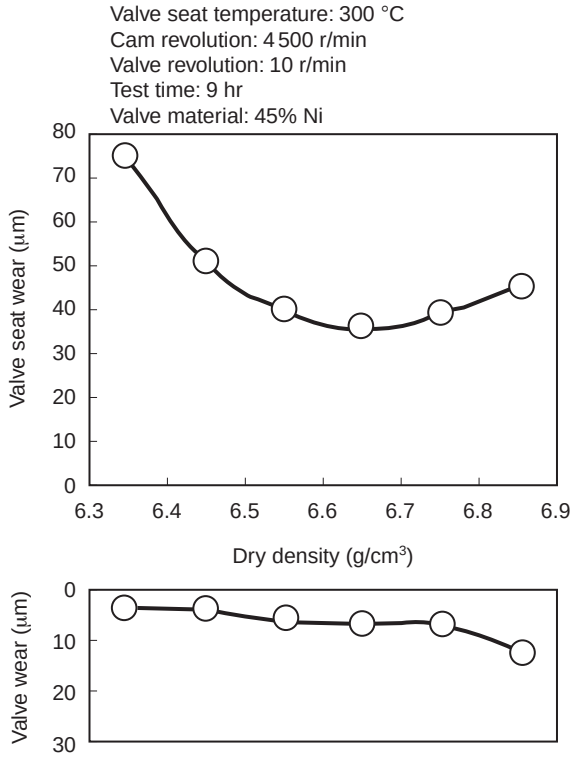


Fig. 17 Effects of dry density for wear amount

The above phenomenon was examined on the oxide layer generation property and the radial crushing strength. Figure 18 shows the result of radial crushing strength test. Figure 19 shows the result of oxidation test. The oxidation increase test was also performed as a comparison using Co powder base material. In the radial crushing test, radial crushing strength tends to increase as density increases.

However, in the results of oxidation test, fluctuations in mass gain to changes in density by oxidation of the base material that used Co powder are few and stable. On the other hand, the developed material without Co powder tends to increase mass gain with density decrease. These facts indicate that increasing density in the powder's composition does not necessarily contribute to an increase in abrasion resistance, and therefore conditions where the density of the developed material is set at 6.55 - 6.75 g/cm³. This density can be achieved by the compressing once and sintering once (1P1S) method.

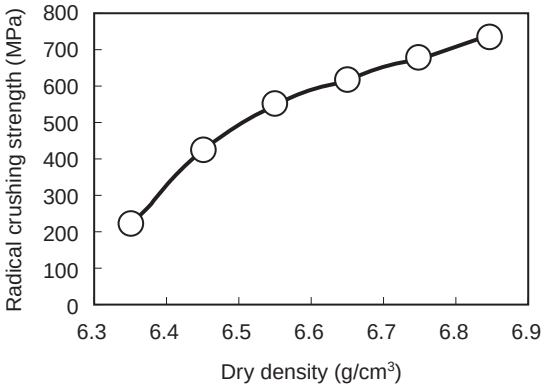


Fig. 18 Effects of dry density for radical crushing strength

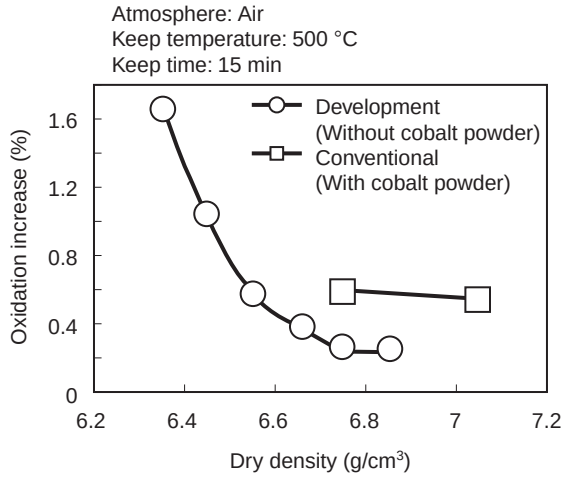


Fig. 19 Effects of dry density for oxidation increase

4.5. Specifications of Developed Material

Table 1 shows the chemical composition, density and hardness of the developed material. Figure 20 shows the internal microstructure. The developed material's structure consists of a mixture of Mo-Ni-Cr-Co hard particles, C-Cr-Mo-W-V-Fe based fine carbide and microscopic cavities in a pearlite layer and high alloy phase base.

5. Performance Evaluation of Developed Material

5.1. Unit Abrasion Test Results

Figure 21 shows the abrasion resistance properties of the developed material and comparison material from a unit abrasion test in which the valve seat temperature and air fuel ratio were controlled. A composite material of stellite hard particles with highest wear resistance, which is the exhaust valve seat material currently used by Honda; Fe-Mo hard particles, Co powder, and 2P2S material, was used as a comparison material. The developed material demonstrates abrasion resistance better than or equal to the comparison material.

Table 1 Chemical composition, density and hardness of developed material

Chemical composition (mass %)									
C	Ni	Cr	Mo	Co	W	V	Cu	S	Fe
1.2	3.6	5.2	5.5	8.0	0.6	0.2	0.6	0.2	Bal.

Density (g/cm³)	Hardness (HRB)
6.65	97

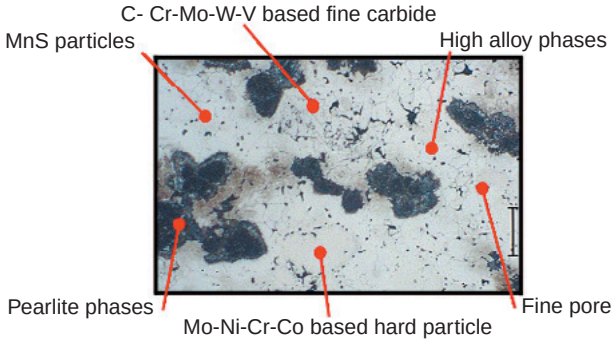


Fig. 20 Microstructure of developed material

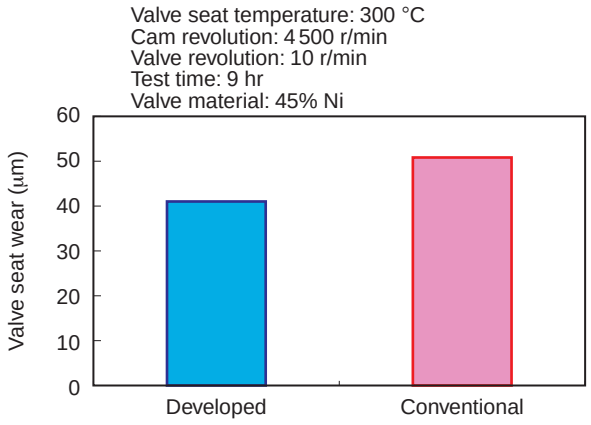


Fig. 21 Wear test result of developed material

5.2. Machinability of the Developed Material

Valve seats also require good machinability in conjunction with abrasion resistance. Figure 22 shows measurement results of cutting resistance value by using a cutting test machine. Figure 23 shows surface roughness profile for valve seats produced on a mass production line. The developed material's cutting resistance value and surface relative roughness after cutting were about the same as those of the present material, and even without post-processes, like resin impregnation for enhanced machinability, the developed material has as much machinability as the present material.

5.3. Cost of Developed Material

Figure 24 shows the powder cost ratio of the developed material and current material, and the raw material cost of which the developed material prior to machining is defined as 100. The powder cost ratio shows that the developed material is more than 40% less costly than the current material.

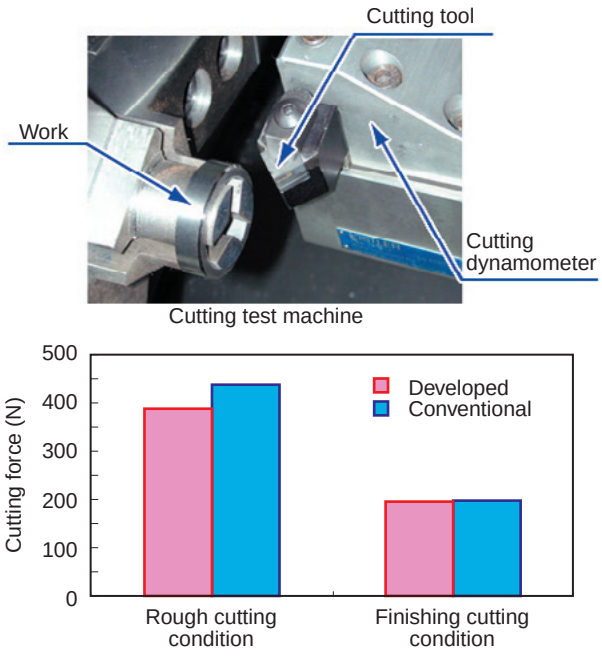


Fig. 22 Result of machining test

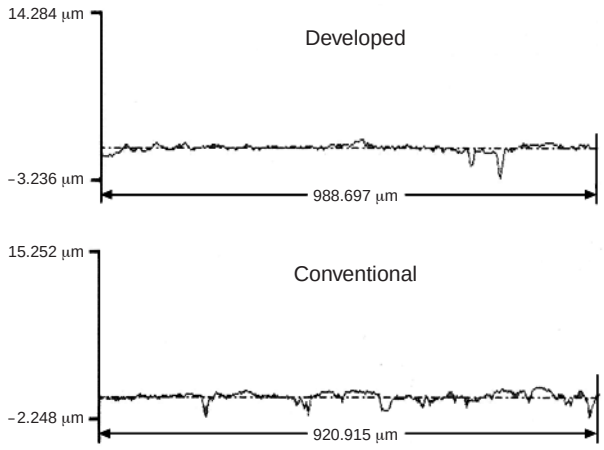


Fig. 23 Surface roughness profile of valve seats

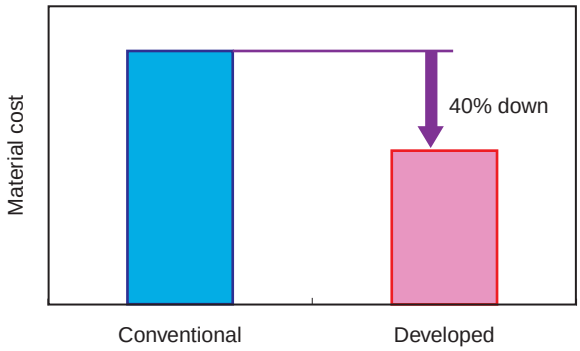


Fig. 24 Cost of developed material

6. Actual Engine Endurance Test Results

Figure 25 shows the bench endurance test results with a super-sports motorcycle from Honda. In both high revolution endurance mode and long life endurance mode, the amount of wear in the developed material was about the same or less than the current material. Actual engine endurance results using different valve materials in other models likewise showed about the same or less wear than in current material.

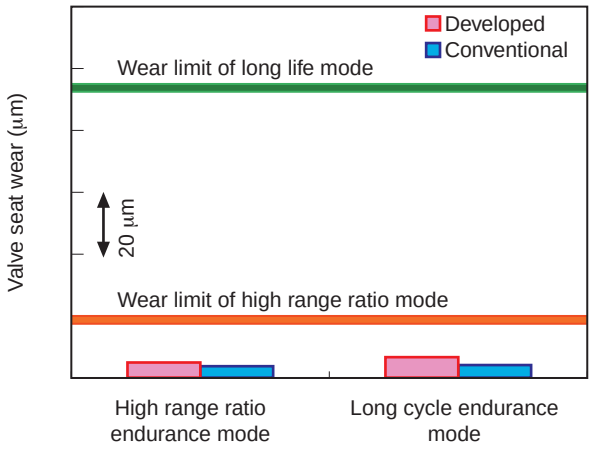


Fig. 25 Endurance test result of developed material

7. Conclusion

An exhaust valve seat material was developed that, while not needing 2P2S (repressed and resintered) processing, infiltration, impregnation or other post-processing, provided abrasion resistance as well as or better than current material while costing 40% less.

(1) An optimal density for abrasion resistance was selected for seat materials not containing Ni or Co powders by balancing oxidation increase and radial crushing strength.
(2) Because excessively adding fine hard particles inhibits oxide layer generation and decreases abrasion resistance, the amount added was optimized.
(3) Heteromorphic iron powder was used instead of spheroidal iron powder as the base powder material in order to produce microscopic cavities.
(4) Less expensive hard particles with low coefficient of friction and high base diffusion were added at optimal levels.

The developed material is being used in the mass produced 2004 model year CBF600F and its use is to be expanded in succession to other mass produced models.

Acknowledgements

The authors would like to express their profound appreciation to the staff members of Nippon Piston Ring Co., Ltd. who collaborated in the development project.

References

(1) Takahashi, T., Kakiuchi, A., Sato, K., Sato, K., Tominga, K.: Development of Exhaust Valve Seat Insert Material for High Performance Engines, SETC Paper 20024310/2002-32-1817

■ Authors ■


Hiroyuki OKETANI


Ryushi TSUBOTA


Masao ISHIDA

Camera Calibration by Ray Tracing

Chiaki AOYAMA*

ABSTRACT

A highly accurate method of camera calibration which works by tracing the light rays incident on the camera has been developed. In this method, the relative position of the point light source is adjusted to position the point light source image in the center of each pixel. Afterwards, the relative distance to the point light source is changed and the relative position of the point light source is adjusted again. A three-dimensional locus of the incident rays to the two point light sources obtained is then estimated from the relative positions. This procedure can be used to determine the relative positions of multiple cameras. The accuracy of the method was verified by calibrating a stereo camera and estimating the three-dimensional position of the point light source. The camera calibration method displayed identical accuracy for an image across an irregularly warped shield, which is conventionally a difficult condition for calibration, as when no shield was present. In addition, it was confirmed that there was deviation from the pinhole camera model (no crossing of incident rays).

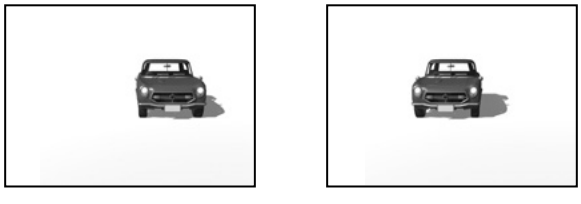
1. Introduction

The ability to recognize the environment is necessary for autonomous robots to perform actions in response to a changing external environment, and cameras mounted in robots are used as image sensors for this purpose[(1) - (4)]. If relative three-dimensional (3D) positions can be accurately estimated, robots can not only move to avoid obstacles, but the recognition ability can also be applied to actions that involve manipulation of the environment, such as grasping objects.

Stereo vision based on the difference in the appearance of images taken with multiple cameras, as shown in Fig. 1, is often used to estimate relative 3D positions between the cameras and the environment.

Binocular stereo vision can be used to calculate the relative 3D position to the target using Eq. (1) if the incident ray from the corresponding position on the target to each camera is known.

For example, the procedure for estimating the relative 3D position (P_x, P_y, P_z) of a headlight in Fig. 1 is as follows. First, the headlight position in the left image that corresponds to the same headlight in the right image is obtained. Next, the incident ray parameters (γ_1, α_1, α_2, x_1, y_1, z_1, x_2, y_2 and z_2 in Fig. 2) that correspond to the two-dimensional (2D) image position (pixel position) of the headlights in each image are derived from values measured beforehand. Finally, these parameters are applied to Eq. (1) to estimate the relative position of the headlight.



Left image Right imate

Fig. 1 Stereo images

* Wako Research Center (HGF)

$$P_x = \frac{x_1 \tan\alpha_1 - y_1 - x_2 \tan\alpha_2 + y_2}{\tan\alpha_1 - \tan\alpha_2}$$
$$P_y = (P_x - x_1)\tan\alpha_1 + y_1 \quad (1)$$
$$P_z = (P_x - x_1)\tan\gamma + z_1$$

In other words, estimation of relative position using stereo vision is divided into two processes. The first process is to estimate the pixel positions that show the same location between images taken from different positions; that is to say to find the correspondence relationship. The second process is to establish the correspondence between the images taken by the cameras and the real space. Various methods have been proposed to determine these two types of correspondences[5] - [10].

This paper describes newly developed camera calibration method to establish the correspondence relationship between images and the real space. The newly developed method increases calibration accuracy by tracing the rays incident on the lens. The method is presented below, together with the verification results.

2. Issues with Conventional Methods

The intensity value of a pixel in an image taken by a camera is proportional to the strength of the ray incident from a certain point on the target and traveled through space to reach the image sensor of the camera. Conversely, the intensity value can be said to be the brightness of the area struck by a straight line extending from the camera reference position if the ray is traced backwards from the image sensor. For example, the image of the robot appearing on the screen corresponds to the brightness of the rays from each position on the robot that pass through the pinhole and illuminate the screen, when using a pinhole camera model as shown in Fig. 3. That is to say, there is a point light source in the 3D space that corresponds to each pixel.

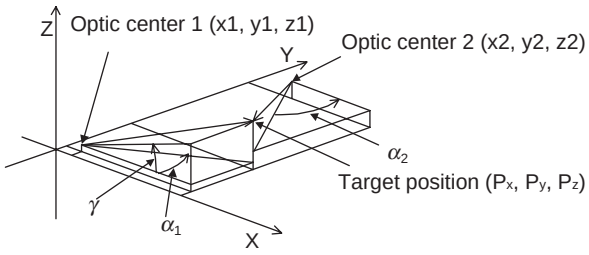


Fig. 2 Coordinate system

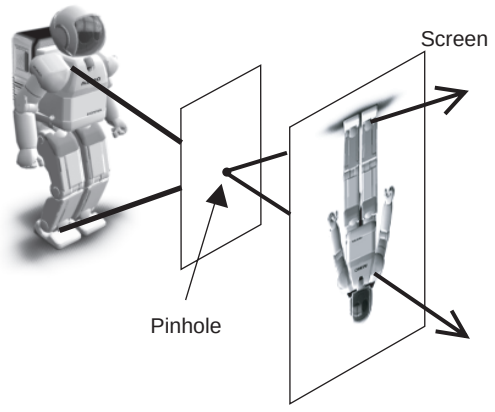


Fig. 3 Pinhole camera model

Camera calibration is the process of establishing the relationship between the positions on this screen, and the path of the light rays passing through the 3D space. The issue of calibration is to estimate these paths.

In a real camera, an image is created by the light passing through the lens assembly. Using a lens normally produces the phenomenon of image distortion whereby straight lines appear as curved lines in the image on a screen. Some types of image processing require an image for which this distortion has been corrected. In these cases as well, distorted image can be corrected to a distortion-free image if the relationship between the positions on screen and the rays is known.

Conventional camera calibration methods estimate the relationship of all pixels by taking a pattern of known size and shape, extracting the positions of several dozen locations with distinguishing features from the image, and then applying a polynomial fit to the relationship between the image position and the actual spatial position. It has been assumed thus far that distortion-free images corrected by the polynomial fit are obtained by the same type of projection as images obtained by pinhole cameras.

In addition, the cameras used by robots must sometimes use a shield in consideration of weather resistance or design factors. These shields are a factor producing irregular and significant image distortion such as that shown in Fig. 4. In these cases, the image distortion cannot be adequately corrected by polynomial-based function approximation, making it impossible to obtain sufficient position estimation accuracy.

3. Calibration Principle and Method

In order to estimate the 3D path of incident rays, this research utilized the principle that if any two points in the space through which a ray passes can be determined, the straight line connecting those two points is the 3D path of that incident ray. Strictly speaking, the ray incident on the lens is an expanding luminous flux, so the path through which the ray passes is not a line. However, in consideration of the fact that the luminous flux is narrowed to an extreme by reducing the aperture of the lens, the luminous flux becomes a single straight line called a principal ray. Here, the principal ray can be thought of as an incident luminous flux that has become a straight line. In addition, as shown in Fig. 2, the path of the ray from the target to the lens is important for image-based 3D measurements, but the internal path of the ray between the lens and the image plane is fixed. Therefore, only the principal ray before entering the lens (“pre-incident principal ray”) is taken into account.

Initially, a simple method for estimating the 3D path of the pre-incident principal ray was considered. Estimation of a ray trajectory utilizes the phenomenon where the position of a light source in the image does not change when the point light source is moved along the path of the ray. First, a point light source is positioned within a 3D space so that the image of the point light source appears in the

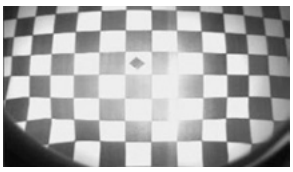


Fig. 4 Example of distorted image

center of a certain pixel, assuming the camera is fixed horizontally. Next, the point light source is moved farther away while maintaining a constant image position on the pixel. The straight line connecting the initial and subsequent positions of the point light source is the path of the pre-incident principal ray. The paths of the pre-incident principal rays for all pixels can be estimated using the procedure above for the entire screen.

Figure 5 shows a 2D representation of this procedure.

However, moving the point light source for the entire screen becomes a challenging issue when this procedure is used for a camera with a wide angle of view, since the point light source must be moved through an enormous space, which makes it impractical.

3.1. Measurement Principle

Instead of moving the point light source, this research used the method of changing the relative 3D position of the point light source by placing the camera on a rotation stage as shown in Fig. 6, and rotating the stage so that the point light source appears at the center of each pixel in the image. The method shown in Fig. 5 moved the point light source vertically while moving it farther away. In contrast, the newly developed method produces relative vertical movement by rotating the camera. As a result, the space needed for this operation is only the narrow range connecting the distant point light source and the camera.

Figure 7 shows a 2D representation of the new method. Here, the camera is rotated so that the light sources located at different distances appear in the center of the same pixel.

In actual measurement, when the light source is moved father away in a straight line, the measurement of continuous intermediate positions are not necessary, and only the first and last positions are sufficient. Therefore, instead of varying the distance for each pixel,

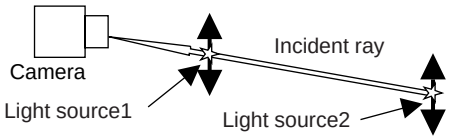


Fig. 5 Simple ray tracing

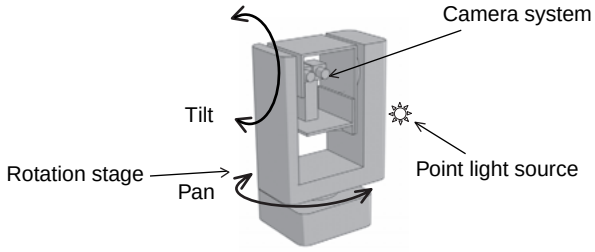


Fig. 6 Relative positions of camera, rotation stage, and point light source

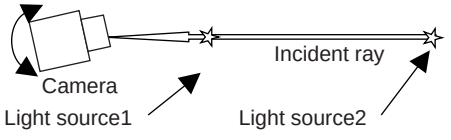


Fig. 7 Ray tracing by new method

the newly developed method obtains the relative positions for all necessary pixels with the fixed point light source, and then repeats the measurements after changing the position of the point light source.

The measurement method for a single measurement cycle is described below.

First, the camera is placed at an appropriate position on a dual axis rotation stage as shown in Fig. 6. The direction in which a light source appears when the camera is rotated by –qtilt and –qpan corresponds to the direction in which the light source appears when the camera is fixed and the light source is rotated by qpan and qtilt around the rotation stage center. (Fig. 8)

The position of the light source at this time (x_1, y_1, z_1) has the following relationship to the position of the light source before rotation $(0_{x1}, 0_{y1}, 0_{z1})$.

$$\begin{pmatrix} x_1 \\ y_1 \\ z_1 \end{pmatrix} = \begin{pmatrix} \cos\theta_{tilt}\cos\theta_{pan} & -\cos\theta_{tilt}\sin\theta_{pan} & \sin\theta_{tilt} \\ \sin\theta_{pan} & \cos\theta_{pan} & 0 \\ -\sin\theta_{tilt}\cos\theta_{pan} & \sin\theta_{tilt}\sin\theta_{pan} & \cos\theta_{tilt} \end{pmatrix} \begin{pmatrix} O_{x1} \\ O_{y1} \\ O_{z1} \end{pmatrix} \quad (2)$$

This position estimation is repeated for all prescribed pixel.

Next, the light source is moved to a position with a different distance to the camera $(0_{x2}, 0_{y2}, 0_{z2})$, and the orientation of the rotation stage is adjusted so that the light source appears in the center of the pixel.

When the respective light source positions are (x_1, y_1, z_1) and (x_2, y_2, z_2) as shown in Fig. 9, the straight line connecting these

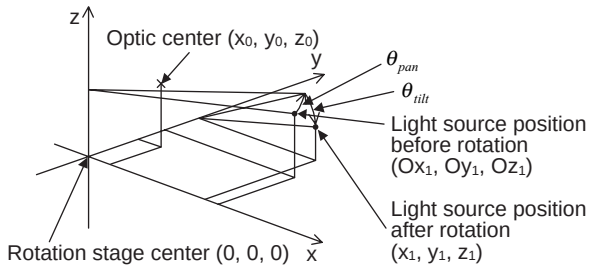
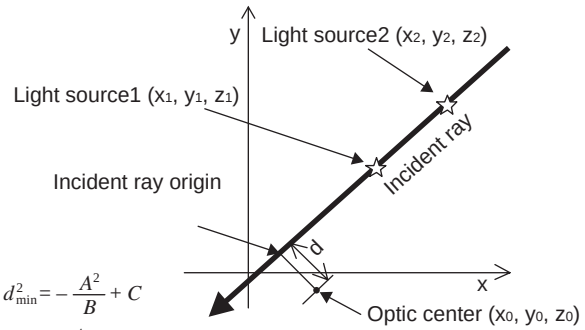


Fig. 8 Relation of positions before and after rotation of camera center and light source



$$d_{\min}^2 = -\frac{A^2}{B} + C$$

$$t_{\min} = -\frac{A}{B}$$

$$A = (x_2 - x_1)(x_1 - x_0) + (y_2 - y_1)(y_1 - y_0) + (z_2 - z_1)(z_1 - z_0)$$

$$B = (x_2 - x_1)^2 + (y_2 - y_1)^2 + (z_2 - z_1)^2$$

$$C = (x_1 - x_0)^2 + (y_1 - y_0)^2 + (z_1 - z_0)^2$$

Fig. 9 Relation between incident light and light source

two positions matches the pre-incident principal ray, and it can be expressed by Eq. (3).

$$\begin{pmatrix} x \\ y \\ z \end{pmatrix} = t \begin{pmatrix} x_2 - x_1 \\ y_2 - y_1 \\ z_2 - z_1 \end{pmatrix} + \begin{pmatrix} x_1 \\ y_1 \\ z_1 \end{pmatrix} \quad (3)$$

This study measured incident rays using the above method, and the results confirmed a deviation from the pinhole camera model in that the rays do not cross at a single point in the manner described by the pinhole camera model. This made it necessary to newly define the principal point that corresponds to the pinhole. This research defined the point at which the sum of the square of the distance d between all incident rays is a minimum as the principal point. In addition, the point at which the distance d from the principal point is a minimum was defined as the base point of the pre-incident principal rays, and the rays are assumed to extend to the light source from this base point.

These definitions make it possible to think of the pre-incident principal ray in separate terms, as those of the base point position (x, y and z in Fig. 2) and the direction (α and γ in Fig. 2). Through this definition, the model is equivalent to the pinhole camera model in case all the base point positions are the same.

3.2. Relative Rotation Method of the Light Source for Each Pixel

The method of displaying the light source in the center of each pixel is described below.

The rotation stage is rotated for each pixel as shown by the processing flow in Fig. 10. The imaging conditions are such that the captured images only show the point light source; that is to say the images show a white spot on a black image. The peak position is estimated as the center of the white spot. When this peak position matches the prescribed pixel with error of constant e or less, the angle of rotation of the rotation base at that time is recorded, and the algorithm moves on to the next pixel. When there is an offset, the offset amount is converted into the corresponding angular value and the stage is rotated by that amount.

The peak position is estimated from the strengths of the adjacent pixels in the top, bottom, left and right directions. When measurements for all prescribed pixels have been finished, the position of the point light source is changed and the process is repeated. After measurement has been performed at different distances, the parameters of the pre-incident principal ray are calculated by the method described in section 3.1, and these results are used as the camera calibration data. When multiple cameras are present, the relative relationship between the cameras is also determined at the same time.

4. Measurement Results of the Pre-Incident Principal Rays

4.1. Measurement Conditions

The cameras used were XC-EI30 (Type 1/3 CCD, 768 × 494 pixels) made by Sony Corporation, and the lenses used were TL-4M (4 mm F2.0) made by TESCOM JAPAN CO., LTD. This combination provides a horizontal view angle of approximately 60°. A frame grabber that performs 8-bit A/D conversion in sync with the pixels was newly developed and used. A double-layer plastic shield was placed in front of two cameras, and the distance between the cameras was approximately 79 mm.

The position of the point light source was varied so that the x coordinate was set at 800 mm and 1 600 mm with the center of rotation of the rotation stage as the origin. The azimuth estimation accuracy was ±0.05 pixels or less.

4.2. Pre-Incident Principal Rays

Figure 11 shows the pre-incident principal rays for the one line in the center of the screen projected onto the X-Y plane. It can be observed that the rays incident from the right hand side of the figure have widening characteristics and thus they do not converge perfectly onto a single point. Widening produced by error in estimating the light source position is approximately 0.3 mm, and the incident rays can be seen here to converge with widening of approximately 0.8 mm, thus verifying deviation from the pinhole camera model. However, note that the straight lines in Fig. 11 are extensions of the pre-incident principal rays, and the actual rays that pass through the lens undergo complex refraction inside the lens. Also, the lens section shown in the figure is a model drawing, and does not represent the actual lens geometry.

The lens used showed a tendency for the base point of the pre-incident principal rays to be located farther back for rays incident from a wider outside angle. Figure 12 shows even greater widening for a super-wide angle lens (TS2V114E made by Pentax Corporation).

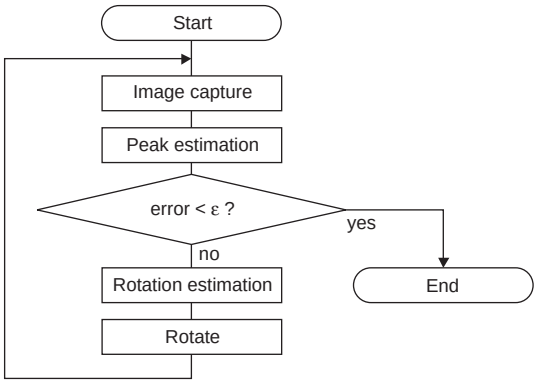


Fig. 10 Direction estimation processing flow

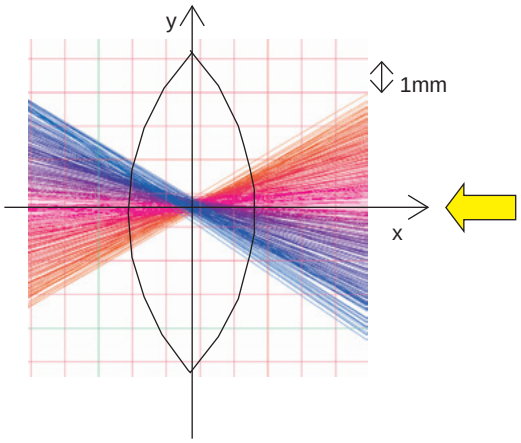


Fig. 11 Incident ray

4.3. Comparison of Accuracy by 3D Position Calculation

In order to compare and verify calibration accuracy with the conventional method, a stereo camera system was configured and calibrated, a point light source was moved to the prescribed positions, and the estimated 3D position of the light source was compared with the actual moved light source position. Comparison was performed for each of the three types of calibration data noted below, both with and without a shield.

Measured values: Measured value data obtained using the newly developed method that takes into account deviation from the pinhole camera model

Approximation values 1: Data approximated using the pinhole camera model, with changes in the base point position eliminated from the measured values, and the principal point matched

Approximation values 2: Data approximated by applying a 5th-order polynomial to the measured values

In addition, the position of the point light source was estimated as follows. The 2D image positions of the point light source were estimated with subpixel accuracy from each of the right and left images. The parameters shown in Fig. 2 that correspond to these image positions were then obtained from the calibration data and applied to Eq. (1) to obtain the 3D position.

The point light source was fixed to 0 in the Z direction, and moved at 0.01 m intervals from 0.8 to 1.6 m in the X direction, and at 0.01 m intervals from –0.4 to 0.4 m in the Y direction.

Generally speaking, the X direction error increases proportionally to the square of the distance, and the Y and Z direction errors increase proportionally to the distance in stereo vision based range estimation methods. Therefore, the error was evaluated by normalization with the square of the distance, and the distance, respectively. For example, when measurement error in the X direction is 12 mm at a position of 2 m, the normalized error is $12/(2^2) = 3$. The measurement is m^{-1} in the X direction, and unitless in the Y and Z directions.

Table 1 summarizes the normalized error (2σ) over the measurement range when there is no shield. The X direction error using measured values with calibration data obtained by the newly developed method was reduced by 50% and 20%, compared to measurement results obtained using calibration data derived from the approximation values 2 and the approximation values 1, respectively.

When the estimation accuracy of the 2D image position of the point light source had error of ±0.5 pixels, the theoretical errors produced by 3D value estimations were 8.7, 0.75 and 1.80 in the X, Y and Z directions, respectively. The measured value errors were half of these amounts, which shows that subpixel estimation in the 2D image works effectively. The reason that a large difference is not seen between Z direction error for the measured values and the approximation values 1 is that only the base point offset contributes to the error.

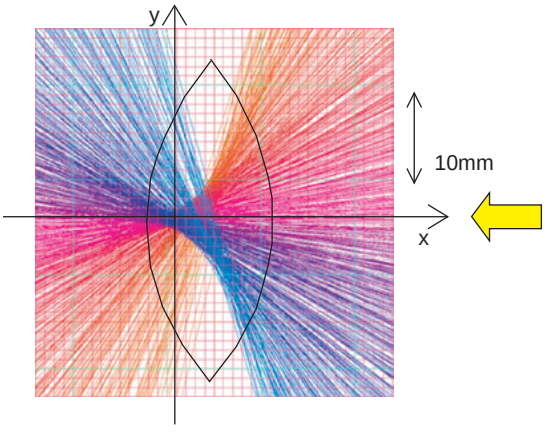


Fig. 12 Ray incident on wide angle lens

Table 1 Difference in error with no shield

	Measured data	Approximation data	
		Pinhole camera	Polynomial
X	±4.2	±5.2	±8.5
Y	±0.23	±0.34	±0.79
Z	±0.22	±0.24	±0.90

Table 2 Difference in error with shield

	Measured data	Approximation data	
		Pinhole camera	Polynomial
X	±4.6	±5.4	±18.5
Y	±0.30	±0.49	±1.28
Z	±0.72	±0.71	±2.80

Table 2 shows the case when a warped shield is attached. This table shows that using measured values reduces the X direction error by 75% and 15% compared to measurement results obtained using the approximation values 2 and the approximation values 1, respectively. The measured value error is greater than when no shield is present, but still less than the approximation values 1 error with no shield.

These results show that the newly developed method achieves calibration with approximately the same accuracy, regardless of whether or not a shield is present. In addition, even when a shield is present, accuracy is higher than when using the pinhole camera model with no shield. Furthermore, there is an obvious improvement in accuracy over the polynomial approximation when irregular distortion is present.

These measurement results showed a reduction in the X direction error of approximately 15 to 20%. However, when using a lens with large aperture, low longitudinal symmetry and complex configuration such as a bright, wide angle lens, the deviation from the pinhole camera model increases as shown in Fig. 12, so this difference is thought to be even greater.

Figures 13 to 15 show 3D graphs of the normalized error in the X direction for the cases when no shields were present. The measured values are shown in Fig. 13, the approximation values 1 in Fig. 14, and the approximation values 2 in Fig. 15. Here, the center of the right camera is located on the x axis of the X-Y coordinate.

The error when using the pinhole camera model increased relative to the measured values at close distances. This is because fluctuation in the base point position due to deviation from the pinhole camera model increases at close distances, where the incident ray angles to the right and left cameras of a stereo camera system increase.

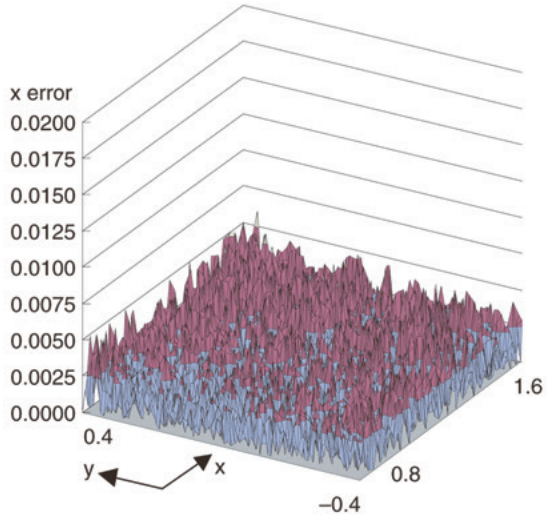


Fig. 13 Measured data with no shield

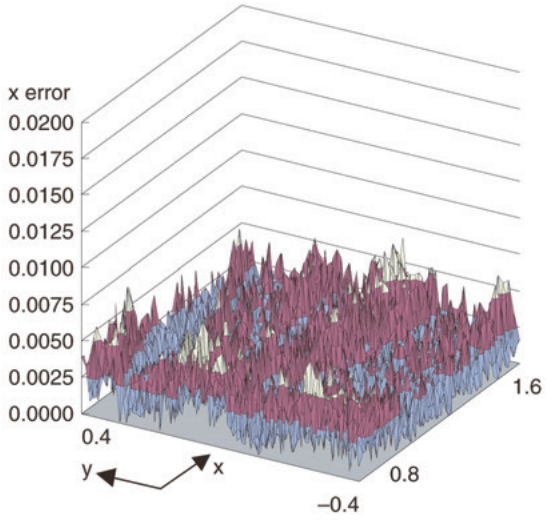


Fig. 16 Measured data with shield

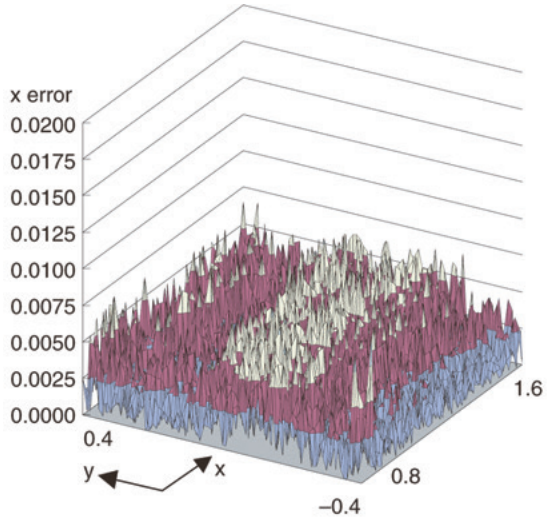


Fig. 14 Pinhole camera model with no shield

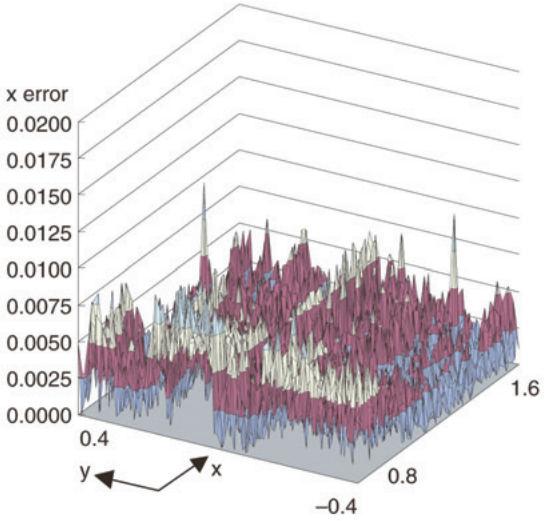


Fig. 17 Pinhole camera model with shield

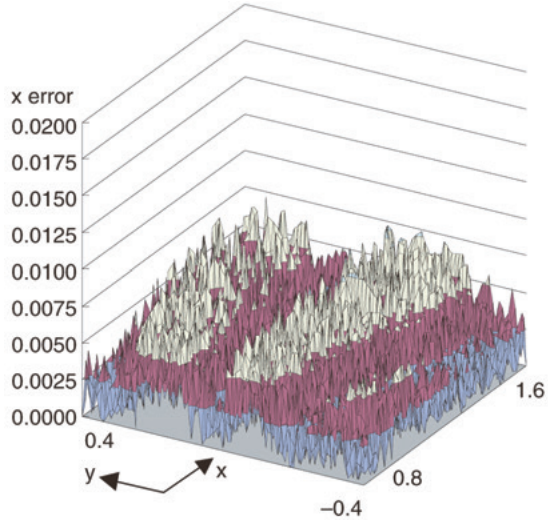


Fig. 15 Polynomial approximation with no shield

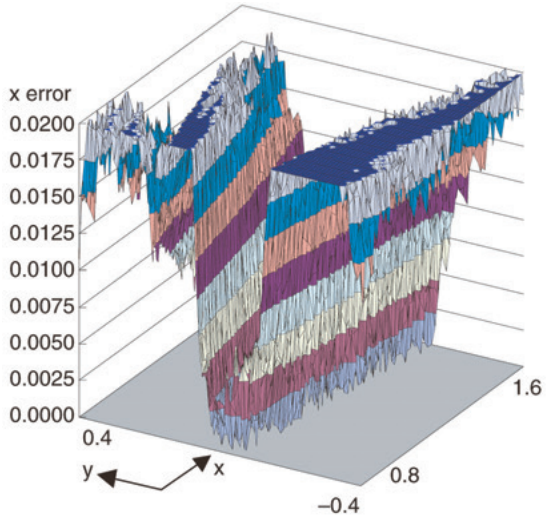


Fig. 18 Polynomial approximation with shield

Figures 16 to 18 show error for the cases when shields were present. Figure 16 shows the measured values, Fig. 17 shows the approximation values 1, and Fig. 18 shows the approximation values 2.

Comparison of Fig. 16 and Fig. 17 shows that the error occurring with the approximation values 1 is also greater at close distances. Figure 18 shows that the distortion cannot be sufficiently corrected over the entire measurement area for the approximation values 2.

As a result, an autonomous robot with two legs and two arms with a shield was able to perform a grasping task that requires accuracy of approximately 1 cm or less including control of the robot system, using this stereo camera system.

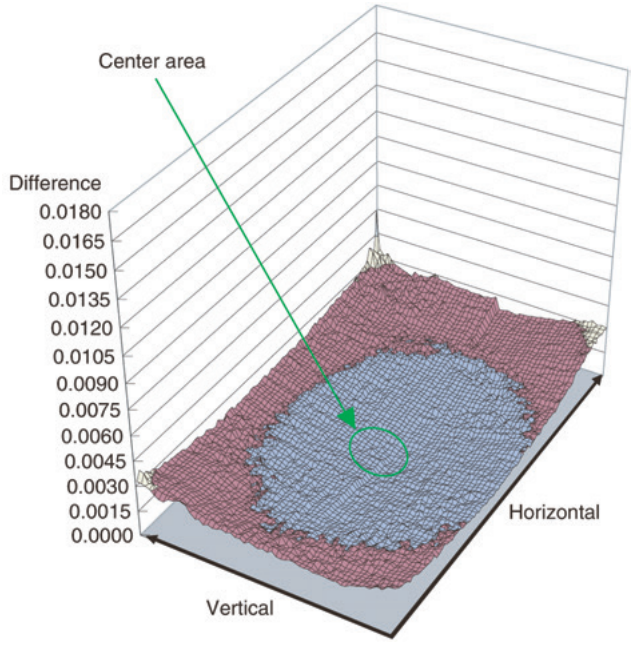


Fig. 19 Error for polynomial approximation with no shield

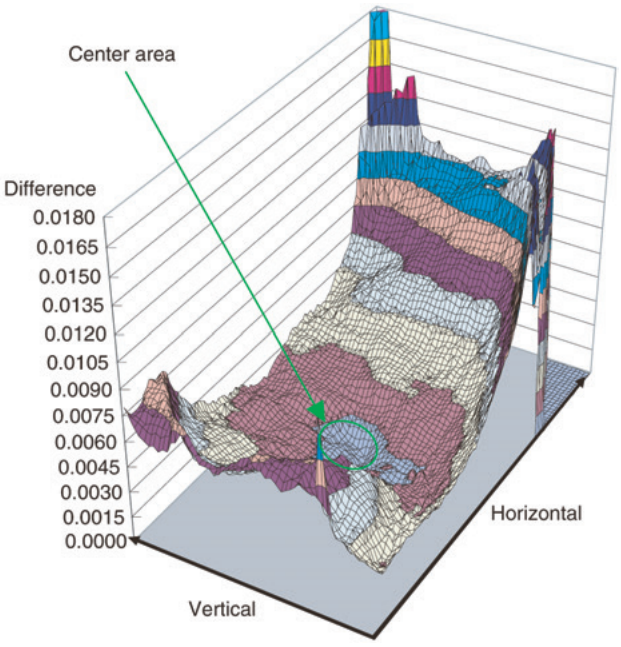


Fig. 20 Error for polynomial approximation with shield

4.4. Irregular Distortion Caused by a Shield

Figures 19 and 20 compare an approximation of distortion by the conventionally used 5th-order polynomial, and measured values obtained by the newly developed system, in order to examine the image distortion irregularity. The lower left portion of the image corresponds to the bottom of the graphs. Tangents of the measured values and approximation values were obtained for the angles a and g shown in Fig. 2, and the square root of the sum of the squares of the difference between tana and tang is displayed on the height axis as the error. Error of one pixel equals approximately 0.0015, and converted to distance error at 1 m, this corresponds to approximately 9 mm in the x direction.

Figure 19 shows the approximation error with no shield, and shows that the error is regular. This error is caused by a spiral offset, so it cannot be eliminated merely by polynomial correction that expands and contracts the image radially from the center of the image distortion.

Figure 20 shows the approximation error with a shield. The undulations in the graph show that the shield causes extremely complex distortion. The range with error of one pixel or less is limited to the purple range around the green circle in the center of the screen. The peripheral areas with error of 0 are areas where calibrations were not performed. This is because the peak positions in these areas could not be estimated due to poor focus, to the extent that there were multiple peaks, and thus the ray path could not be estimated.

5. Conclusion

This paper presented a camera calibration method that takes deviation from the pinhole camera model into account by tracing the path of the rays incident on a camera, and the accuracy of a stereo camera system that uses these measurement results.

This study confirmed the following items.

(1) Camera calibration can be performed accurately, even when there is irregular image distortion.

(2) The incident rays do not converge, and instead spread around the principal point.

A stereo camera system with camera calibration performed using this newly developed method obtained more accurate, relative 3D position estimation results than conventional methods, and made it possible for a robot to perform grasping motion.

References

(1) Sakagami, S., Watanabe, R., Aoyama, C., Matsunaga, S., Higaki, N., Fujimura, K.: The intelligent ASIMO: system overview and integration, Proceedings of the 2002 IEEE/RSJ International Conference on Intelligent Robots and Systems(IROS), Vol. 3, p. 2478-2483 (2002)

(2) Higaki, N., Yokoyama, T., Fujimura, K.: Gesture Recognition Algorithm for Understanding Man-Machine Interaction and Its Adaptation for New ASIMO, HONDA R&D Technical Review, Vol. 15, No.1, p. 95-102 (2003)

(3) Goldberg, S., Maimone, M., Matthies, L.: Stereo Vision and Rover Navigation Software for Planetary Exploration, 2002 IEEE Aerospace conference Proceedings, Vol. 5, p. 2025-2036 (2002)

(4) Sabe, K., Fukuchi, M., Gutmann, J., Ohashi, T., Kawamoto, K., Yoshigahara, T.: Obstacle Avoidance and Path Planning for Humanoid Robots using Stereo Vision, Proceedings of the IEEE International Conference on Robotics and Automation (ICRA), Vol. 1, p. 592-597 (2004)
(5) Faugeras, O., Hotz, B., Mathieu, H., Vieville, T., Zhang, Z., Fua, P., Theron, E., Moll, L., Berry, G., Vuillemin, J., Bertin, P., Proy, C.: Real time correlation-based stereo: algorithm, implementations and applications, INRIA Research Report 2168 (1994)
(6) Kanade, T., Okutomi, M.: A stereo matching algorithm with an adaptive window, IEEE Transactions on Pattern Analysis and Machine Intelligence, Vol. 16, No. 9, p. 920-932 (1994)
(7) Zhang, Z., Deriche, R., Faugeras, O., Luong, Q.: A Robust Technique for Matching Two Uncalibrated Images Through the Recovery of the Unknown Epipolar Geometry, Artificial Intelligence Journal, Vol. 78, p. 87-119 (1996)
(8) TSAI, R.: A Versatile Camera Calibration Techniquie for High-Accuracy 3D Machine Vision Metrology Using Off-theShelf TV Cameras and Lenses, IEEE J. Robotics and Automation, Vol. 3, No. 4, p. 323-344 (1987)
(9) Shih, S.: Accuracy analysis on the estimation of camera parameters for active vision systems, Proceedings of the 13th International Conference on Pattern Recognition, p. 930-5, Vol. 1, (1996)
(10) Shih, S.: Kinematic calibration of a binocular head using stereo vision with the complete and parametrically continuous model, Proceedings of the SPIE - The International Society for optical Engineering, Vol. 1825, p. 643-57 (1992)

■ Author ■



Chiaki AOYAMA

Technical Papers Sumbitted to Out-of-company: July, 2004 to December, 2004

(English Papers only)

Date	Conference	Title	Author	Organization
2004.7.1	American Society of Mechanical Engineers/ Journal of Engineering for Gas Turbines and Power: Transactions of the ASME/ Vol.126	Micro-scale Radial-Flow Compressor Impeller Made of Silicon Nitride-Manufacturing and Performance	Sangkyun Kang James P.Johnston Toshiyuki Arima Minoru Matsunaga Hideaki Tsuru Friedrich B.Printz	Samsung Advanced Institute of Technology Stanford University Wako Research Center Wako Research Center Wako Research Center Stanford University
2004.7.11-16	The American Carbon Society/ Carbon2004 (USA)	Development of Carbon material for Natural Gas Storage	Hiroshi Ogasa	Tochigi R&D Center
2004.7.31	JSAE/ Review of Automotive Engineering Vol.25, No.3	Method of Controlling Arc Welding on an Ultrathin Sheet	Koji Ueda Akira Yanagita Takeshi Yamagami Manabu Murakami	Tochigi R&D Center Tochigi R&D Center Tochigi R&D Center Tochigi R&D Center
		Development of CAE Technology Applicable to the Concept Stage of BIW	Takayuki Fujii Shigeo Fujita Yasushi Yoshizawa	Tochigi R&D Center Tochigi R&D Center Tochigi R&D Center
2004.8.23-27	AVEC2004 technical committee/AVEC2004 (Ahnem, Neitherland)	Optimum Steering and Braking Control Stratagies in Obstacle Avoidance Maneuvers	Shinichiro Horiuchi Shinya Nohtomi Kazuyuki Okada	Nihon University Tochigi R&D Center Tochigi R&D Center
		Vehicle Dynamic feeling Study with a Focus on the On-Center Steering Feeling of North-American Highway Driving	Hiroyuki Tokunaga Jinghong Yu Jed Aston Chad Gilsinger John Shutway	Tochigi R&D Center HONDA R&D AMERICAS, INC. OHIO CENTER HONDA R&D AMERICAS, INC. OHIO CENTER HONDA R&D AMERICAS, INC. OHIO CENTER HONDA R&D AMERICAS, INC. OHIO CENTER
2004.8.30-31	Int. Association of Vehicle System Dynamics (IAVSD)/ 3rd Int. Tyre Colloquium Tyre Models For Vehicle Dynamics Analysis (TMVDA 04)/Int. Journal of Vehicle System Dynamics by Swets & Zeitlinger (Vienna, Austria)	Evaluation of Tire Models for Durability Loads Prediction Using "Suspension on Drum" Environment	Hitoshi Haga	Tochigi R&D Center
2004.9.1	SAE International/ automotive engineering international September 2004	Bringing down the noise	Hideki Matsuoka Tetsuo Mikasa Hirotomi Nemoto	Tochigi R&D Center Tochigi R&D Center Tochigi R&D Center
2004.9.1-4	IEEE Control Systems Society/Conference on Control Applications (Taipei, Taiwan)	Control System Design for Obstacle Avoidance System using Model Predictive Control	Yukihiro Fujiwara Shuichi Adachi	Tochigi R&D Center Utsunomiya University
2004.9.5-9	World Energy Council/19th World Energy Congress/ Energy End-Use Technologies for the 21st Century (Sydney, Australia)	Transportation	Takanori Shiina Robert Shock	Tochigi R&D Center US Lawrance Livermore National Lab.
2004.9.9-10	AVL List GmbH/ 16th International AVL Conference "Engine & Environment"/Engine & Environment 2004 (Graz, Austria)	The New Honda 2.2L i-CTDi Diesel Engine	Kotaro Yamamoto Kenichi Nagahiro Ikuro Hara	Honda R&D Europe (Deutschland) GmbH Tochigi R&D Center Tochigi R&D Center

2004.9.13-14	Institut fur Zweiradsicherheit e. V. /International Motorcycle Conference: Safety-Environment-Future (Munich, Germany)	Exploratory Study of an Airbag for a Large Scooter-Type Motorcycle	Takeshi Kuroe Satoshi Iijima Hideo Namiki	Asaka R&D Center Asaka R&D Center Asaka R&D Center
		Development of Electronically Controlled Hydraulic Rotary Steering Damper for Motorcycles	Takeshi Wakabayashi Kiyotaka Sakai	Asaka R&D Center Asaka R&D Center
2004.9.16-19	The Society of Materials Science, Japan/ The 3rd International Conference on Very High Cycle Fatigue (Shiga, Japan)	Very High Cycle Fatigue Strengths of Thin Sheet Metals	Yoshinari Okada Hitoshi Ishii Takeshi Yamada	Tochigi R&D Center Shizuoka University Shizuoka University
		Evaluation of giga-cycle fatigue property by ultrasonic fatigue testing and its application to automotive parts	Ishii Kazuo Toru Yagasaki Yoshinari Okada	Tochigi R&D Center Tochigi R&D Center Tochigi R&D Center
2004.9.19-22	Organizing Committee Chair/ High Nitrogen Steel 2004 Proceedings (Ostend, Belgium)	High Nitrogen austenitic stainless steel for high temperature applications	Takashi Katsurai Tadao Nishiyama Shuji Hamano Takeshi Koga Tetsuya Shimizu	Tochigi R&D Center Tochigi R&D Center Daido Steel Col., Ltd. Daido Steel Col., Ltd. Daido Steel Col., Ltd.
2004.9.20-22	Active04/Active04 (USA)	Active Nosise and Vibration Control System for the V6-engine with Cylinder-on-Demand System	Toshiro Inoue Hideki Matsuoka Hisashi Sano Hirotomi Nemoto Satoru Minowa	Tochigi R&D Center Tochigi R&D Center Tochigi R&D Center Tochigi R&D Center Tochigi R&D Center
	ISMA/ ISMA2004 International Conference on Noise and Vibration Engineering (Leuven, Belgium)	Sensitivity Analysis for Structural Optimization Using Eigenvalue and Eigenvector of Component Stiffness Matrix	Kohei Furuya Takuya Yoshimura Akira Suto Koji Saito	Tokyo Metropolitan University Tokyo Metropolitan University Tochigi R&D Center Tochigi R&D Center
2004.9.21-23	The S2P International Conferences/ The 8 th International Conference S2P Semi Solid Processing of Alloys and Composites (Cyprus, Greece)	Establishment of a Manufacturing Technology for the High Strength Aluminum Cylinder Block of Diesel Engine Applying a Rheocasting Process	Masakazu Yamazaki Koichi Kuroki Tetsuji Umemoto Takahiro Suenaga Atsushi Suzuki Takeshi Masaki	Tochigi R&D Center Honda Engineering Co., Ltd. Honda Engineering Co., Ltd. Honda Engineering Co., Ltd. Honda Engineering Co., Ltd. Honda Engineering Co., Ltd.
2004.9.27-30	SAE/2004 Small Engine Technology Conference and Exhibition (Graz, Austria)	Development of Positive Crankcase Ventilation System of Four-stroke Engine for Small Motorcycles	Ryuji Moriyama Yuki Muraoka Kazuo Fujihara	Asaka R&D Center Asaka R&D Center Asaka R&D Center
		Practical Application of Combustion Simulation Using CFD for Small Engine of Two-Wheeled Vehicle	Yasuo Murakami Hitoshi Kurosaka Hiroshi Kamiya	Asaka R&D Center Asaka R&D Center Asaka R&D Center
		Development of Rolling Bearing Model for Mechanical Dynamic Analysis Considering Elastic Properties	Junya Saito Tatsuya Iwamoto Osamu Kudo	Asaka R&D Center Asaka R&D Center Asaka R&D Center
		Establishment of Analysis Method for Pulse Feeling of Four-Stroke, V-twin Engine, American-type Motorcycles	Kunihiro Osada Ryuta Niimura Keikichi Shimokobe	Asaka R&D Center Asaka R&D Center Asaka R&D Center
		Research into New Emission Control Techniques for Motorcycles to Achieve the EURO-3 Regulation	Shunji Akamatsu Tomoya Kono Mamoru Uraki Hiroaki Miyata	Asaka R&D Center Asaka R&D Center Asaka R&D Center Asaka R&D Center
		A Trial of Improving Thermal Efficiency by Active Piston Control —Speed Control Effect of Combustion Chamber Volume Variation on Thermal Efficiency—	Masatoshi Suzuki Satoshi Iijima Yasuo Moriyoshi Masaki Sano	Asaka R&D Center Asaka R&D Center Chiba University Chiba University

		Numerical Examinations on the Effect of Active Piston-Movement Control	Yasuo Moriyoshi Masaki Sano Masatoshi Suzuki Satoshi Iijima	Chiba University Chiba University Asaka R&D Center Asaka R&D Center
		Study of Coaxial Counter Rotating Rotary Tilling System at Front Rotary Type Compact Walking Tractor	Yoshitaka Ohta Susumu Ohkubo Keiji Iino Masatoshi Nagaoka Keiji Nagano Nobuchika Katagiri	Asakahigashi R&D Center Asakahigashi R&D Center Asakahigashi R&D Center Asakahigashi R&D Center Asakahigashi R&D Center Asakahigashi R&D Center
		Development of Easy Operation Control System for Small Hybrid Snow Thrower	Tsutomu Wakitani Yoshihiko Yamagishi Toshiaki Kawakami Tsutomu Mizoroke	Asakahigashi R&D Center Asakahigashi R&D Center Asakahigashi R&D Center Asakahigashi R&D Center
2004.9.28-30	Global Powertrain Congress/ Global Powertrain Congress (USA)	Development of V6 Engine with Variable Cylinder Management	Katsumi Noguchi Masayuki Ichige Makoto Segawa Hideki Matsuoka	Tochigi R&D Center Tochigi R&D Center Tochigi R&D Center Tochigi R&D Center
2004.9.29-30	VDI Wissensforum IWB GmbH/ Numerical Analysis and Simulation in Vehicle Engineering/ VDI-Berichte1846-(2004) 603-615 (Wurzburg, Germany)	New Body-in-White Concept through Topology Optimisation	Takayuki Fujii Yasuhiko Sato Sadato Shibuya Udo Jankowski Martin Muller Bechtel Peter Schneider	Tochigi R&D Center HONDA R&D EUROPE (DEUTSCHLAND) GMBH Tochigi R&D Center TECOSIM GmbH TECOSIM GmbH TECOSIM GmbH
2004.10.4-6	Institut fur Kraftfahrwesen Aachen/ 13th AACHEN COLLOQUIUM “Automobile and Engine Technology” (Aachen, Germany)	Study on Gasoline HCCI Engine Equipped with Electromagnetic Variable Valve Timing System	Yasuhiro Urata Moriyoshi Awasaka Junichi Takanashi Noritaka Kimura	Tochigi R&D Center Tochigi R&D Center Tochigi R&D Center Tochigi R&D Center
		The New 2.2L Diesel Engine for Passenger Cars from HONDA	Ikuro Hara Isao Kaneko Kenji Fujiki Masami Ohshima	Tochigi R&D Center Tochigi R&D Center Tochigi R&D Center Tochigi R&D Center
		Technical Description of the IMA System	Hiromitsu Sato	Tochigi R&D Center
2004.10.12	SAE International/ SAE Brake Colloquium & Exhibition, Panelist for panel discussion (Anaheim, USA)	Brake NVH -Approach method & subjects for Vehicle development	Takeshi Ito Noriyuki Sato Tetsuya Yamaguchi	Tochigi R&D Center Tochigi R&D Center Tochigi R&D Center
2004.10.18-22	ITS Japan/ 11th World Congress on ITS NAGOYA (Nagoya, Japan)	Research of Collision Mitigation brake System	Kenji Kodaka	Tochigi R&D Center
		Data Transmission Measurement with DSRC type Experimental Equipment of Inter-Vehicle Communication	Hiroshi Mashimo Nobuyoshi Asanuma Hideo Tsutsui Kiyohito Tokuda	Tochigi R&D Center Tochigi R&D Center Oki Electric Industry Co., Ltd. Oki Electric Industry Co., Ltd.
		Evaluation Method of Motorcycle Driver’s Distraction with Using Riding Simulator	Mutsumi Katayama Yutaka Kamata	Asaka R&D Center Asaka R&D Center
2004.10.25-28	SAE/ 2004 SAE Powertrain & Fluid Systems Conference & Exhibition (Tampa, USA)	A Study of Shockless Combustion Change Control of Direct Injection Gasoline Engine	Ken Ogawa Isao Komoriya Hiroshi Tagami Masahiro Takeuchi	Tochigi R&D Center Tochigi R&D Center Tochigi R&D Center Tochigi R&D Center
		DEVELOPMENT OF A HIGH PERFORMANCE AND HIGH FUEL ECONOMY FOUR-VALVE DIRECT-INJECTION ENGINE WITH A CENTER-INJECTION SYSTEM	Kaoru Horie Yutaka Kohda Ken Ogawa Hiroyuki Goto	Tochigi R&D Center Tochigi R&D Center Tochigi R&D Center Tochigi R&D Center

2004.10.26 -28	The International Association for Natural Gas Vehicles (IANGV)/ NGV2004 (Buenos Aires, Argentina)	Development of Light Weight Fuel Container for Adsorbed Natural Gas Vehicles	Nagatsugu Mukaibo Mitsuru Sayama Hiroshi Ogasa	Tochigi R&D Center Tochigi R&D Center Tochigi R&D Center
		Development of Adsorbent for Natural Gas Storage	Hiroshi Ogasa Yoshiyuki Morita	Tochigi R&D Center Tochigi R&D Center
2004.10.30	JSAE/ Review of Automotive Engineering Vol.25, No.4	Automotive Air Conditioning System Control Countermeasures for Uneven Solar Radiation at Low Solar Altitudes	Isao Tsunoda	Tochigi R&D Center
2004.10.30 -11.2	The Japan Society of Mechanical Engineers/ Design & Systems Division/ CJK-OSM3 95-100 (Kanazawa, Japan)	Practical Multi-discriplinary/Multi-objective Shape Optimization System for conceptual vehicle body design	Takayuki Fujii Satoshi Miyata Motoyuki Hotta	Tochigi R&D Center Engineous Japan, Inc. Engineous Japan, Inc.
2004.12.14 -16	The Molecular Simulation Society of Japan/ The 18th Conference on Molecular Simulation (Kyoto, Japan)	First-principles Molecular Dynamics Approach to Vibrationally Excited States Dynamics of Water	Masahiro Hirota Masayoshi Kitada Hajime Hirata Ewa Broclawic Keiko Chiba Yumiko Sasaki Hideyuki Tsuboi Michihisa Koyama Momoji Kubo Akira Miyamoto	Tochigi R&D Center Tochigi R&D Center Tochigi R&D Center Tohoku University Tohoku University Graduate School Tohoku University Graduate School Tohoku University Tohoku University Graduate School Tohoku University Graduate School Tohoku University Graduate School
2004.12.20	JSAE/ AVEC International Work Shop 2004 (Tokyo, Japan)	Collision Mitigation brake System	Kenji Kodaka	Tochigi R&D Center
2004.12.23	SAE/ SAE 2003 Transactions	Rear-end Collision Velocity Reduction System	Kenji Kodaka Makoto Otabe Yoshihiro Urai Hiroyuki Koike	Tochigi R&D Center Tochigi R&D Center Tochigi R&D Center Tochigi R&D Center

Editor's Postscript

The work of writing technical reports and papers can be considered an integral part of development and research activities. It should be considered that the research and development works have not been completed until the research results is reported in writing. Paper is the evidence that this research was accomplished before it was done anywhere else, and writing the paper should be one of the important rights of the engineer.

Engineers, however, set aside their time for everyday research activities. For one who is unaccustomed to writing, when the engineer decides to write a technical paper, the engineer understands the difficulty of organizing research results and putting them into writing again. The point is not to simply write down what one did in the research just in the order things were done. Rather, the activity of technical writing involves an opportunity to rethink what are the true issues, the novelty, the originality, the utility. Also it involves the difficulties to make sentences and to think how to organize and present the materials so that people can understand what is presented in the paper. In other words, engineers realize that the technical paper has a mission it must fulfill, which is to convey research results to people in an easily understandable form.

Writing this editor's postscript turned out to be an exercise in rethinking the significance of the act of writing, separately from the creation of technical documentation. It made me wonder whether I could handle the assignment of writing so that readers would pick up the assertions contained within the text, and so that the content would remain in their memories the way a moving novel lingers in the mind when one has finished reading it. Needless to say, I myself am not a literary writer, so I do not expect to be able to accomplish anything as fine as that. Even as I think this, however, I see that 16 years have passed since I first contributed a paper to Volume 1 of the *Honda R&D Technical Review*, and now here I have become a member of the editorial board and we are up to Volume 17. I have had a number of opportunities to contribute papers during the intervening period, but sometimes I have asked myself whether I have made much progress in my writing ability.

Nevertheless, recording research and engineering results in writing is to create a document that conveys that content while at the same time making a contribution to society in the form of that writing. *The Technical Review* provides us the ideal opportunity to make the most of that possibility as well as the proof that we did indeed live as Honda engineers during that particular time. The existence of this *Technical Review* is our great good fortune, and I am extremely grateful.

It is my hope that many engineers will continue in the times ahead to make active use of the *Technical Review* as a technical communication tool. That is, by contributing papers here, they can experience the effort of putting their research results into organized written form, and of presenting them to the world, in addition to which they will receive evaluations by other engineers.

(Yamashita)

Honda R&D Technical Review English Version Vol.17 No.1

The following associates provided us with their cooperation and expertise:

Matt	Alexander	Honda R&D Americas, Inc. Ohio Center
Karen	Arneson	American Honda Motor Co., Inc.
Bobbie	Burke	Honda R&D Americas, Inc. Ohio Center
Matt	Chany	Honda R&D Americas, Inc. Ohio Center
Mary	Christopherson	Honda North America, Inc.
Dennis	Chung	Honda R&D Americas, Inc. Ohio Center
Paul	Dehart	Honda R&D Americas, Inc. Ohio Center
Brian	Doklovic	Honda R&D Americas, Inc. Ohio Center
Andrew	Fox	Honda R&D Americas, Inc. Ohio Center
Lee	Goldring	Honda North America, Inc.
Hisayuki	Goma	Honda R&D Americas, Inc. Ohio Center
Ian	Haggerty	Honda R&D Americas, Inc. Ohio Center
Saemi	Hirayama	Honda R&D Americas, Inc. Ohio Center
Hiroshi	Inutsuka	Honda R&D Americas, Inc. Ohio Center
Tsuyoshi	Ishii	Honda R&D Americas, Inc. Ohio Center
Michael	Ishmael	Honda R&D Americas, Inc. Ohio Center
Tony	Mascadri	Honda R&D Americas, Inc. Ohio Center
Tad	Nishimura	Honda R&D Americas, Inc. Ohio Center
Daryl	Nolt	Honda R&D Americas, Inc. Ohio Center
Brian	Nutwell	Honda R&D Americas, Inc. Ohio Center
Richard	Owens	Honda R&D Americas, Inc. Ohio Center
Derek	Scheetz	Honda R&D Americas, Inc. Ohio Center
Kyle	Vargason	Honda R&D Americas, Inc. Ohio Center
Adam	Wangerin	Honda R&D Americas, Inc. Ohio Center
Mark	Wenden	Honda R&D Americas, Inc. Ohio Center
William	Willen	American Honda Motor Co., Inc.

